AFIT/DS/AA/93-4

CHARACTERIZATION OF FATIGUE DAMAGE IN A METAL MATRIX COMPOSITE (SCS-6/TI-15-3) AT ELEVATED TEMPERATURE

DISSERTATION

Brian P. Sanders, Captain, USAF

AFIT/DS/AA/93-4

Approved for public release; distribution unlimited

AFIT/DS/AA/93-4

CHARACTERIZATION OF FATIGUE DAMAGE IN A METAL MATRIX COMPOSITE (SCS-6/TI-15-3) AT ELEVATED TEMPERATURE

DISSERTATION

Presented to the Faculty of the Graduate School of Engineering

of the Air Force Institute of Technology

Air University

In Partial Fulfillment of the

Requirements for the Degree of

Doctor of Philosophy

Brian P. Sanders, B.S., M.S.
Captain, USAF

November 1993

Approved for public release; distribution unlimited

AFIT/DS/AA/93-4

CHARACTERIZATION OF FATIGUE DAMAGE IN A METAL MATRIX COMPOSITE (SCS-6/TI-15-3) AT ELEVATED TEMPERATURE

Brian P. Sanders, B.S., M.S.
Captain, USAF

Approved:

[signature]	3 Dec 1993
[signature]	3 Dec 1993
[signature]	3 Dec 1993
[signature]	3 Dec 1993

Accepted:

[signature]

Institute Senior Dean

Acknowledgements

I would like to thank the Air Force Office of Scientific Research for sponsoring this work. Without this support I would have no material and therefore no test data.

I would like to express my deepest gratitude to my advisor, Professor Shankar Mall, who had faith when others did not. He always managed to clear the fog and gently guide me in the right direction when I was going astray. However, he also provided me with the freedom to explore almost any area I chose, even when the outcome was completely unclear. Additionally, I would like to thank all the other Professors at the Air Force Institute of Technology (AFIT) under whom I studied under. They reignited my interest in the fundamentals of engineering and mathematics that I had almost lost, but I surely never will again.

I would like to thank all of the AFIT Aerospace Department Laboratory Technicians, Mark, Jay (The Ultimate Technician), Andy, and Dan (The SEM Man). They never failed to provide me with anything I asked for or any assistance I requested (no matter how crazy the idea was).

Finally, I would like to extend my love and appreciation to my wife, Cathy. She put up with me through all the odd hours, lost weekends, and other times during

this endeavor when I was being extremely difficult. We were married 3 weeks before I entered the program, so maybe now we can actually have a normal marriage.

Table of Contents

List of Figures

List of Tables

Abstract

The fatigue characteristics of a unidirectional titanium based Metal Matrix Composite (MMC) were investigated at elevated temperature (427°). A hybrid strain controlled loading mode was used to subject the 0° and 90° laminas to fatigue. This hybrid control mode did not allow the MMC to experience any compressive stresses on the lamina level.

To fully understand the fatigue behavior of the MMC under this hybrid strain control mode, fatigue tests, microscopy, and analytical modeling were performed concurrently. First, the fatigue tests provided data on the fatigue life and mechanical response of the MMC. Second, the initiation and progression of fatigue damage mechanisms were identified using several microscopy techniques. Using this information, fatigue life curves were generated, which related the specimen fatigue life and damage mechanisms to the applied strain level. Third, analysis techniques were applied to predict the stress-strain response of the MMC. This provided further insight into the lamina fatigue behavior.

Based on this combination of activities, the initiation and progression of damage and deformation in the laminas were identified. When loading was parallel to the fiber direction, the fatigue behavior was initially dominated by

creep deformation of the matrix. This was accompanied by plastic deformation of the matrix for those specimens subjected to fatigue above a maximum strain of .55%. Then, depending on the maximum strain, the specimen failure was a result of either fiber fractures or the development and progression of matrix cracks. In contrast, when loading was perpendicular to the fiber direction, the fatigue response was first dominated by the initiation of fiber-matrix interface damage. Then, if the maximum strain was greater than .35%, the dominate damage mechanism was matrix cracks. Below this strain level, the damage was a mixture of small matrix cracks and the propagation of fiber-matrix interface damage. Further, the analysis for this loading direction included unique methods to account for the fiber-matrix interface damage. This hybrid approach involving experiments, microscopy, and analytical modeling provided a better understanding of the fatigue behavior of the MMC.

CHARACTERIZATION OF FATIGUE DAMAGE IN A METAL MATRIX COMPOSITE (SCS-6/Ti-15-3) AT ELEVATED TEMPERATURE

I. Introduction

Increasing interest in programs such as the National Aerospace Plane (NASP) and High Temperature Engine Technology Program (HITEMP) have sparked a search for new materials that can withstand severe environments such as thermomechanical loadings. Metal Matrix Composites (MMC) offer a promising solution. These composites are composed of a high strength, light weight, metal alloy matrix reinforced with high strength fibers which provide high specific stiffness. This combination of materials can be used at elevated temperatures without any serious degradation of mechanical properties.

The structures designed with these materials will experience a variety of temperature and loading conditions. Figure 1.1 shows the typical temperature and load profiles for an aircraft engine turbine disk. Furthermore, leading edge temperatures for applications such as the NASP are expected to exceed 1100°C (2000°F) [47]. These examples

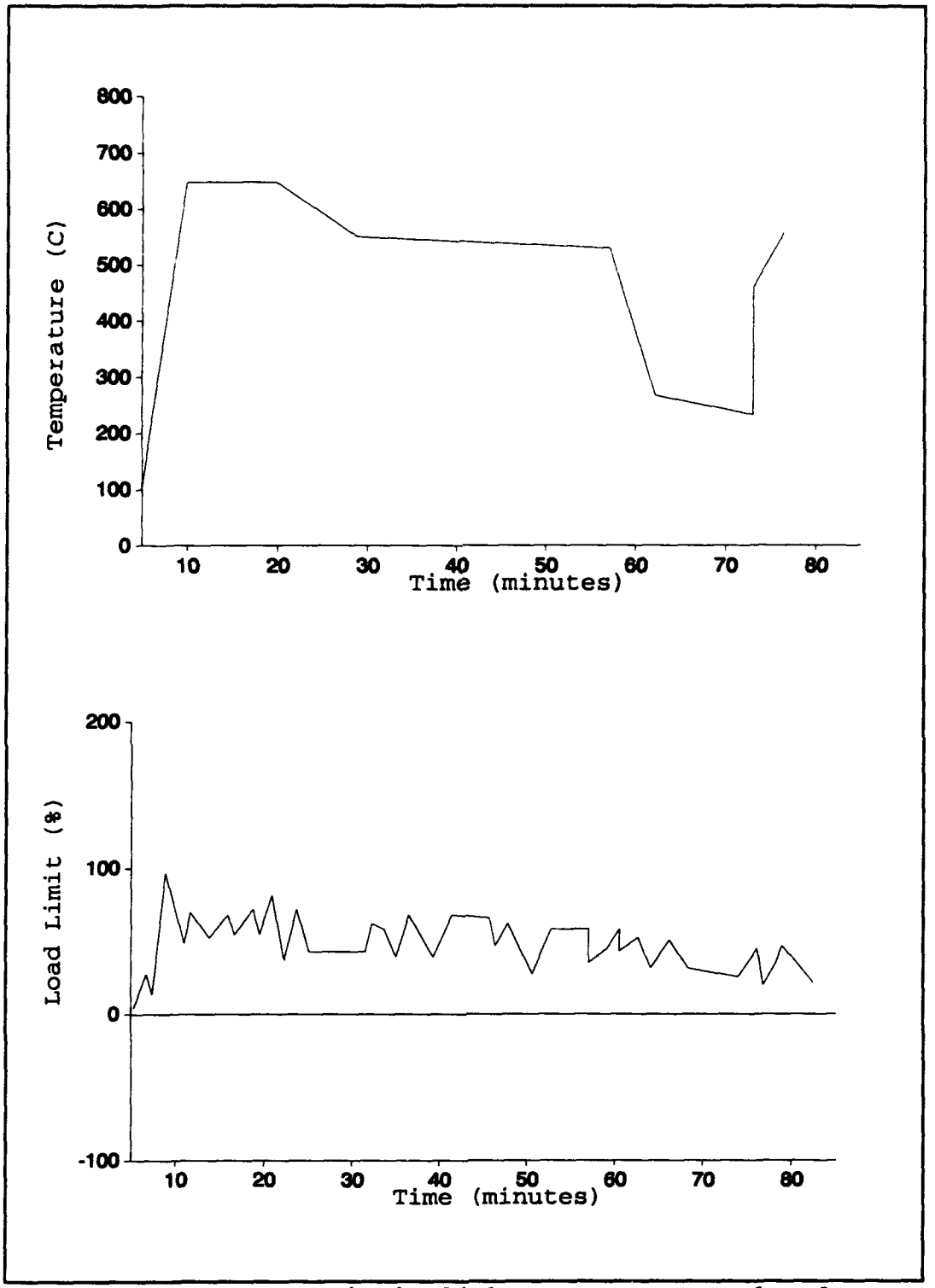

Figure 1.1 Typical Flight Component Load and Temperature Profiles [88]

demonstrate the need for understanding the thermomechanical fatigue (TMF) response of a MMC.

MMCs have properties useful for high temperature applications. However, they have some characteristics that result in unique damage mechanisms and prevent existing analysis tools from accurately predicting their fatigue response. Perhaps the most evident problem stems from a mismatch in the coefficient of thermal expansion (CTE). Although both materials have low CTEs, the CTE of the matrix is typically much larger than that of the fiber. This mismatch results in two major problems. First, large residual thermal stresses develop as the composite is cooled down from the processing temperature. When the matrix CTE is larger than the fiber, the longitudinal and hoop stresses of the matrix are tensile while the corresponding fiber stresses are compressive (Figure 1.2). These residual thermal stresses may induce damage in the as-received composite [26, 68, 102]. Second, when the MMC is subjected to thermal fatigue, the matrix expands and contracts at a different rate than the fiber. This results in thermomechanical fatigue of the fiber-matrix interface. Newaz and Majumdar [80], and Mall and Ermer [71] have found that matrix microcracks develop when the MMC was exposed only to thermal cycling.

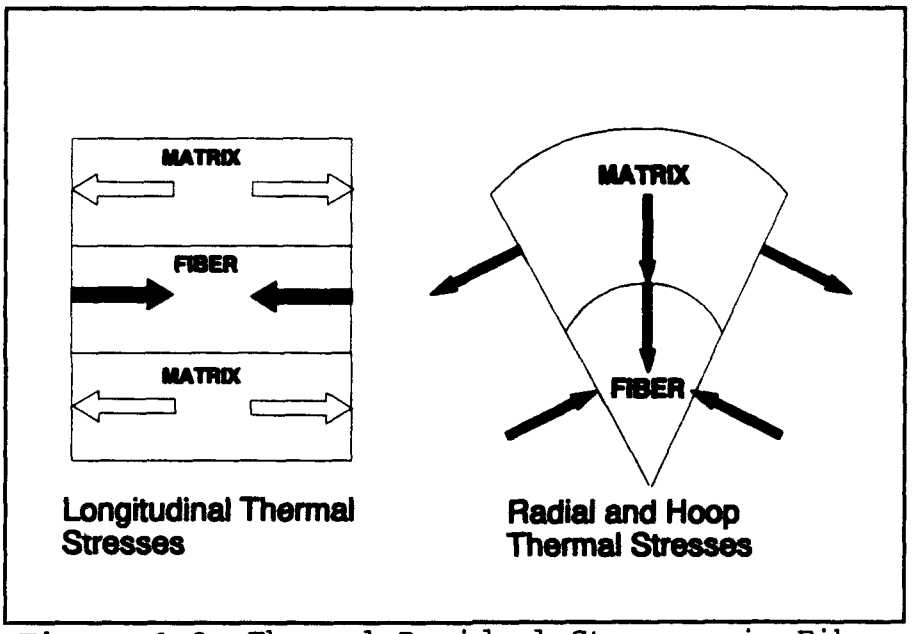

Figure 1.2 Thermal Residual Stresses in Fiber and Matrix

Another unique characteristic of MMCs is the interphase or reaction zone between the fiber and the matrix (Figure 1.3). This interphase zone results from the high reactivity of the titanium matrix with the carbon-rich coating on the fibers [60]. Johnson et al. [54] showed that both fiber and matrix material exists in this zone, so effectively a third material is present. To analyze a composite with an interphase zone, Hopkins and Chamis [48] have developed a unique set of equations. This set of equations modifies the traditional rule of mixtures to include the effects of this zone on the lamina response. However, the properties of the interphase zone are difficult to predict, and it is unstable when subjected to fatigue. A few studies [26, 89, 101] have

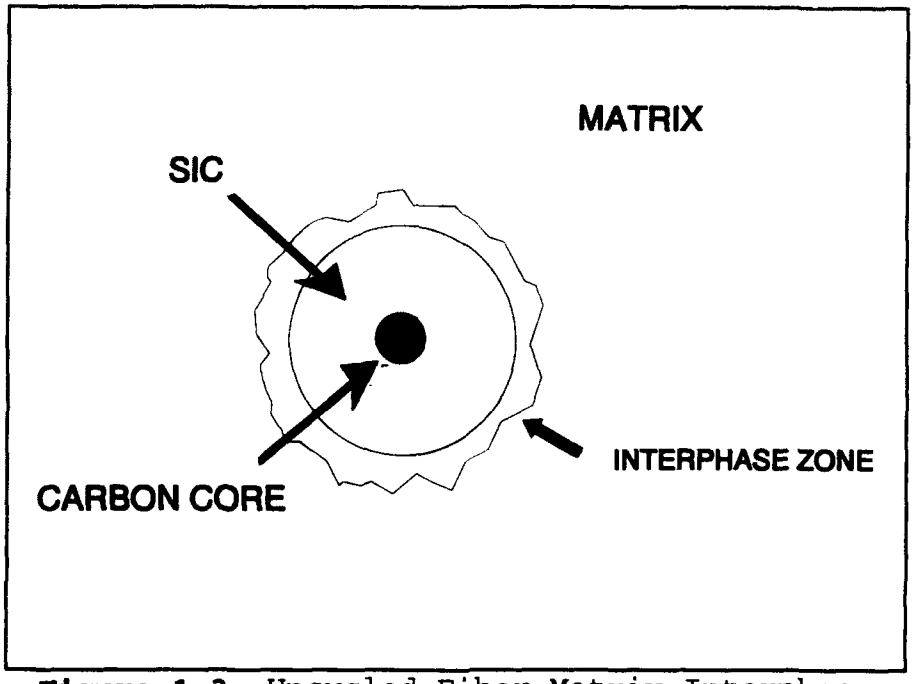

Figure 1.3 Uncycled Fiber-Matrix Interphase Zone

shown that the interphase zone grows, cracks, and separates from the fiber under thermal, isothermal, and thermomechanical loading conditions.

Virtually every investigation of a MMC has identified the interphase zone and residual thermal stresses as key elements toward understanding the initiation and progression of fatigue damage. Therefore, any study of a MMC must carefully consider these two special areas.

Although understanding the TMF characteristics of MMCs is important, few experimental investigations have been conducted for these materials. Several of these [30-35] have been performed under the load control mode. According

to Mitchell [78], materials in most engineering applications are actually strain controlled, but only a few investigations [35, 9] have been performed using this loading condition. Hence, there is a need for additional comprehensive investigations of MMCs under the strain controlled loading mode.

The objective of this study was to provide a foundation for MMC lamina to laminate relationships in the TMF environment under the strain controlled loading mode. This is best achieved by first understanding the fatigue behavior of a unidirectional MMC in isothermal conditions. Obtaining a thorough understanding of the MMC in this environment requires a combination of fatigue testing, microscopy, and analytical modeling. This research investigated the lamina mechanical response and fatigue life versus strain range relationships, and the initiation and progression of damage dependence on the applied strain range. Micromechanical analysis techniques were applied to understand the lamina stress response as a function of fatigue cycles. This established a complete picture of the lamina fatigue behavior, which can be extended in future work to understand the behavior of multi-angle laminates.

The objective of the research was accomplished by performing fatigue tests on a model MMC. The MMC chosen for this research was the Ti-15V-3Cr-3Al-3SN (w/o) or Ti-15-3

alloy reinforced with 36 volume percent continuous silicon carbide fibers (SCS-6). This composite has a high strength-to-weight ratio, good thermal resistance, and is designed for applications up to 704°C [67]. The fatigue environment was a hybrid strain control mode [9] at 427°C. Several fatigue tests were performed on the SCS-6/Ti-15-3 unidirectional MMC and the Ti-15-3 unreinforced alloy or neat matrix. For the MMC, the fatigue tests were conducted with the fibers parallel and perpendicular to the loading direction. The results from these tests provided information on the MMC mechanical response and fatigue cycles to failure. Also, fatigue life curves, as a function of the applied strain, were generated. Microscopy techniques were then used to identify the following fatigue damage and deformation mechanisms: (1) fiber fractures, (2) fiber-matrix interface damage, (3) matrix cracks, (4) matrix plastic deformation, and (5) matrix creep deformation. Combining the results from the experiments and microscopic analysis, the fatigue curves were partitioned to reflect a relationship between strain range, fatigue life, and the dominant damage and deformation mechanisms.

Micromechanics techniques were applied to predict the fatigue response of the MMC. A concentric cylinder model was employed to model the longitudinal (fibers parallel to the loading direction) fatigue behavior of the MMC. On the

other hand, a unit cell model was used to predict the MMC transverse (fibers perpendicular to the loading direction) fatigue behavior. A unique method was proposed to include the fiber-matrix interface damage observed in the transversely loaded MMC. Only one static test at the desired application temperature was required to calibrate this model. Also, an empirical scheme was proposed to characterize the elastic-viscoplastic deformation of the matrix. The scheme required data obtained from only a few relaxation tests and a static test conducted on the neat matrix. This analysis provided an insight into the MMC fatigue behavior that could not be experimentally measured or observed through the microscopic analysis.

This dissertation contains a description of the above mentioned efforts. First, previous experimental and analytical investigations of MMCs are reviewed. Second, a complete description of the test equipment and techniques used in this study is provided. Third, a discussion of the experimental results is presented. This includes examples of the lamina mechanical response, microscopy analyses, and fatigue life analyses. Fourth, a description of the micromechanical models and the results obtained from these models are presented and compared to the experimental results. Fifth, the conclusions and recommendations that were drawn from this work are discussed.

II. Background

Previous studies of Metal Matrix Composites (MMCs) have focused on building an understanding of the thermal fatigue, isothermal fatigue, and thermomechanical fatigue response of these materials. Both experimental and analytical investigations have been performed in an attempt to characterize MMCs under these conditions. This chapter provides a brief review of some previous studies. A background of frequently used terminology and testing techniques are discussed first. This is followed by a review of recent experimental investigations and some models currently available for the analysis of MMCs. Finally, a brief introduction to the models used in this study are presented.

Thermomechanical Testing of MMCs

Experimental Techniques

The first step in characterizing the fatigue behavior of a MMC is to understand the environment to which the material will be exposed in actual aerospace applications. Figure 1.1 showed typical load and temperature profiles which may be experienced by a MMC component. These profiles are quite complex. Before getting to this level, the MMC must first be tested in more basic and controlled

environments. These simplified conditions enable the researcher to isolate certain fatigue characteristics. It provides the basics and a good start to understand the more complex behavior. This section discusses some of the typical loading conditions used to characterize the behavior of MMCs.

Control Mode

MMCs are typically subjected to fatigue using either the load or strain control mode. Both of these terms are frequently used throughout this dissertation and are described here. In the load control mode, the load applied to the specimen is the independent variable, and the strain is the dependent variable. The load range is determined by the ratio of the minimum stress to the maximum stress:

$$R=\frac{\sigma_{min}}{\sigma_{max}} \qquad (1.1)$$

R is typically greater than zero so that the specimen is not subjected to compressive stresses. Since the specimen will not buckle under these conditions, this allows for the use of a thinner, less expensive, MMC. For many aerospace applications materials are strain controlled [78], so testing a MMC in this manner is desirable. In this control mode, the strain is the independent variable, and the load is the dependent variable.

A special consideration when using the strain control mode is buckling of the test specimen. When a MMC is subjected to fatigue at elevated temperatures, matrix creep deformation will result in a relaxation of the composite stress without a loss in stiffness. Compressive loads are then required to achieve the minimum strain level [35], and a thin test specimen may buckle in this case [85]. To prevent this, either thicker specimens or special test apparatus must be used, or a special control technique must be applied. Bartolotta and Brindley [9] employed a passive control system to monitor the minimum stress of the specimen. Once this stress achieved a zero value, the minimum strain was increased by a small increment. As a result, the specimen was not subjected to compressive stresses, so it did not buckle. This is a hybrid strain control mode and is described in more detail in Chapter III.

Static, Relaxation, and Creep Tests

Some important characteristics of a MMC can be obtained in tests environments other than fatigue. These include, but are not limited to, the static or monotonic test, the relaxation test, and the creep test. Data are gathered from these tests about the material properties and responses as a function of temperature and loading rates.

Perhaps the simplest of all loading conditions is the static test. This involves increasing the applied load or

strain until the specimen fails. Testing is usually performed over a range of temperatures and loading rates to determine the strain rate and temperature dependence of some material properties. These may include the elastic modulus, ultimate tensile strength, and the yield stress or proportional limit. The temperature dependence of a typical MMC tested in the monotonic loading condition is shown in Figure 2.1, while the strain rate dependence of many MMCs is shown in Figure 2.2.

MMCs often exhibit significant time dependent deformations at the elevated temperatures [18, 51]. This behavior can be characterized, in part, by relaxation and creep tests. Both are usually performed in isothermal conditions. The typical stress relaxation in a material when subjected to a constant strain input appears in Figure 2.3, while Figure 2.4 shows the accumulation of strain (creep) when a material is exposed to a constant stress input. A constitutive model developed from these tests data can be applied to predict the material response when subjected to fatigue.

Fatigue Environments

As mentioned earlier, to characterize the fatigue response of a MMC requires understanding its behavior in some simplified conditions. This section discusses some special tests environments (thermal fatigue, isothermal

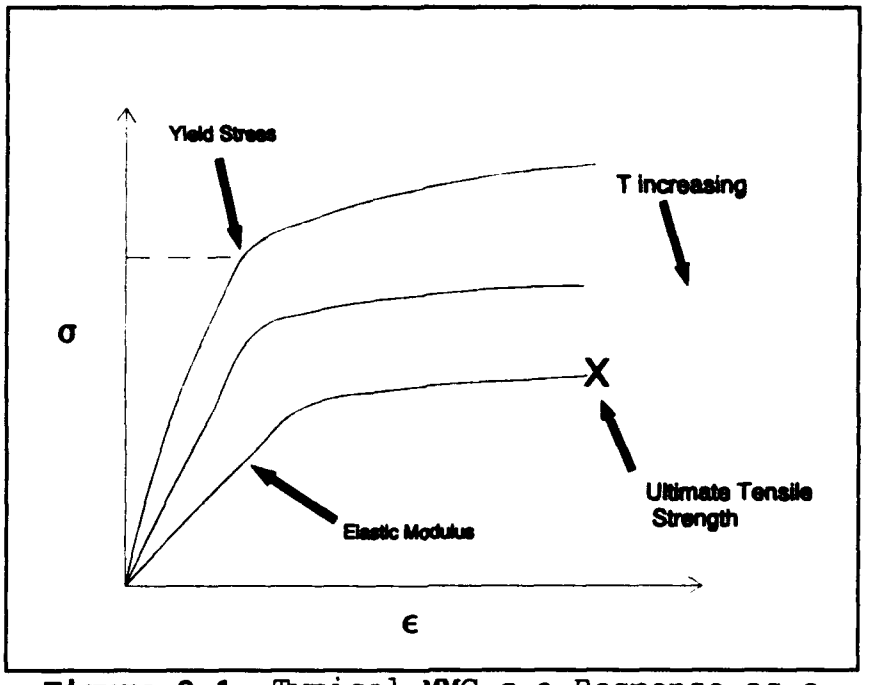

Figure 2.1 Typical MMC σ-ϵ Response as a Function of Temperature

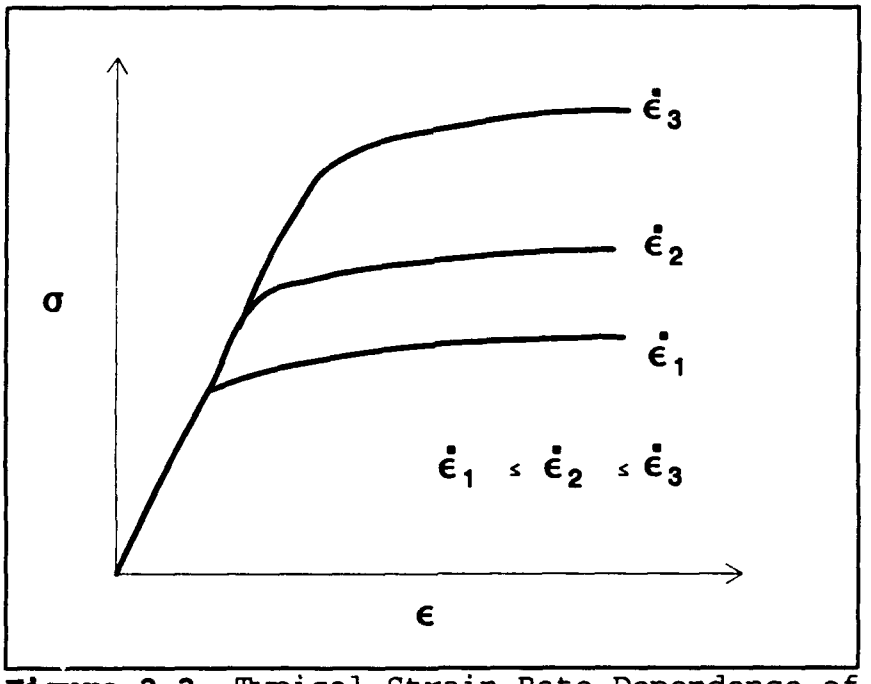

Figure 2.2 Typical Strain Rate Dependence of a MMC at Constant Temperature

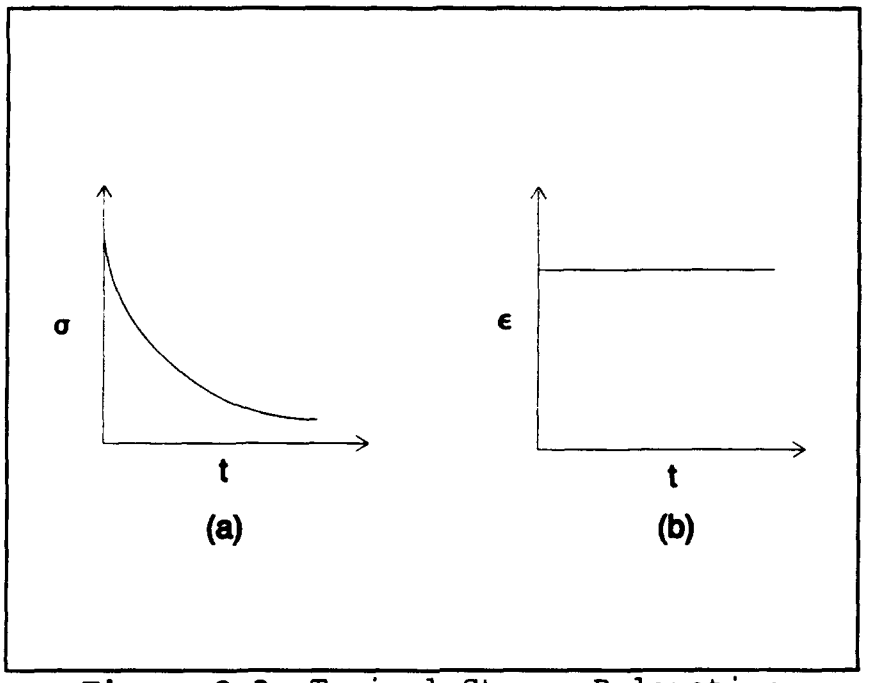

Figure 2.3 Typical Stress Relaxation Response of a Material

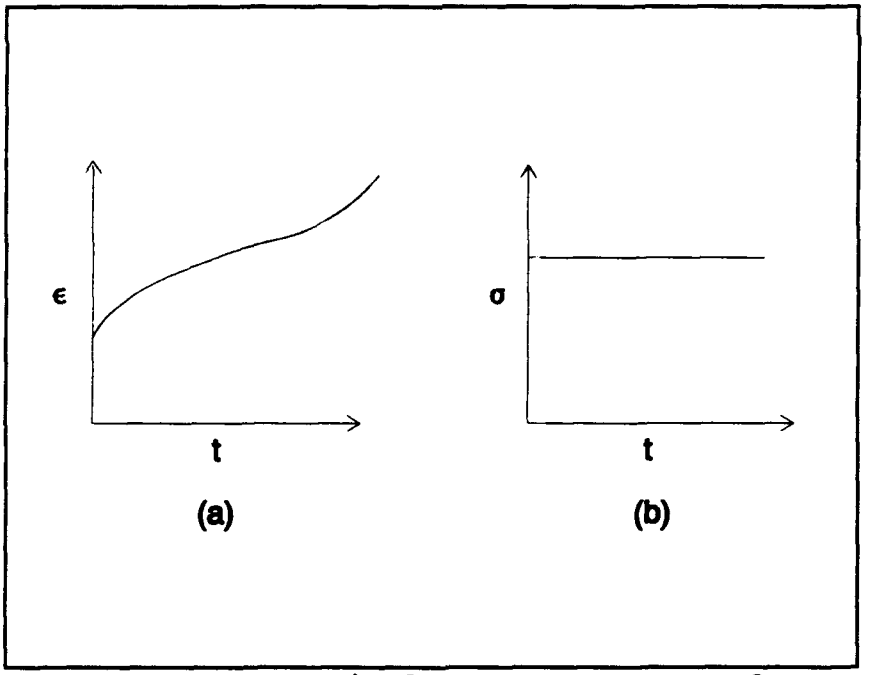

Figure 2.4 Typical Creep Response of a Material

fatigue, and thermomechanical fatigue) used to isolate the composite response and damage mechanisms.

Thermal Fatigue (TF) involves cycling the temperature while the specimen stress is held constant. This is usually accomplished by varying the temperature over a specified range using the sawtooth wave function (Figure 2.5). It was mentioned in Chapter I that the coefficient of thermal expansion (CTE) of the matrix is typically larger than that of the fiber. This results in fluctuating stresses at the fiber-matrix interface when the specimen is exposed to thermal cycling, so this environment isolates damage mechanisms due to thermal fatigue alone.

Another method used to isolate fatigue damage is the isothermal fatigue (IF) test. In this environment, the temperature is held constant while cycling a mechanical load. A typical temperature and load profile for an IF test is shown in Figure 2.6. Since the thermally induced stresses are constant in this case, this test environment provides an opportunity to isolate damage mechanisms due solely to applied loading.

The techniques described above help to characterize the fatigue behavior of MMCs, but they are still simplified versions of many aerospace environments (Figure 1.1). The exact profile shown in Figure 1.1 may be impractical to

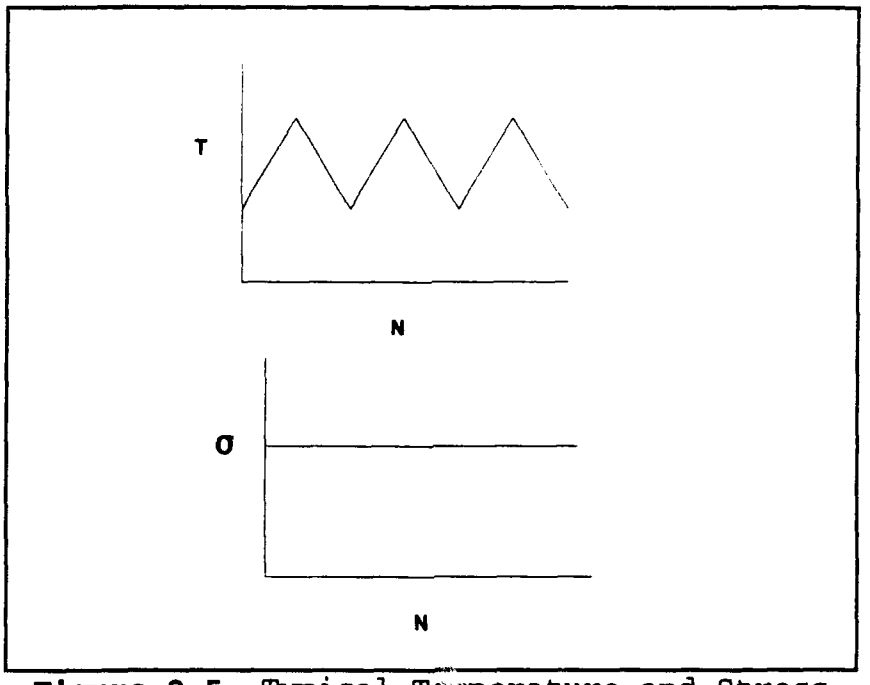

Figure 2.5 Typical Temperature and Stress Profiles for a TF Test

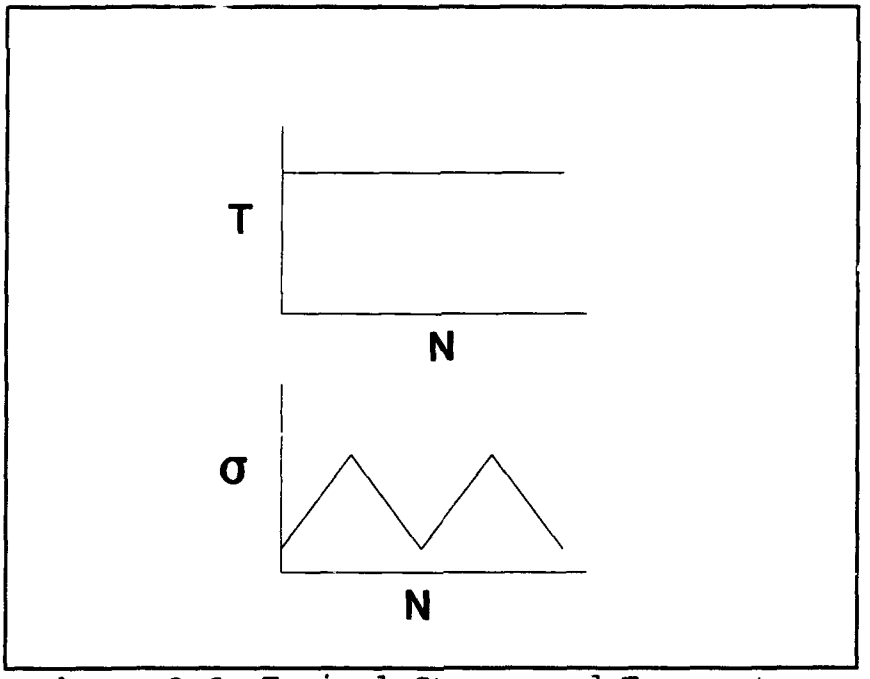

Figure 2.6 Typical Stress and Temperature Profiles for a IF Tests

simulate. A step in this direction is the thermomechanical fatigue test (TMF). The TMF test provides a controlled method which approaches the actual aerospace environment. In this case, a specimen is subjected to both thermal and mechanical fatigue. These parameters can be cycled in-phase (IP), so that the maximum (minimum) temperature and load are reached simultaneously (Figure 2.7a). Also, the temperature can be cycled out-of-phase (OP), so the temperature lags the load profile by some angle Φ (Figure 2.7b). These cyclic profiles may become more complex by imposing hold times on the temperature, load, or both [88].

Data Analysis

Fatigue damage of MMCs is complex, and the methods to relate damage to the fatigue life are not well established. In contrast, damage (crack growth) in a monolithic material typically develops along a single plane. There are experimental techniques available for measuring this crack length, [39] and there exists methods to predict the rate of crack growth [16, 88]. From which, the fatigue life can be predicted. In composites the fatigue damage may be quite different. Depending on the load level, cracks may develop and propagate in the fiber, matrix, or both [85]. These cracks may progress around the fiber, through the fiber, along the fiber-matrix interface, or continue through the matrix (Figure 2.8). The specimen fracture may not result

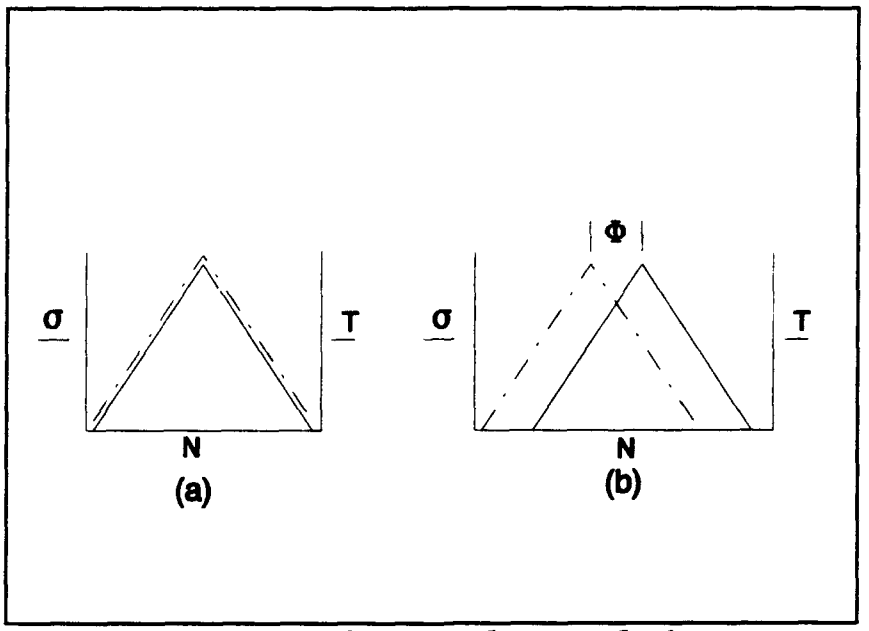

Figure 2.7 In-Phase and Out-of-Phase TMF Profiles

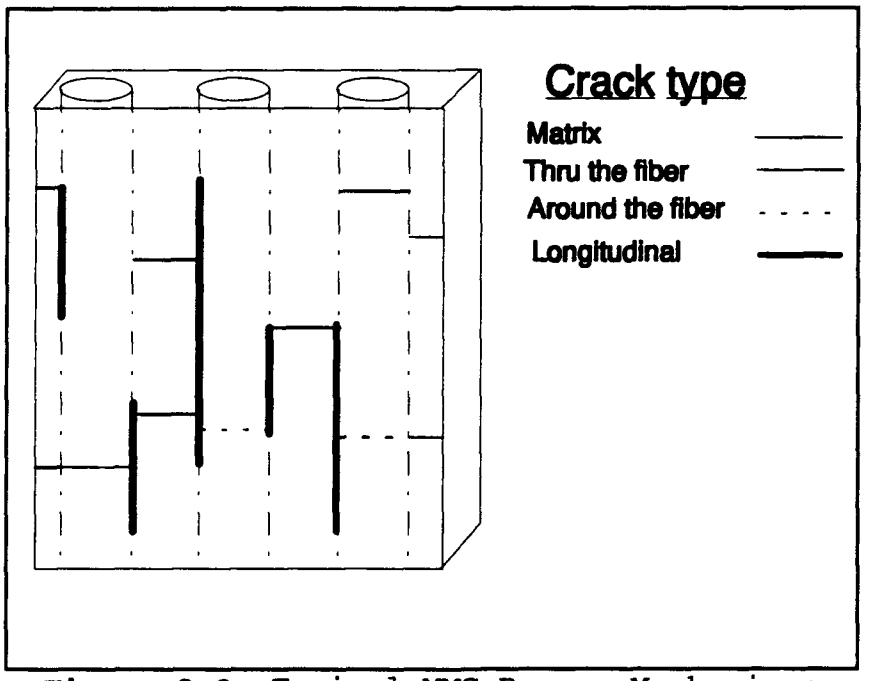

Figure 2.8 Typical MMC Damage Mechanisms

from a single crack but by the coalescence of several cracks. Therefore, crack growth itself is not a sufficient method to determine the fatigue life of a MMC. Neither can the growth of many of these cracks be directly measured. From the experiments described above, data are obtained on the mechanical response of a specimen. Studying the changes in these data over the fatigue life provides an understanding of the initiation and growth of damage in the specimen. A few methods for examining these data are described next.

Material Response Histories

One type of information frequently used to study a MMC loaded in fatigue is a history of the stress-strain response (Figure 2.9). Any hysteresis in these curves suggests that some damage or deformation has occurred in the specimen. Thus, studying the stress-strain response provides a method to quantify the initiation and growth of damage and deformation in a MMC.

Another method of studying the lamina response is to plot the change in the dependent variable as a function of the fatigue cycles. For example, in the load controlled mode, the maximum and minimum strain in a fatigue cycle are plotted. These values are plotted for several cycles over the fatigue life (Figure 2.10). In the strain controlled mode, the maximum and minimum stress are plotted as a

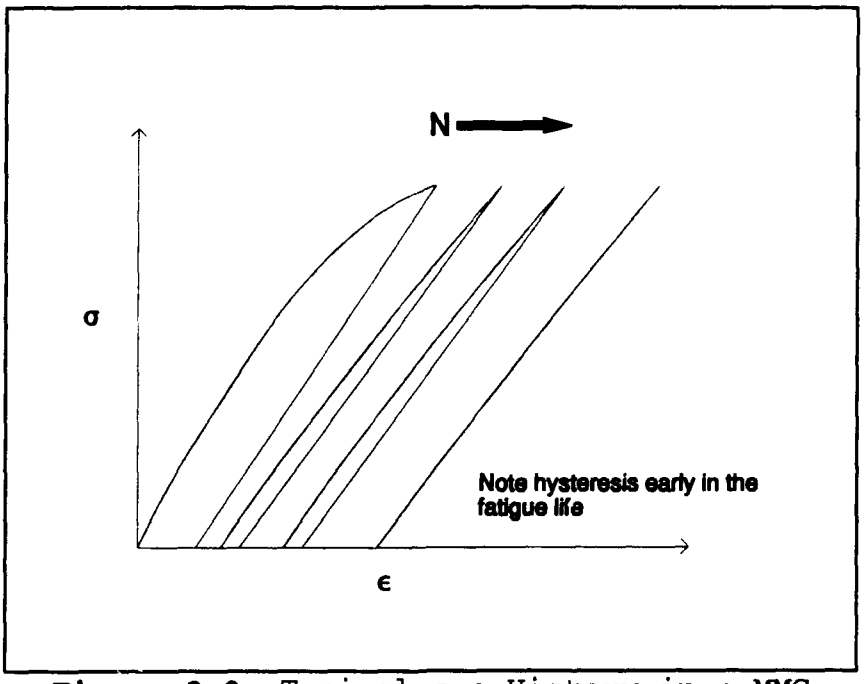

Figure 2.9 Typical σ-ϵ History in a MMC

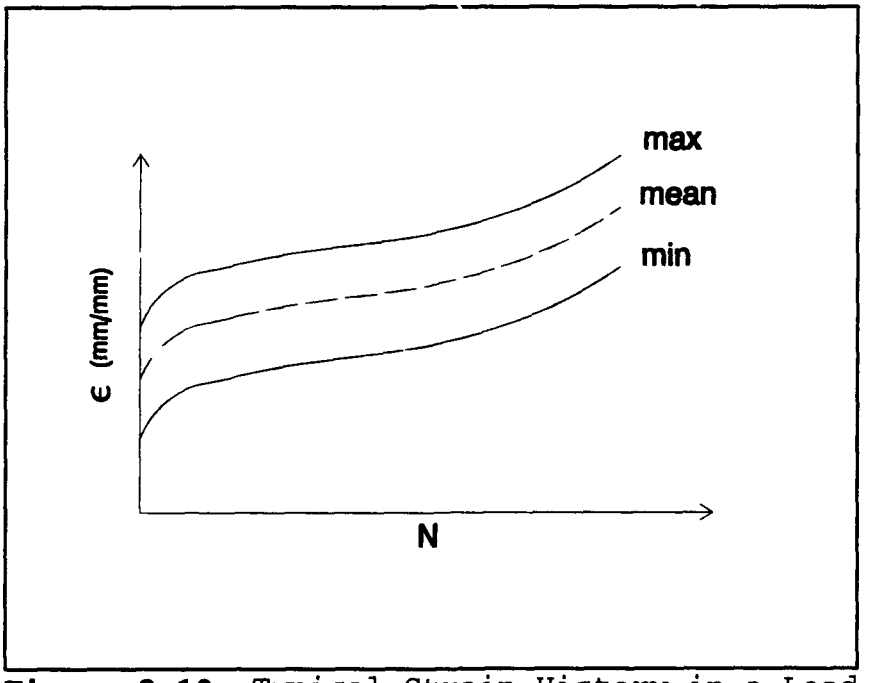

Figure 2.10 Typical Strain History in a Load Controlled Fatigue Test

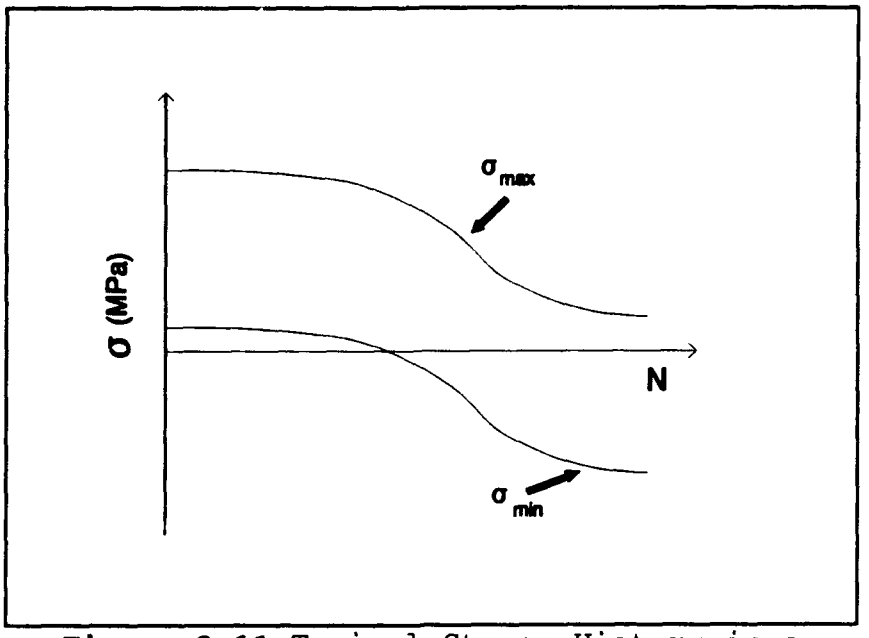

Figure 2.11 Typical Stress History in a Strain Controlled Fatigue Test

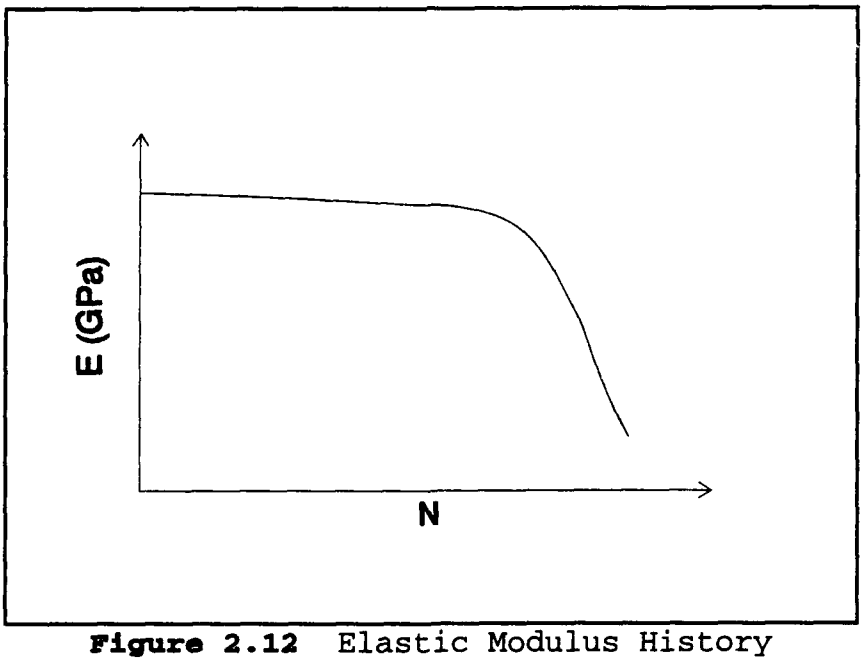

Figure 2.12 Elastic Modulus History

function of fatigue cycles (Figure 2.11). Any change in the dependent variable is an indication of damage or deformation in the specimen.

Finally, measuring a change in some material properties also provides a method to quantify damage in a MMC. In composites, the modulus as a function of fatigue cycles is generally used [83, 53, 101]. A typical history of the modulus for a MMC subjected to fatigue is shown in Figure 2.12. Any loss in stiffness is an indication of damage.

Fatigue Life Curves

It is desirable to show a relationship between the fatigue life of a specimen and the applied load or strain. One such method for plotting these data has been suggested by Talreja [106]. In this method, three regions of damage were correlated to the fatigue life of a unidirectional polymeric composite. This is shown schematically in Figure 2.13. Region I corresponds to fiber breakage and the resulting fiber-matrix interfacial debonding. The scatter band in this region accounts for variations in fiber strength and matrix ductility. Damage in Region I is characterized as non-progressive. Non-progressive damage is defined as damage that results in a rapid failure of the specimen without any prior degradation in the specimen response. On the other hand, progressive damage is defined as damage that grows from an early stage of fatigue life to

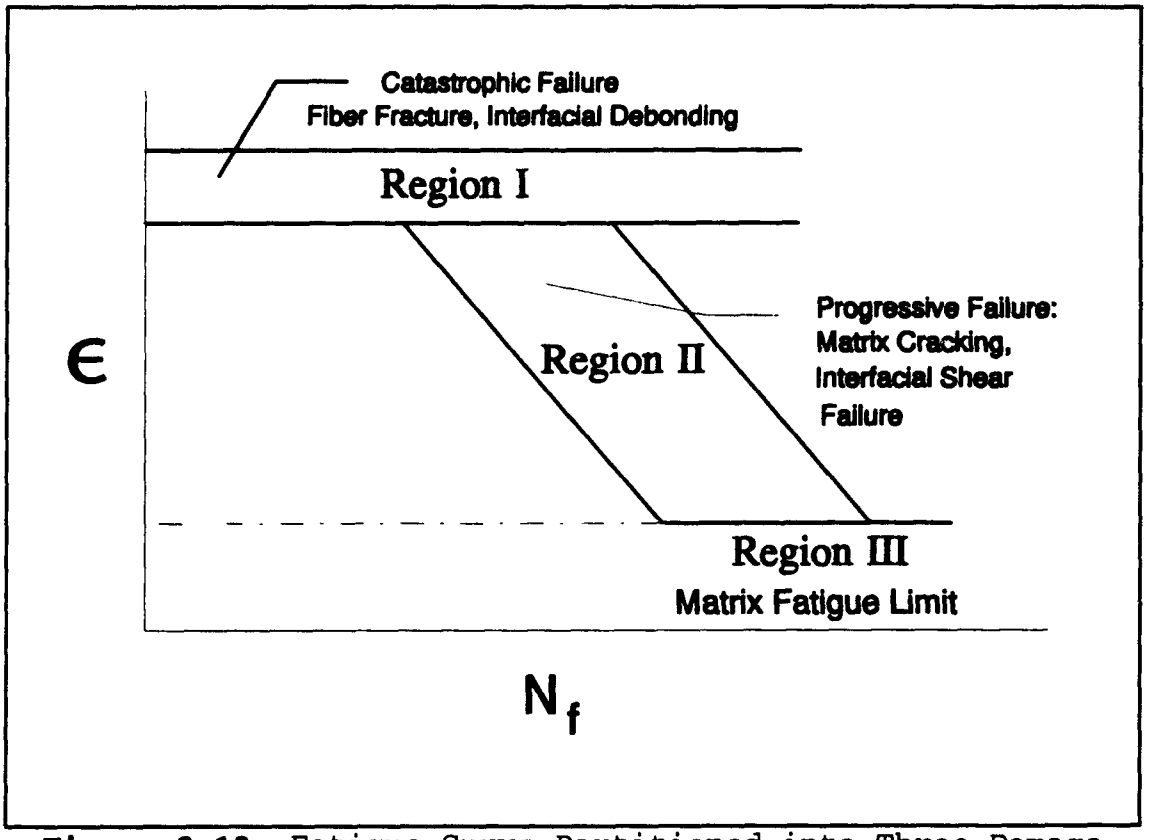

Figure 2.13 Fatigue Curve Partitioned into Three Damage Regions

the final specimen failure. Region II corresponds to progressive fatigue damage. Damage mechanisms in Region II include matrix cracking and fiber-matrix interface failure. Region III corresponds to the matrix fatigue limit. In this region, matrix cracking, if it does occur, is non-propagating. Thus, the three region fatigue curve provides a useful tool for depicting a relationship between the damage mechanisms, the fatigue life, and the applied load or strain.

In this section a few of the experimental techniques used in testing of MMCs were presented. Some of the more predominate testing environments were discussed. Also, a few methods to examine the experimental data were reviewed. These methods demonstrated how the initiation and progression of damage in a MMC subjected to fatigue could be identified. With this background of definitions, a review of some recent work in testing of MMCs is presented next.

Recent Studies In Metal Matrix Composite Testing

Few experimental studies are available for the SCS-6/Ti-15-3 composite system. The available work has involved: static testing at room and elevated temperatures, TF, IF and TMF under load control, and a few strain controlled tests in isothermal conditions. The emphasis for this previous work has been to understand the mechanical property degradation and investigating the characteristic damage mechanisms in MMCs. This section provides a brief review of some of the main static and fatigue investigations of the SCS-6/Ti-15-3 MMC.

Learch and Saltsman [63] performed static tests on the SCS-6/Ti-15-3 composite. The application temperatures were room temperature and 427°C (800°F). Tensile specimens were loaded in the strain mode control at a rate of .0001 mm/mm/s. The lamina and laminate orientations were $[0]_8$,

$[90]_8$, $[90/0]_{2s}$, $[0/90]_{2s}$, $[\pm30]_{2s}$, $[\pm45]_{2s}$, and $[\pm60]_{2s}$. Several damage states were identified and were found to be highly influenced by the fiber architecture.

Majumdar and Newaz [68] performed static tests on the 0° and 90° SCS-6/Ti-15-3 laminas. Tests were performed at room temperature and 538°C (1000°F). Specimens were loaded in the strain control mode at a strain rate of .002 mm/mm/s. They observed that inelastic deformation of the 0° lamina was dominated by matrix plasticity. Reaction zone cracks and grain boundaries were the main sites for dislocation and slip-band nucleation. Conversely, inelastic deformation of the 90° lamina occurred by both fiber-matrix interface damage and matrix plasticity. A characteristic three-stage deformation behavior was identified. Deformation in Stage I was elastic. Inelastic deformation in Stage II was dominated by fiber-matrix interface damage, but some microyielding of the matrix did occur. In Stage III, matrix plasticity became largely concentrated in intense shear bands between the fibers, which lead to crack initiation and specimen failure.

Johnson et al. [54] tested five different lay-ups of the SCS-6/Ti-15-3 system at room temperature under the load control mode. In static test conditions, they found that the off-axis plies (90° and 45°) suffered fiber-matrix interface failures at stress levels as low as 140 MPa (20

Ksi), which is below the composite yield stress. This significantly affected the mechanical properties of the laminate. Fatigue tests were performed to determine the number of cycles to failure versus the stress range. For laminates containing 0° plies, it was found that the stress in the 0° fiber could be used to correlate the fatigue lives.

Ermer [26] tested the 0° SCS-6/Ti-15-3 MMC under TF. The temperature range was 149-427°C (300-800°F). A degradation in the reaction zone was noted after the first 500 thermal cycles and progressed as TF continued. No significant degradation in the ambient mechanical properties were observed. Gabb et al. [32] also noted that TF did not reduce the mechanical response of the uniaxial specimens at elevated temperature. Additionally, Ermer found matrix cracks in areas were the fibers were closely spaced. Mall and Ermer [71] showed that these cracks developed and propagated due to the higher state of stress in these areas relative to locations were normal fiber spacing was observed.

Newaz and Majumdar [80] performed TF tests on the quasi-isotropic ($[0/\pm45/90]_s$) SCS-6/Ti-15-3 MMC. The temperature range was 316-649°C (600-1200°F). As with Ermer, they observed matrix cracking and fiber-matrix interface damage. Microscopic analysis at the specimen edge

showed the presence of fiber-matrix debonding and ply-to-ply separation (delamination) in the 45° and 90° plies. The propensity for debonding was found to be greater when the fibers were closely spaced. An attempt was made to model the initiation of the matrix cracks due to thermal cycling. However, neither a closed form solution nor finite element analysis proved successful.

Both Ermer [26], and Newaz and Majumdar [80] found that there was a noticeable change in the strain as a function of thermal cycles. The strain initially increased, which was probably due to the coalescence of micro-cracks in the as-received material. Then it decreased to a constant value. The ensuing decrease might have been the result of age hardening of the matrix [101], which led to an increase in the stiffness of the specimen.

Gabb et al. [32] looked at the 0° SCS-6/Ti-15-3 MMC under IF and TMF conditions. They found that the MMC had a good IF resistance at 300°C (570°F). This behavior was also observed at 550°C (1020°F) for low cyclic stresses. At 550°C and high cyclic stresses, the stress relaxation in the matrix reduced the composite fatigue resistance. They found that matrix cracks initiated from the fiber-matrix interfaces and foil laminations. Finally, they observed that TMF substantially degraded the composite fatigue

resistance. This degradation was produced by TMF damage mechanisms associated with the fiber-matrix interfaces.

Majumdar and Newaz [67] performed IF and TMF tests of a SCS-6/Ti-15-3 quasi-isotropic ($[0/\pm45/90]_s$) MMC. The TMF and IF tests were performed in load control over a temperature range of 316-649°C (600-1200°F) and 649°C (1200°F), respectively. For the TMF specimens, a good correlation was obtained between the measured strain range and the TMF life. On a stress range basis, the TMF life was significantly shorter than the IF life. For the specimens subjected to IF, damage mechanisms consisted of transverse microcracks oriented perpendicular to the loading axis. In specimens tested under TMF, similar transverse microcracks were observed very close to the fracture surface. Additionally, significant interply delamination, parallel to the loading axis, was observed both near and away from the fracture surface. Most of the microcracks originated at the fiber-matrix interface or in the fiber-matrix reaction zone.

Schubbe [101] conducted in-phase (IP) and out-of-phase (OP) TMF tests on the $[0/90]_{2S}$ SCS-6/Ti-15-3 MMC. Schubbe employed the load control mode over a temperature range of 149-427°C (300-800°F). An attempt was made to correlate the damage by defining a damage parameter

$$D = \left(1 - \frac{E}{E_o}\right) \tag{2.2}$$

where E_o was the initial modulus and E was the instantaneous modulus. Damage values in the range of .1-.2 were found at the failure points of the specimens. However, no correlation between the tests parameters and the path to this point could be made. Schubbe also noted that there was a significant increase in the modulus for many of the specimens tested. This was most likely due age hardening of the matrix.

Gayda et al. [34] conducted IF tests at 300°C (570°F) and 550°C (1020°F), under the strain control mode on the Ti-15-3 matrix alloy. They noted that the fatigue life at 550°C was superior to that at 300°C, which was due to a difference in the mean stress. At 300°C there was negligible stress relaxation, and the mean tensile stress was constant throughout the test. As a result, they found that the stress range after half of the fatigue life (half life) was essentially unchanged. At 550°C the mean stress approached zero, and the stress ratio went to -1 by the half life. Thus at 550°C, stress relaxation in the matrix had a significant effect on the fatigue life.

Pollock and Johnson [85] conducted isothermal static and IF tests on the Ti-15-3 matrix alloy and SCS-6/Ti-15-3 0° MMC. The matrix alloy was subjected to fatigue under the

strain control mode, while the load control mode was used for the MMC. Tests were conducted at room temperature and 650°C (1200°F). For the matrix alloy, they found that the room temperature modulus was independent of the control mode, but the ultimate tensile strength was 19% lower in the strain controlled mode. At 650°C the elastic response was the same for each test. At this same temperature, the inelastic response was dependent on the control mode. These observations indicated a dependence on the loading history. Also, several laminates containing 0° plys were tested in fatigue at 650°C. The fiber reinforcement was found to significantly increase the static and fatigue strengths of the laminates over that of the matrix material at elevated temperature, but the increase was insignificant at room temperature. Initial damage, in either the fibers or the matrix, was partitioned as a function of the life and strain range in the constituents. They found that high strains and short lives resulted in multiple fiber fractures with no signs of matrix cracking. At low strains and long fatigue lives, extensive matrix cracking was observed, and there was no fiber damage away from the fracture surface. It was also observed that the matrix was too weak to cause fiber-matrix interface failure prior to matrix yielding at 650°C. The laminate fatigue life was hypothesized to be a function of the stress in the 0° fibers. When comparing the room

temperature to the high temperature fatigue lives, a larger scatter band was observed at the elevated temperature.

Gayda and Gabb [35] performed constant amplitude, strain control tests on the 90° SCS-6/Ti-15-3 MMC and the Ti-15-3 neat matrix at 426°C. They found that the fatigue life of the MMC was shorter than that of the neat matrix. Additionally, they observed that fiber spacing and the fiber-matrix interface bond strength had a significant effect on the stress-strain response of the lamina.

This section summarized some recent experimental work on the SCS-6/Ti-15-3 system. From this review, major observations and findings can be summarized as follows:

1) The high strength of the matrix, relative to the fiber, makes it a significant load carrying component for MMCs.

2) The fiber-matrix interface is a dominant factor in the fatigue life under all loading conditions.

3) TMF life is consistently shorter than IF life.

4) Transverse microcracking in off-axis plies (90° and 45°) is a predominant damage mechanism.

5) The stiffness of Ti-15-3 matrix increases when exposed to elevated temperatures.

6) Closely spaced fibers are sources of damage in the as-received MMC and the MMC subjected to fatigue.

7) No study is available which addresses the stated objectives of this investigation.

Analytical Models

Some models have been developed to analyze the fatigue response of a MMC. A few models for predicting the response of a unidirectional MMC and a MMC laminate are reviewed in this section. Also, a brief introduction is given to the models that were used in this study.

Unidirectional Models

The concentric cylinder model [40, 41] has been adopted by a few researchers [23, 34] to predict the response of the 0° lamina subjected to fatigue. Figure 2.14 shows a schematic of the concentric cylinder model (CCM). The CCM is a cylindrical matrix surrounding a cylindrical fiber.

Assuming axisymmetric, generalized plane strain conditions, the model is capable of predicting axial (σ_z) radial (σ_r) and tangential (σ_t) stresses in the matrix and fiber. These stresses and strains are based on solving for the radial displacement

$$u_r = Ar + \frac{B}{r} \qquad (2.3)$$

where r is the radial coordinate and A and B are constants.

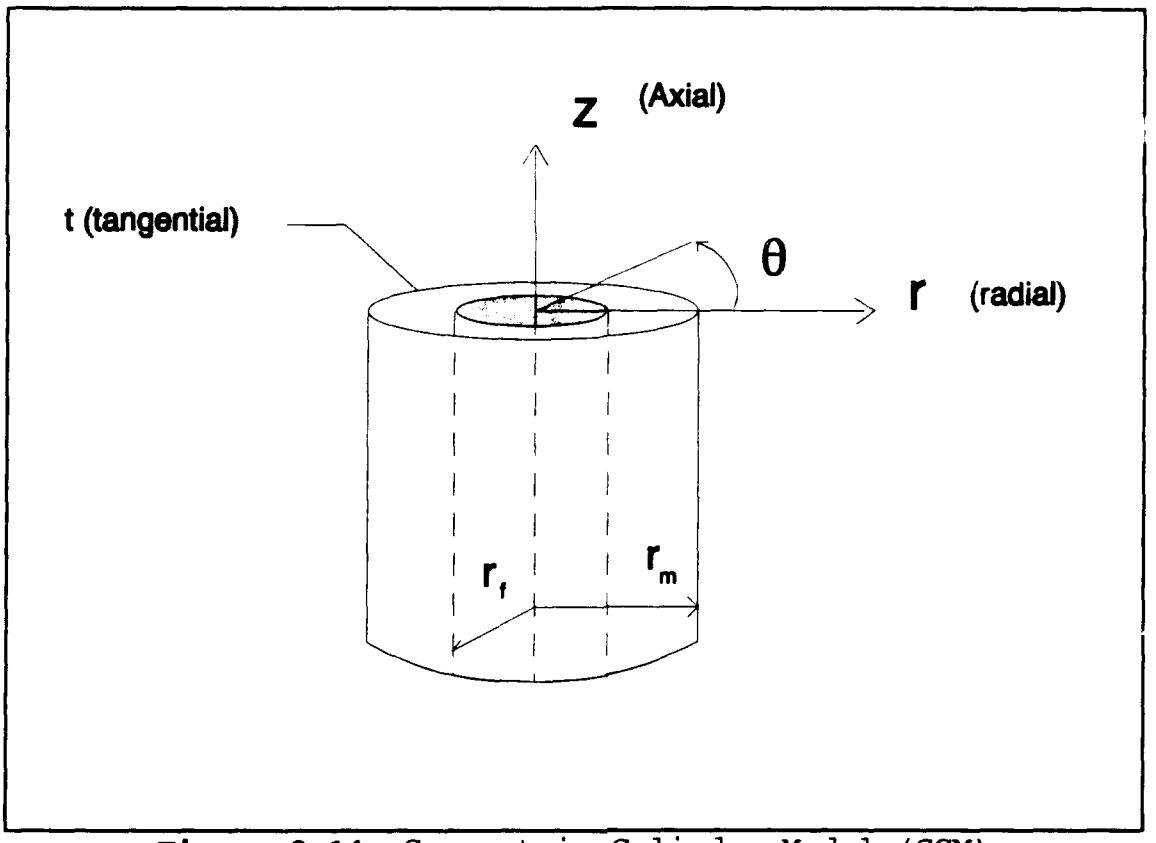

Figure 2.14 Concentric Cylinder Model (CCM)

For the fiber and matrix Equation 2.3 has the form

$$u_{r_m} = A_m r + \frac{B_m}{r} \qquad for\ r_f \le r \le r_m$$
$$u_{r_f} = A_f r \qquad for\ r \le r_f \qquad (2.4)$$

where r_f and r_m refer to fiber and matrix radial coordinates, respectively (Figure 2.14).

To solve for the unknowns in Equation 2.4, the following boundary conditions must be satisfied:

$$u_f(r_f) = u_m(r_f)$$
$$\sigma_r(r_m) = 0 \qquad (2.5)$$
$$\sigma_{r_m}(r_f) = \sigma_{r_f}(r_f)$$

Finally, it is easy to incorporate different constitutive models into a computer code based on the CCM. Gayda et al. [34] used a simple empirical scheme to model the matrix creep deformation. Coker and Ashbaugh [23] have employed the theories of Bodner [14] to model the elastic-viscoplastic behavior of the matrix.

Unlike the longitudinal response of a MMC, the transverse response of a MMC is heavily influenced by the fiber-matrix interface damage. Most classical micromechanics theories can not be applied since certain boundary and compatibility conditions would be violated. Some attempts have been made to model this behavior but have had limited success.

Highsmith et al. [47] used the self consistent model (SCM) to determine the transverse material properties and the stress response of a MMC under some general loading conditions. The SCM is shown schematically in Figure 2.15. Essentially, this is a concentric cylinder model in an infinite medium of orthotropic composite material. The system of equations to determine the stresses, or strains, in the fiber and matrix are similar to those explained for the CCM, but a few more boundary conditions are imposed to

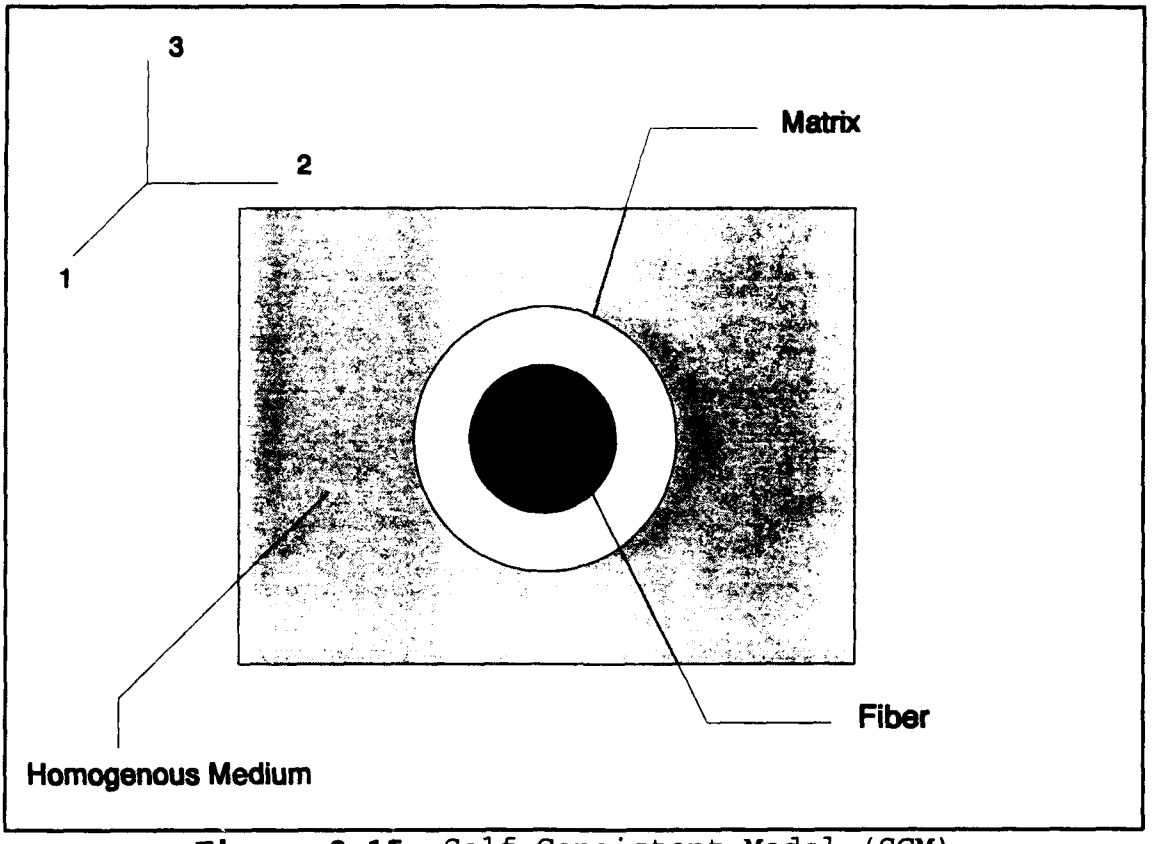

Figure 2.15 Self Consistent Model (SCM)

account for the third material (the orthotropic infinite medium). Since some compatibility and boundary conditions would be violated, this approach is not capable of modeling damage a MMC.

A few studies [54, 81, 82, 93] have modeled the transverse response of a MMC with the finite element method (FEM). A typical finite element mesh is shown in Figure 2.16. If gap elements are contained in the mesh, the fiber-matrix interface damage can be modeled. A good insight into the distribution of stress can be obtained through either a

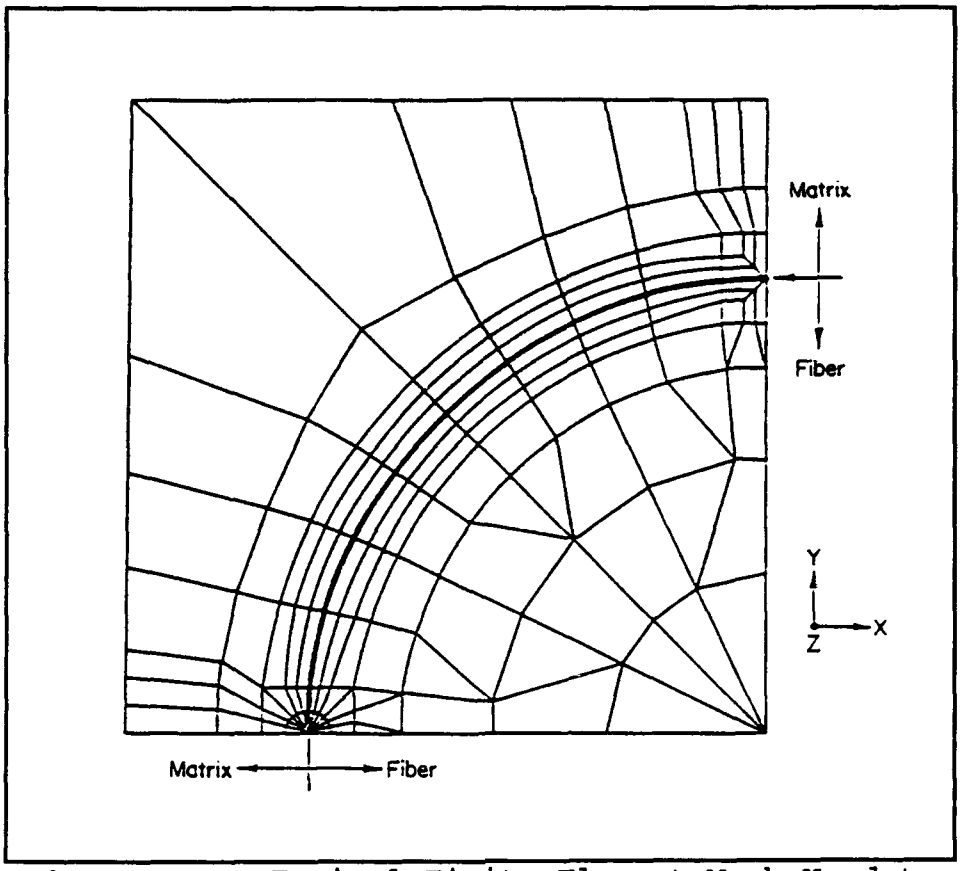

Figure 2.16 Typical Finite Element Mesh Used to Analyze a MMC [80]

two-dimensional or three-dimensional solution. However, even for one fatigue cycle, the solutions are extremely time consuming, so it is not practical to study the fatigue response of a MMC using this method.

Finally, Gayda and Gabb [35] successfully modeled the transverse response of the SCS-6/Ti-15-3 unidirectional MMC with a series of springs (Figure 2.17). Alternate rows of matrix elements and fiber-matrix elements were used to

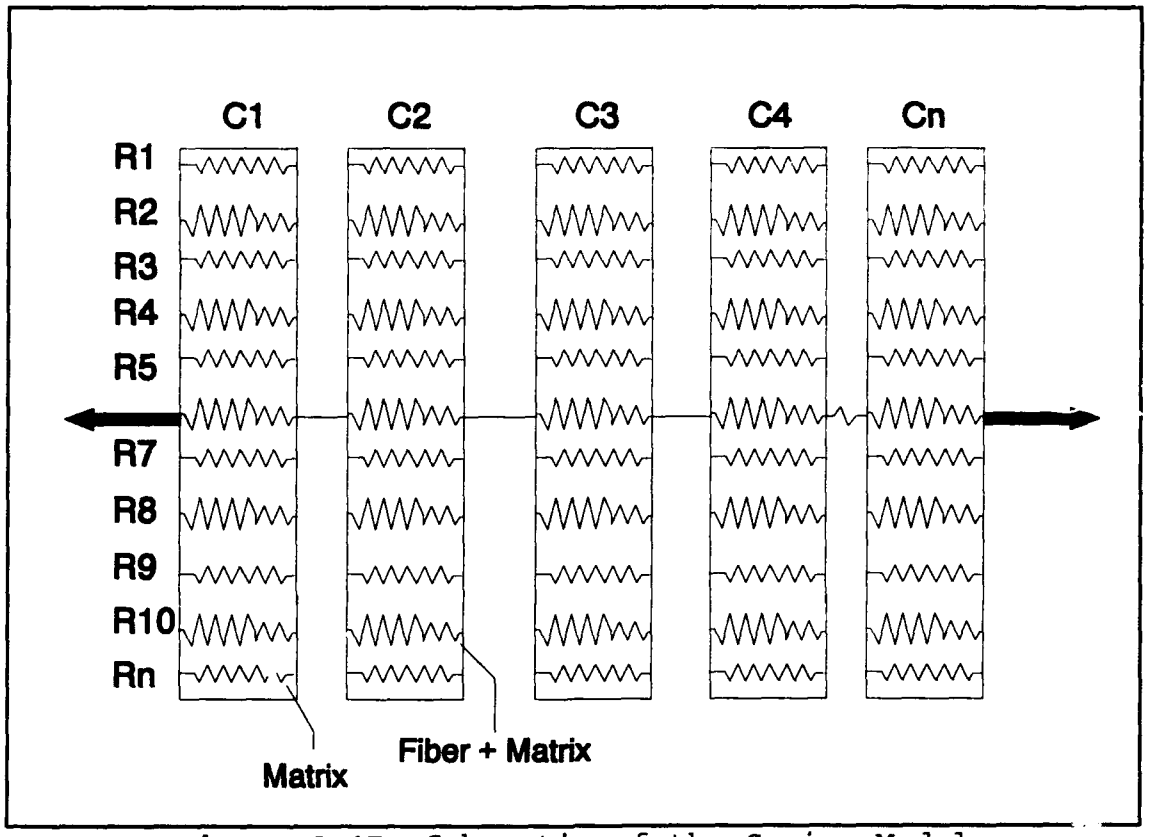

Figure 2.17 Schematic of the Spring Model

simulate the unidirectional lamina. To account for random fiber spacing, the fiber fraction of the fiber-matrix elements were varied. The stiffness of each element (K_e) within a column was defined by

$$K_e = \frac{1}{\left(\frac{L_f}{E_f} + \frac{1-L_f}{E_m}\right)} \qquad (2.6)$$

where E_f is the fiber modulus, E_m is the matrix modulus, and L_f is the fiber content of an element. From this consideration, the stiffness of each column (C1, C2,... Cn)

shown in Figure 2.17 was calculated by summing the individual element stiffnesses. An incremental displacement of each column was then computed by dividing the load increment by the total column stiffness. Total lamina displacement was then calculated by summing the displacements of all the columns in series.

The spring model took into account fiber-matrix interface damage, matrix plastic deformation, and matrix creep deformation. The interface damage was modeled by assigning a bond strength to each fiber-matrix element. When the stress in an element exceeded this bond strength, the stress of that element was set equal to zero. Any stress carried by this element was then transferred to the remaining elements within the column. An element could not sustain a tensile load (tensile stiffness equals zero) after it had failed but could sustain a compressive load. Matrix plastic deformation was accounted for by using a simple isotropic hardening rule. Finally, using data from relaxation tests, a virtual creep stress was calculated for each column to simulate the time dependent deformation (matrix creep).

Aboudi has developed a continuum model for predicting the average behavior of a unidirectional, fiber-reinforced composite whose constituents are elastoplastic work hardening materials. The derived constitutive theory is

summarized in Reference 2. This model has been incorporated in a computer program called EPC [43].

The Aboudi model, or method-of-cells, is based on the assumption that the continuous fibers extend in the x_1 direction and are arranged in a doubly periodic array in the x_2-x_3 directions (Figure 2.18a). As a result of this periodic arrangement, it is sufficient to analyze a representative cell as shown in Figure 2.18b. The model is formulated to predict the average behavior of the composite using a first order theory in which the displacements in each subcell are expressed linearly in terms of the distances from the center of the subcell. The effective constitutive relations are generated by imposing continuity of displacements and tractions across the boundaries of the individual subcells. Closed-form expressions that relate the overall applied stresses to the stresses in the fiber and the individual subcells of the matrix predict the effective response of the composite under arbitrary loading conditions.

The present continuum theory assumes that both the fiber and matrix are elastic in the linear region and plastic work-hardening in the nonlinear region. The elastic-viscoplastic formulation of Bodner [14] was used to characterize the material in the inelastic region. This unified theory can characterize the plastic behavior of a

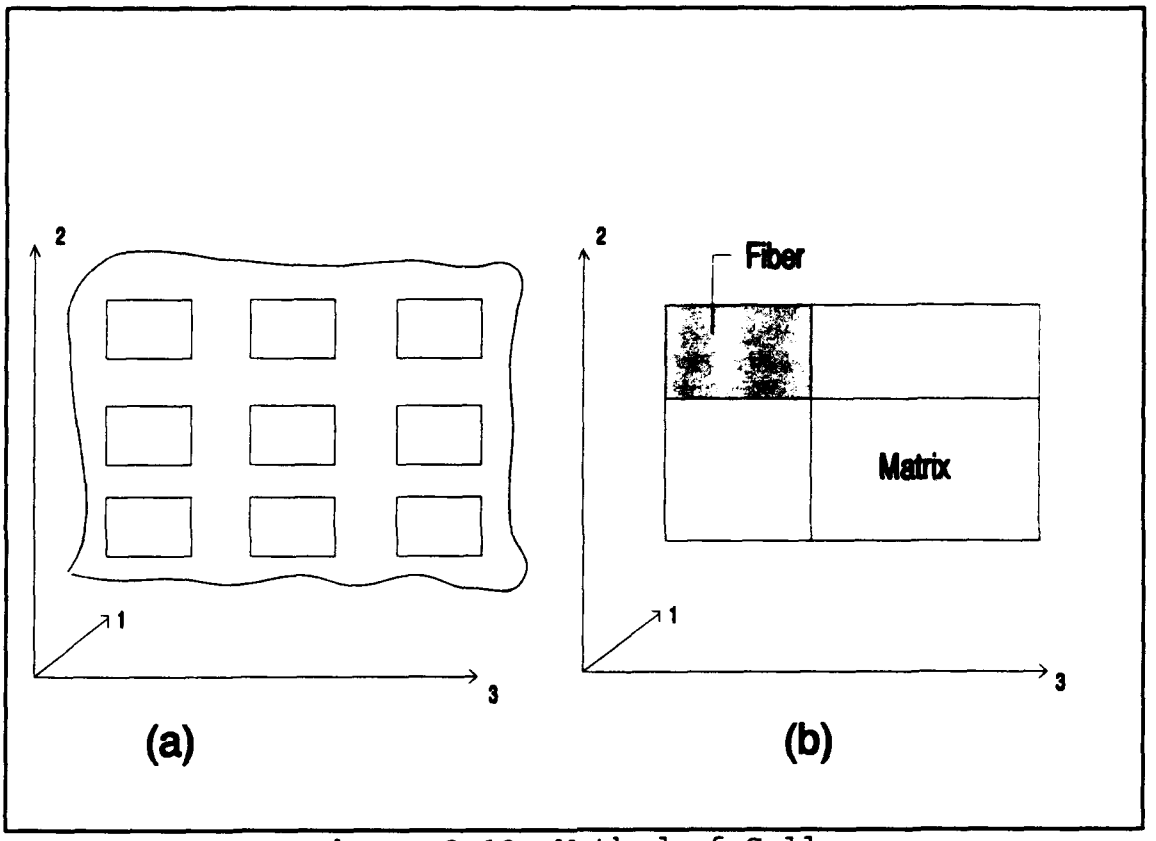

Figure 2.18 Method-of-Cells

material with isotropic work-hardening and temperature dependent properties. Anisotropic hardening with the multidimensional Bauschinger effect can also be incorporated in the unified theory of Bodner [14]. For an elastic-plastic material with isotropic hardening, the plastic strain rates are given by the Prandtl-Reuss flow rule where plastic incompressibility is assumed.

Laminate Models

A few models have been developed to predict the laminate fatigue behavior of MMCs. These models may include off-axis plies. Among them are METCAN (METal matrix Composite ANalyzer) and AGLPLY. The next few pages provides a review of these models.

METCAN

METCAN [22] (METal matrix Composite ANalyzer) is a FORTRAN based computer code designed to perform linear and nonlinear analysis of MMCs. METCAN is based on the multi-cell model (MCM) to predict the behavior of the fiber, matrix, and interphase regions in a MMC. The MCM (Figure 2.19) is partitioned into three distinct subregions to characterize the through-the-thickness nonuniformity of structure and constituent material properties.

Based on the strength of materials approach, Hopkins and Chamis [48] developed a unique set of micromechanics equations for use in the analysis of MMCs. Fundamental principles of displacement, compatibility, and force equations were used in formulating the set of equations. This set of micromechanics equations are derived for the transversely isotropic case (isotropic in the X_2-X_3 plane) under the assumption of isotropic constituent materials. Finally, Chamis et al. [22] adopted this formulation into the computer code METCAN.

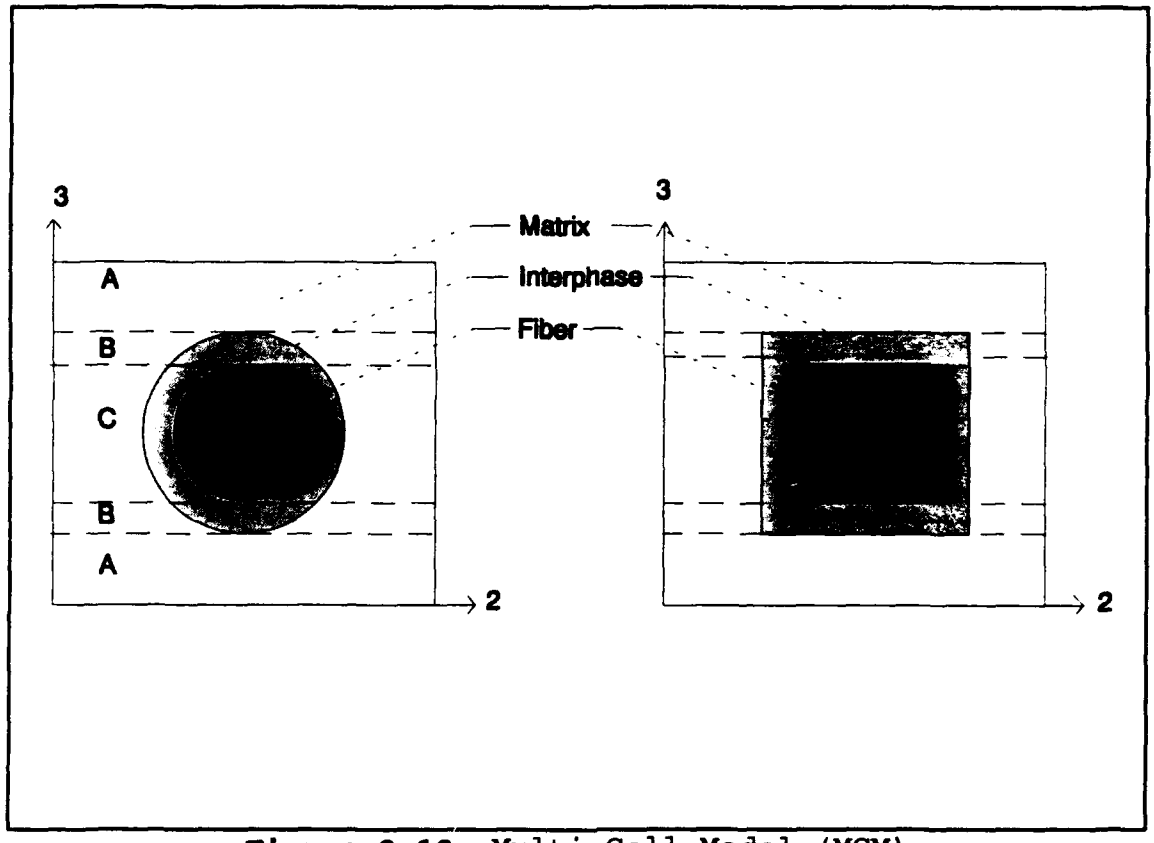

Figure 2.19 Multi-Cell Model (MCM)

The equations mentioned above are closed form expressions derived to give equivalent pseudo homogenous properties for a unidirectional fiber reinforced ply. They encompass expressions for ply equivalent mechanical properties, ply equivalent thermal properties, ply in-plane uniaxial strengths, and thermomechanical constituent stresses. These ply properties are then used in various orientations to predict average properties of a laminate. In the process, the program calculates component parameters

that include stresses in the fiber, matrix, and if desired, the interphase region of the MMC.

METCAN can be used to predict various composite properties and thermal and mechanical responses under the load controlled condition [17] [64]. The model cannot predict permanent matrix deformation (plasticity and creep) nor does it include damage mechanisms such as fiber or matrix cracking, and fiber-matrix interface damage. These damage mechanisms can be simulated by the application of the power law relationship [21]

$$\frac{P}{P_o} = \left(\frac{T_F - T}{T_F - T_o}\right)^n \left(\frac{S_f - \sigma}{S_f - \sigma_o}\right)^m \left(\frac{\dot{S}_f - \dot{\sigma}_o}{\dot{S}_f - \dot{\sigma}}\right)^l \left(\frac{\dot{T}_F - \dot{T}}{\dot{T}_F - \dot{T}_o}\right)^k \cdots \cdots \left(\frac{N_{MF} - N_M}{N_{MF} - N_{MO}}\right)^q \left(\frac{N_{TF} - N_T}{N_{TF} - N_o}\right)^r \left(\frac{t_F - t}{t_F - t_o}\right)^s \tag{2.7}$$

where the variables are defined as follows:

- P Property of interest
- T Temperature
- S_f Fracture stress determined at T_o conditions
- σ Stress
- N_M Number of mechanical cycles
- N_T Number of temperature cycles
- t time

The additional subscripts F and O denote the final and reference values, respectively. Also, the dotted terms denote the time rate of change of the variables. Exponents n, m, l, k, q, r, and s are determined from the observed or

expected behavior. Each term in Equation 2.7 relates to a different property effect. Once each of these terms are calibrated, Equation 2.7 can simulate the behavior of a MMC under a variety of loading conditions. However, this calibration requires extensive experimentation.

AGLPLY

Another model used for laminate analysis is AGLPLY [7]. AGLPLY is a two-dimensional laminate code based on the vanishing fiber diameter (VFD) model [6]. The VFD model consist of an elastic-plastic matrix unidirectionally reinforced by continuous elastic fibers. Both constituents are assumed to be homogenous and isotropic. The fibers are assumed to be of very small diameter, so that although they occupy a finite volume fraction of the composite, they do not interfere with the matrix deformation in the transverse and longitudinal directions. Figure 2.20a shows a schematic of the VFD. It also can be represented by parallel fiber and matrix bars or plates with axial coupling (Figure 2.20b).

If the cartesian coordinates are chosen so that x_1 coincides with the fiber direction, the second-order tensor components of the stress and strain are expressed as

$$\sigma = [\sigma_{11}\sigma_{22}\sigma_{33}\sigma_{12}\sigma_{13}\sigma_{23}]^T$$
$$\epsilon = [\epsilon_{11}\epsilon_{22}\epsilon_{33}\gamma_{12}\gamma_{13}\gamma_{23}]^T \qquad (2.8)$$

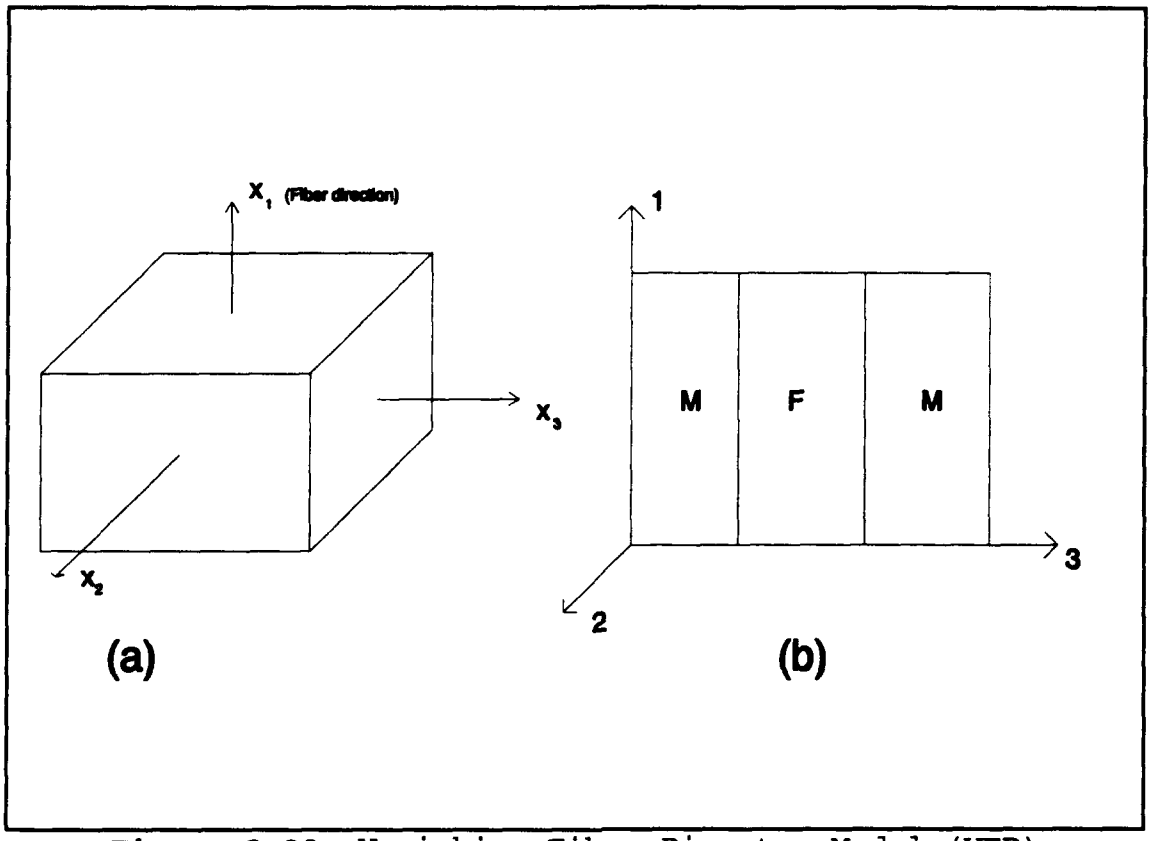

Figure 2.20 Vanishing Fiber Diameter Model (VFD)

where $\gamma_{ij} = 2\epsilon_{ij}$; i, j =1,2,3; i ≠ j; are the engineering shear strain components.

For equilibrium and compatibility, several requirements are imposed on the material model shown in Figure 2.20. The average stress in each constituent can be related to the overall composite stress in the longitudinal, or fiber, direction as

$$\bar{\sigma}_{11} = v_f \sigma^f_{11} + v_m \sigma^m_{11} \qquad (2.9)$$

where a bar over a symbol denotes overall composite stress or strain, and the subscripts f and m denote quantities

related to the fiber and matrix. The volume fractions v_f and v_m are such that $v_f + v_f = 1$. The other stress components in each constituent are assumed to be uniform and obey the following equilibrium equations:

$$\begin{aligned} \bar{\sigma}_{22} &= \sigma^f_{22} = \sigma^m_{22} \\ \bar{\sigma}_{33} &= \sigma^f_{33} = \sigma^m_{33} \\ \bar{\sigma}_{12} &= \sigma^f_{12} = \sigma^m_{12} \\ \bar{\sigma}_{13} &= \sigma^f_{13} = \sigma^m_{13} \\ \bar{\sigma}_{23} &= \sigma^f 23 = \sigma^m_{23} \end{aligned} \qquad (2.10)$$

The only constraint in the model is in the longitudinal, or fiber, direction; the fiber and matrix must deform equally:

$$\bar{\epsilon}_{11} = \epsilon^f_{11} = \epsilon^m_{11} \qquad (2.11)$$

The other strain components can be related to the overall strain as

$$\bar{\epsilon}_{ij} = v_f \epsilon^f_{ij} + v_m \epsilon^m_{ij} \quad (ij \neq 11) \qquad (2.12)$$

The model is capable of elastic-plastic analysis. AGLPLY treats the fiber as a linear elastic material, but the fiber properties may be a function of temperature. Since the fibers are elastic up to failure, the inelastic strains of the lamina are caused by the matrix. This model is not capable of modeling the damage in a lamina. Finally, Mirdamadi et al. [77] have extended this model to include time dependent matrix properties in a program called VISCOPLY.

Proposed Models

In this study, the analytical techniques were required to model the longitudinal and transverse fatigue behavior of the SCS-6/Ti-15-3 MMC. These models provided information which could not be experimentally measured or observed by microscopic analysis. Thus additional insight into the experimentally observed behavior of the MMC could be gained.

Any model selected for use needed to be practical to apply and be capable of simulating inelastic deformations, such as matrix plasticity, matrix creep, and fiber-matrix interface damage. Two models were chosen to perform the analysis. For predicting the longitudinal response, the CCM was used. A model similar to the MCM [79] was used to predict the response when the MMC was subjected to a load perpendicular to the fiber direction. The second model included some unique methods to characterize the effect of fiber-matrix interface damage on the lamina response. Each model predicted the thermal residual stresses caused by processing. A linear isotropic hardening rule governing matrix flow was adopted for each model, and a relaxation scheme was developed to predict the time dependent behavior of the matrix.

Both models provided the required information on the fatigue behavior of the MMC. These data were then used to support and explain the experimental observations. The

models were easy to apply and required a minimum amount of experimental data to calibrate. Also, they provided a foundation from which to build a laminate analysis.

III Test Equipment & Procedures

This chapter provides a detailed description of the material, test equipment, and procedures used in this study. A section is included to discuss key features and material properties of the SCS-6/Ti-15-3 Metal Matrix Composite (MMC). This composite involved laborious preparation prior any testing or microscopic analysis. These procedures are described starting with the pre-test specimen preparation. Elevated temperature fatigue testing of MMCs has some unique equipment requirements, so a section is included to explain the experimental setup. Finally, the equipment used in the microscopic analysis is reviewed.

Material and Specimen Description and Preparation

Material Description

The MMC used in this investigation was the eight ply Ti-15V-3Cr-3Al-3Sn (w/o) metal alloy reinforced by approximately 36 volume percent continuous Silicon-Carbon fibers (SCS-6). The fibers have a nominal diameter of 0.142 mm. These fibers have an inner carbon core enclosed in a cylinder of bulk SiC with alternating layers of silicon and carbon. The final layer being carbon [60]. Some key room temperature properties of the fiber and as-received

Table 3.1 Key Material Properties of SCS-6 Fiber and Ti-15-3 Neat Matrix

	Fiber	Matrix
E (GPa)	400	82
α (10^{-6} mm/mm/C)	4.9	10.
ν	.25	.36
σ_{utl} (MPa)	3550	865
Yield Stress		865

neat matrix are shown in Table 3.1. As mentioned in Chapter I, there is a large difference in the coefficient of thermal expansion (CTE) between the fiber and matrix for most MMCs. For the SCS-6/Ti-15-3 MMC, the CTE of the matrix is almost twice that of the fiber (Table 3.1). This results in large residual stresses (Figure 1.2) after cool down from the processing temperature of around 1000°C. It has been shown [102] that these stresses can result in processing damage in the as-received MMC. This subject is discussed in more detail in Chapter IV.

Specimen Description and Preparation

Before testing, the test specimens must be machined and prepared. Pre-test specimen preparation involved: an initial inspection of the as-received plates, cutting the specimen from the plates, heat-treating the specimen, and

polishing the specimen edge to remove any damage from cutting. This section discusses these pretest specimen procedures.

Initial Plate Inspection

The first step in preparing a test specimen was a non-destructive evaluation of the as-received plates. Each plate had the nominal dimensions of 305mm x 305mm x 1.55 mm. The MMC plate was manufactured by the Avco Specialty Metal, Textron Corporation. They were produced by hot isostatic pressing (HIP-ing) alternating layers of fibers and matrix together. The exact procedures are proprietary. To maintain compatibility among test results, a plate of 16 matrix foils alone was also manufactured. This is called a "neat-matrix." Each plate was inspected for internal fiber damage, gross matrix cracking, and ply delamination using ultrasonic immersion through transmission testing. No processing damage was evident from this evaluation.

Specimen Geometry

A decision must be made on the specimen geometry prior to cutting the plates. Three specimen designs (rectangular, rectangular dogbone, and the hourglass) currently used in MMC experimental research are shown in Figure 3.1. Gayda and Gabb [36] performed load control tests on the unidirectional SCS-6/Ti-15-3 MMC at elevated temperature. They used both the rectangular and dogbone specimen designs.

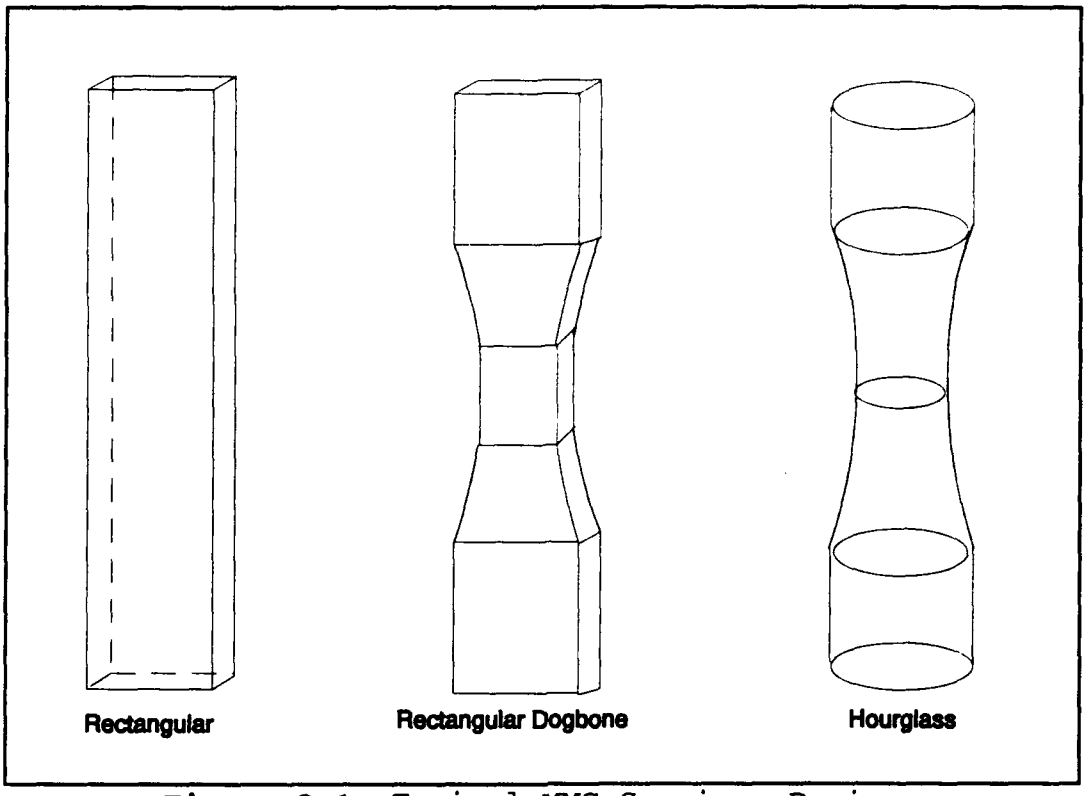

Figure 3.1 Typical MMC Specimen Designs

It was observed that the fatigue life was not affected by the specimen design, and all of the rectangular specimens failed in the hot zone. For this investigation, the most accessible means of cutting the specimens was the diamond saw, which cannot be used to make the dogbone design. Therefore, rectangular specimens, with nominal dimensions of 152.4 mm x 12.7 mm, were used for this investigation.

Heat Treatment

Schubbe [101] performed load controlled TMF tests using the as-received SCS-6/Ti-15-3 MMC. The temperature range was 149-427°C. Increases in the modulus, due to age

hardening of the matrix, up to 20% were observed early in the fatigue life. A way to stabilize the microstructure, thus minimizing diffusion induced property changes, is to heat treat the specimen prior to testing.

Learch et al. [62] performed a study to investigate the effect of heat treatment on the Ti-15-3 neat matrix and the SCS-6/Ti-15-3 MMC. They aged samples of the matrix and MMC at temperatures ranging from 300-700°C for periods of 24 to 168 hours. Depending on the temperature and time, they observed significant changes in some material properties. Additionally, it was noted that the material must be protected from oxidation at temperatures greater than 550°C. This can be accomplished by heat treating the specimen in an inert environment. Several studies [35, 58, 59, 63] have heat treated the Ti-15-3 material system at 700°C for 24 hours in an Argon atmosphere. In an attempt to be compatible with these investigations, the specimens used in this study were subjected to the same heat treatment.

Polishing Procedures

The final preparation before testing was to grind and polish the specimen edges to remove any damage from cutting. A Buehler number 8 platen mounted on a Buehler Maximet was used for this procedure. Diamond suspension was applied to the platen as an abrasive agent in the following progression: 45 micron, 15 micron, 9 micron, and then 6

micron. The 45 micron diamond suspension removes any damage from the cutting process and flattens the side of the specimen. This still leaves long, deep, scratches in the specimen, which inhibits the clarity of edge replicas. As the diamond suspension becomes finer, these scratches are removed. The edge of a typical specimen after this procedure is shown in Figure 3.2. Scratches were still present, but they were easily distinguished from matrix or fiber cracks in an edge replica.

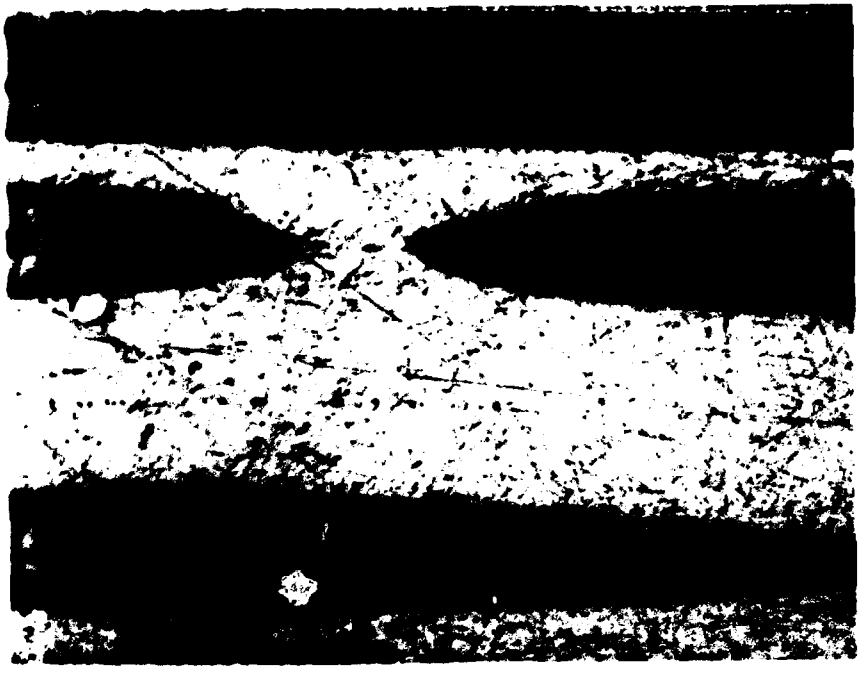

Figure 3.2 Specimen Edge After Polishing (100X)

Experimental Equipment

The test system used in this study consisted of the following three subsystems: a mechanical loading subsystem, a temperature control subsystem, and a data acquisition subsystem. A block diagram of the entire test system is shown in Figure 3.3. This section identifies the type of equipment used in each subsystem.

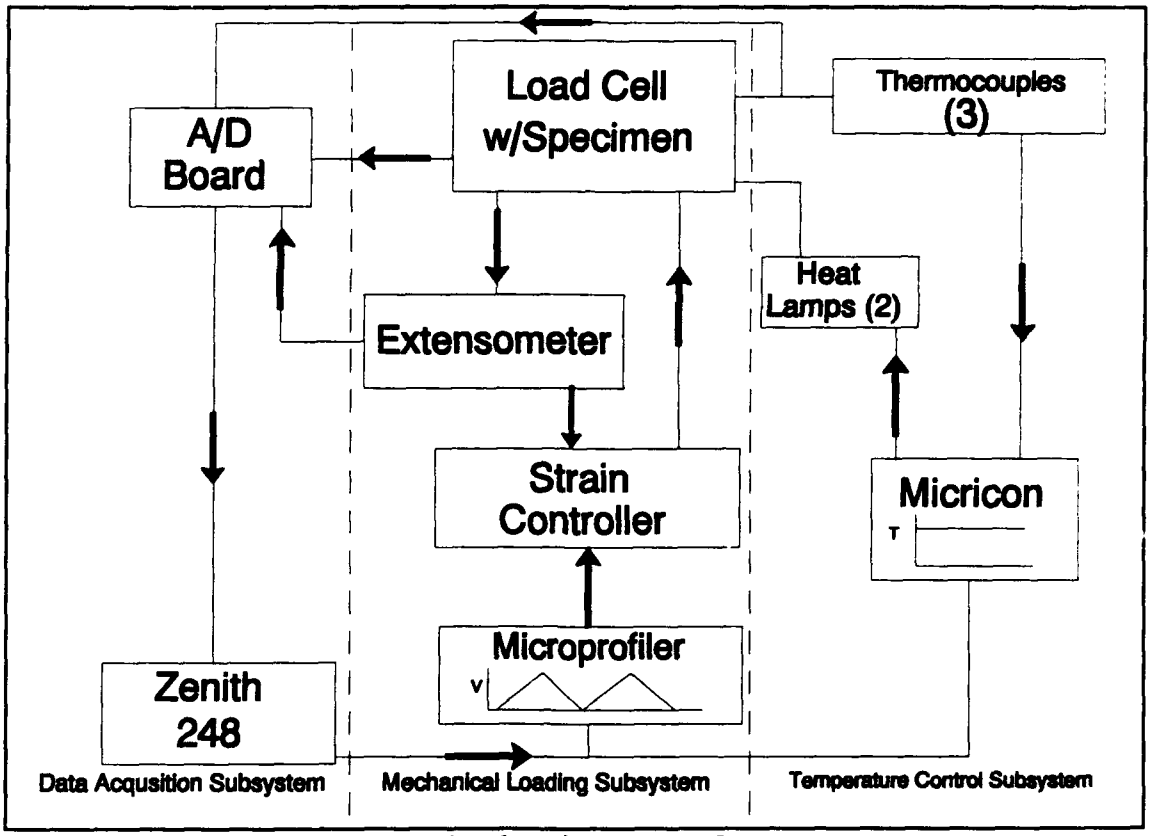

Figure 3.3 Block Diagram of Test System

Mechanical Loading Subsystem

All of the relaxation and fatigue tests were conducted on a 22 Kip servo-hydraulic (Material Test System (MTS) model 810) test frame. This test frame was configured with 100 MPa water cooled, hydraulic grips. A MTS quartz rod, air cooled, extensometer (model 632.50B-4) measured the displacement inside the 12.7 mm gauge length (Figure 3.4). The MTS Microprofiler (model 458.91) served as the function generator. This in conjunction with a MTS DC Controller (model 458.11) and the quartz rod extensometer provided the closed-loop system to maintain the desired mechanical parameters.

Temperature Control Subsystem

The elevated temperature environment was controlled by two 1000 watt, tungsten filament, water cooled, parabolic strip heaters. The strip heaters were controlled by a Micricon (model 82322) controller [76]. To minimize thermal gradients in the gauge section, the strip heaters were slightly offset from one another (Figure 3.5). Three Chromel-Alumel (type-K) thermocouples were used as temperature feedback transducers. Two of these were connected to the Micricon, and one was used as part of the data acquisition subsystem.

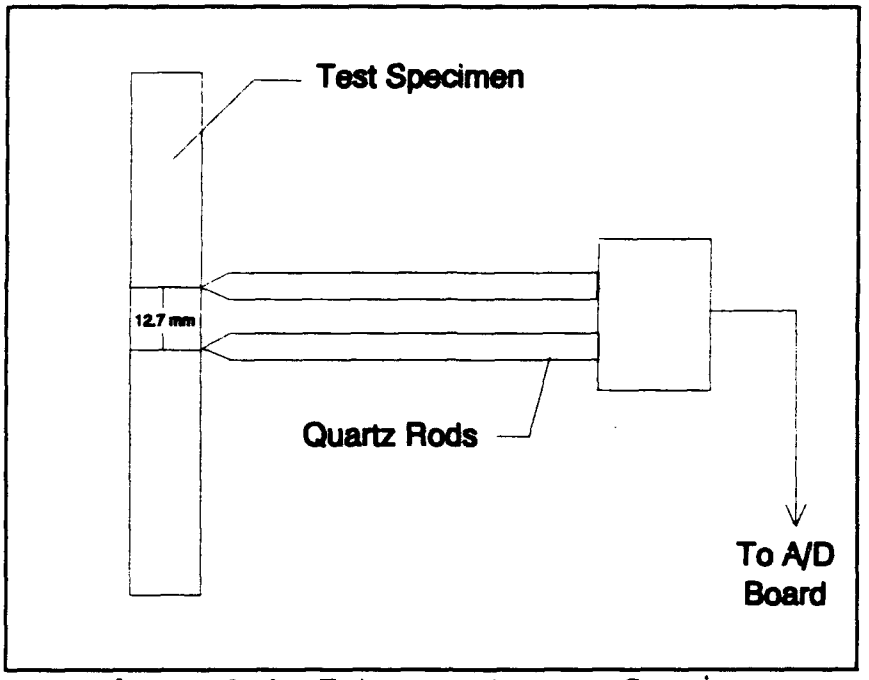

Figure 3.4 Extensometer on Specimen

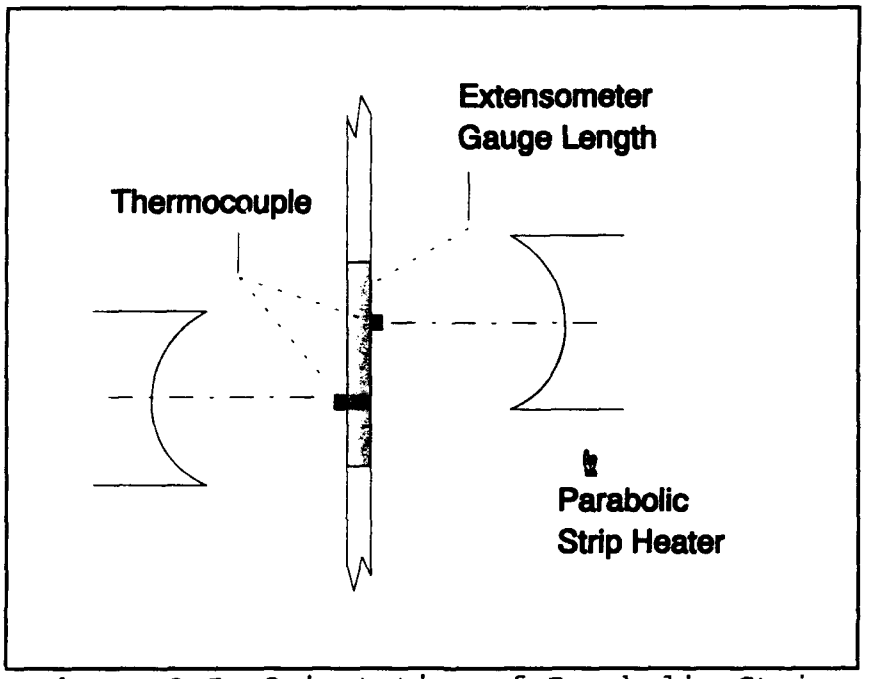

Figure 3.5 Orientation of Parabolic Strip Heaters to the Gage Section

Data Acquisition Subsystem

A Personal Computer (PC) was required to monitor the test parameters and gather the required data for storage on the hard disk. The PC utilized in this study was a Zenith 248 configured with a 80286 microprocessor and a 80287 math coprocessor. A software program was written by the student in Microsoft QuickC to: provide all the base instructions to the Micricon and the Microprofiler to generate their specific functions, monitor the test parameters, and gather temperature, stress, and strain data for any given cycle.

To prevent a test specimen from buckling, a passive feedback and control system was used [9]. This system was only activated after the stress and strain data over a cycle was acquired. If the minimum stress was close to zero, the Microprofiler program was updated to increase the minimum output voltage. Thus, the specimen never experienced any compressive stresses. This resulted in an increasing ratio of the minimum strain to the maximum strain (Figure 3.6), which will be referred to as the decreasing amplitude or hybrid strain control mode.

The output voltages of the transducers (load cell, extensometer and one thermocouple) were read from a Techmar Labmaster analog-to-digital (A/D) converter board. The sampling frequency of the A/D board was measured at approximately 7,500 samples per-second per-channel. One

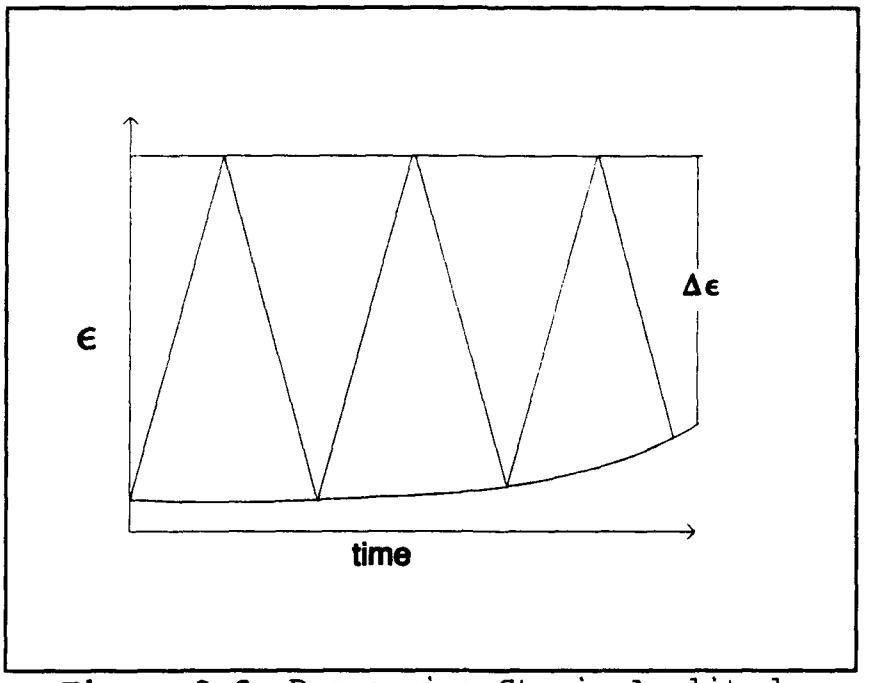

Figure 3.6 Decreasing Strain Amplitude Profile

thousand pairs of voltage data were gathered on any given cycle. These data were then converted to stress and strain values. Every fifth pair of these values were written to a data file and saved on the hard disk. A sample stress-strain curve, consisting of the 200 data points saved to a disk file, is shown in Figure 3.7. This is practically a continuous curve, providing an accuracy on the order of a few MPa. A separate data file was also built during a test which contained a record for each cycle. An extract from this type of file is shown in Table 3.2. Each record consists of: the cycle number, maximum and minimum stress levels, maximum and minimum strain levels, current

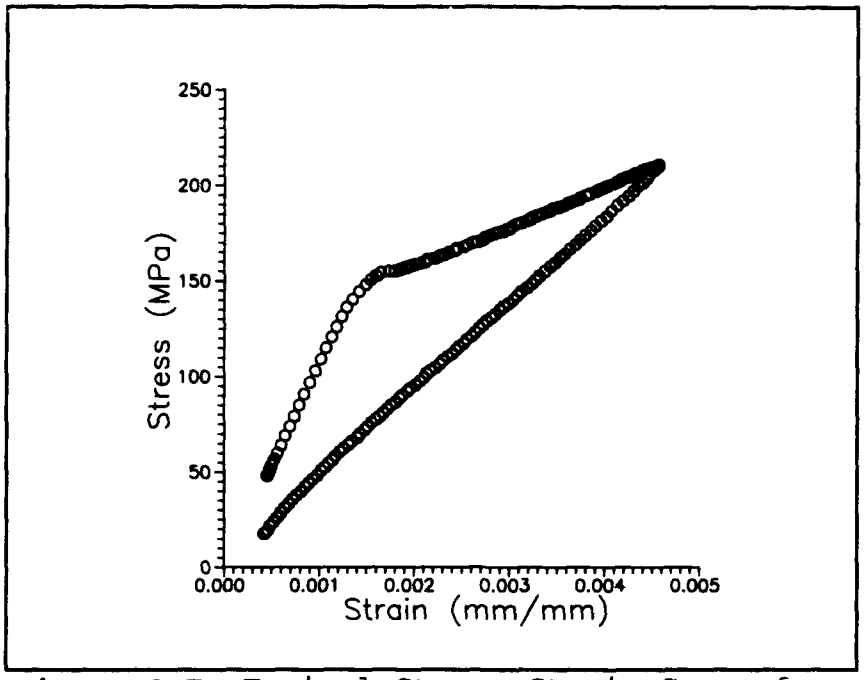

Figure 3.7 Typical Stress-Strain Curve from a Data File (200 points)

Table 3.2 Extract from Fatigue Test Data File

Cycle	Stress (MPa) Max	Min	Strain (mm/mm) Max	Min	T (°C)	Modulus (GPa)
1	211.0	17.7	0.00457	0.00042	425	42.47
5	203.6	18.5	0.00449	0.00043	427	43.70
10	201.2	18.5	0.00449	0.00043	427	43.21
.....						
200	187.2	13.5	0.00450	0.00050	426	42.03
.....						
345	174.5	1.2	0.00450	0.00053	428	42.04
350	173.7	1.6	0.00452	0.00054	427	41.64
354	173.7	1.6	0.00452	0.00054	427	41.64

temperature inside of the gage section, and the modulus. These data files provided all the information required to generate the post fatigue test plots.

Experimental Procedures

Experimental procedures for this research involved performing: initial material measurements, relaxation tests, fatigue tests, and, periodically, interrupting some fatigue tests to obtain edge replicas. Finally, data reduction was performed after each test. This section describes these procedures along with test matrices.

Material Property Measurements

The first series of tests involved measuring the properties of the as-received and aged material. A room temperature and elevated temperature (427 °C) modulus was measured for each specimen in the as-received condition. The coefficient of thermal expansion (CTE) was also measured. After each specimen was heat treated, and these material properties measured again.

Fatigue and Relaxation Tests

Relaxation and fatigue tests were conducted at 427°C. Test matrices for the neat matrix and the 0° and 90° laminas are shown in Tables 3.3, 3.4, and 3.5, respectively. These strain levels were selected based on static tests data available in the literature [63]. From these data, the

Table 3.3 Ti-15-3 Test Matrix

Specimen #	Test Type	ϵ_{max} (%)
1	R	.5
2	R	.6
3	R	.3
4	R	.5
5	R	.4
6	F	.7
7	F	.5
8	F	.4
9	F	.25
10	F	.6

R = Relaxation
F = Fatigue

Table 3.4 $[0]_8$ Test Matrix

Specimen #	Test Type	ϵ_{max} (%)
1	F	.6
2	F	.7
3	F	.5
4	F	.5
5	F	.5
6	F	.45
7	F	.7
8	F	.7
9	F	.5
10	F	.5
13	F	.4

F = Fatigue

Table 3.5 $[90]_8$ Test Matrix

Specimen #	Test Type	ϵ_{max} (%)
1	F	.25
2	F	.4
3	F	.1
4	F	.2
5	F	.45
6	F	.3
7	F	.2

F = Fatigue

maximum strain levels were chosen in the linear and non-linear regions of the stress-strain curves. All of the fatigue tests were run under the strain controlled loading mode at a strain rate of 0.002 mm/mm/s. The initial ratio of the minimum strain to the maximum strain was set to 0.05. For the relaxation tests, each specimen was loaded at a strain rate of .002 mm/mm/s, which matched the strain rate in fatigue.

Edge replicas were periodically taken during some fatigue tests. In this technique, a permanent impression of the specimen edge is produced on a cellulose acetate film [53]. The advantage of this method is that the replica can be taken while the specimen is still in the test machine. Replicas were taken at room temperature while the specimen

was being subject to 75% of the maximum observed load. Each replica was then examined for details of damage.

Following each test the data were processed. Data analysis consisted of plotting the histories of the stress, strain, modulus, and stress-strain response. These curves were described in Chapter II.

Post Test Specimen Preparation, Procedures, and Equipment

After completion of a fatigue test, specimens were studied to identify damage mechanisms. Some untested specimens were also examined, which helped to identify damage in the as-received MMC. Each specimen was viewed over a wide range of magnifications using optical microscopes, scanning electron microscopes (SEM), and transmission electron microscopes (TEM). A detailed understanding of the damage mechanisms were obtained in this manner. This section describes the specimen preparation, procedures, and equipment used for this analysis.

Initial Post-Mortem Review

The first step to identify damage was a low magnification viewing on an Epiphot optical microscope. This revealed such damage mechanisms as fiber cracks on the specimen edge and, when a specimen did fail, gave some insight to how the specimen failed. For example, was the fracture surface the result of a static overloading or was

it the result of matrix cracking. This initial review was from the fracture surfaces of the failed specimens.

Specimen Preparation - Optical and SEM

To gain a more detailed understanding of the damage, the specimens were sectioned. Samples of each specimen were taken perpendicular and parallel to the loading direction (Figure 3.8). This was accomplished using a low speed diamond saw. These samples were then mounted in Epomet molding compound and polished.

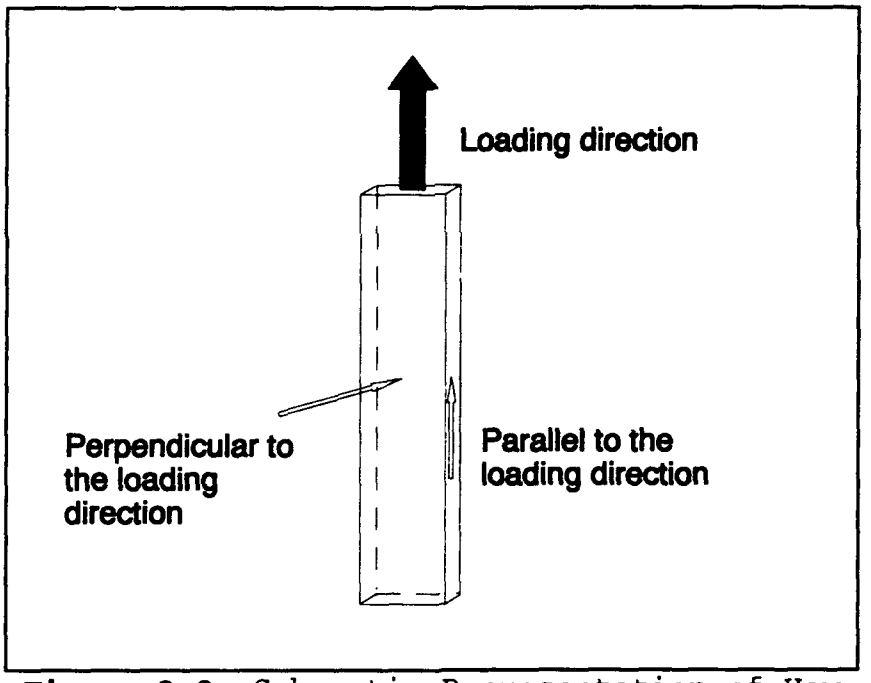

Figure 3.8 Schematic Representation of How Test Specimens were Sectioned

A labor intensive polishing procedure was required view the fine details of the damage. This procedure started with

a rough grinding of a sample using a Buehler number 8 platen mounted on a Buehler Maximet. A 45 micron diamond suspension was applied to the platten first to remove any deep scratches that occurred from sectioning. Using this same diamond suspension, some of MMC samples were ground down to the top of the first layer of fibers. A decreasing progression of diamond suspension (15 micron, 9 micron, and then 6 micron) was then applied to the platten. This provided a smooth surface to the naked eye, but, for viewing at the high magnifications, the specimens still required further polishing.

After the initial polishing on the Maximet, each sample was run through a series of Buehler Vibromets. The Ti-15-3 matrix is a much softer material than the hard ceramic SCS-6 fiber. As a result, the procedure described above polished more of the matrix away then the fiber. To get the fiber and matrix onto an even plane, the first Vibromet contained a stainless steel mat in solution of 1 micron diamond paste and Hyperez OS lubricant. After 20-30 minutes on this Vibroment, the specimens were then placed on a series of two Vibromets for no less than eight hours. The first contained a perforated texmet cloth in a solution of 1 micron diamond paste mixed with Hyperez OS lubricant, while the second contained a nylon cloth over a perforated texmet in a solution of .5 micron diamond paste mixed with Hyperez OS

lubricant. A final polishing was done on a Vibromet with on a micron cloth in a .06 micron Colloidal Silica Neutral Solution (MasterMet). The specimens were on this last vibromet for about an hour. After this polishing procedure is completed, the specimens were ready for either a microscopic analysis or to be etched. The etching procedure is described next.

The purpose of going through such a laborious polishing process was to view the samples in a great amount of detail. To reveal different features, a sample is often etched in a acid based solution (etchent). Three etchents were used in this research. A solution of 10% molybdic acid and 90% distilled water was used for the as-received material. After heat treating and fatigue testing, Krolls etchent was used to highlight the microstructure and damage mechanisms. A slightly different etchent was used when it was desired to observe the matrix slip bands [59]. In this case, the specimen had an additional heat treatment at 427°C for 24 hours in an Argon atmosphere prior to sectioning and polishing. This additional heat treatment precipitated the α-phase along the slip bands. A solution of 3% ammonium bifluoride and 97% distilled water was then used. This solution attacks the α-phase, making the slip bands easier to identify.

At this point, the samples were ready to be investigated using optical and scanning electron microscopes (SEM). The optical microscope gave good insight into the change in microstructure, damage mechanisms, and the development of matrix slip bands. Once an overall optical review was complete, some key areas were investigated at higher magnifications using an AMRAY 1810D SEM. The SEM provided a detailed view of the damaged regions, such as the debonded fiber-matrix interfaces, matrix cracks, and fiber cracks.

Specimen Preparation - TEM

Besides optical and SEM microscopy, some specimens were examined using a transmission electron microscope (TEM). TEM is a useful tool in identifying microstructure characteristics and deformation mechanisms on a small scale (on the order of a few microns). Majumdar and Newaz [68] used a TEM to identify dislocations in the as-received and static tested SCS-6/Ti-15-3 composite. For this research, a JOEL 200KV TEM was used to compare matrix deformation characteristics of the as-received, aged, tested specimens.

TEM requires an extremely thin sample to allow for the transmission of electrons. The samples were prepared as follows. A few 2-3mm thick samples were first cut from a specimen. These samples were then reduced to a thickness of 15-17 microns using a procedure similar to that described

above for the optical and SEM sample preparation. A VCR Inc. Dimpler was then used to grind a concave depression in the sample. The progression of diamond suspension used with the dimpler was: 6 micron, 3 micron, and then 1 micron. The thickness of the dimpled section is approximately 10-12 microns at this point. Each sample was then Ion-milled. This resulted in a small hole in the sample, around which the sample was thin enough to allow for the transmission of electrons.

IV. Experimental Results and Discussion

This chapter concentrates on discussing the results obtained from the experiments and damage mechanisms observed from microscopic analysis. Through systematic experimentation, the fatigue behavior of the Ti-15-3 neat matrix and SCS-6/Ti-15-3 unidirectional MMC were characterized. For the MMC, the 0° and the 90° (fibers parallel and perpendicular, respectively, to the loading axis) laminas were tested in fatigue. Microscopy techniques were then used to identify damage. In Chapter VI, analytical models were applied to characterize, quantitatively, the fatigue behavior of these laminas. The methodologies used in developing these models were based on the information explained in this chapter.

Initial Material Characterization

Material characterization begins with a thorough understanding of the material properties and microstructure of the untested specimens. This section discusses some differences between the: as-received neat matrix, heat-treated neat matrix, as-received MMC, and the heat-treated MMC. Of particular interest in this study was the change in Young's modulus due to age hardening of the matrix, which is reviewed briefly. The microstructure evolution of the

Ti-15-3 neat matrix and SCS-6/Ti-15-3 MMC subjected to different environments were also investigated. This data provided a baseline to which the specimens tested in fatigue were compared.

Material Properties

Table 4.1 shows the summary of Young's modulus for the Ti-15-3 neat matrix at room temperature. Both the as-received (unaged) and post heat treated (aged) values are shown. It was observed that the as-received neat matrix had an average modulus of 82 GPa ± 3 GPa at room temperature. This increased slightly to 85 GPa ± 5 GPa after heat treating, but this was less than 4% increase. Given the scatter in the data, the modulus was considered to have remained constant after heat treating.

Consistent with the neat matrix, no measurable changes were observed in the composite modulii. Table 4.2 shows the measured room temperature, longitudinal, modulus for the SCS-6/Ti-15-3 MMC. The average value for the as-received MMC was measured to be 203 GPa ± 9 GPa. This average was nearly unchanged for the heat treated MMC, which was 204 GPa ± 11 GPa. Table 4.3 shows the measured room temperature, transverse, modulus for the SCS-6/Ti-15-3 MMC. In this case, the average modulus was measured to be 120 GPa ± 4 GPa, while the average heat treated value was 116 GPa ± 4

Table 4.1 Measured Neat Matrix Properties

Specimen #	Modulus (GPa) E_{unaged}	E_{aged}	α (mm/mm/°C) (10^{-6})
1		81	10.5
2		89	10.2
3	81	89	
4		87	
5		89	10.2
6		89	10.8
7		86	9.73
8		91	10.6
9	83	83	
10	80	77	
11	86	80	
12	79	77	
Avg	82	85	10.33

Table 4.2 Measured $[0]_8$ Lamina Properties.

Specimen #	Modulus (GPa) E_{unaged}	E_{aged}	α (mm/mm/°C) (10^{-6})
1	215	197	
2	197	199	
3	197	188	6.68
4		215	
5	199	199	6.44
6	211	197	
7		216	
8		203	
9		205	6.59
10		201	6.42
11		183	6.44
12		193	6.33
13		223	6.54
Avg	203	204	6.49

Table 4.3 Measured $[90]_8$ lamina properties.

Specimen #	Modulus (GPa) E_{unaged}	E_{aged}	α (mm/mm/°C) (10^{-6})
1	127	115	
2		108	9.07
3	120	117	9.21
4	114		9.25
5	120	121	
6	116	117	8.58
7	117	116	8.82
8	121	122	
Avg	120	116	8.99

GPa. Again, these values were considered to be constant within the experimental scatter.

Micromechanics Predictions

These measured values of Young's modulus were found to be in good agreement with analytical predictions. The strength of materials equations for calculating the longitudinal modulus (E_l) and transverse modulus (E_t) of a composite are [55]:

$$E_l = E_f * v_f + E_m * (1 - v_f) \quad \textbf{(4.1)}$$

$$E_t = \frac{E_m * E_f}{E_m v_f + E_f (1 - v_f)} \quad \textbf{(4.2)}$$

where E_f and E_m are the modulus of the fiber and matrix,

respectively, and v_f is the fiber volume fraction[1] of the MMC. Using the following constituent values:

$$E_f = 400GPa$$
$$E_m = 85GPa$$
$$v_f = .36$$

Equation 4.1 predicts 198 GPa for the longitudinal modulus, while Equation 4.2 predicts 119 GPA for the transverse modulus. Hence, the measured modulii agreed well with micromechanics predictions.

Microscopy- Microstructure Analysis and Processing Damage

Although it was not the objective of this study to perform an exhaustive metallurgical analysis, a basic understanding of the matrix microstructure and its evolution was desired. This section discusses the microstructure transformation from the as-received material to the heat treated material and its affect on the composite response. Processing damage was identified in this initial review, which assisted in isolating these damage mechanisms from those induced by fatigue.

Ti-V Phase Diagram

Before proceeding with a discussion on the microstructure, it is helpful to review a phase diagram of a alloy similar to the Ti-15-3. This provides a better

[1] This was an average volume fraction measured by using the SEM to count the fibers contained within a specified area.

understanding of the effect of the processing temperature and heat treating temperature on the microstructure. For the Ti-15V-3Al-3Sn-3Cr (weight percent (w/o)) matrix alloy the major solute is vanadium (V). A phase diagram of the Ti-V metal alloy will be sufficient for this discussion (Figure 4.1).

For Ti-15-3 (w/o), the atomic percent (a/o) of vanadium is also 15. Figure 4.1 shows the material is a single phase body-centered-cubic (β-phase) alloy at the processing temperature (1000°C). Theoretically, this single β-phase will be maintained after quenching from this temperature. This is because the α-phase (hexagonal-closed-packed (hcp) structure) does not have time to form.

The heat treatment temperature of 700°C was just slightly below the β transus temperature (Figure 4.1). Holding the specimen at this temperature for extended periods of time will transform the microstructure from the metastable β-phase alloy to a stable two phase (β + α) alloy. Although the composition of the Ti-15-3 is slightly different, similar transformations in the microstructure were observed in the neat matrix and MMC.

As-Received Microstructure

Figure 4.2 shows the microstructure of the as-received Ti-15-3 neat matrix. This material, as with the composite, was manufactured by a hot isostatic pressing (HIP-ing)

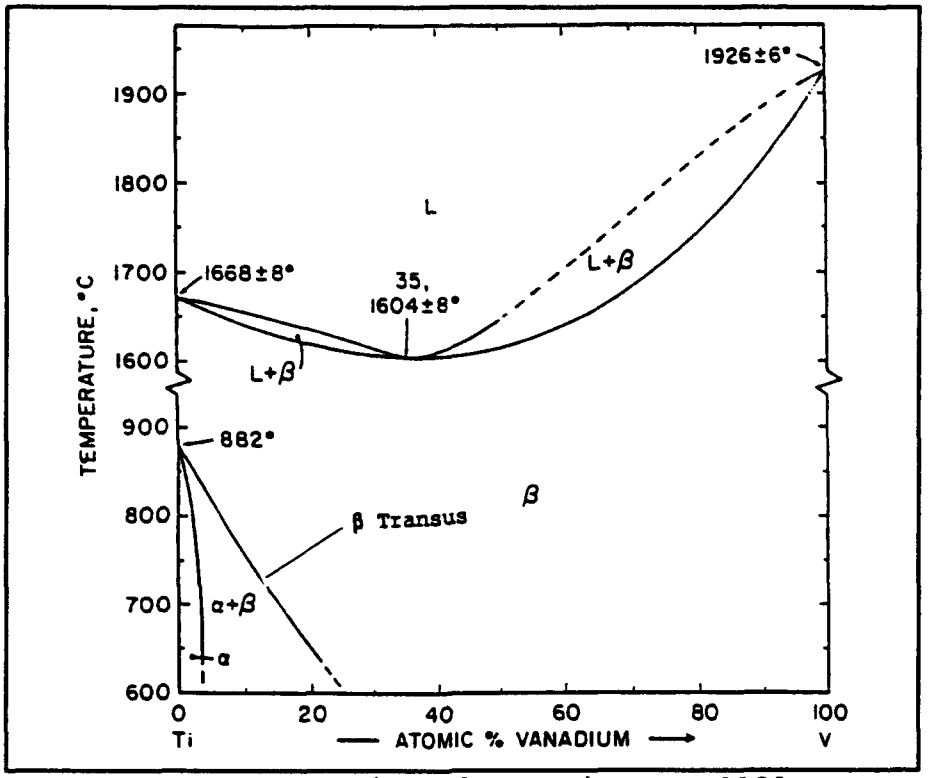

Figure 4.1 Ti-V Phase Diagram [98]

technique using foils of Ti-15-3. The foil boundaries can be identified by the dark horizontal lines extending through the length of the specimen. The dark blotchy areas occurring along the foil boundaries and grain boundaries are believed to be a solute lean β'-phase [62]. This phase has been observed in other β-Ti alloys [4, 8]. β' is metastable phase which forms in solute rich metastable beta titanium alloys where the precipitation of α-phase is sluggish [62].

Figure 4.3 shows the as-received composite. A slightly different microstructure was observed compared to the neat matrix. A higher density of β' was observed inside the

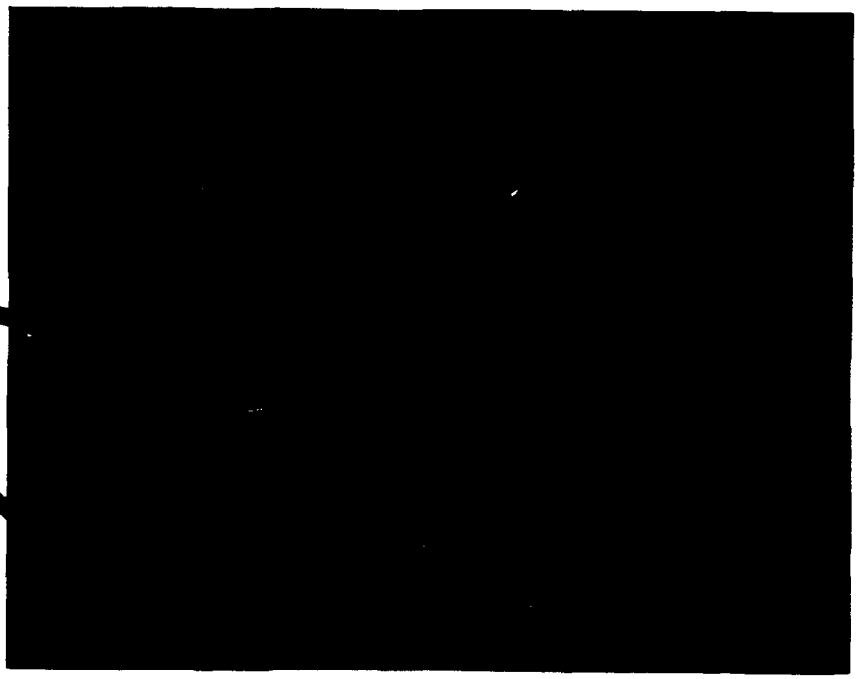

Figure 4.2 As-received Microstructure
Ti-15-3 Neat Matrix (500X)

Figure 4.3 As-Received Microstructure
SCS-6/Ti-15-3 (500X)

grains. Also, a distinct precipitate free (depleted) zone exists around the fibers. This depleted zone was probably due to the reaction of the alloy with the carbon rich coating on the fiber [62].

Heat Treated Microstructure

Figure 4.4 shows the neat matrix after heat treating. Several α-phase precipitates (long needles) were observed to have formed inside the grains. Large α-phase particles had precipitated out at the grain boundaries, replacing the β'-phase. Finally, an α-depleted zone was observed around the grain boundaries.

As in the previous case, a different microstructure was observed in the aged composite when compared to the aged neat matrix. Figure 4.5 shows the SCS-6/Ti-15-3 MMC after the same heat treatment. Again, large α-phase precipitates were observed at the grain boundaries, and an α-depleted zone was observed around these boundaries. Comparing this with the aged neat matrix (Figure 4.4) shows that the quantity of α-phase precipitated in the grains was less than that in the neat matrix. This was particularly evident in the area immediately surrounding the fiber. This depleted zone has been shown to be softer than the surrounding material [62]. As a result, the composite may yield at lower stress levels than the aged neat matrix [63].

Figure 4.4 Heat Treated Microstructure Ti-15-3 Neat Matrix (500X)

Figure 4.5 Heat Treated Microstructure SCS-6/Ti-15-3 (500X)

Processing Damage

In general, the integrity of the as-received composite was good. Upon closer examination, however, some processing damage (i.e. the HIP-ing procedure) was observed. Figure 4.6 shows a cross-section of the aged composite at a location where the fibers were very close. Tiny radial cracks were observed in the interphase zone. Some of these cracks extended into the matrix. This type of processing damage has been observed in other titanium based MMCs [26, 60, 68, 102].

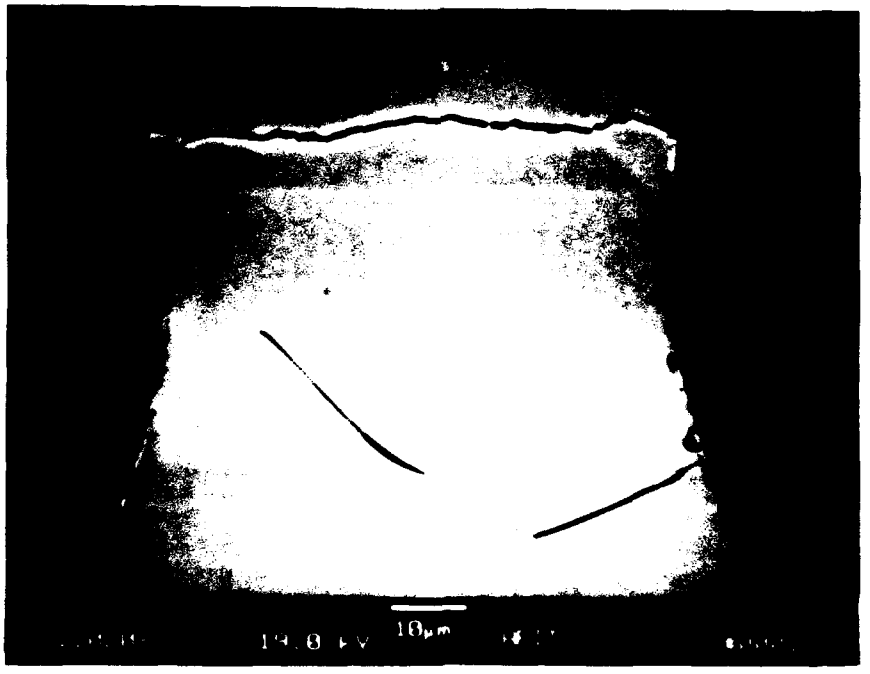

Figure 4.6 Processing Damage in the MMC (1020X)

These interphase and matrix cracks were localized in just a few regions of the specimen. It was previously shown that measured values of the Young's modulii agreed well with micromechanics predictions. This indicates that these cracks had no measurable affect on the room temperature properties of the composite. It has been shown [102] that the processing damage observed in Figure 4.6 was the result of high residual tensile stresses (Figure 1.2) in the matrix and interphase zone. Sullivan and Buesking [102] showed that the hoop stresses in fiber and matrix are higher when an interphase zone was present. Mall and Ermer [71] showed that the general state of stress in the matrix increases when the fiber spacing decreases. These factors lead to cracks developing in the interphase zone and matrix.

Summary of Initial Material Characterization

This section briefly reviewed some characteristics of the Ti-15-3 neat matrix and SCS-6/Ti-15-3 MMC. The review consisted of: material property measurements, the initial condition of the as-received and aged Ti-15-3 neat matrix, and the initial condition of the as-received and aged MMC. It was found that the Young's modulus of both the neat matrix and the MMC were unchanged after heat treating. There was some matrix and interphase damage observed in the untested composite. This damage was localized to the areas were fibers were closely spaced and had no measurable affect

on the room temperature modulii of the MMC. Finally, it was observed that the fiber-reinforced matrix aged slower that the neat matrix.

Neat Matrix

The response of the SCS-6/Ti-15-3 MMC when subjected to fatigue is affected by a combination of inelastic deformations in the fiber and matrix. In the strain control mode, the fatigue behavior of the matrix can dominate the composite response. It is therefore desirable to characterize the behavior of the neat matrix, and then use this information to develop relationships between the neat matrix and the fiber-reinforced matrix. This section discusses the results from experiments conducted on the neat matrix, which included relaxation tests at 427°C and strain controlled fatigue tests at 427°C.

Relaxation Tests

The major objective for performing the relaxation tests was to determine baseline properties so that the fatigue behavior of the matrix, both neat and fiber-reinforced, could be predicted. The following paragraphs concentrate on describing the response of the neat matrix when subjected to a constant strain input. In Chapter V, this information was used to develop a relaxation scheme to predict the fatigue response of the MMC and neat matrix.

The relaxation tests were performed at nominal strain levels of .3%, .5%, and .6%. Figure 4.7 shows the stress relaxation of the Ti-15-3 neat matrix when subjected to a constant strain input at these levels of strain. It was observed that the rate at which the stress relaxed was dependent on the applied strain. For example, the stress relaxed faster as the strain level increased. This shows that the material has a dependence on the loading history [85]. As expected, the rate at which the stress relaxed decreased with respected to time. It will be shown in Chapter V that this behavior can be characterized by a function of both the applied strain and time.

An unusual response was observed during these relaxation tests. Compressive stresses developed in all of the tests, and an equilibrium stress was never obtained. The specimens either buckled or the controller interlock of the test machine was tripped before a constant stress was achieved. Two additional tests were run at .4% and .5% on two other test machines configured in the same manner. This same behavior was observed in both cases.

Gayda and Gabb [35] performed relaxation tests on the neat matrix at 426°C. None of their tests exhibited this behavior. The exact reason for the discrepancy was not clear after the tests were performed. It was suspected that the different results can be attributed to differences in

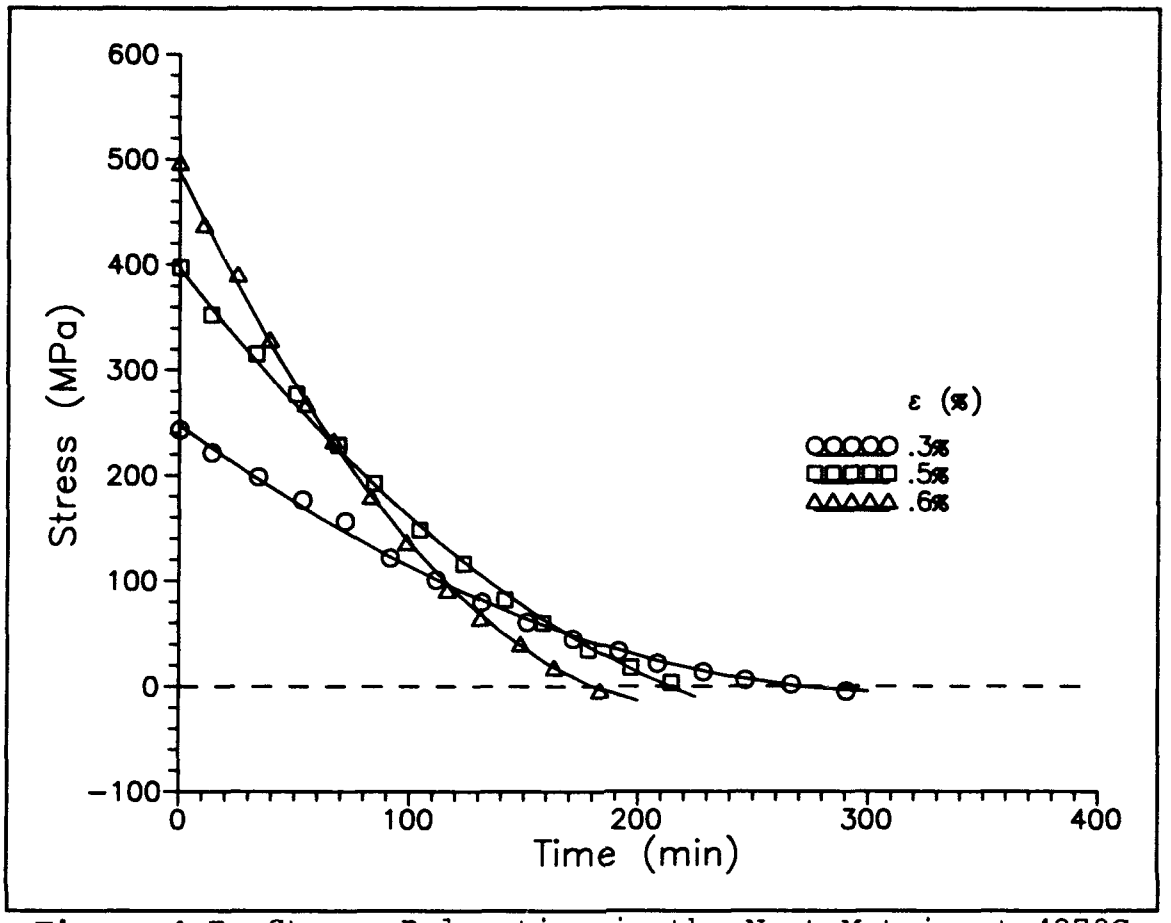

Figure 4.7 Stress Relaxation in the Neat Matrix at 427°C

the experimental setups. For example, the hot zone for the specimens tested in this study was localized to a region around the gage length (Figure 3.5), while the grips were at approximately room temperature. This is known as a cold-grip setup, and results in a thermal gradient in the specimen. In Gayda and Gabb's investigation, the entire specimen and the grips were at the application temperature (426°C). This is a hot-grip setup, and no thermal gradients exists in this case. Other investigations [57] have shown

differences in the material response when using the hot-grip and cold-grip configurations.

The strain level dependence observed in the experiment was also unexpected. It was thought that the stress would take longer to relax at the higher levels of strain, and a simple time shift would then collapse the data on to a master curve [35]. This was clearly not the case in these tests. Since the tests results were repeatable, this may also be a characteristic of the cold-grip configuration.

Albeit, the phenomena discussed above are unusual. Since all of the tests were conducted in the same experimental configuration, compatibility among the tests results was maintained. The data obtained from these relaxation tests were therefore considered to be representative of the material behavior in fatigue.

Fatigue Tests

In addition to the relaxation tests, a series of strain controlled fatigue tests were conducted on the neat matrix. These data were used in Chapter VI to validate a scheme developed to predict the time dependent behavior of the matrix. These data were also useful for comparing to the counterparts from the MMC tested in fatigue.

Fatigue Response

Figure 4.8 shows the histories of the maximum stress, as a function of time, for the neat matrix subjected to

fatigue. The maximum strains levels were .25%, .4%, .5% and .7%. It was observed that the rate of change in the maximum stress was a function of the maximum strain, which is similar to that observed in the relaxation tests (Figure 4.7). For an equivalent maximum strain, the rate at which the stress relaxed was slower in the fatigue tests. This was expected since the fatigue response was an accumulation of the creep deformation at the different strain levels in the fatigue cycle, as opposed to the relaxation tests where the strain was held constant. The rate at which the stress relaxed also changed over time, which again is similar to the results observed in the relaxation tests. These similarities suggests that the fatigue behavior of the matrix can be predicted with the data obtained from relaxation tests, which will be shown in Chapter VI.

Elastic Modulus History

Previous studies [89, 101] of the SCS-6/Ti-15-3 composite have shown that the elastic modulus increased during fatigue testing at elevated temperature. As mentioned in Chapter III, the objective of heat treating the material prior to testing was to remove this variable. Figure 4.9 shows the elevated temperature modulus, as a function of time, for the neat matrix specimens subjected to fatigue. An average increase of 10% was observed in the

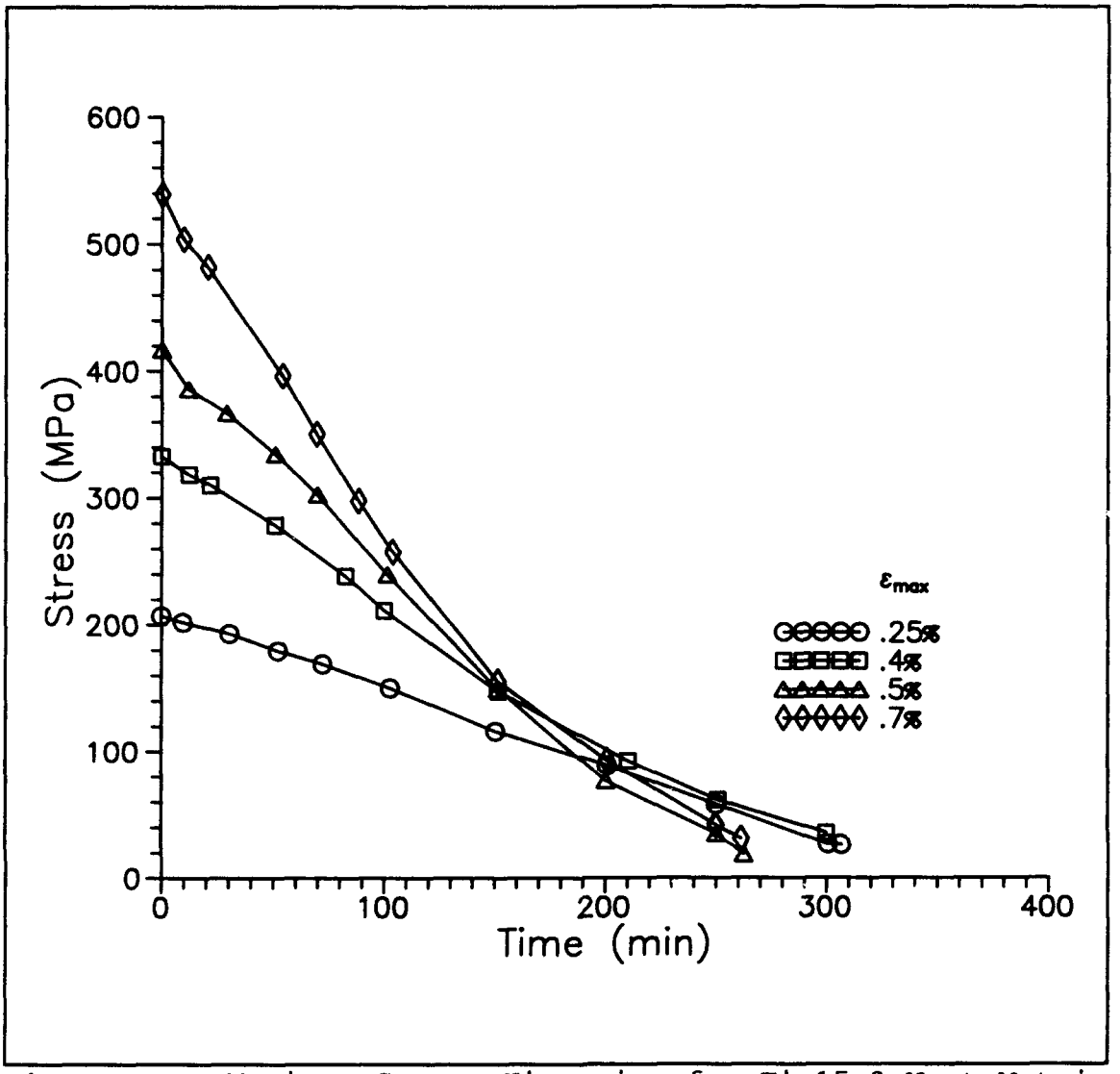

Figure 4.8 Maximum Stress Histories for Ti-15-3 Neat Matrix Subjected to Fatigue

elastic modulus. This implies that heat treating the material was not enough to stabilize the modulus.

It was desired to determine the maximum change in the modulus of the neat matrix due to thermal exposure only.

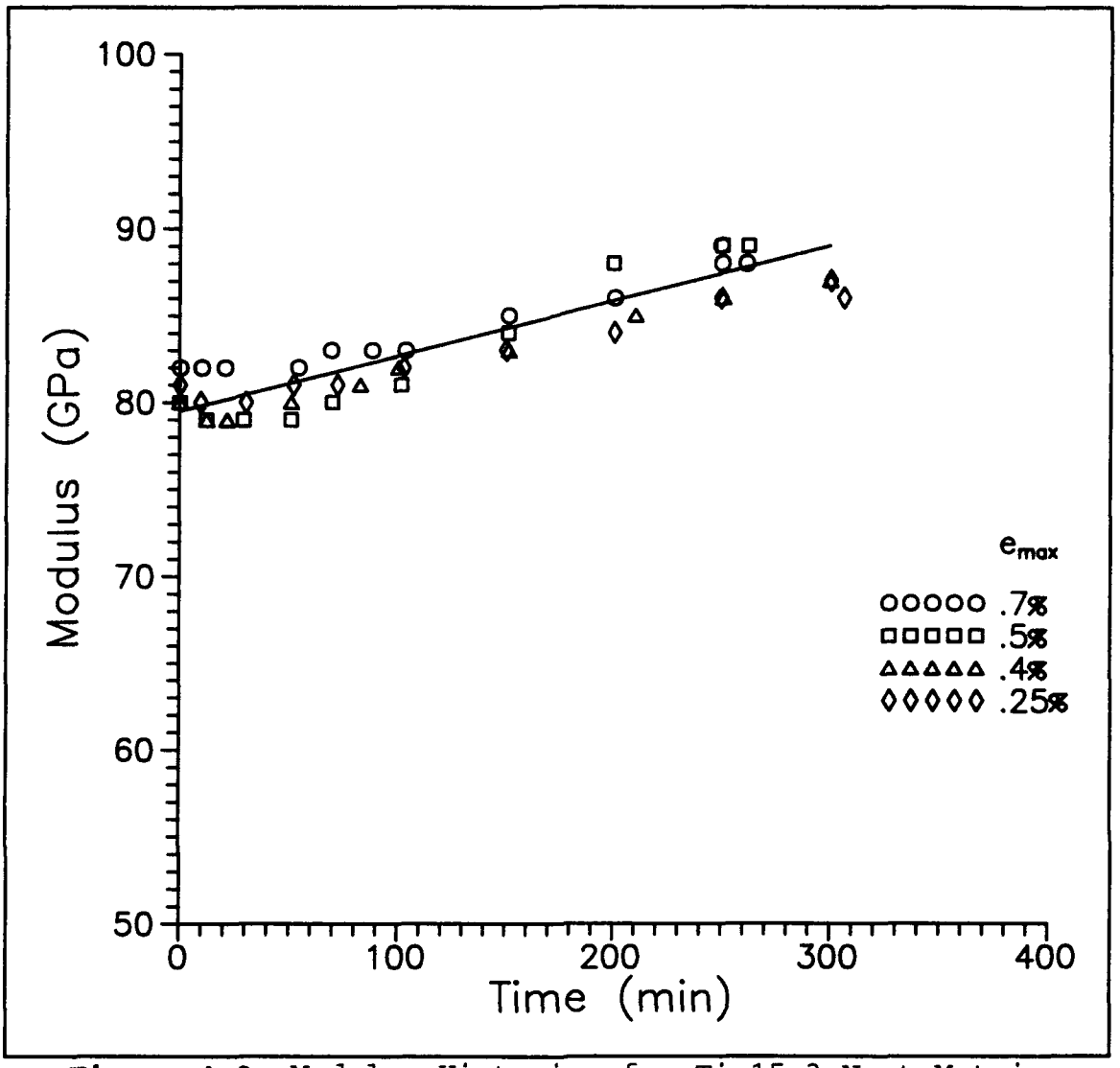

Figure 4.9 Modulus Histories for Ti-15-3 Neat Matrix Subjected to Fatigue

This would provide an upper bound of the modulus for the fiber-reinforced matrix. A heat treated, neat matrix, specimen with no load was exposed laboratory air at 427°C.

Figure 4.10 shows the change in the room temperature modulus as a function of time for this specimen. Other values of the modulus shown are: the room temperature modulus for the specimens tested in fatigue, the modulus t elevated temperature for the specimens tested in fatigue, and the room temperature modulus for the specimens subjected to a constant strain input.

For the specimen held at a zero load, the modulus increased by 20% in the first 11 hours (660 min). After this the modulus stabilized at a value of 110 GPa. Similar increases in this material property have been observed in other studies [33, 62] with the Ti-15-3 neat matrix. Since the modulus remained constant for the next 13 hours, this was assumed to be the maximum stiffness the matrix, either neat or fiber-reinforced, would achieve at 427°C.

The rate of change in the modulus between the specimen held at a zero load was compared to the specimens that were tested in fatigue and those subjected to a constant straininput (Figure 4.10). There was no measurable difference. These results imply that mechanical loading had no affect on the modulus. Instead, this suggests that the increase in stiffness was the result of a diffusion process.

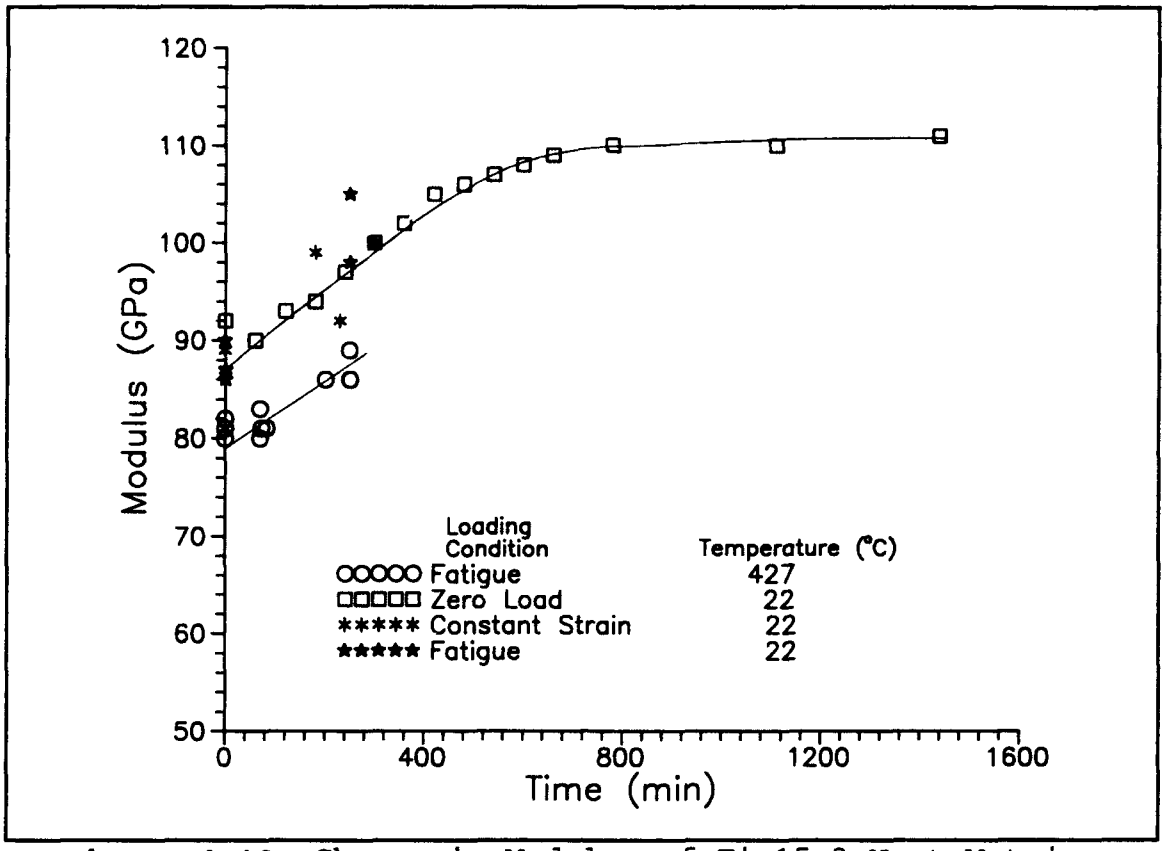

Figure 4.10 Change in Modulus of Ti-15-3 Neat Matrix, Various Loading Conditions

Effect of Changing Matrix Modulus on the MMC Fatigue Response

Using Equations 4.1 and 4.2 the effect of the increasing modulus of the neat matrix on the fiber-reinforced matrix can be approximated. Some of the fatigue tests for the 0° lamina ran as long as three weeks (500 hours). It was shown above that the highest value the room temperature modulus of the neat matrix would achieve was 110 GPa. This would equate to a only 7% increase in stiffness for the undamaged 0° lamina. On the other hand, the 90°

lamina tests lasted no longer that 5 hours. From figure 4.10, the room temperature modulus of the neat matrix would be 95 GPa. This would equate to a 10% increase in the transverse stiffness. It will be shown later that these increases were never observed due to the concurrent development of damage in the laminas.

In some fatigue tests, the modulus of a MMC increased after an initial reduction. Later in this chapter, this initial reduction will shown to be due to fatigue damage, and the subsequent increase is correlated to the increase in the matrix stiffness discussed here. This suggests that the effect of an increasing stiffness of the matrix may serve to mask some of the damage present in the composite.

Microscopy - Damage Mechanisms

For the strain controlled fatigue tests performed in this work, the matrix was found to contain most of the fatigue dependent characteristics. Thus, to characterize the composite, it was beneficial to understand the behavior of the neat matrix. This section concentrates on identifying the damage and deformation mechanisms observed in the tests described above.

Microscopy - Relaxation Tests

There were two objectives to be met by running the relaxation tests. As previously mentioned, the primary objective was to determine baseline properties of the

relaxation behavior, and then relate these properties to the fatigue response of the neat matrix and MMC. A secondary objective was to determine: if there were any changes in the microstructure due to the different loading conditions (i.e. constant strain vs. fatigue), and if any damage mechanisms were dependent on the loading conditions. This section concentrates on the second objective.

Figure 4.11 shows a typical specimen after a relaxation test. This should be compared to its counterpart from the untested, heat treated, neat matrix (Figure 4.4). There was no significant difference in the microstructure. This implies that this loading condition had no affect on the microstructure. There was no evidence of any damage (i.e. matrix cracking or foil delamination).

An additional effort in this direction was pursued using transmission electron microscopy (TEM). This enabled a more detailed view of the microstructure of the matrix and would provide evidence of the type of deformation occurring. Figure 4.12 shows a TEM photograph for the as-received material. As in the optical analysis, a single phase (β) alloy was observed. Figure 4.13 shows a TEM photograph of the neat matrix after heat treating, which is the pretest specimen baseline condition. Large α-phase precipitates (long needles) were observed in a matrix of beta. These two

⇔

Loading
Direction

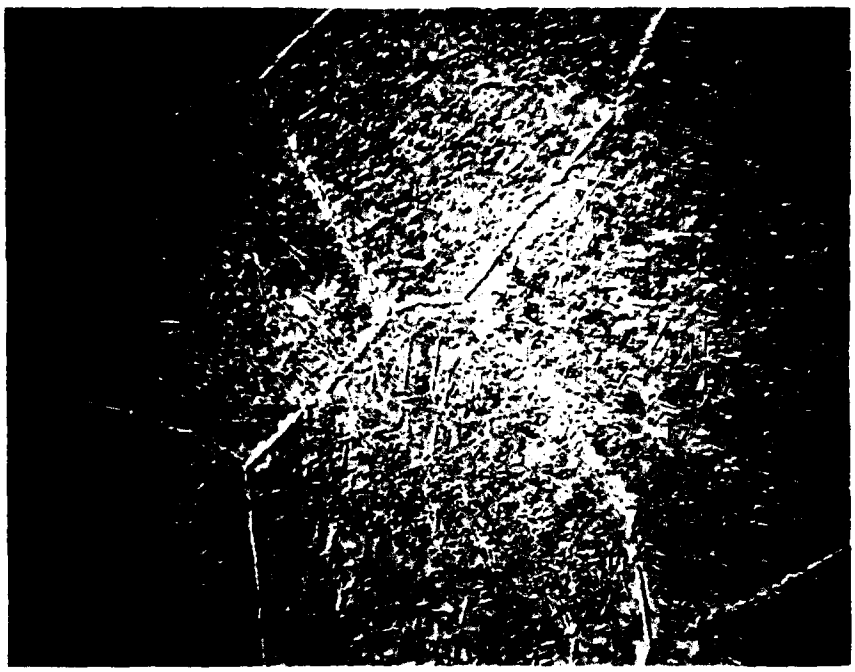

Figure 4.11 Neat Matrix Microstructure After a Relaxation Tests (500x)

Figure 4.12 As-Received Neat Matrix

Figure 4.13 Heat Treated Neat Matrix

photographs provided the microstructure evolution and condition prior to testing.

The typical microstructure after a relaxation test is shown in Figure 4.14. The microstructure was again similar to the aged specimen (Figure 4.13). Further, there were no signs of dislocations in the β-phase or the α-phase precipitates. The absence of observable dislocations suggests that the creep deformation was taken up by the softer β-phase.

Fatigue Tests

Optical microscopy was also performed on the specimens tested in fatigue. Figure 4.15 shows the condition a

Figure 4.14 Neat Matrix After a Relaxation Test

typical specimen after a fatigue test. The loading direction was perpendicular to plane of the paper. This figure should be compared to the untested, aged, neat matrix (Figure 4.4). As with the specimens subjected to a constant strain, no significant differences in the microstructure was observed. So the loading condition had no effect on the microstructure. There was no evidence of foil delamination or matrix cracking either. As in the relaxation tests, this shows that the primary deformation mechanism was matrix creep.

Figure 4.15 Neat Matrix After a Fatigue Test (500X)

Microstructure Comparison

A comparison was made between: specimens loaded at a constant strain, specimens tested in fatigue, and a specimen exposed to elevated temperature (427°C) under a zero load condition. This was performed to determine if the increase in the elastic modulus could be attributed to a change in the microstructure. Figure 4.16 shows the microstructure of the specimen held at a zero load. This should be compared to the microstructure of a specimen after a relaxation test and a specimen after a fatigue test (Figures 4.11 and 4.15, respectively). It should be reemphasized that all of these

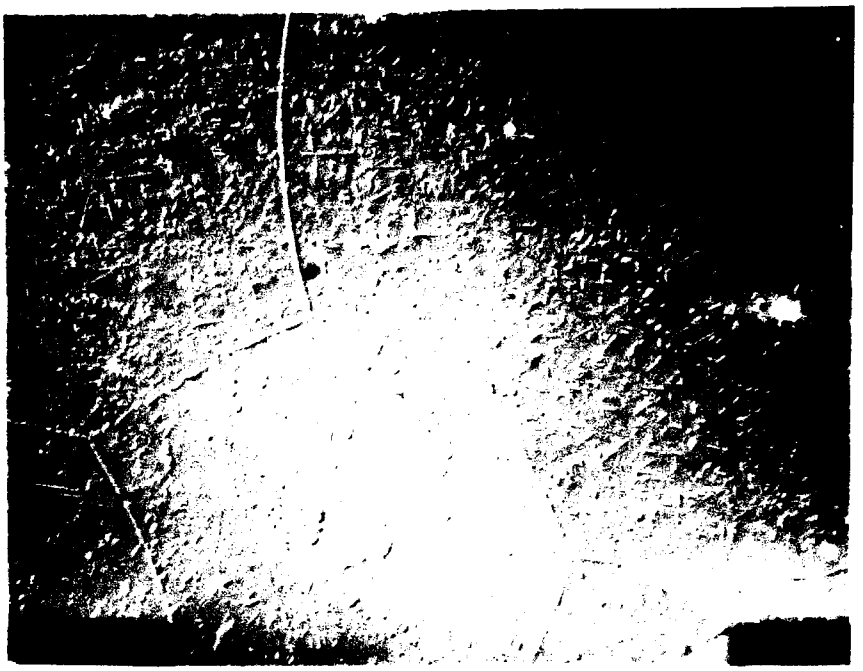

Figure 4.16 Neat Matrix After 24 Hrs at No Load, 427°C (500X)

specimens were heat treated prior to testing, so they had a similar pretest microstructure (Figure 4.4). Even after exposing the neat matrix to these various loading conditions, no differences in the microstructures could be observed. This implies that the increase in the modulus cannot be attributed to a change in the microstructure.

Any further effort in this direction was well beyond the scope of this study. However, these results suggests a different direction, such as hydrogen diffusion [25], needs to be explored to explain why the increase in the elastic modulus occurs. For this study, it was sufficient to

quantify the change in the elastic modulus and its affect on the composite response, which was shown earlier.

Summary Ti-15-3 Neat Matrix

This section discussed the behavior of Ti-15-3 neat matrix at 427°C. It included results from: relaxation tests, fatigue tests, and a microscopy analysis. For the specimens subjected to a constant strain input, stress relaxation of the matrix was observed to be a function of the applied strain level and time. A similar dependence was observed for the specimens tested in fatigue. Microscopy revealed no signs of matrix cracking or foil delamination for either of the two loading conditions. Hence, when the maximum strain level was less than or equal to .7%, the fatigue behavior of the neat matrix under the hybrid strain control mode was dominated by matrix creep.

0° Lamina

Having gained an insight into the fatigue behavior of the neat matrix, fatigue tests and a microscopic analysis were performed on the 0° lamina (fibers parallel to the loading direction). The next few sections discuss the findings from these fatigue tests and the ensuing microscopic analysis. A fatigue life diagram was developed from this information. This diagram related the fatigue

lives to the failure modes as a function of the maximum strain.

0° Lamina Fatigue Response

A set of seven fatigue tests were conducted on the 0° lamina. The maximum applied strain levels were .77%, .75%, .7%, .6%, .5%, .45% and .4%. These levels were chosen so that a fatigue curve, such as that shown in Figure 2.13, could be developed. This section discusses the lamina fatigue response observed from the experiments. A more detailed explanation of the fatigue behavior of the constituents is pursued in Chapter VI.

Table 4.4 shows the summary of the observed failure modes for the 0° lamina. Also shown are two regions on the fatigue curve as discussed in Chapter II (Figure 2.13). As shown, it consisted of two regions:

Table 4.4 Summary of 0° Lamina Failure Modes

Maximum Strain (%)	Failure Mode	Fatigue Curve Region
>.73	Fiber Fracture	I
<.73	Matrix Cracking	II

failure dominated by fiber fractures (Region I), and failure dominated by matrix cracking (Region II). The

fatigue response of the lamina for these two failure modes varied significantly and are discussed next.

Region I - Fiber Dominated Failure Mode

Stress-Strain Response

Figure 4.17 shows the typical history of the stress-strain response for a specimen which exhibited a fiber dominated failure mode. This particular case was for a specimen subjected to fatigue at a maximum strain of .77%. The nonlinear stress-strain response was only observed on the first fatigue cycle. A permanent residual strain (ϵ_p) was present after the specimen was unloaded to a zero load. This nonlinear behavior was attributed to the matrix plastically deforming above a strain level of approximately .55%. It has been shown [68] that matrix slip bands in the 0° SCS-6/Ti-15-3 MMC initiate at approximately this same strain level (i.e. .55%). Matrix slip bands provide the physical evidence of plastic deformation. This deformation mechanism can also be verified by noting that the linear loading modulus and unloading modulus were equivalent. The stress-strain responses on the subsequent fatigue cycles were linear, but the maximum stress relaxed. In Chapter V, it will be shown that this reduction in stress was due to creep deformation of the matrix.

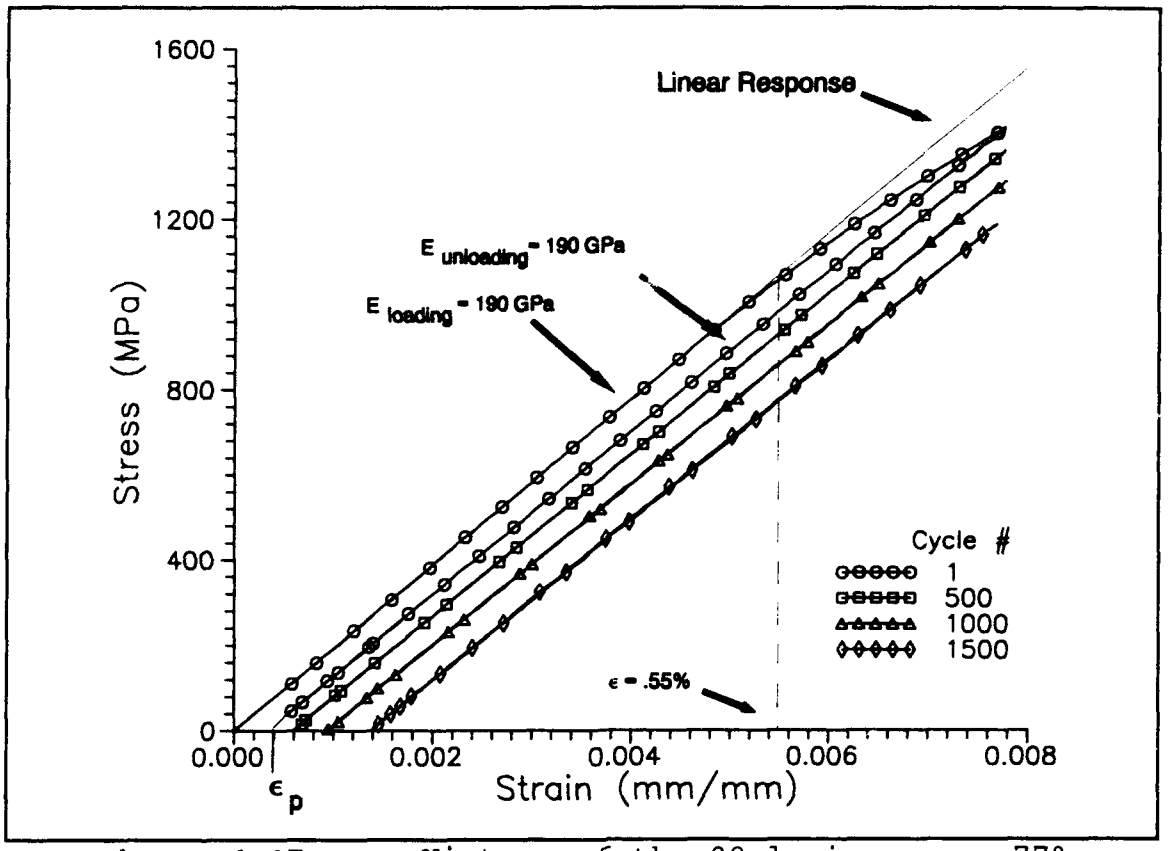

Figure 4.17 σ-ϵ History of the 0° lamina, ϵ_{max}=.77%

Stress and Modulus Histories

Figure 4.18 shows the histories of the maximum stress, minimum stress, and modulus for this same specimen. It was observed that the modulus remained constant over the entire fatigue life. This suggests that the drop in the maximum stress was a result of matrix creep. Thus, the fatigue response was dominated by creep deformation of the matrix. This was accompanied by matrix plastic deformation on the first loading cycle, which initiated at a strain level of .55%.

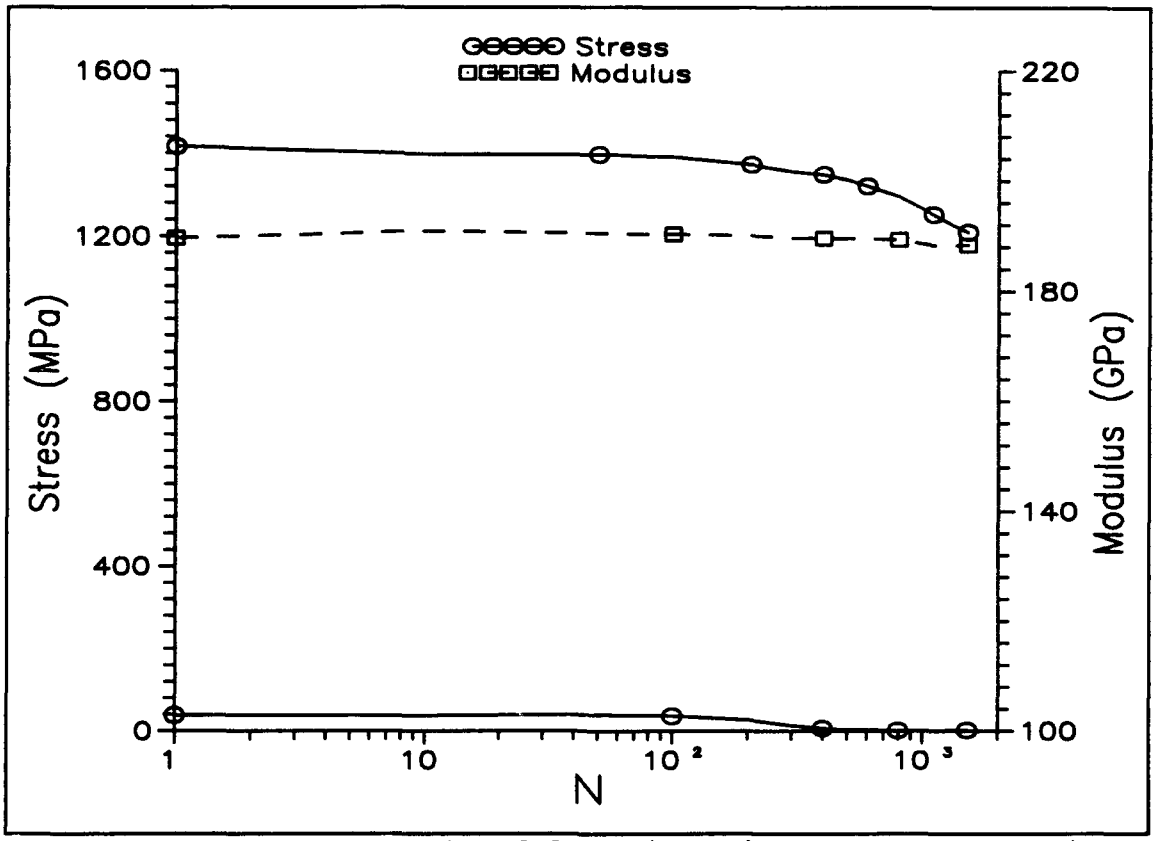

Figure 4.18 Stress and Modulus Histories for a 0° Lamina, ϵ_{max}= .77%

As will be shown later, fractography revealed extensive fiber pullout when a specimen was subjected to fatigue with a maximum strain greater than .73%. This is indicative of a failure dominated by fiber fractures. Thus, even though the response was dominated by matrix creep, the specimen failure was dominated by fracture of the fibers. The lack of any measurable drop in the modulus shows that the fiber failure was rapid, and occurred, at most, over just a few fatigue cycles.

Region II - Matrix Dominated Failure Mode

Stress-Strain Response

Figure 4.19 shows the typical history of the stress-strain response for a specimen whose dominant failure mode was matrix cracking. The particular case shown is for a specimen loaded in fatigue at a maximum strain of .6%.

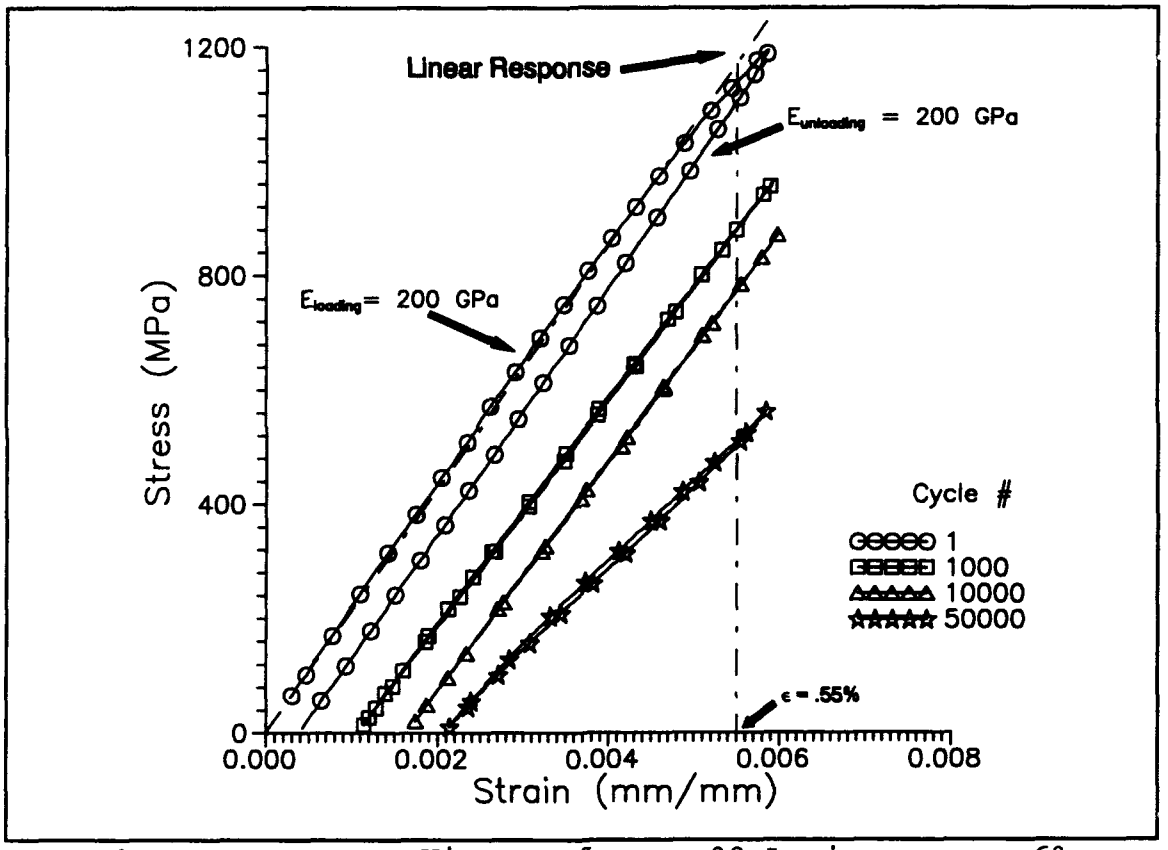

Figure 4.19 σ-ϵ History for a 0° Lamina, ϵ_{max}= .6%

As in the previous case, a nonlinear stress-strain relationship was observed in the first fatigue cycle, which was a result of plastic deformation of the matrix. For

approximately the next 20,000 fatigue cycles the stress-strain response was linear. At approximately 32,000 cycles, the response started to show a slight nonlinear behavior, and a hysteresis in the stress-strain curve was observed. Optical microscopy revealed that this was due to the development of matrix cracks, which will be shown later.

Table 4.4 showed that matrix cracking was the dominant failure mode for specimens tested in fatigue at maximum strains less than .73%. Except for the first loading cycle, the same stress-strain response described above was observed in all of these cases. When the a specimen was subjected to fatigue at a maximum strain less than .55%, the first loading cycle was linearly elastic[2].

Stress and Modulus Histories

Figure 4.20 shows the histories of the maximum stress, minimum stress, and modulus for the same case. To highlight the progression of damage and deformation, the stress response was partitioned into two stages, which are shown in Figure 4.20. The details of these stages are discussed next.

Stage I

The lamina response in Stage I was dominated by matrix creep. In Chapter VI, it will be shown that the creep deformation can be partitioned into two substages (Ia and

[2]See Appendix A for the additional experimental results.

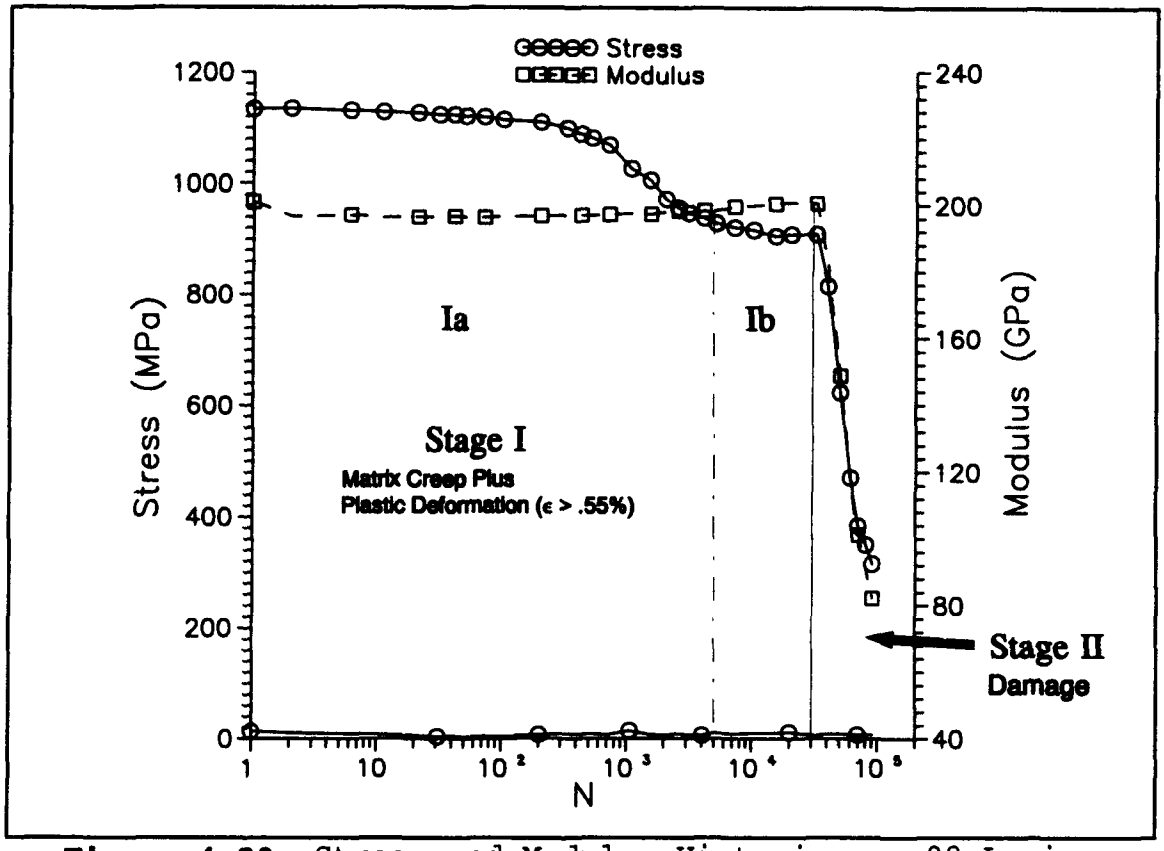

Figure 4.20 Stress and Modulus Histories - 0° Lamina ϵ_{max}=.6%

Ib), as shown in Figure 4.20. During substage Ia, creep deformation of the matrix resulted in a relaxation of the lamina stress. For specimens loaded above a maximum strain of .55%, matrix creep was accompanied by plastic deformation of the matrix. Substage Ib was defined at the point in the fatigue life were the mean stress of the lamina was constant. The analysis will show that, in this substage, the matrix creep in tension was exactly matched by that occurring in compression (self-equilibrating matrix creep).

Finally, the modulus of the specimen remained constant in both substages. This further indicates that Stage I was dominated by matrix deformation (creep and plasticity) and not damage.

Stage II

Stage II was defined by a another change in the lamina response. In this stage, a reduction in the lamina stress was again observed. Instead of the modulus remaining constant, as was observed in subst. e Ia where the stress also dropped, a decrease in the stiffness occurred. This simultaneous reduction in the lamina stiffness and stress suggested that this behavior was the result of fatigue damage. It will be shown later that extensive matrix cracking was observed in specimens that exhibited this response.

It is difficult to define the fatigue life of a specimen that exhibits this behavior. For example, in the load control mode, the strain will show a rapid increase at the end of the fatigue life when the failure mode is dominated by matrix cracking. This results in a fracture of the specimen and provides a clear definition of the fatigue life. The situation is different for this damage mechanism in the strain control mode. As shown above, when damage develops, the specimen will not fracture. Instead, the stress will continue to drop as the damage continues to

accumulate. The definition of the fatigue life is unclear in this case, and some other failure criteria must be defined. In this investigation, the fatigue life was conservatively defined when a concurrent and rapid drop in both the stress and modulus occurred, which was defined above as Stage II.

0° Lamina Fatigue Response Summary

In summary, the fatigue response of the 0° lamina was described by two stages. This is shown schematically in Figure 4.21. This figure combines the fatigue response for both of the failure modes discussed above. The physical evidence of these failure modes and the plastic deformation are given in the next section, while the details of the matrix creep are shown in Chapter VI. Stage I was broken down into two substages. In substage Ia, the response was dominated by matrix creep, but it was accompanied by plastic deformation of the matrix when the maximum strain was greater than .55% (first loading cycle only). In this substage, fiber breakage resulted in the specimen fracture for those specimens tested in fatigue when the maximum strain was greater than .73%. For specimens subjected to fatigue with a maximum strain level less than .73%, a period of self-equilibrating matrix creep developed (substage Ib). This was an incubation period for cracks to develop in the matrix. As these cracks began to propagate, a concurrent

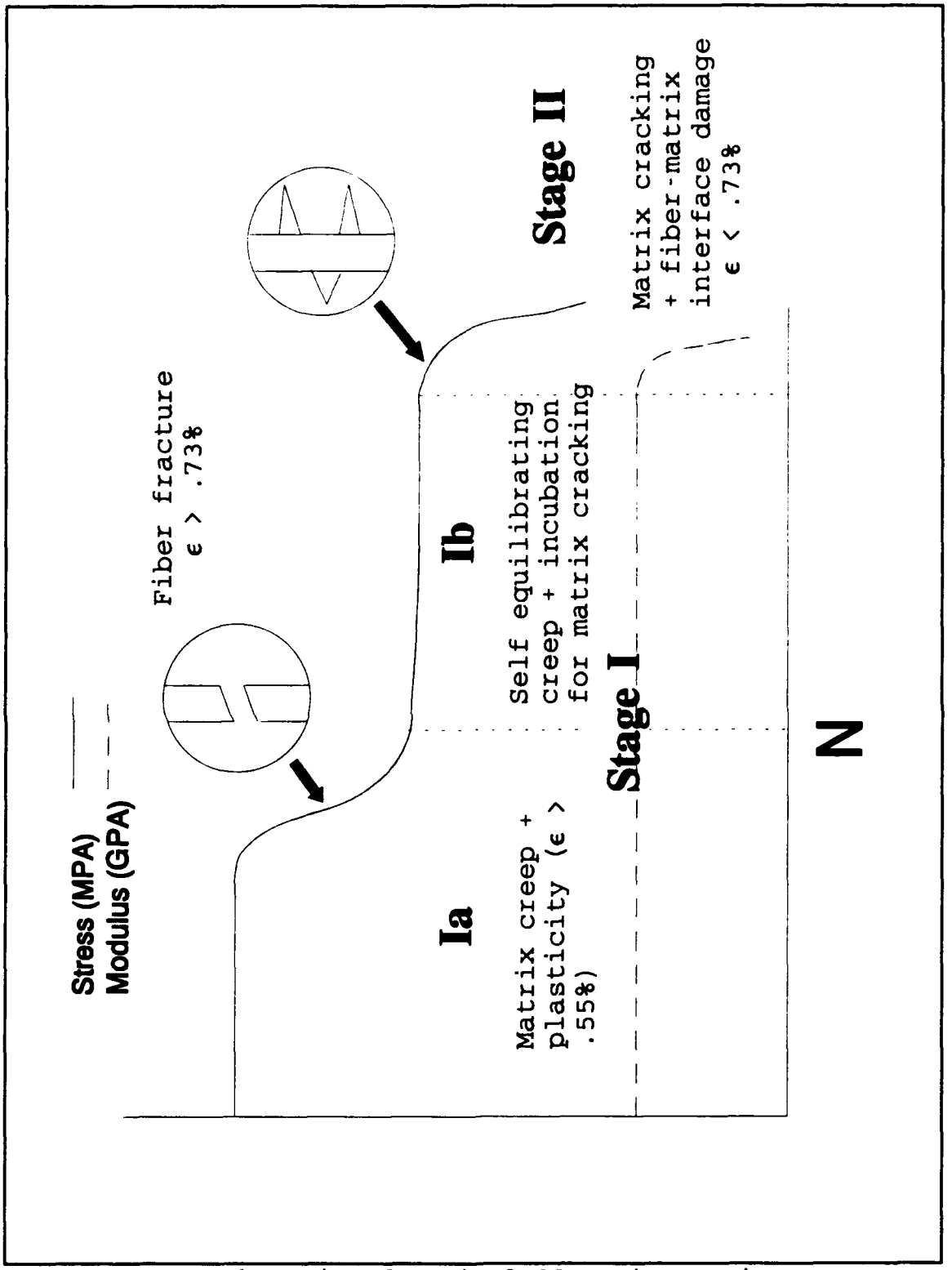

Figure 4.21 Schematic of Typical 0° Lamina Fatigue Response and Damage Mechanisms

decrease in the modulus and maximum stress was observed. This was defined as the Stage II and was dominated by the propagation of the matrix cracks.

Microscopy - Damage Mechanisms

In the previous section, the fatigue behavior of the 0° lamina was discussed with reference to the mechanical response. This section provides the physical evidence of the damage mechanisms, which are discussed with reference to Region I and Region II on the fatigue life diagram (Figure 2.13). The failure modes are discussed first. This is followed by showing evidence of matrix plastic deformation. To better understand the progression of damage for the matrix dominated failure mode, a few additional fatigue tests were run, which were stopped at key times in the fatigue life. This microscopic analysis coupled with the mechanical response and micromechanical analysis (Chapter VI) provided the complete characterization of damage and deformation mechanisms of the specimens tested in fatigue.

Failure Modes

Region I - Fiber Dominated Failure Mode

Figure 4.22 shows a typical fracture surface for a specimen that exhibited a fiber dominated failure mode. This particular case was for a specimen subjected to fatigue with a maximum strain of .75%. Several fibers were observed to have pulled out of the matrix.

Figure 4.22 0° Lamina Fracture Surface, ϵ_{max}= .75% (41.6X)

Figure 4.23 shows the condition of the matrix between failed fibers. The dimple patterns in the matrix represent the coalescence of micro-voids, which is characteristic of ductile fracture. This conclusively shows that the fibers failed first, which was then followed by ductile failure of the matrix. Hence, this provides the physical evidence that fiber fracture was the dominant failure mode for specimens that failed in fatigue at a strain level greater than .73%.

Region II - Matrix Dominated Failure Mode

Extensive cracks in the matrix were observed for those specimens which were tested in fatigue with a maximum strain level less than .73%. Figure 4.24 shows the first

Figure 4.23 0° Lamina Fracture Surface, ϵ_{max} =.75% (298X)

layer of fibers for the specimen tested at a maximum strain of .6%. Several matrix cracks were observed. Figure 4.25 shows that, in addition to matrix cracking, severe fiber-matrix interface damage also occurred. This shows that the matrix cracks progressed along the fiber-matrix interface. These damage mechanisms explain the reduction in modulus, and therefore the stress, observed in Stage II of the fatigue life (Figure 4.21).

Figure 4.26 shows an untested, aged, specimen. When comparing this to Figure 4.25, it can be observed that the reaction zone was thicker in the specimen subjected to fatigue. This is evidence of the environmental damage, which occurs by oxygen seeping in from the specimen surface

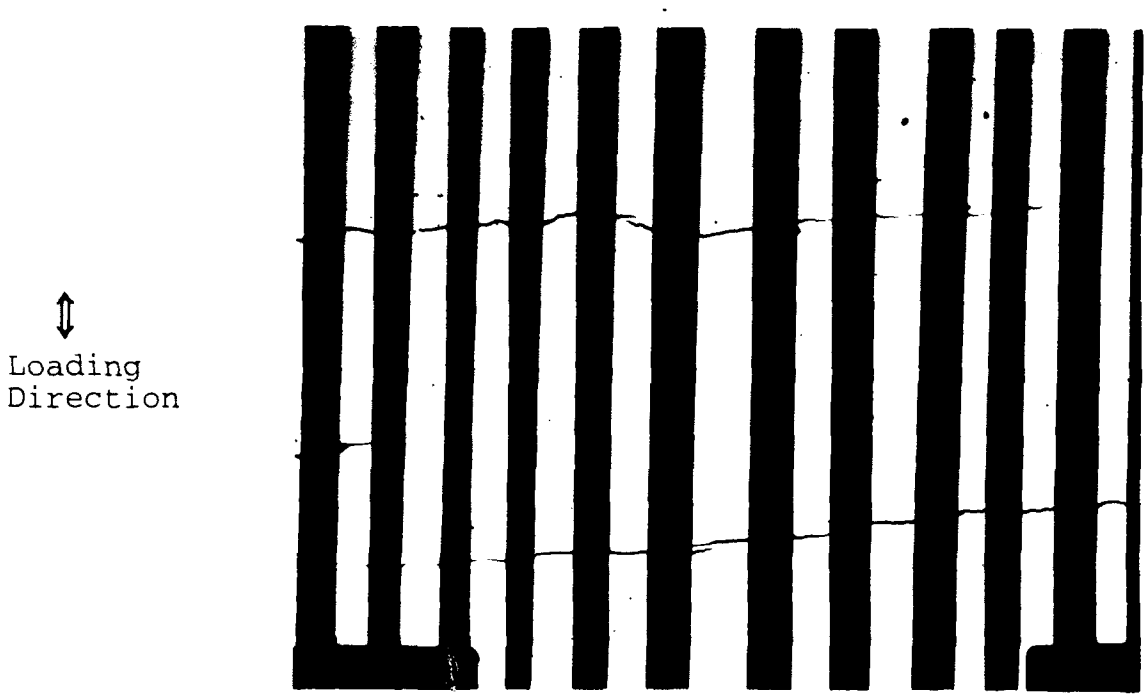

Figure 4.24 First Fiber Layer - 0° Lamina ϵ_{max}=.6% (100X)

Figure 4.25 Fiber-Matrix Interface Damage 0° Lamina - ϵ_{max}=.6% (200X)

Figure 4.26 Untested, Aged, 0° Lamina (200X)
No Oxidation on Interphase Zone

and/or the matrix cracks and oxidizing the reaction zone [30, 70]. This oxidation will to make the reaction zone more brittle, which may lead to an increase in the fatigue damage.

Matrix Yielding (Slip Bands)

Figure 4.27 shows the condition of the matrix at the first layer of fibers for a specimen subjected to fatigue at a maximum strain of .7%. Matrix slip bands were observed in several grains. This is evidence of matrix plastic deformation [59].

Figure 4.27 Matrix Slip Bands in 0° Lamina, ϵ_{max}=.7% (100X)

Figure 4.28 shows the first layer of fibers for the specimen tested in fatigue at a maximum strain of .6%. The matrix slip bands were again observed. This confirms that the matrix deformed plastically at this strain level. Since the subsequent fatigue cycles were linear, this plastic deformation must have occurred on the first fatigue cycle. Finally, no such phenomenon was observed for those specimens subjected to fatigue below a strain level of .55%.

The fiber-matrix interface separation was observed in several locations. Figure 4.29 shows a typical area where the fiber-matrix interface separation occurred. The matrix slip bands were also observed at these locations. This

Figure 4.28 Matrix Slip Bands in 0° Lamina, ϵ_{max} =.6% (200X)

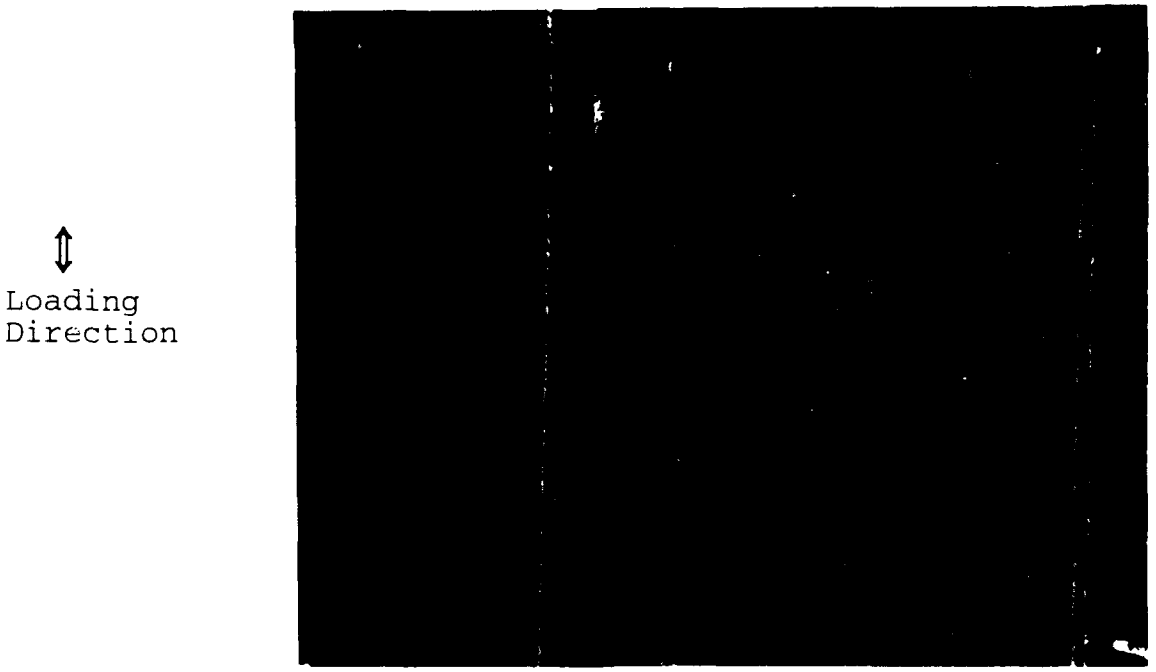

Figure 4.29 Debonded Interface in 0° Lamina (400X)

indicates that the matrix plastically deformed first. Then, as local necking occurred, the matrix separated from the fiber.

Damage Progression

Approach to Identifying the Damage Progression

To study the progression of damage, four additional fatigue tests were run at maximum strain levels of .5% and .7%, with two replicated at each strain level. These values were chosen so that damage initiation and progression below and above the matrix proportional limit could be documented. The tests were stopped, and the specimens were section at the following times in the fatigue life:

(1) In substage Ia before any large reduction in the stress was observed

(2) When the mean stress became constant (substage Ib) This approach coupled with the failure mechanisms described above characterized the progression of damage in the 0 ° lamina.

Substage Ia

Figures 4.30 and 4.31 show the condition of the specimens in Stage Ia for maximum strain levels of .5% and .7%, respectively. There was no evidence of fiber or matrix damage. This provides extra evidence that the response in this substage was dominated by matrix deformation and not damage.

⇕
Loading
Direction

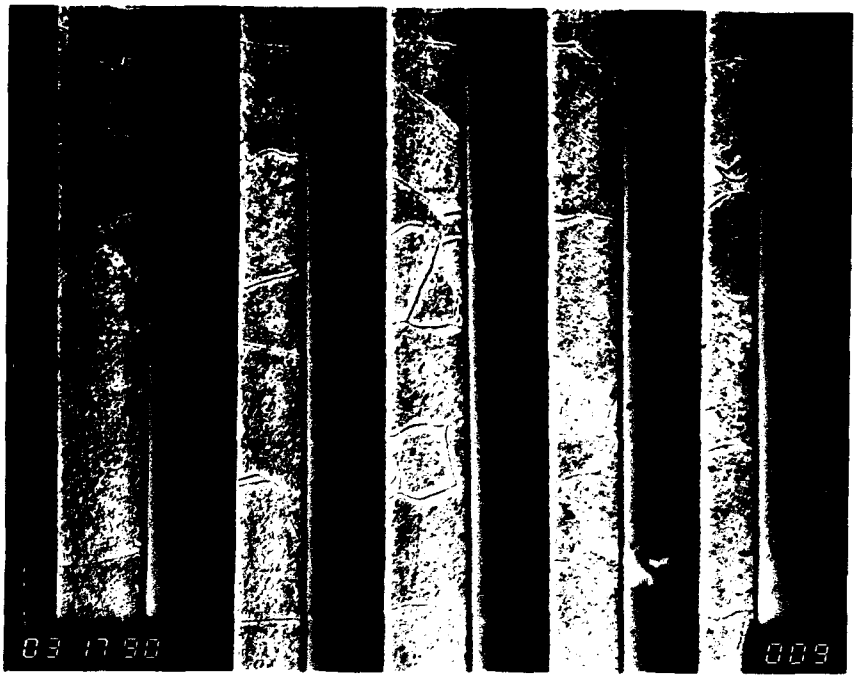

Figure 4.30 Typical 0° Lamina Condition in Substage Ia - ϵ_{max} =.5% (100X)

⇕
Loading
Direction

Figure 4.31 Typical 0° Lamina Condition in Substage Ia - ϵ_{max} =.7% (100X)

The specimen tested in fatigue at a maximum strain level of .7% (Figure 4.31) did not show the matrix slip bands, but a non linear stress-strain response was observed in the first cycle. As previously shown (Figure 4.27), the slip bands became visible later in the fatigue life for a specimen subjected to fatigue at this same level of strain, and the initial fatigue responses were identical. A possible explanation for this is given next.

Majumdar and Newaz [68] showed that matrix slip bands initiated in the 0° SCS-6/Ti-15-3 MMC loaded above a strain level of .55%. In that study, the specimen was not heat treated prior to testing, so the microstructure was similar to that shown in Figure 4.3. When the matrix plastically deforms the dislocations occur in the soft β-phase [59]. The additional heat treatment described in Chapter III, which was also employed by Majumdar and Newaz, precipitates α-phase along these dislocations [59]. The etchent then attacks the α-phase to reveal these slip bands. In the case of testing the as-received MMC, the majority of the α-phase precipitated by the post-test heat treatment would occur along the slip bands, making them easily visible.

The situation was different in this study. It was previously shown that after the initial heat treatment a large density of α-phase was present in the matrix (Figure 4.5). Early in the fatigue life the slip bands may have

been masked by the α-phase already present. As fatigue continues, additional dislocations may develop along the slip bands, which will make them more visible.

Substage Ib

Figures 4.32 and 4.33 show the condition of the specimens tested in fatigue at maximum strain levels of .5% and .7%, respectively. These specimens were subjected to fatigue until a constant mean stress was observed in the lamina (beginning of substage Ib). No matrix cracks were observed, but both specimens showed cracked fibers. The majority of these were located close to the molyweave. In some instances the fiber cracks were also found at locations were the molyweave was not present (Figure 4.32). Figure 4.34 shows a typical crack in a fiber. At this point in the fatigue life, the crack showed no signs of inducing damage to the fiber-matrix interface.

It is interesting to note that, when the maximum strain was greater than .73%, these fiber cracks resulted in the rapid fracture of the specimen. On the other hand, for the two cases discussed here, no reduction in specimen stiffness was measured during this substage (Figure 4.21), so these cracked fibers had not affected the specimen response. Since no other damage was observed, the reduction in stress in substage Ia was considered to be dominated by matrix creep.

Molyweave

⇕

Loading
Direction

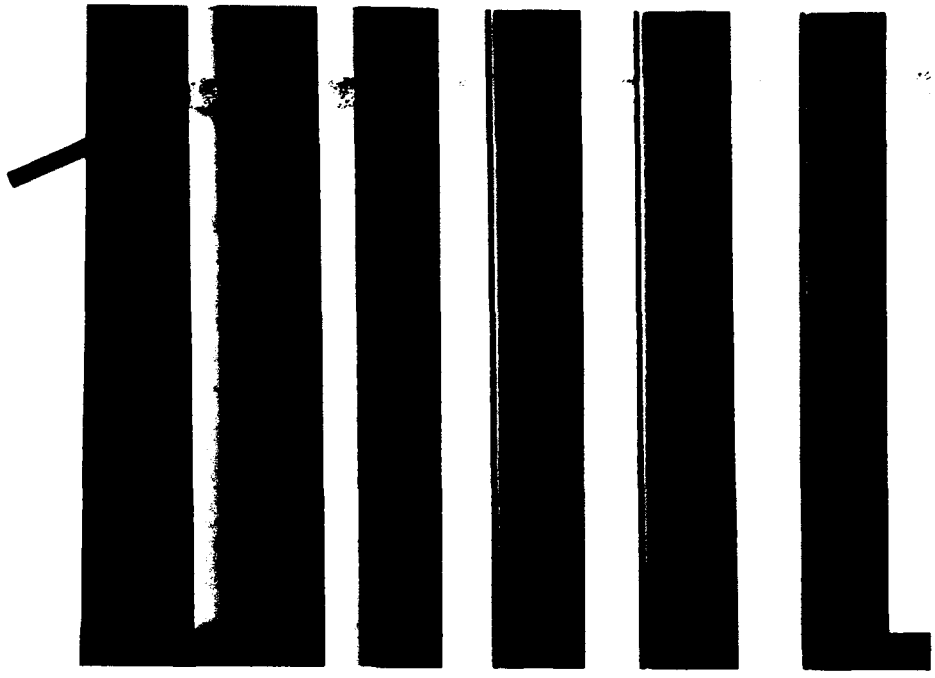

Figure 4.32 Typical 0° Lamina Condition in Substage Ib, ϵ_{max} =.5% (100X)

⇕

Loading
Direction

Figure 4.33 Typical 0° Lamina Condition in Substage Ib, ϵ_{max} =.7% (100X)

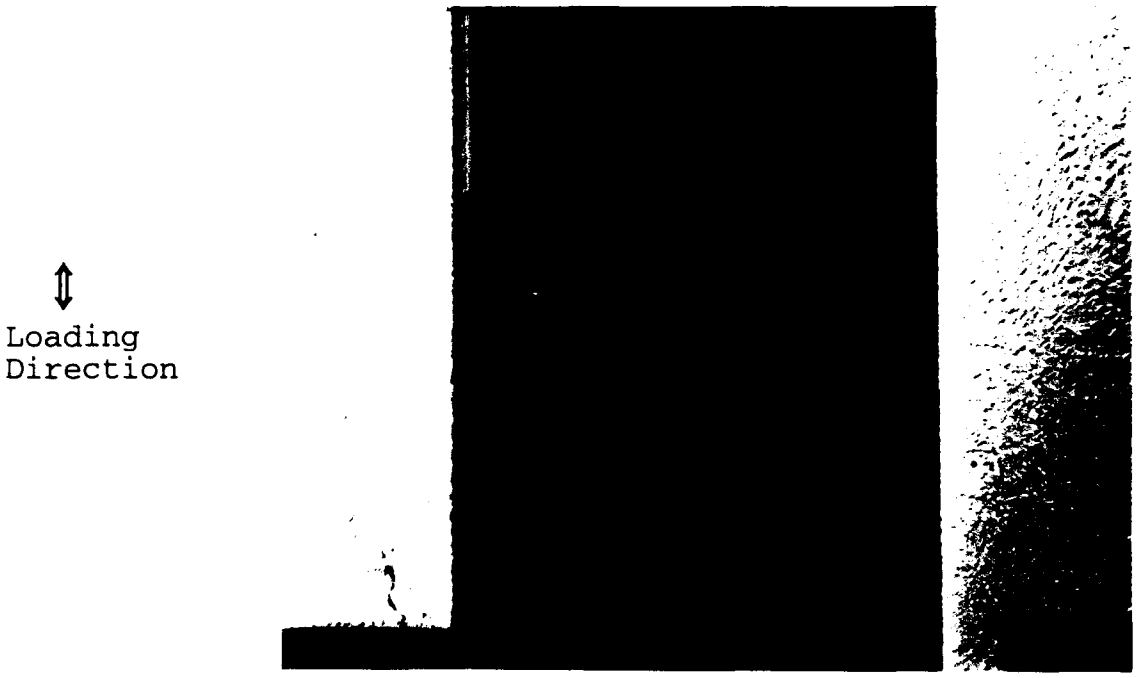

Figure 4.34 Typical Fiber Crack in 0° Lamina, Substage Ib, ϵ_{max} =.5% (500X)

Effect of Cracked Fibers

It was shown above that cracked fibers were present after substage Ia. These cracked fibers did not propagate or contribute to any other fatigue damage in either case. As fatigue continued, the tiny fiber cracks observed at the end of substage Ia had more of an effect on the fiber-matrix interface damage. Figure 4.35 shows a typical fiber crack in the specimen tested in fatigue at a maximum strain level of .5%. This specimen was subjected to fatigue until a reduction in the modulus was measured, which defines the beginning of Stage II (Figure 4.21). It can be observed that the fiber crack extended into the fiber-matrix

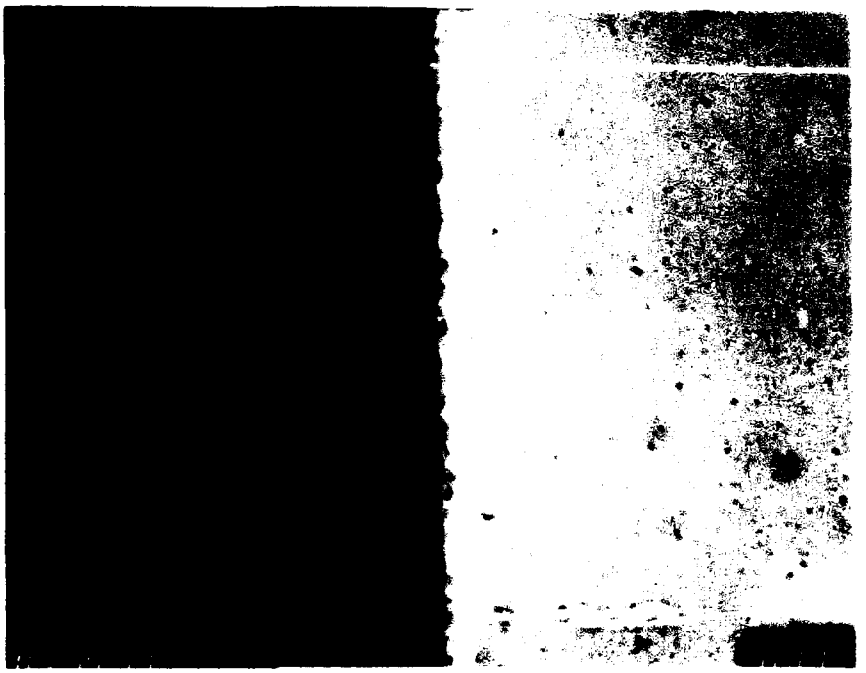

Figure 4.35 Fiber Crack in Stage II, ϵ_{max}= .5% (1000X)

interface region. Once this occurred, the crack then progressed longitudinally along the interface. This suggests that, as the number of fatigue cycles increases, the fiber cracks progressed into the interface region.

The development of matrix cracks was not observed to be related to this damage mechanism. For example, in the regions were the fiber-matrix interface failure occurred due to the cracked fibers, there were no signs of matrix cracks. Thus, matrix cracks were still the dominant damage mechanism for specimens subjected to fatigue with a maximum strain level than .73%.

Fatigue Life Analysis

It is desirable to develop fatigue curves which relate the fatigue life to the failure modes. The information gathered from the fatigue tests and the microscopic analysis provides the data base to achieve this goal. In this section, the fatigue life of the 0° lamina was plotted as a function of the maximum applied strain. The failure mechanisms found in the previous section were used to partition the fatigue curve into three regions. For comparison, another fatigue curve was also plotted using data from previous studies that employed the load control mode.

Definition of Specimen Failure

As previously mentioned, in the strain control mode, the specimen fracture does not always occur. An alternative failure criteria must therefore be defined. Bartolotta and Brindley [9] defined failure when either the specimen fractured or when a simultaneous drop in the maximum stress ($\sigma_{max} \geq 30$ MPa) and modulus ($E \geq 10$ GPA) occurred. For this study, the failure was defined by one of two criteria. The first one was the specimen fracture, which was previously shown to occur for the fiber dominated failure mode. The second failure criterion was conservatively defined to be when a sharp and simultaneous reduction in the maximum stress and modulus occurred. This was defined previously as

Stage II (Figure 4.21), which was observed for the matrix dominated failure mode.

Fatigue Life - Strain Control

Figure 4.36 shows the fatigue life of the 0° SCS-6/Ti-15-3 MMC at 427° as a function of the maximum applied strain. Fatigue data, available in the literature, of the Ti-15-3 neat matrix were also plotted. Based on the microscopic analysis, the fatigue curve was partitioned into the following three regions: fiber dominated failure mode (Region I), matrix dominated failure mode (Region II), and the matrix fatigue limit (Region III). The details of these three regions are discussed next.

Region I- Fiber Dominate Failure Mode

Fatigue life in Region I was dominated by fiber fractures. In this study, two specimens were subjected to fatigue in this region (maximum strain levels of .75% and .77%). Both of these specimens failed in substage Ia (Figure 4.21). It was shown that the fatigue response of these specimens was dictated by matrix plasticity and matrix creep, but the failure was due to fiber fractures (Figure 4.22).

In addition to the fatigue life data of the 0° MMC generated in this study, some test data from monotonic loading conditions were also plotted [63]. This aided in defining the scatter band in Region I. This scatter band

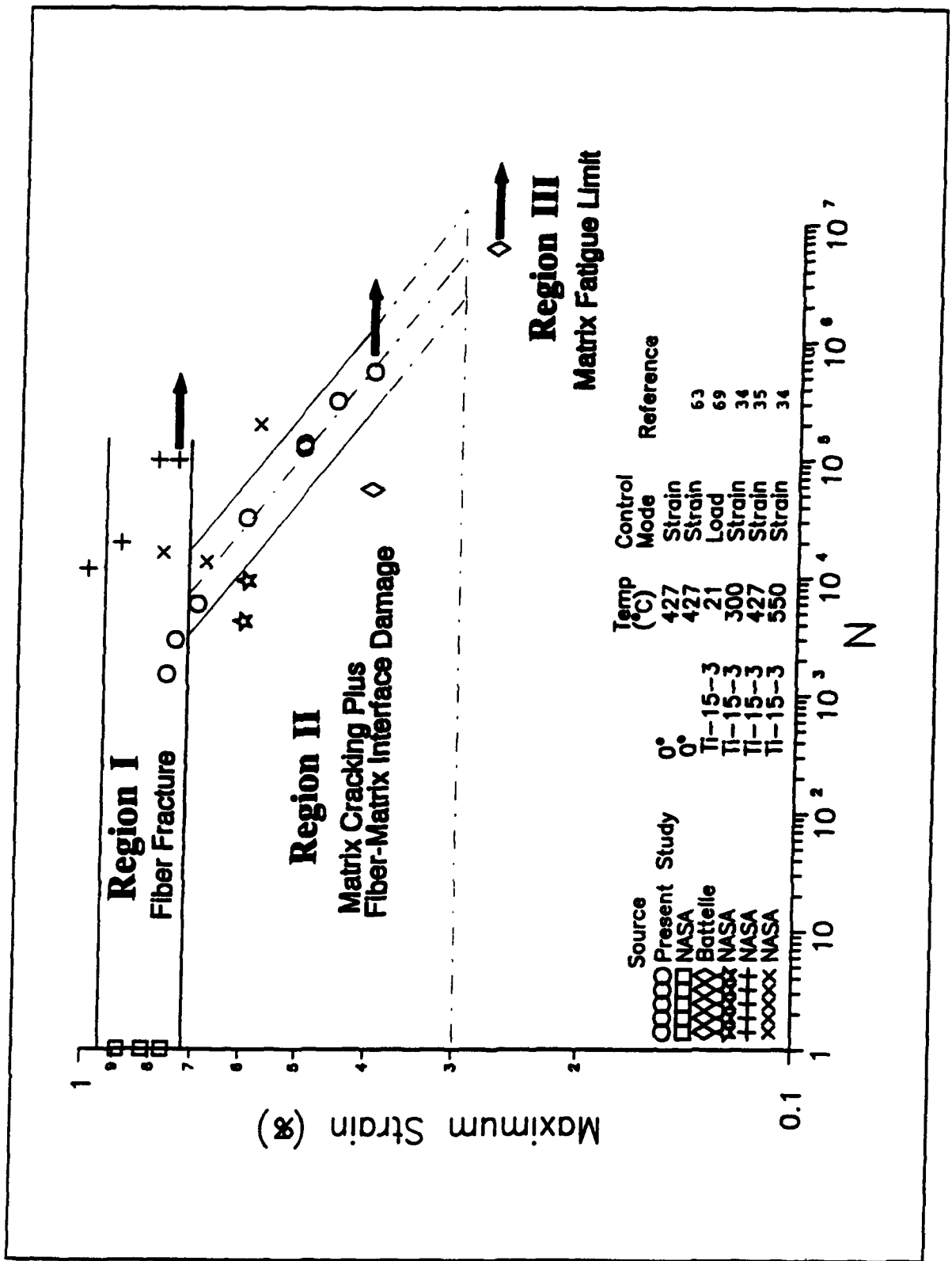

Figure 4.36 0° Lamina Fatigue Life Diagram - Strain Control

can be attributed to several factors. Among them are: variations in fiber strength, fiber spacing, and matrix ductility [106]. The effect of these variations was apparent by comparing the maximum strain level used in this study with the monotonic test data. It can be observed that the specimen tested in fatigue at a maximum strain level of .77% had a fatigue life of 1,500 cycles. On the other hand, a specimen failed at just a slightly higher strain level during the monotonic loading condition. Similar observations have been observed in polymeric composites [106]. This demonstrates that this is an area where the fatigue life has a large scatter band and can be predicted only with consideration of the statistical techniques.

For comparison, some data available in the literature [34, 35, 69] on the fatigue life of the neat matrix were plotted in Figure 4.36. In this region, it was observed that the fatigue life of the neat matrix was longer than the MMC fatigue life. This illustrates the effect that the fiber-matrix interface has on damage in the MMC.

Region II - Matrix Dominated Failure Mode

In Region II the fatigue life was dominated by the matrix cracks. It was previously shown, that specimens tested in this region had a two stage behavior: Stage I, which was shown to be dominated by matrix creep, and Stage II, which was shown to be dominated by the development of

matrix cracks. The latter was manifested by a simultaneous drop in the specimen stiffness and stress, which, as mentioned above, was where the fatigue life was defined. This response was observed for specimens subjected to fatigue below maximum strain of .73%.

It was observed that the fatigue life in this region had less scatter than in Region I[3]. A steady increase in fatigue life for a decreasing applied strain was observed. As mentioned above, the primary damage mechanism for specimens tested in this region was matrix cracks. This suggests that the fatigue life can be predicted by characterizing a relationship between the development and progression of the matrix cracks to the applied strain level.

Region III

Region III was defined as the matrix fatigue limit. In this region, there will be no fatigue damage in the matrix, or at least, the fatigue damage does not propagate to cause the specimen failure [106]. There is no standard number of cycles for where this region is defined. In this study, the fatigue limit was defined when no failure occurred by 10^7 cycles.

[3] The dashed line in this region was drawn to show the general trend of the data. A factor of two (solid lines) is generally considered an acceptable scatter band in fatigue testing.

Majumdar and Newaz [69] performed loaded control tests on the neat matrix at room temperature. For a specimen loaded in fatigue with a maximum stress of 100 MPa (maximum strain of .27%), there was no change in the specimen response after 6,300,000 fatigue cycles. From this data point, the maximum level of strain at which the fatigue limit would be encountered was conservatively estimated to be .3%.

Fatigue Life - Strain Control vs. Load Control

The fatigue life of the 0° MMC under the strain control mode was compared with data available in the literature under the load control mode. As mentioned in Chapter II, the maximum strain and minimum strain in the load control mode increases during a fatigue test, but the strain range typically remains constant under isothermal conditions [33, 69]. Investigations employing the load control mode typically plot the fatigue cycles to failure as a function of the strain range. This method was used for this study. Since the strain range was not constant for the tests conducted in this study (Figure 3.6), the strain range measured at the half-life was used for the specimens subjected to fatigue under the hybrid strain control mode.

Figure 4.37 shows the fatigue life, as a function of strain range, for both the strain control mode and load control mode (isothermal conditions). The three regions

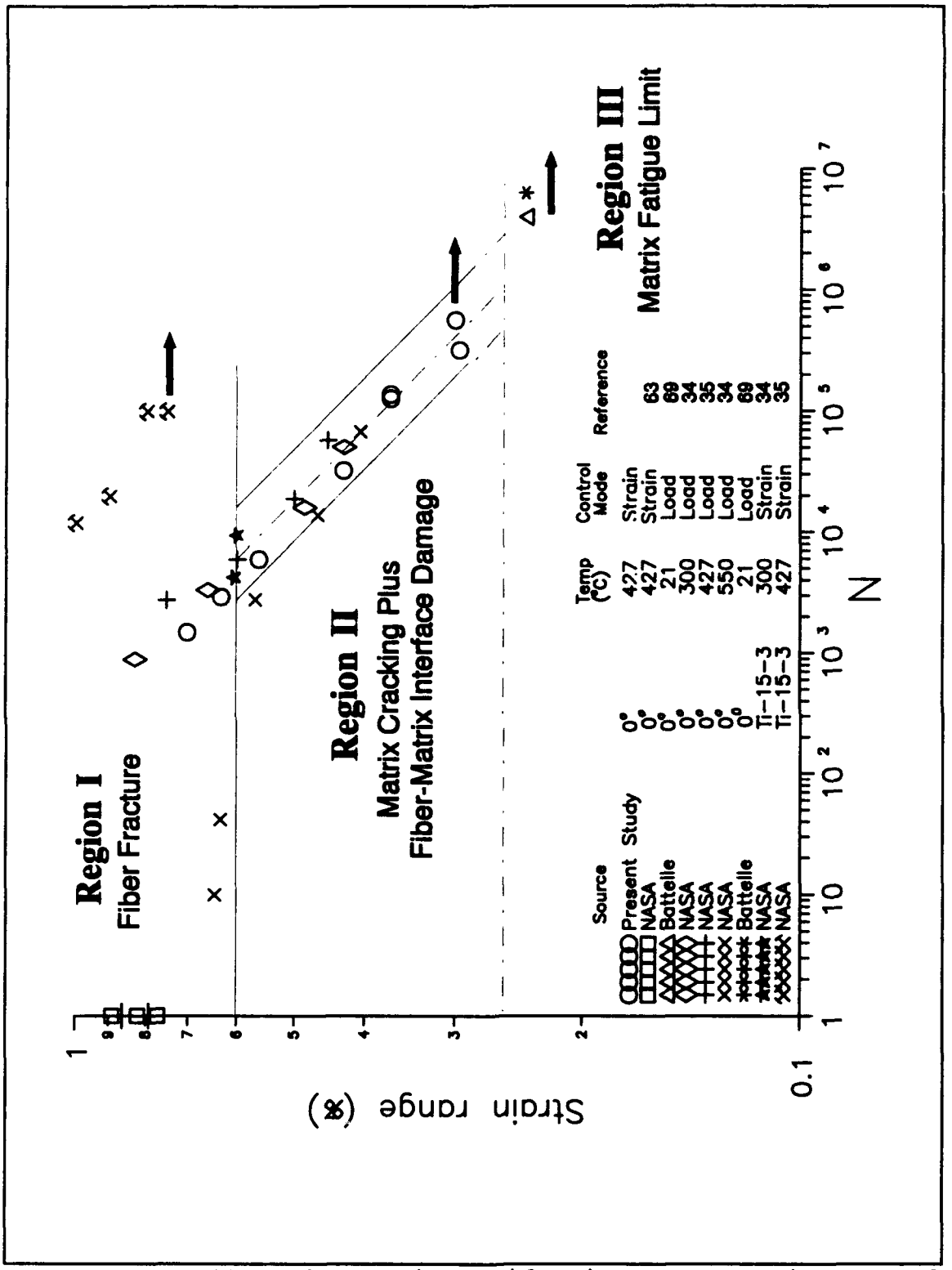

Figure 4.37 0° Lamina Fatigue Life Diagram - Strain Control vs. Load Control

described in Figure 4.36 are shown. Each region was shifted down to account for the change in scale, but the data points defining the regions remained the same. For example, in Figure 4.36 the partition between Regions I and II was estimated at .73%. This was because the specimen that failed in fatigue at a maximum strain of .75% ($\Delta\epsilon$ = .62%) exhibited a fiber dominated failure mode, while the specimen subjected to fatigue at a maximum strain .7% ($\Delta\epsilon$ = .58%) exhibited a matrix dominated failure mode. On a strain range basis, this partition now falls at approximately .6%. The partition between regions II and III was chosen in a similar manner.

A through understanding of the damage mechanisms, such as that obtained in this study, was not available for the load control mode. So the discussion of Figure 4.37 is limited to a few salient observations. First, as previously described, Region I was defined as the fiber dominated failure mode. A large scatter in the data was observed in this region. The data from the load control fatigue tests also show a large scatter above a strain range of .6%. This suggests that these specimens were also dominated by fiber fractures. Second, as observed by Majumdar and Newaz [69], below a strain range of .6% (Region II) the fatigue lives fall within a narrow scatter band. The data obtained from the strain controlled fatigue test fell well within this

scatter band. This indicates that the fatigue life depends on the strain range in this region.

A final noteworthy observation from Figure 4.36 is the lack of temperature dependence on fatigue life in Region II. This may be the result of how the different damage and deformation mechanisms accumulate. For example, consider that the total damage is a linear summation of different mechanisms (i.e. matrix cracks, matrix creep, fiber cracks). As the temperature changes, the accumulation of damage due to some mechanisms may be slower, but the contribution to the total damage from other mechanisms (i.e. creep) may increase at the same time. Thus, when the total damage is the same, the fatigue lives will also be equivalent.

Summary of 0° Lamina Behavior

The fatigue behavior of the 0° SCS-6/Ti-15-3 MMC lamina has been characterized under the strain control loading mode at 427°C. Two distinct failure modes were identified: fiber fractures, and matrix cracking. Microscopic analysis revealed that for specimens tested in fatigue at strain levels greater than .73%, fiber fractures were the dominant damage mechanism. For this failure mode, the fatigue response dominated by matrix creep and plastic deformation, but fiber fractures led to specimen failure. On the other hand, for specimens tested in fatigue with a maximum strain less than .73%, matrix cracking was shown to be the dominant

failure mechanism. In this case, the fatigue response was partitioned into two stages. The first stage was dominated by creep deformation of the matrix. Plastic deformation of the matrix was also observed in this stage for those specimens loaded above a strain level greater than .55%. The second stage was shown to be dominated matrix cracks. Finally, the fatigue life was plotted as a function of maximum applied strain. This curve was partitioned into three regions of damage.

90° Lamina

Having gained insight into the fatigue behavior of the neat matrix and the 0° lamina, fatigue tests and microscopic analysis were performed on the 90° lamina (fibers perpendicular to the loading direction). The next few sections discuss the results from the fatigue tests and the ensuing microscopic analysis. A three region fatigue life diagram was generated based on the findings from the experiments and microscopic analysis.

Fatigue Behavior

First Cycle Stress-Strain Response

Before proceeding with a discussion on the fatigue behavior, a few unique characteristics of the stress-strain response of the 90° lamina are presented. This will help to better understand the selection of strain levels chosen to

characterize this lamina, and it will facilitate the discussion of the results obtained from the fatigue tests.

Figure 4.38 shows the first cycle stress-strain response for a specimen that was loaded to a maximum strain of .45%. A nonlinear response was observed to have initiated at a strain level of approximately .1%. Previous studies [54, 68] have shown that this nonlinearity was dominated by the initiation of fiber-matrix interface damage, rather than plastic deformation of the matrix. This damage causes a gap to open between the fiber and matrix

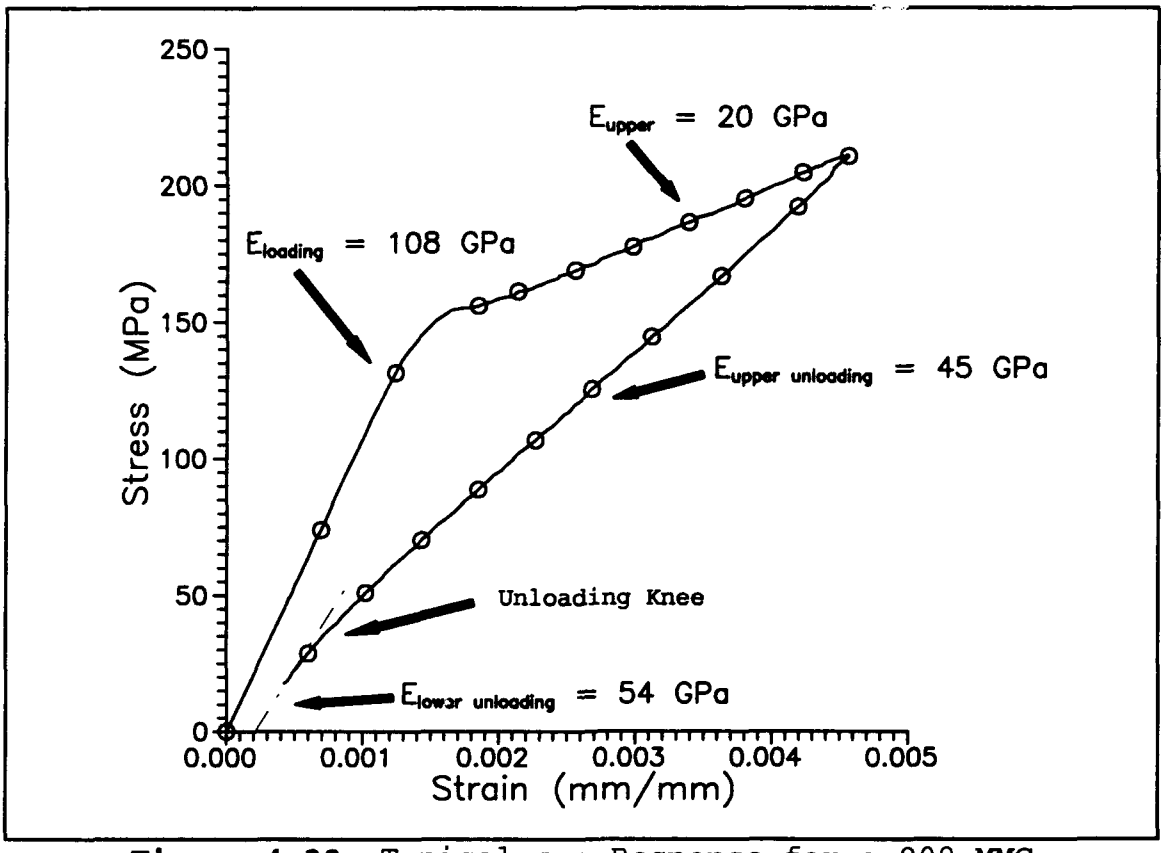

Figure 4.38 Typical σ-ϵ Response for a 90° MMC

and, as a result, the specimen stiffness was reduced. Due to this damage, the unloading modulus was also significantly lower than the initial loading modulus. Another knee can be observed when the specimen was unloaded. This is a result of the gap, between the fiber and matrix, closing [82,93], which leads to an increase in the unloading stiffness. This discussion illustrated the effect that the fiber-matrix interface damage has on the response of the 90° lamina. As will be shown shortly, all of the damage in this lamina is related to the presence of the fiber-matrix interface.

Majumdar and Newaz [68] characterized the initial stress-strain response of the 90° SCS-6/Ti-15-3 lamina at room temperature. They identified three stages of loading-unloading behavior (Figure 4.39). Stage I was described as a linearly elastic response (i.e. no fiber-matrix interface damage or matrix plasticity). In Stage II and Stage III, however, inelastic deformation was observed. Inelastic deformation in Stage II was shown to be dominated by the fiber-matrix interface damage. A secondary mechanism was shown to be matrix plasticity. This can be observed by noting that a small residual strain was present after unloading to zero load. In Stage III, a second knee in the loading curve was observed at a strain level of approximately .5%. Also, a larger residual strain was present upon unloading to a zero load. It was shown that

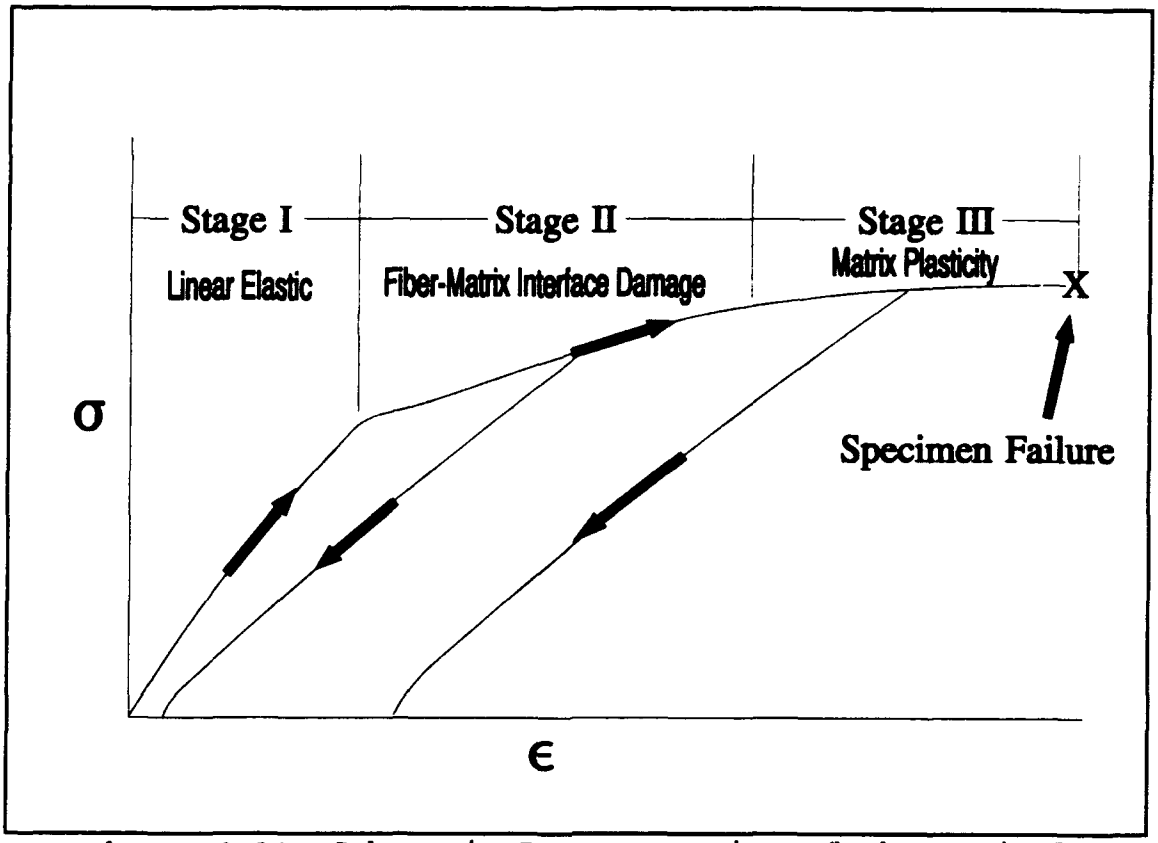

Figure 4.39 Schematic Representation of the Typical Loading-Unloading Response of a 90° MMC

this behavior was dominated by the plastic deformation of the matrix.

The concept of three stages proposed by Newaz and Majumdar can also be used at elevated temperature. This proved to be a useful tool in selecting the strain levels to characterize the fatigue behavior. Figure 4.40 shows a static test of the 90° lamina at 427°C. The stages proposed by Newaz and Majumdar are highlighted. For this study, the 90° laminas were loaded in fatigue at maximum strain levels

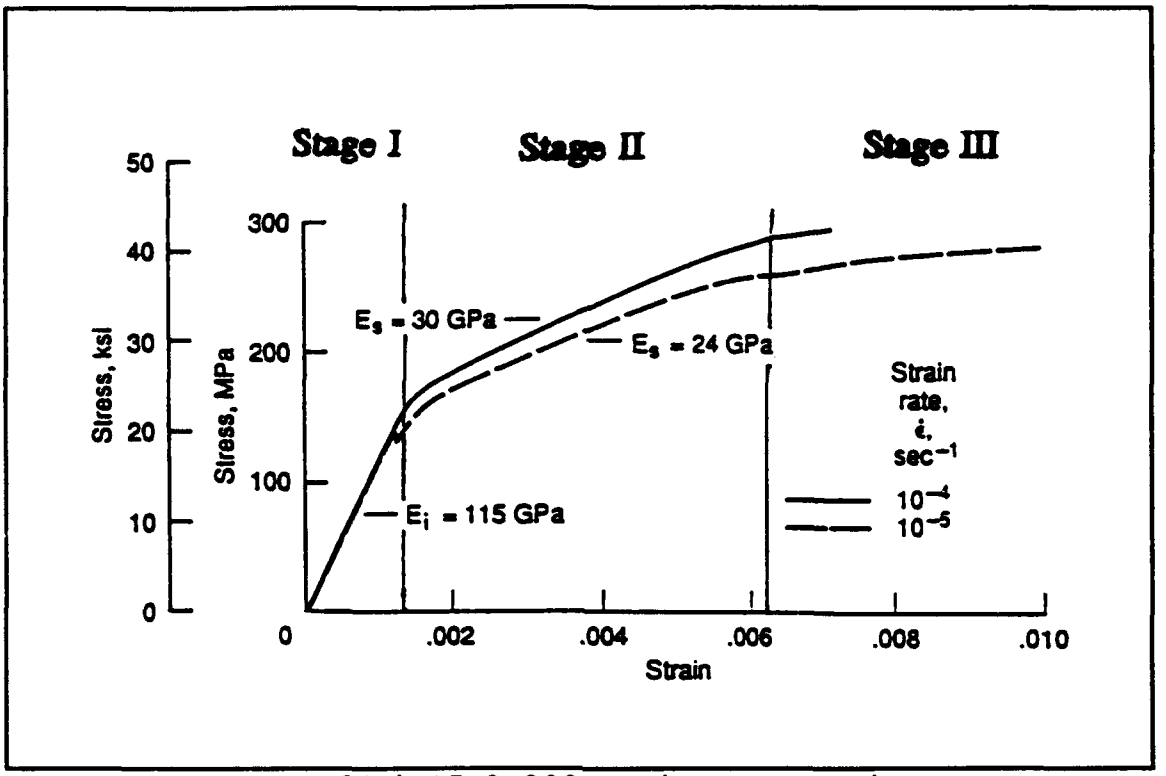

Figure 4.40 SCS-6/Ti-15-3 90° Lamina Monotonic σ-ϵ Curve at 427°C [63]

of .1%, .2%,.25%, .3%, .4%, and .45%, all of which fall into Stages I and II (Figure 4.40). Testing the lamina at these strain levels helped to develop the relationship between the fatigue life and damage mechanisms (Figure 2.13). With this above background information, a more detailed discussion of the fatigue response is presented next.

90 Lamina Fatigue Response

Six strain controlled fatigue tests were conducted on the 90° lamina. Table 4.5 shows a summary of the dominant

failure modes and the associated regions on the fatigue curve (Figure 2.13).

Table 4.5. Summary of the 90° Lamina Failure Modes

Maximum Strain (%)	Failure Mode	Fatigue Curve Region
>.35	Matrix Cracks	I
<.35	Matrix Cracks, Interface Damage	IIa
<.23	Interface Damage	IIb

The failure modes were different than those described in Chapter II. It was observed that for specimens tested in fatigue with a maximum strain greater than .35%, the fatigue behavior was dominated by the propagation and coalescence of matrix cracks. In these cases the specimens fractured. When the maximum strain was in the range of .23% to .35%, the dominant damage mechanisms were small matrix cracks and a progression of the fiber matrix-interface damage. The specimens did not fracture in these cases. The specimen fracture also did not occur for those specimens subjected to fatigue at strain levels less than .23%, and, as shown in Table 4.5, the damage was limited to a the breakdown of the fiber-matrix interface. The details of the fatigue behavior in these regions are discussed next.

Region I - Matrix Cracking

Stress-Strain Response

Figure 4.41 shows the typical history of the stress-strain response for a specimen which exhibited matrix cracking as the dominant failure mode. This particular case was for a specimen subjected to fatigue with a maximum strain of .45%. A nonlinear response was observed on the first fatigue cycle. This was previously mentioned to be

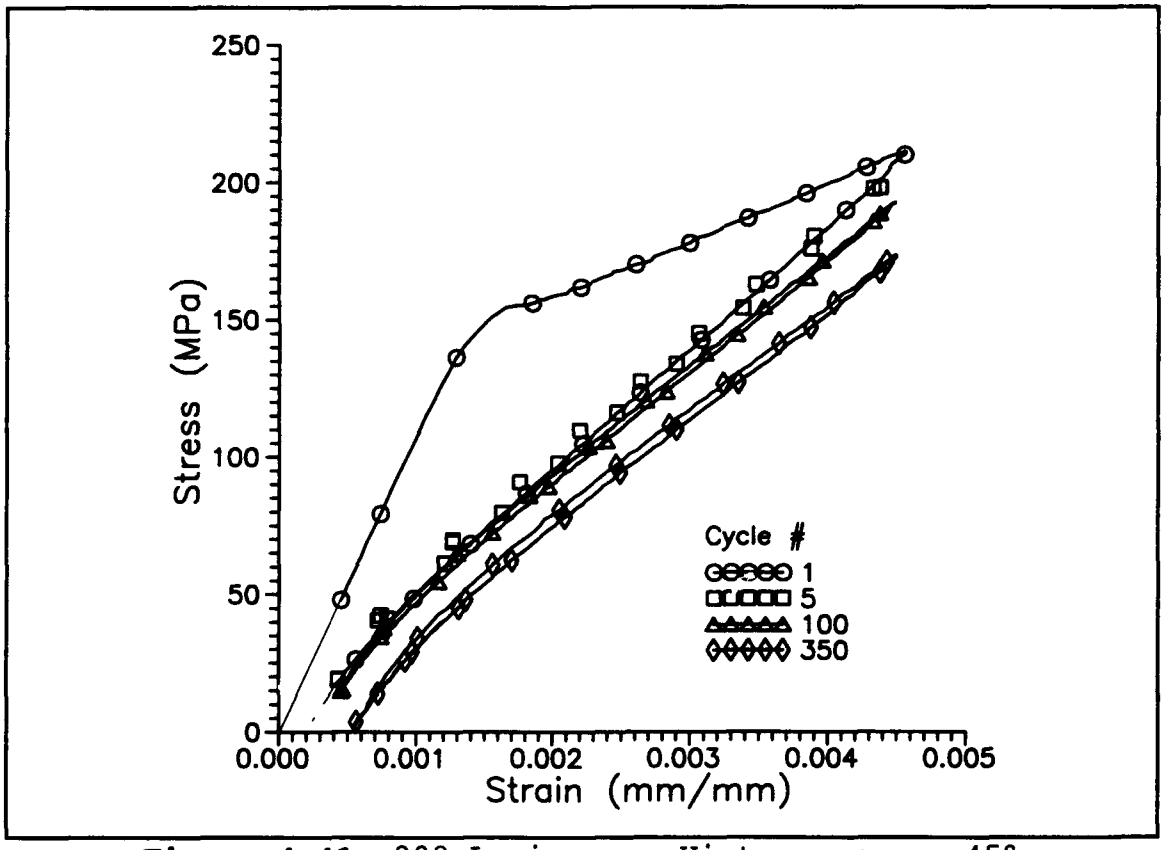

Figure 4.41 90° Lamina σ-ϵ History, ϵ_{max}= .45%

dominated by the initiation of the fiber-matrix interface damage. By extrapolating the unloading curve to a zero load (dashed line), a small residual strain was observed. This indicates that some plastic deformation of the matrix had occurred [68]. It will be shown later that plastic deformation of the matrix initiates at a strain level of approximately .23%.

After the first loading cycle, a small hysteresis was still observed in the subsequent stress-strain curves (Figure 4.41). Although the majority of the fatigue damage initiated on the first cycle (large hysteresis), the hysteresis in these curves suggests that the damage was rapidly propagating. This behavior was typically observed early in the fatigue life for the specimens that had developed matrix cracks. As will be shown shortly, the fiber-matrix interface damage may progress without showing any measurable hysteresis in the stress-strain response. Thus, this response was most likely due to the initiation and propagation of the matrix cracks.

Stress and Modulus Histories

Figure 4.42 shows the histories of the maximum stress, minimum stress, and modulus[4] for the specimen tested in fatigue at a maximum strain of .4%. As in the previous

[4] See Appendix B for details on how the modulus was measured for the 90° laminas tested in fatigue.

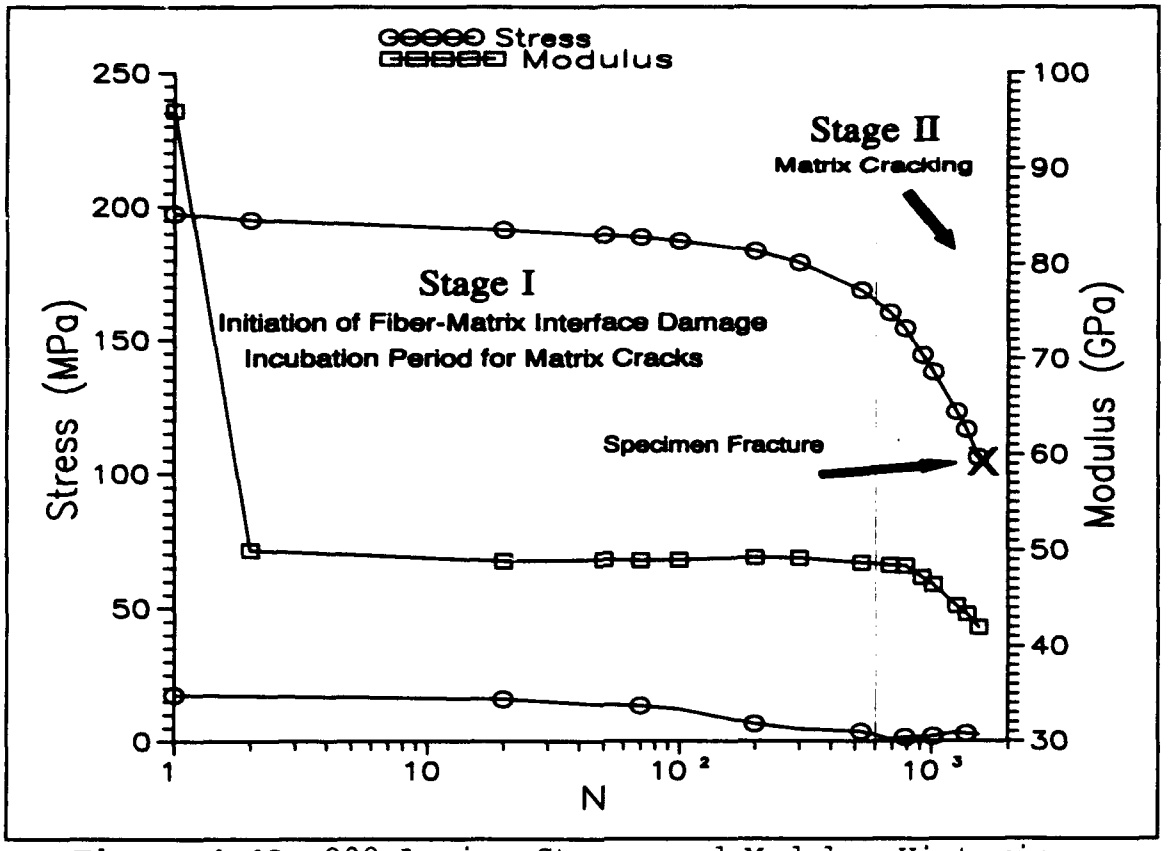

Figure 4.42 90° Lamina Stress and Modulus Histories, ϵ_{max}= .4%

case, this specimen also fractured, and the microscopic analysis revealed that the dominant damage mechanism was matrix cracking. For discussion purposes, the fatigue response was partitioned into two stages to show the progression of damage.

The response in Stage I was dominated by the initiation of the fiber-matrix interface damage on the first loading cycle. This can be observed by the large reduction in the loading modulus. A small drop in the maximum stress was

observed in this stage. The analysis (Chapter VI) will shown that this relaxation of the stress was not due to matrix creep, so it must be due to the development of matrix cracks and possibly the progression of fiber-matrix interface damage. It was suspected that a corresponding decrease in the modulus was not observed due to age hardening of the matrix, which has been discussed previously (Figure 4.10).

In Stage II, a simultaneous reduction in the maximum stress and the modulus was observed. The micromechanical analysis (Chapter VI) will show that creep deformation of the matrix accounts for only a small percentage of the reduction in stress. Thus, the Stage II response was dominated by the propagation of matrix cracks. Specimen fracture occurred when these cracks coalesced.

The above discussion suggests the following progression of damage for the specimens tested in fatigue above a strain level of .35%:

(1) fiber-matrix interface damage initiates on the first loading cycle (Stage I)

(2) An incubation period for matrix cracks (Stage I)

(3) Matrix cracks began to propagate (Stage II)

(4) Matrix cracks begin to coalesce and the specimen fractures (Stage II).

The physical evidence of these damage mechanisms will be shown later.

Region IIa - Progressive Fiber-Matrix Interface Damage and Matrix Cracking

Stress-Strain Response

Figure 4.43 shows the typical stress-strain response for a specimen that exhibited a combination of matrix cracks and a progression of the fiber-matrix interface damage. This particular case is for a specimen subjected to fatigue with a maximum strain level of .25%. As expected, the stress-strain response on the first fatigue cycle was nonlinear and a large hysteresis was observed. This was previously mentioned to be due to the initiation of the fiber-matrix interface damage. Some of the subsequent curves also showed a slight hysteresis. As discussed earlier, this implies that damage (matrix cracks) was continuing to occur well beyond the first fatigue cycle.

Later in the fatigue life, the stress-strain response became nearly linear, and no hysteresis was observed. It was suspected that this response was due to the matrix cracks being arrested. In Chapter VI, the analysis will show that the propagation of fiber-matrix interface damage becomes the dominant damage after the matrix cracks are arrested.

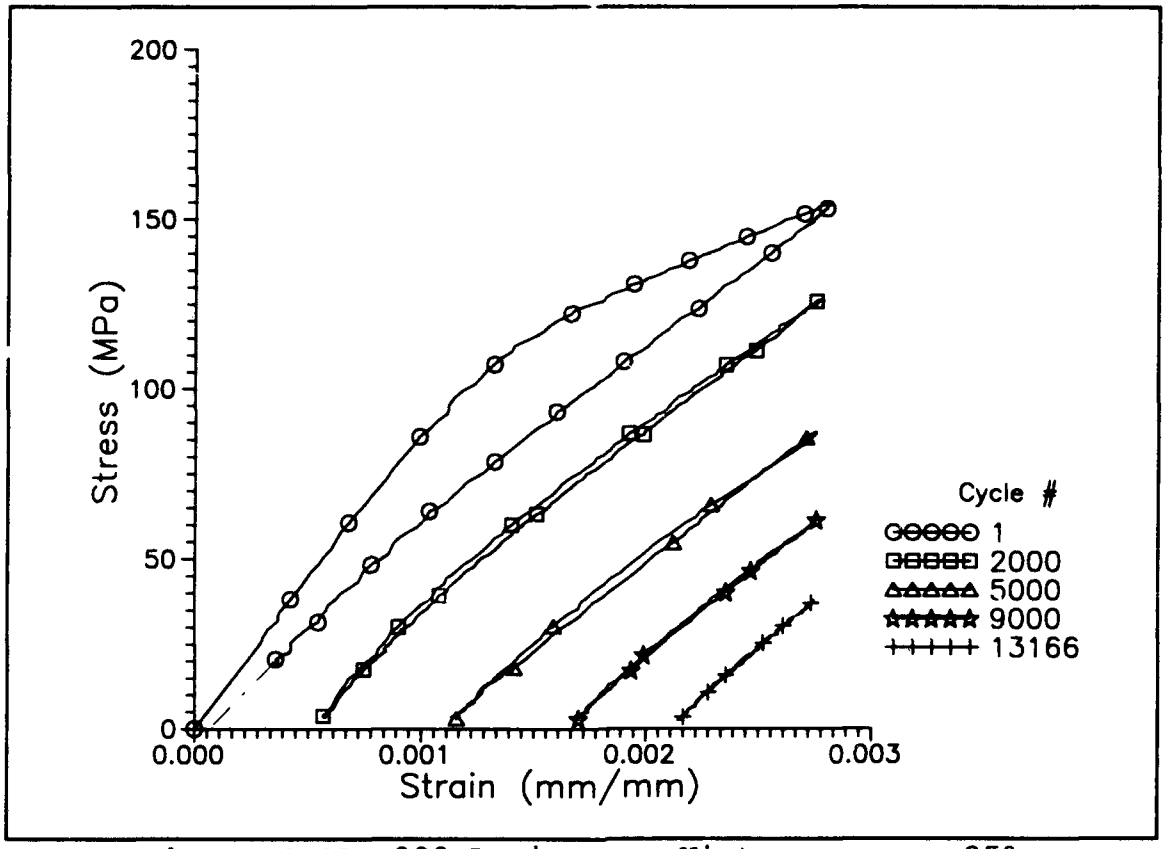

Figure 4.43 90° Lamina σ-ϵ History, ϵ_{max}= .25%

Stress and Modulus Histories

Figure 4.44 shows the histories of the maximum stress, minimum stress, and modulus for the above case. As before, the mechanical response was split into two stages to show the progression of damage. In Stage I the response was similar to that described for the previous failure mode. However, in Stage II the response was different. In this stage, the matrix cracks started progress, which can be observed by the reduction in the modulus. Microscopy will reveal that matrix cracks developed but did not coalesce, so

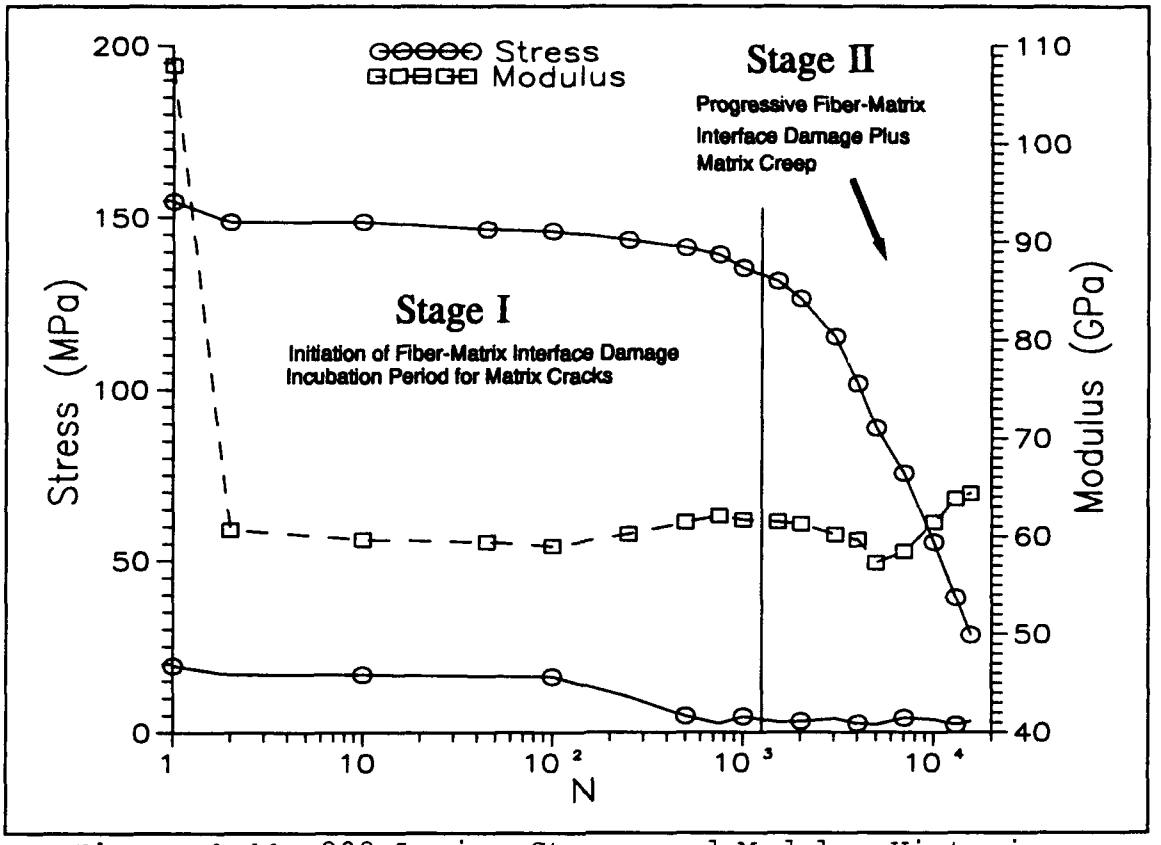

Figure 4.44 90° Lamina Stress and Modulus Histories, ϵ_{max}= .25%

the specimen did not fracture. The stress continued to relax instead. The analysis (Chapter VI) will show that some of the stress relaxation is the result of matrix creep. Further, the microscopic analysis will reveal that the fiber-matrix interface damage progressed when the matrix cracks were arrested, so this mechanisms also contributes to the reduction in stress.

The above discussion suggests the following damage progression for the specimens tested in fatigue with a maximum strain in the range of .23% to .35%:

(1) fiber-matrix interface damage initiates during the first loading cycle

(2) An incubation period for matrix cracks

(3) Matrix cracks begin to propagate but are arrested due to a drop in stress

(4) Fiber-matrix interface damage begins to propagate Also, due to the longer fatigue life, creep deformation of the matrix has more time to accumulate and contribute to the reduction in the stress. The evidence of these damage mechanisms will be shown shortly.

Region IIb - Progressive Fiber-Matrix Interface Damage

For all of the specimens loaded in fatigue below a strain level of .23%, the fatigue behavior was similar. The only difference occurred on the first loading cycle. For a maximum strain of .2%, a slight hysteresis was observed on the first loading cycle[5], but, as will be shown shortly, a linearly elastic stress-strain response was observed for the case of when the maximum strain was .1%.

Stress-Strain Response

Figure 4.45 shows the history of the stress-strain response for the specimen loaded in fatigue at a maximum

[5] See Appendix B for additional experimental results of the 90° lamina.

strain level of .1%. The first cycle response was linearly elastic. This indicates that there was no initiation of the fiber-matrix interface damage. The subsequent stress-strain responses were also linear, so this specimen showed no measurable signs of damage (i.e. no hysteresis).

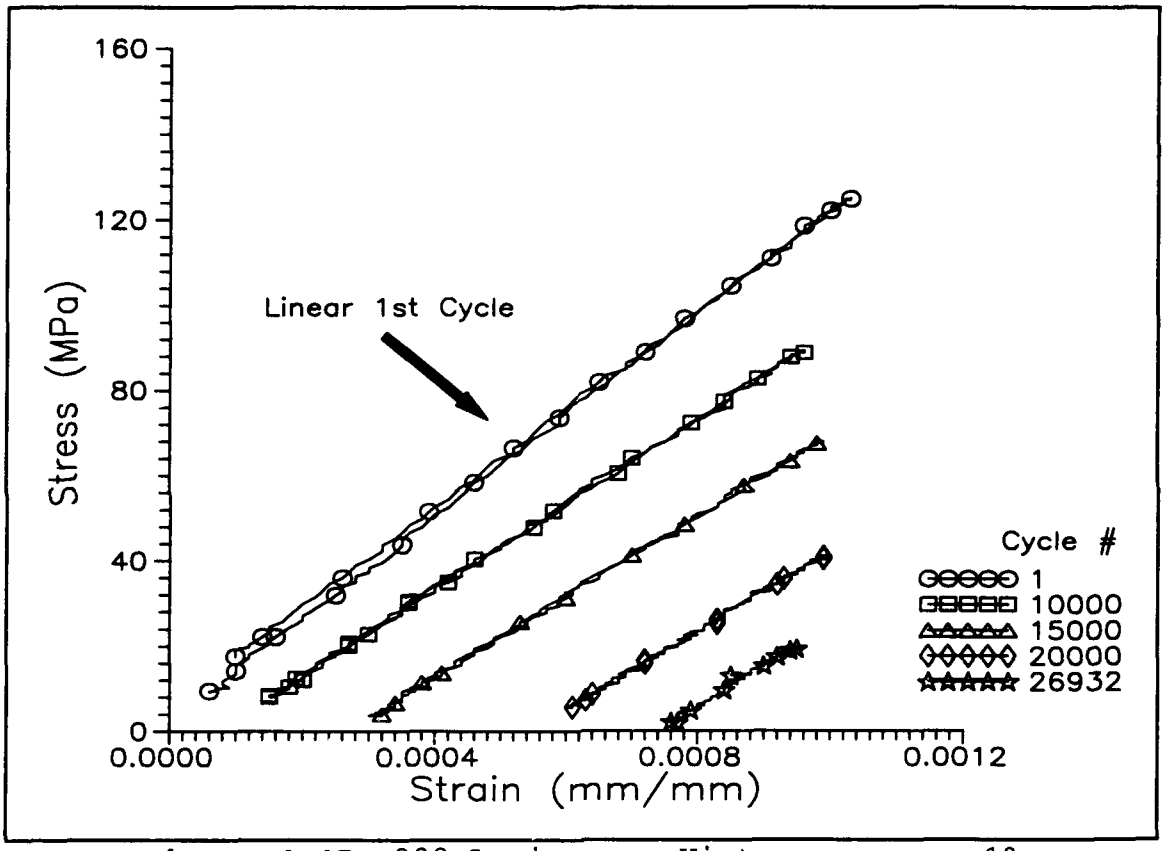

Figure 4.45 90° Lamina σ-ϵ History, ϵ_{max}= .1%

Stress and Modulus Histories

Figure 4.46 shows the histories of the maximum stress, minimum stress, and modulus for the above case. The typical two stage response is shown. In Stage I, it was observed

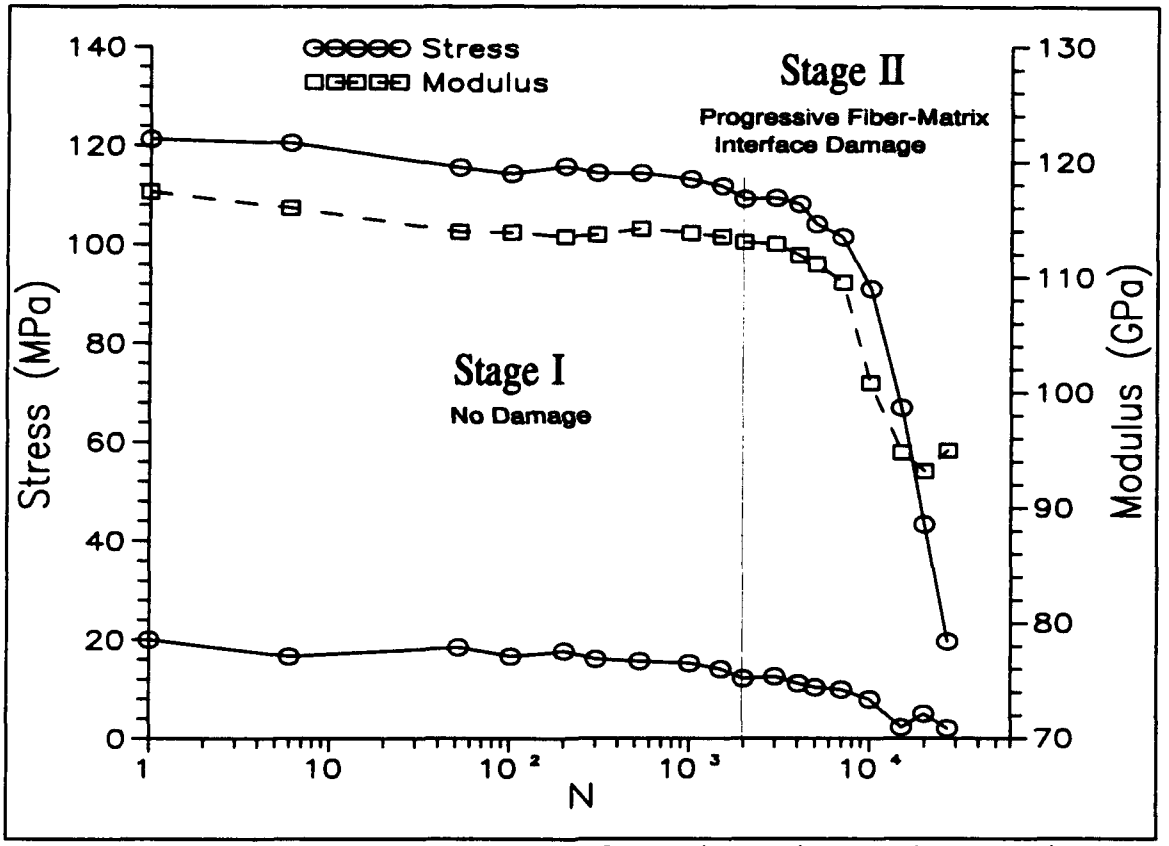

Figure 4.46 Stress and Modulus Histories - 90° Lamina
ϵ_{max}= .1%

that both the stress and modulus remained constant. A simultaneous decrease in the stress and specimen stiffness was then observed (Stage II), so some damage did initiate in fatigue.

In Chapter VI, the analysis will show that the propagation of fiber-matrix interface damage becomes the dominant damage mechanism at later times in the fatigue life. The micromechanical analysis (Chapter VI) will reveal that the matrix creep accounted for only a small percentage

of this total relaxation of the stress. It will be shown later that this response was due mainly to the initiation and progression of the fiber-matrix interface damage. As in the previous cases, the reduction in the specimen stiffness ceased to occur. The reason for this will be discussed next.

Modulus Behavior

Figure 4.47 compares the histories of the modulus, as a function of time, for a neat matrix specimen with that of two 90° laminas. All three of these specimens were subjected to fatigue. The initial stiffness reduction for the 90° specimen tested at a maximum strain level of .25% was explained earlier. This discussion concentrates on the modulus response later in the fatigue life.

It was observed that the modulus of the neat matrix showed a measurable increase after approximately 60 minutes. This has been discussed previously, and it was found to be due to the age hardening of the matrix (Figure 4.9). This same behavior can be assumed to occur in the fiber-reinforced matrix. Thus, in the MMC, there are two competing mechanisms. The first is the accumulation of damage, which results in a reduction in the modulus. The second mechanism was an increasing stiffness of the matrix. When the modulus of the MMC shows a reduction, this implies that the damage was the dominant mechanism. On the other

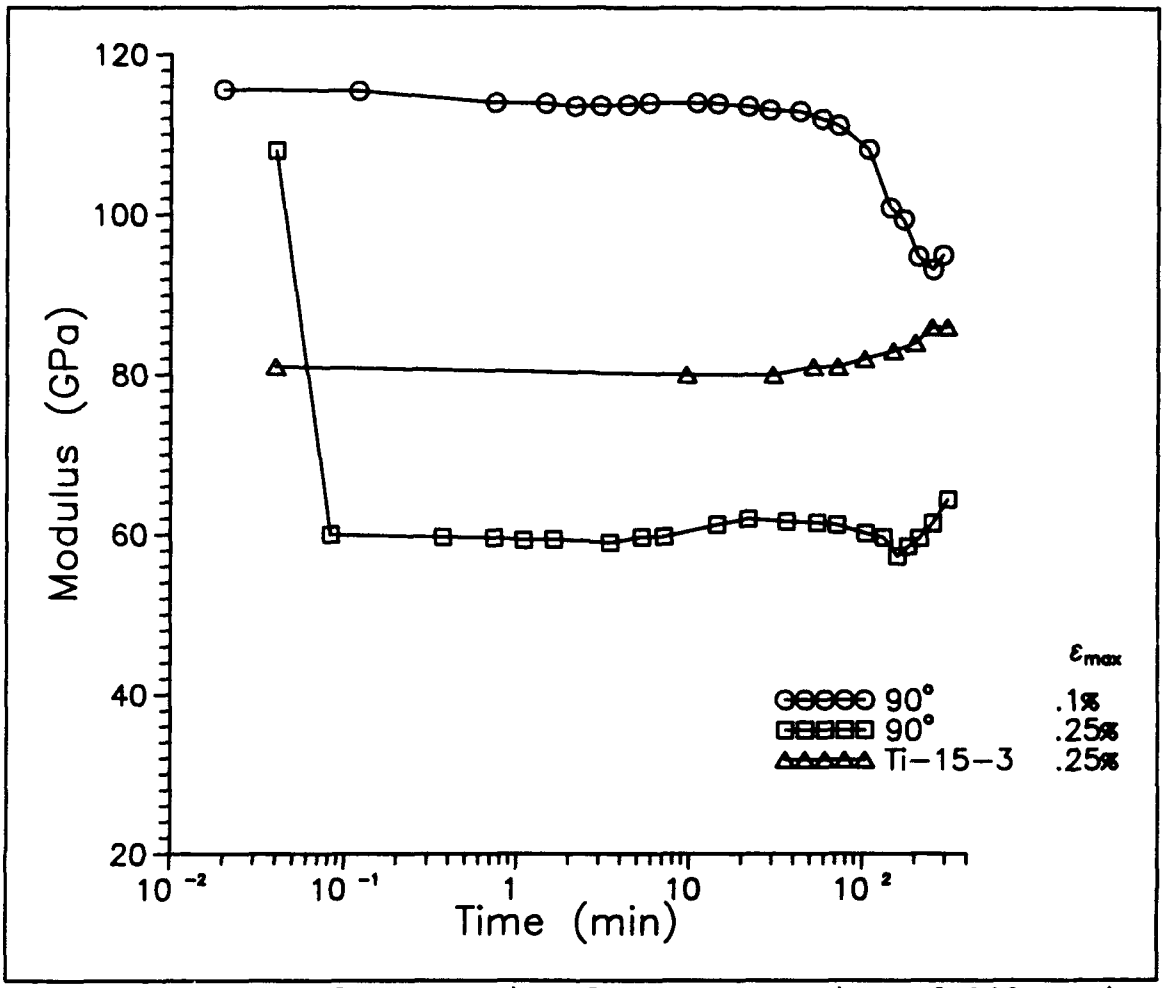

Figure 4.47 Modulus vs. Time for Neat Matrix and 90° Lamina

hand, when the modulus was increasing, age hardening of the matrix was the dominant mechanism. The increase in the matrix stiffness probably served to mask some of the fatigue damage. If no increase in the matrix stiffness had occurred, the specimens would have shown a slightly lower modulus than measured.

Fiber-Matrix Interface Damage Progression

All specimens tested in fatigue showed a drop in the modulus after the first fatigue cycle when the maximum strain was greater than .1%. Figure 4.48 compares the first cycle unloading modulus as a function of the maximum strain. It was observed that the unloading modulus decreased with an increase in the level of applied strain. This was explained earlier to be due to the initiation of the fiber-matrix interface damage. Based on this observation, it is proposed in this study that the fiber-matrix interface damage be considered as a progressive damage mechanism. For example, the extent of interface damage increases with an increase in the applied strain (Figure 4.49). This phenomenon lowers the initial unloading stiffness with an increase in the applied strain. As fatigue continues, this approach allows for a progression of the fiber-matrix interface damage. In Chapter V this concept is applied to model the fatigue response of the 90° lamina.

90° Lamina Fatigue Response Summary

The fatigue response and damage mechanisms of the 90° lamina are summarized in Figure 4.50. This figure combines the typical fatigue responses for both regions on the fatigue curve and the characteristic damage mechanisms discussed above. The physical evidence of these damage mechanisms are given in the next section, and the support

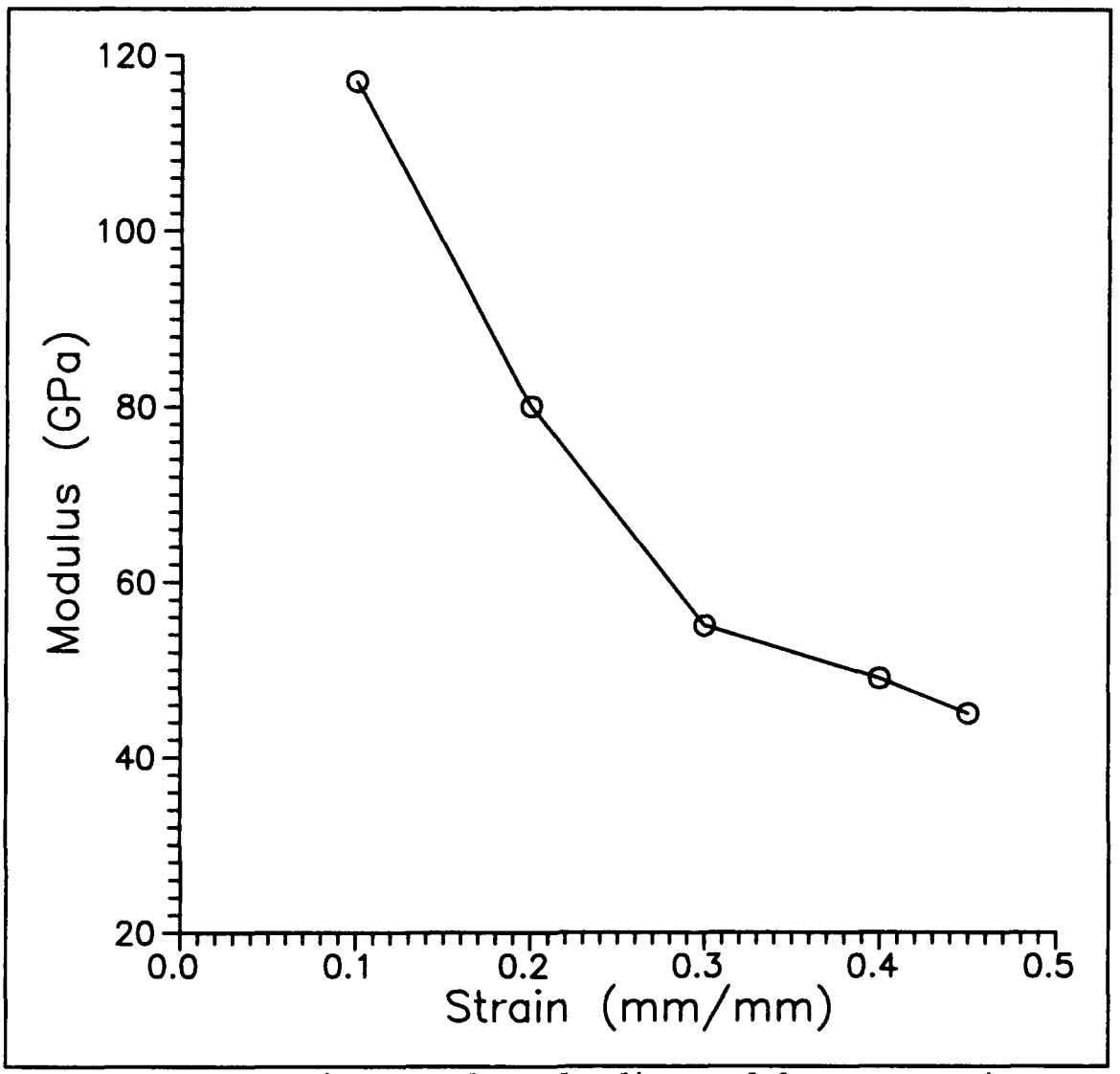

Figure 4.48 First Cycle Unloading Modulus vs. Maximum Strain for 90° Lamina

for the matrix creep deformation will be shown in Chapter VI.

The fatigue response was partitioned into two stages. In Stage I, for those specimens subjected to fatigue above a strain level of .1%, the response was dominated by the

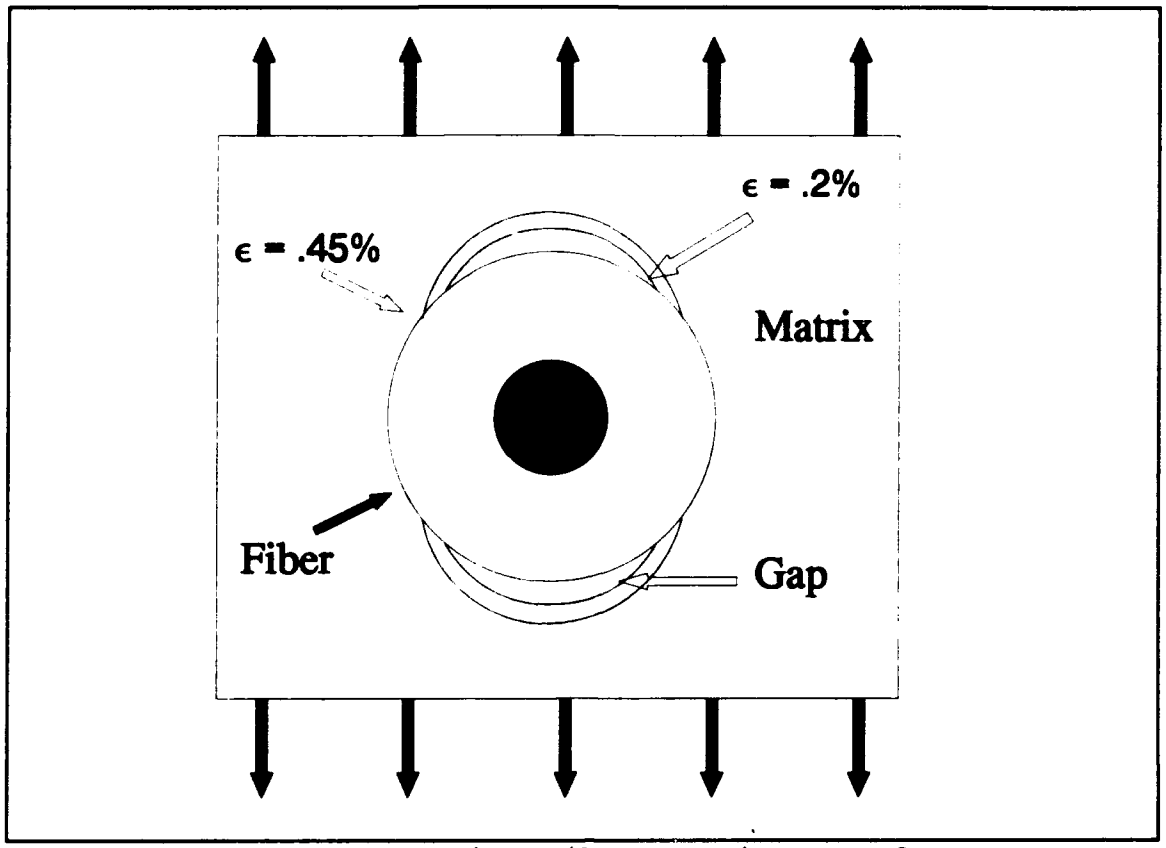

Figure 4.49 Progressive Fiber-Matrix Interface Damage

initiation of fiber-matrix interface damage. This stage was also an incubation period for matrix cracks. Then a simultaneous decrease in the modulus and stress was observed, which was defined as Stage II. For specimens tested with a strain level greater than .35%, the matrix cracks propagated and coalesced to induce specimen fracture. When fatigue occurred below a strain level of .35%, the matrix cracks were arrested. As a result, a combination of matrix creep and a progression of the fiber-matrix interface

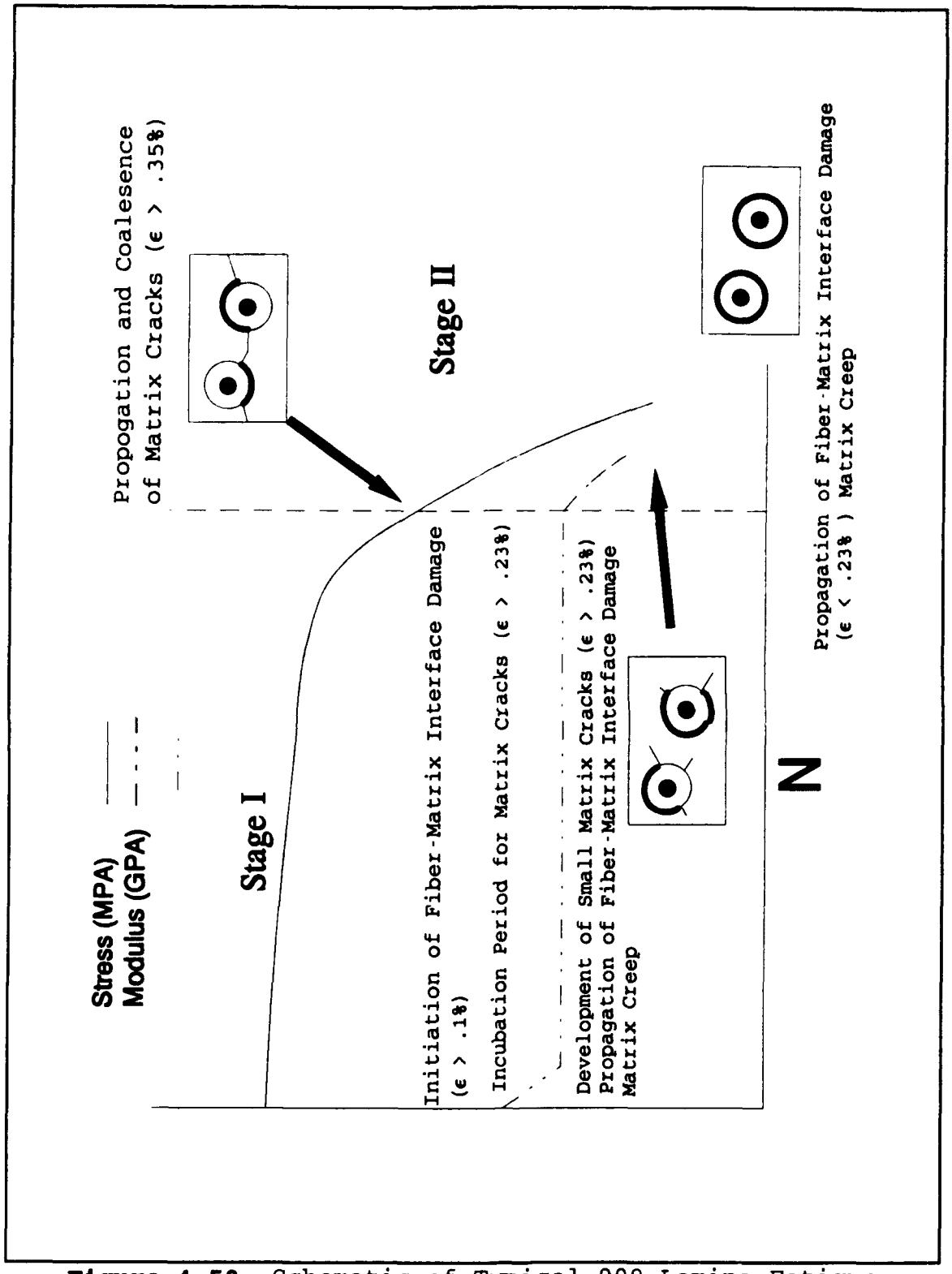

Figure 4.50 Schematic of Typical 90° Lamina Fatigue Response and Damage Mechanisms

damage led to large reductions in the maximum stress. For a maximum strain level below .23%, the only damage observed was the fiber-matrix interface damage, which was also accompanied by matrix creep.

Microscopy - Damage Mechanisms

In the previous section, the fatigue behavior of the 90° lamina was discussed with reference to the mechanical response. This section identifies the damage mechanisms observed from the fractographic analysis. The damage mechanisms are discussed with reference to the fatigue curve (Figure 2.13)

Region I - Matrix Cracking

The specimens subjected to fatigue with a maximum strain greater than .35% fractured. Figure 4.51 shows a typical cross section of the specimen tested in fatigue with a maximum strain of .4%. Intense matrix cracking was observed on several planes. They eventually coalesced into a single crack, which led to fracture of the specimen. It was observed that portions of the fiber-matrix interface were still intact. This implies that matrix cracking was the dominant damage mechanism after the initiation of the fiber-matrix interface damage.

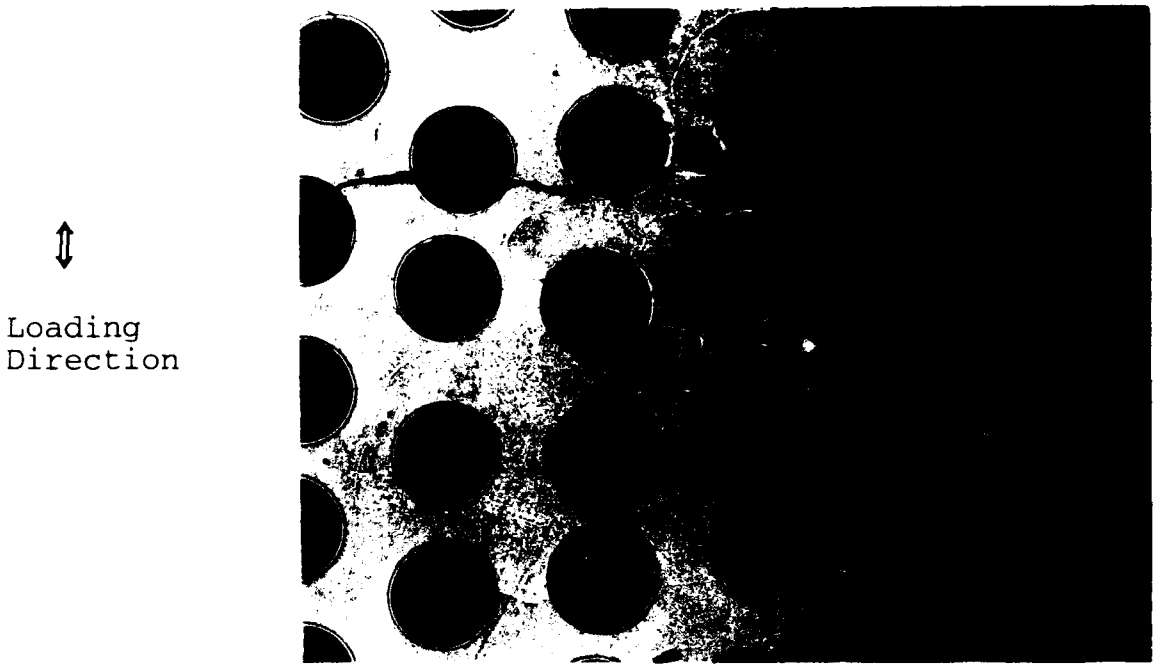

Figure 4.51 Cross Section of 90° Lamina, ϵ_{max}= .4% (100X)

Region IIa - Progressive Fiber-Matrix Interface Damage and Matrix Cracking

When a specimen was subjected to fatigue below a maximum strain of .35%, the specimen fracture did not occur. There was some matrix cracking observed when the maximum strain was greater than .23%. Figure 4.52 shows a typical cross section of the specimen tested with a maximum strain level of .25%. Some matrix cracking was observed, but they did not propagate through the specimen.

Figure 4.53 shows a typical damaged area of a specimen tested in this region. Small matrix cracks were observed propagating out of the fiber-matrix interface. These cracks

⇔

Loading
Direction

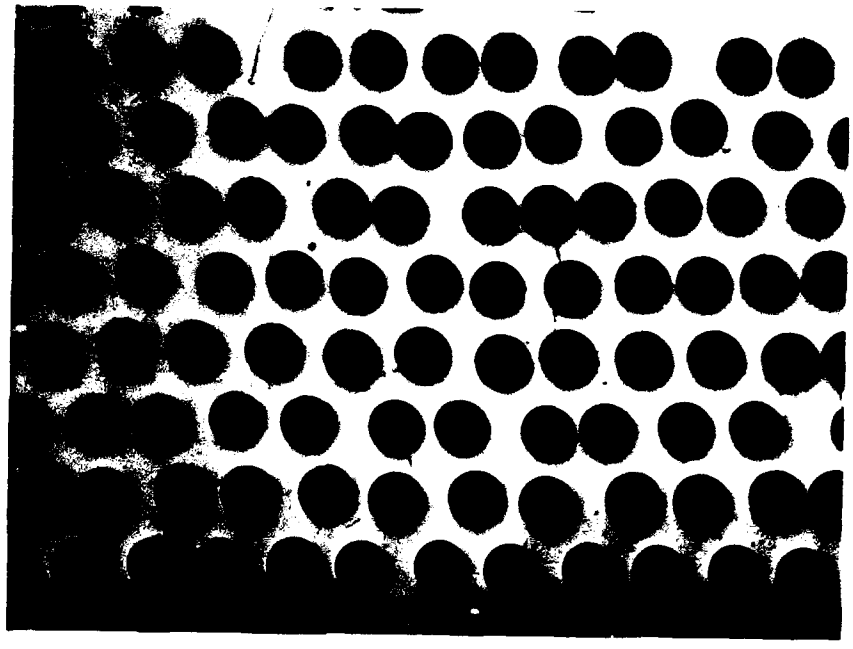

Figure 4.52 Cross Section of 90° Lamina, ϵ_{max}= .25% (50X)

⇕

Loading
Direction

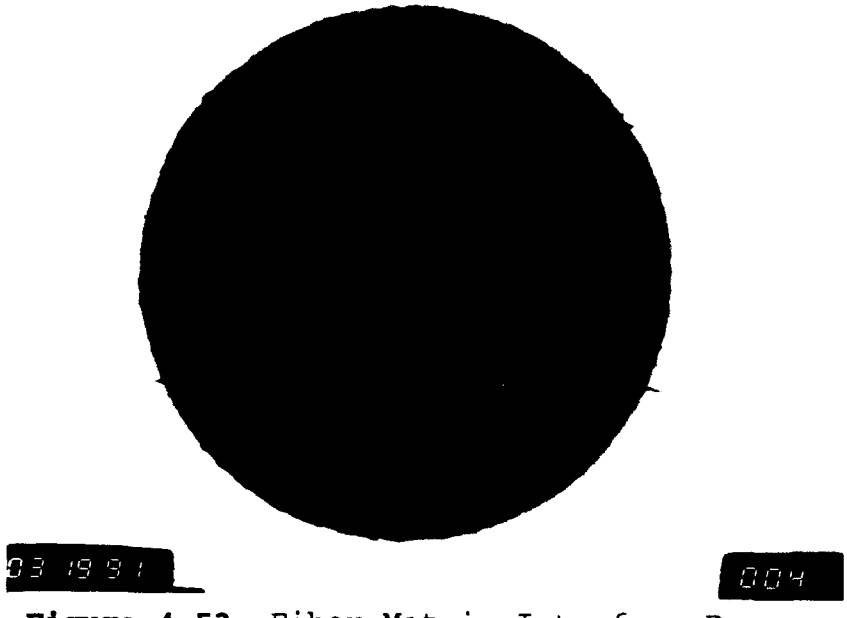

Figure 4.53 Fiber-Matrix Interface Damage in 90° Lamina, ϵ_{max}= .3% (500X)

partially explain the reduction the modulus observed in Stage II (Figure 4.21).

Figure 4.54 shows a higher magnification photograph of a typical damaged area for the specimen subjected to fatigue at a maximum strain level of .25%.

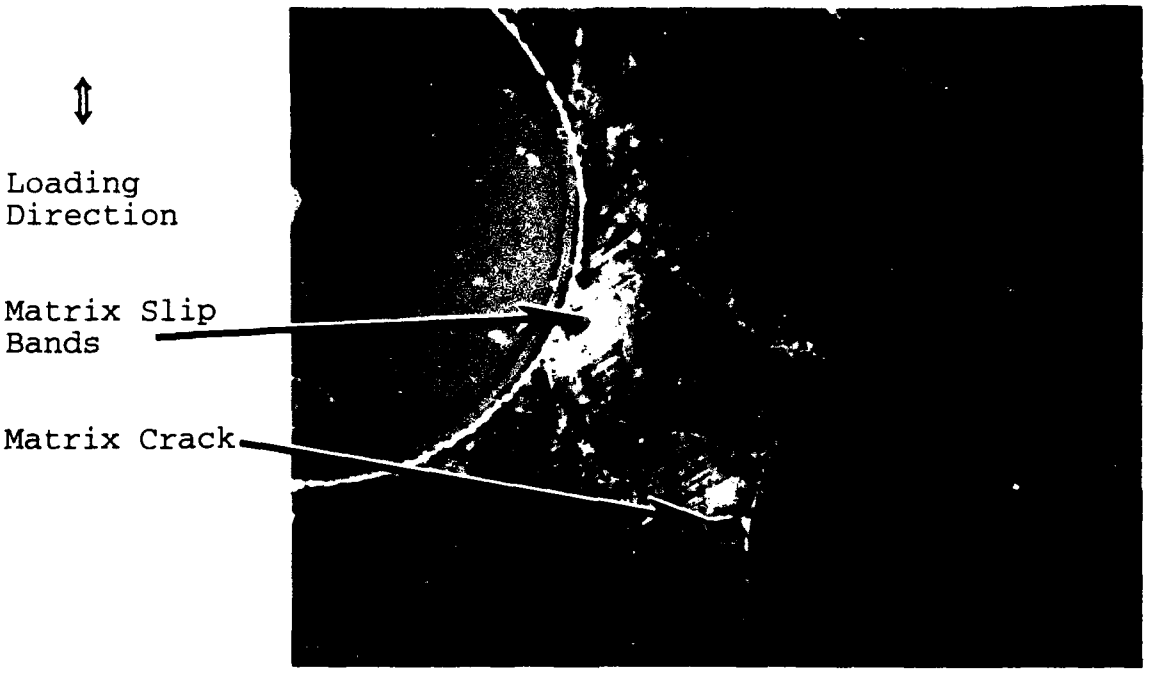

Figure 4.54 Matrix Crack and Slip Bands in 90° Lamina, ϵ_{max}= .25%

Slip bands (i.e. matrix plastic deformation) were observed emanating out of the fiber-matrix interface regions. A crack was observed to have propagated along these slip bands. This shows that the matrix cracks formed where some localized work hardening of the matrix had occurred [68]. Finally, there were no signs of slip bands when fatigue occurred below the this level of strain. This implies that

plastic deformation of the matrix initiates at a strain level of approximately .25%.

Region IIb - Progressive Fiber-Matrix Interface Damage

Figure 4.55 shows a typical cross section of the specimen tested in fatigue at a maximum strain of .2%. There was no evidence of the matrix cracks. Figure 4.56 shows a typical damaged interface for this specimen. There were no small matrix cracks emanating out of the failed interface, but almost the entire interface was observed to have been damaged. This shows that the fatigue response of this specimen was dominated by the progression of the fiber-matrix interface damage.

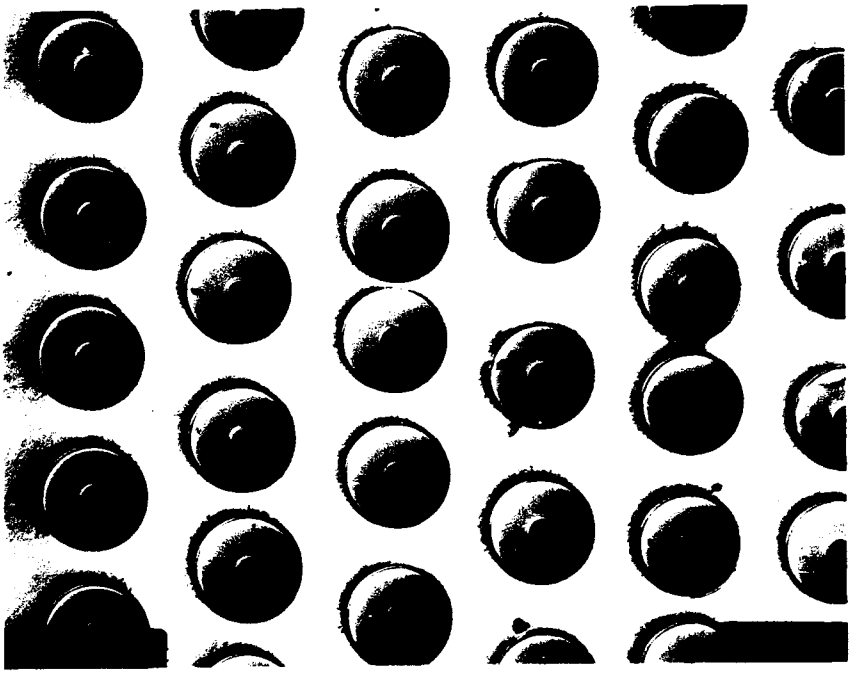

⇕

Loading Direction

Figure 4.55 Cross Section of 90° Lamina, ϵ_{max}= .2% (100X)

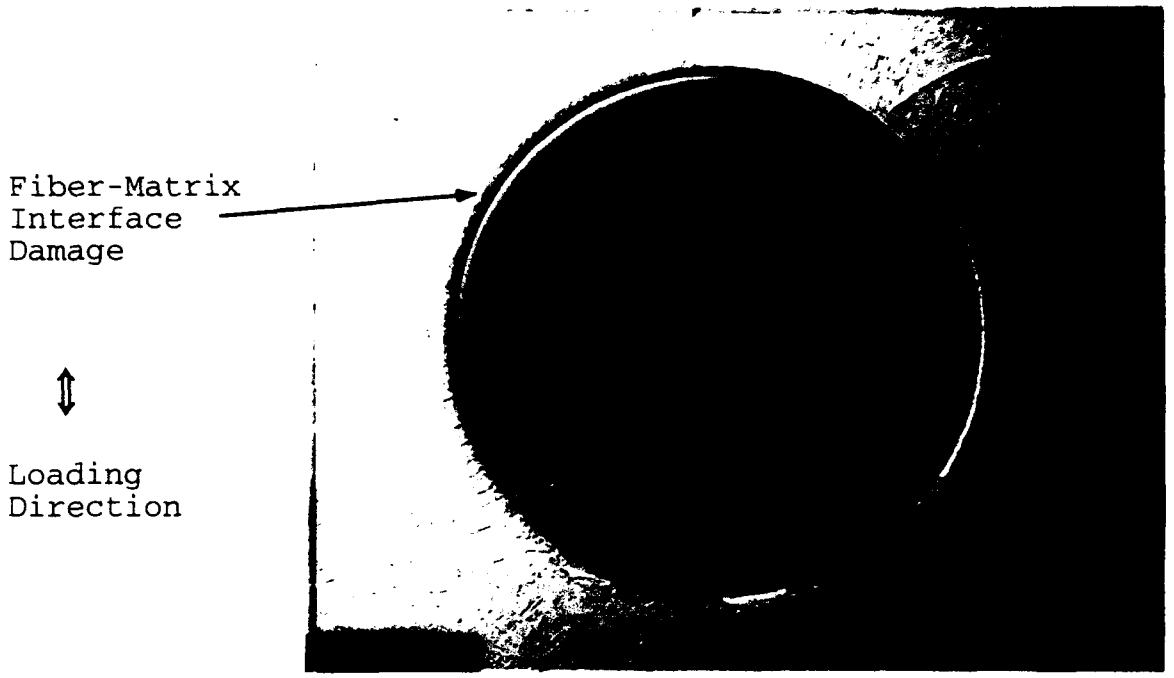

Figure 4.56 Fiber-Matrix Interface Damage in 90° Lamina, ϵ_{max}= of .2% (500X)

As in the previous case, the general condition of the specimen subjected to fatigue with a maximum strain of .1% was good. As expected, there were no matrix cracks, but some fiber-matrix interface damage did initiate. Figure 4.57 shows a typical damaged fiber-matrix interface for this specimen. Partial failure of the interface was observed. It was shown that a reduction in modulus occurred for this specimen (Figure 4.46), which can now be attributed to this damage.

Since the history of the stress-strain response was linear (Figure 4.45), this interface breakdown must have progressed over several hundred, or several thousand

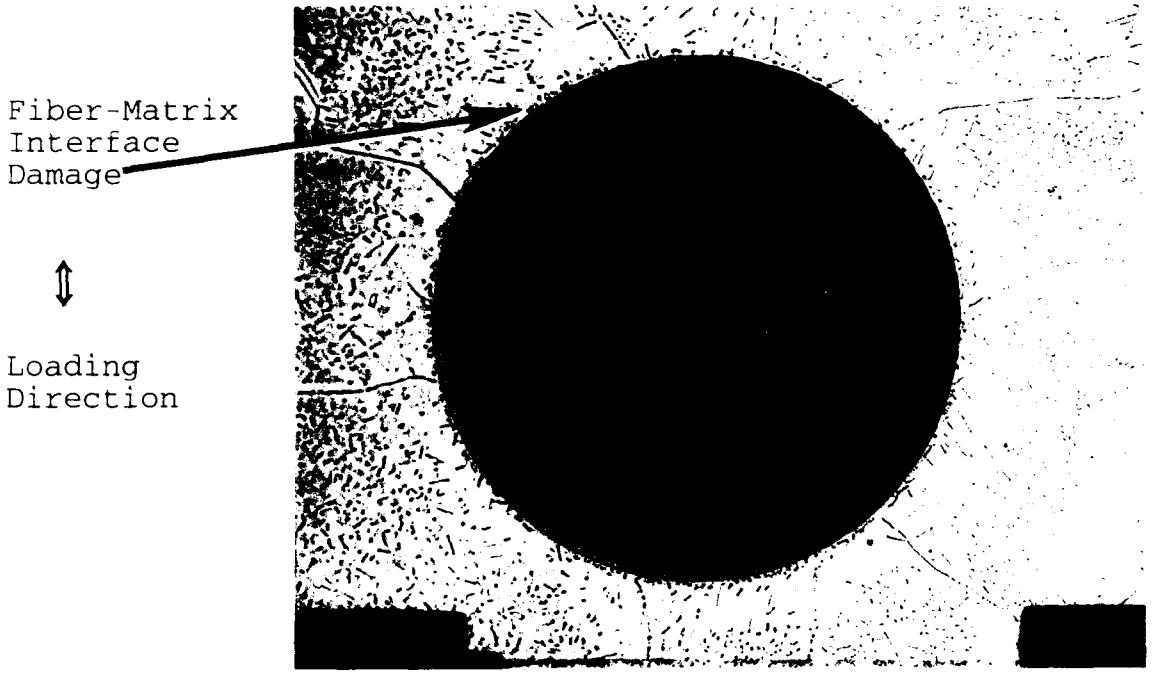

Figure 4.57 Fiber-Matrix Interface Damage in 90° Lamina, ϵ_{max}= .1% (500X)

fatigue cycles. This is opposed to the sudden damage that occurs on at higher levels of strain. As was shown previously, the later case was manifested in a bilinear stress-strain response. It was observed that fewer fiber-matrix interfaces were damaged than in any of the previous cases. An increase in the number of fiber-matrix interface failures, with increasing load, has been observed in other studies of the SCS-6/Ti-15-3 MMC [63].

Fiber-Matrix Interface Failure Distribution

It was suggested previously that the fiber-matrix interface failure was a progressive event (Figure 4.48). The above findings suggests that this may only address one

part of the actual physical phenomenon. It was shown above that more and more of the fiber-matrix interfaces failed as the strain level increased. The frequency of failed interfaces increased dramatically when the maximum strain was increased from .1% to .2%. Thus, in addition to the progressive fiber-matrix interface damage, these observations suggests that the interface damage has a statistical distribution. These concepts are further explored in Chapter V.

Fatigue Life Analysis

It is desirable to develop fatigue curves which relate the specimen fatigue life to the dominant damage mechanisms. The information from the fatigue tests and the microscopic analysis provides the data base to achieve this goal. In this section, the fatigue life was plotted as a function of the maximum applied strain level. The damage mechanisms found in the microscopic analysis were used to partition the fatigue curve into three regions.

Failure Definition

As mentioned earlier, in the strain control mode, the specimen fracture does not always occur. In addition to specimen fracture, another failure criteria must therefore be defined. Gayda and Gabb [35] performed constant amplitude strain controlled fatigue tests on the 90° SCS-6/Ti-15-3 lamina at 427°C. When the specimen fracture did

not occur, they defined failure to be a 75% reduction in maximum stress. It was desired to compare this data with the data obtained from the hybrid stain control mode used in this study. Therefore, the 75% reduction in lamina stress was used to define failure when the specimen fracture did not occur. This failure criteria was also used to define the fatigue life of the neat matrix.

Fatigue Life - Strain Control

Figure 4.58 shows the fatigue life of the 90° lamina as a function of maximum applied strain. The data obtained from fatigue tests conducted in this study on the neat matrix and data available in the literature [34] for the 90° lamina are also shown. The data obtained from Reference 34 were for the constant amplitude strain controlled mode at 427°C. Based on observations from the microscopic analysis, the fatigue curve was partitioned into three regions. These regions are discussed in more detail next.

Region I - Matrix Cracking

Region I was defined by the applied strain levels that induced fracture of the specimen. In this region, matrix cracking was shown to be the dominant damage mechanism. The effect of damage can be observed by comparing the fatigue lives of the composite to that of the neat matrix at the similar strain levels. In the cases where the maximum

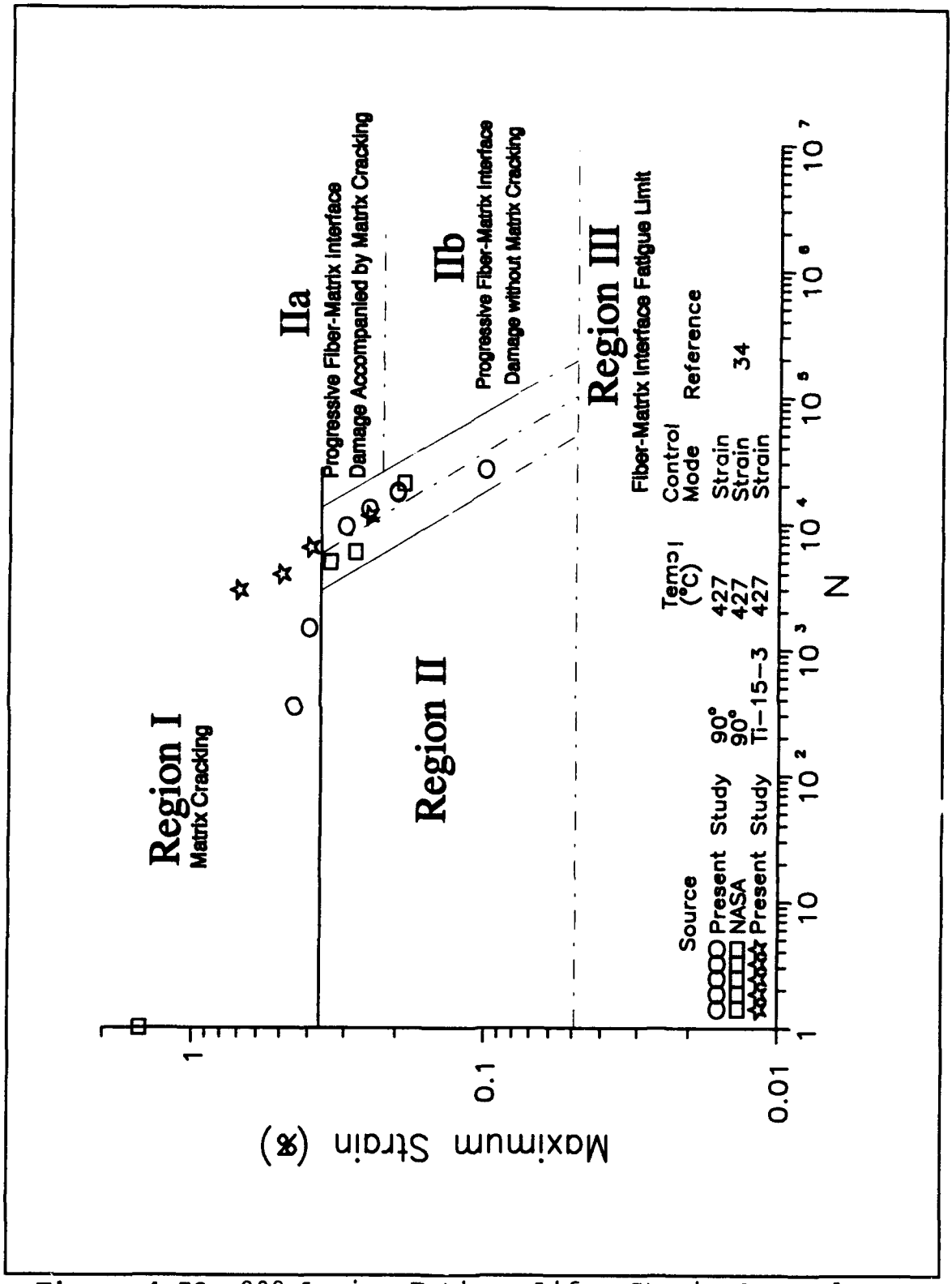

Figure 4.58 90° Lamina Fatigue Life, Strain Control

strain levels were .4% and .45%, the composite fatigue life was much shorter.

The difference in the fatigue lives was due to the development of damage in the MMC. It was previously shown that the fatigue response of the neat matrix was dominated by the creep deformation. The presence of the fibers result in damage to the MMC at the fiber-matrix interface. There are also stress concentrations due to the presence of the stiff fiber. This results in the matrix plastically deforming in these areas, which followed by the development of matrix cracks (Figure 4.54). The propagation of these cracks result in specimen fracture and a shorter fatigue life than the neat matrix.

Region II - Progressive Fiber-Matrix Interface Damage and Matrix Cracking

Region II was defined by the specimens that showed a 75% reduction in the maximum stress. It has been shown that the fatigue response and damage mechanisms in this region were slightly different, so two subregions were created. These differences are highlighted in Figure 4.58.

It was observed that the fatigue life of the composite was similar to the neat matrix in this region. This would imply that response of the MMC was dominated by matrix creep. However, it has been shown, in this study, that the damage mechanisms were not the same. The reduction in

stress for the neat matrix was due solely to creep deformation. The reduction in the lamina stress was a combination of the fiber-matrix interface damage, and matrix cracking in addition to matrix creep; the secondary damage mechanisms (matrix cracking and matrix plasticity) do not occur in Region IIb.

The convergence of the fatigue lives is a result of the total accumulation of these mechanisms. As fatigue damage accumulates in the MMC the stress relaxes. This has the effect of slowing the rate of matrix creep (Figure 4.7 and 4.8). The similarities in the fatigue life were a result of the total accumulation of creep in the neat matrix, and, in the case of the MMC, the accumulation of the matrix deformation and fatigue damage.

A good correlation of the data was observed between the two types of strain control techniques in this region. The fatigue life of all specimens fell within acceptable limits of each other. Acceptable limits in fatigue testing is generally defined by a factor of two, and the scatter in the data is well within these limits (solid lines). Thus, for this region, the hybrid strain control mode was considered an acceptable method to characterize the fatigue life of the 90° lamina.

Region III - Fiber-Matrix Interface Fatigue Limit

Region III was defined were no fiber-matrix interface damage would occur. There were no fatigue tests run in this region nor was any data available in the literature. This point was approximated based on the experiments and the micromechanical analysis conducted in Chapter VI. It was shown earlier that the stress-strain response for the specimen subjected to fatigue at a maximum strain of .1% was entirely linear (Figure 4.45), but some damage did initiate at the fiber-matrix interface (Figure 4.57). Thus, a strain level sufficiently lower than .1% needed to be selected. From the analysis, it can be shown that the residual thermal stresses at the fiber-matrix interface are overcome at a strain level of approximately .05%. No fiber-matrix interface separation would occur below this strain level. Based on these observations, the fatigue limit of the fiber-matrix interface was taken at the strain level of .05%.

Fatigue Life - Strain Control vs. Load Control

For comparison, the fatigue life of the 90° MMC under the strain control mode was plotted along with data available in the literature under the load control mode. For reasons explained when discussing the fatigue life of the 0° lamina, the data were plotted on a strain range basis. Figure 4.59 shows the fatigue life, as a function of strain range, for both the strain and load controlled mode.

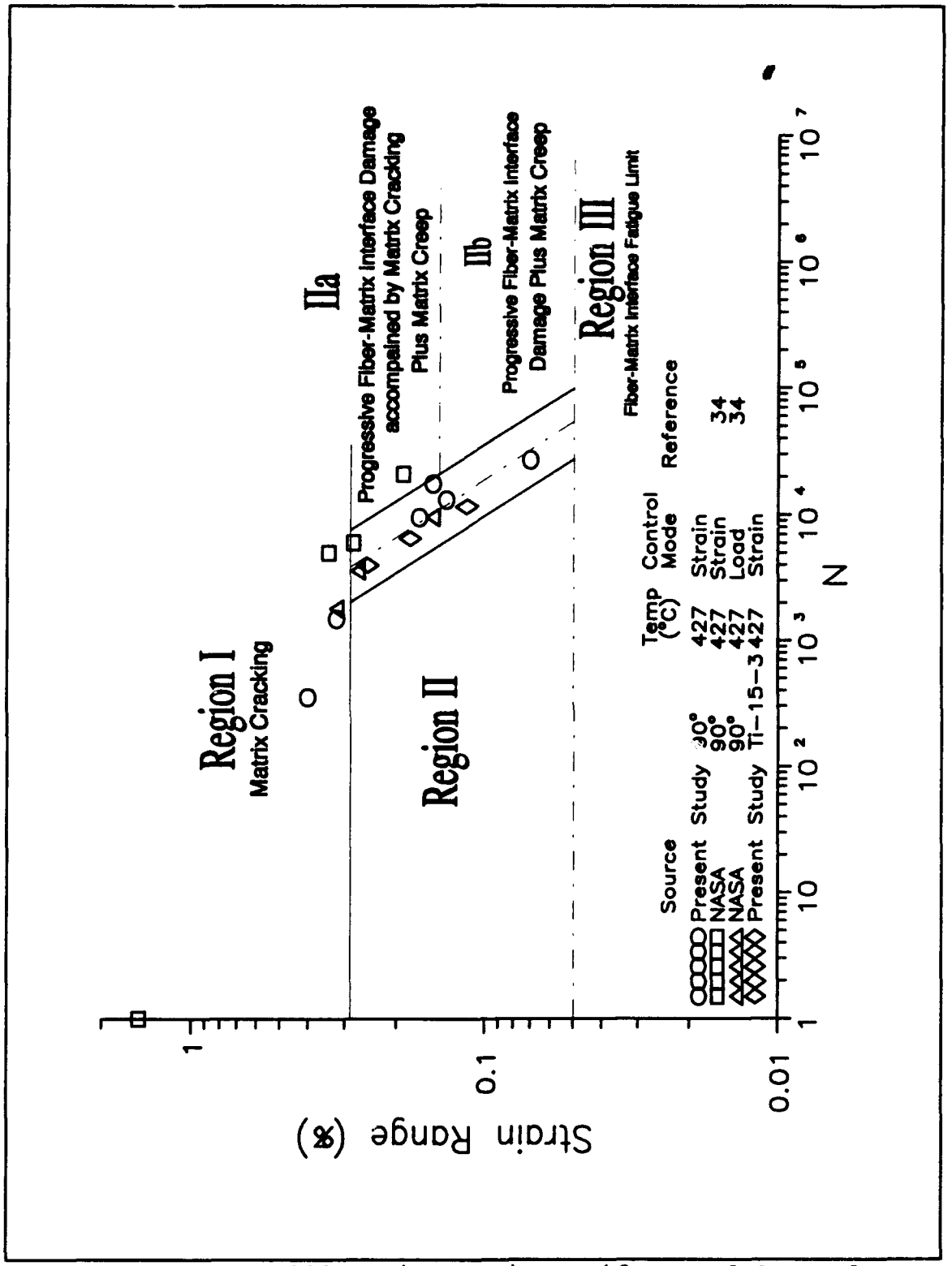

Figure 4.59 90° Lamina Fatigue Life, Load Control vs. Strain control

Also, the three regions described in Figure 4.58 are shown. As in the case of the 0° lamina, the regions were shifted down to account for the change in scale, but the damage mechanisms that defined each region remained the same.

The data to get as through an understanding of the fatigue damage mechanisms as that obtained in this study were not available for the load control case. Further, as can be observed in Figure 4.59, only a limited amount of data were available for the 90° lamina, so this discussion is limited to providing a brief explanation of the similarities of the fatigue lives in Region II.

It was observed that the scatter band in Region II was narrow (i.e. less than a factor of two as shown by the solid lines). Even though the fatigue lives were similar, the damage mechanisms between the two control modes were probably not equal. The fatigue lives were defined by specimen fracture when using the load control mode. In load control, the matrix cracks were not arrested at any strain level. This is contrary to the situation in the strain controlled mode. It was shown before that the cracks are arrested in strain control when the maximum strain is below .35%. This implies that the convergence of the fatigue lives is a sum of the total damage and deformation mechanisms, as was discussed in the fatigue life of the 0° lamina. This suggests that an evolutionary law, relating

the different damage and deformation mechanisms, can be developed and applied to predict the fatigue response under each control mode.

Summary of 90° Lamina Behavior

The fatigue behavior of the SCS-6/Ti-15-3 90° lamina has been characterized. It was shown that the fatigue response was strongly influenced by the fiber-matrix interface damage. The initiation of this damage occurred on the first fatigue cycle at a strain level above .1%. For the specimens subjected to fatigue with a maximum strain level greater than .35%, matrix cracks propagated into adjoining planes, which eventually resulted in fracture of the specimen. On the other hand, when the maximum strain level was less than .35%, the progression of the matrix cracks was arrested by a reduction in the maximum stress. A progression of the fiber-matrix interface damage then became the dominant mechanism. When fatigue occurred below a maximum strain level of .23%, only the fiber-matrix interface damage was observed. Finally, the fatigue life of the 90° lamina was plotted as a function of maximum applied strain. The fatigue curve was partitioned into three regions based on the observed damage mechanisms.

Summary of Experimental Results

This chapter characterized the fatigue behavior of the Ti-15-3 neat matrix, 0° SCS-6/Ti-15-3 MMC, and 90° SCS-6/Ti-15-3 MMC. The specimens were subjected to fatigue using a hybrid strain control mode at elevated temperature (427° C). Conclusions based on the observed behavior are summarized below:

Neat Matrix Relaxation and Fatigue Responses

(1) The Ti-15-3 neat matrix behaves viscoplastically at 427°C.

(2) The stress relaxation of the neat matrix was observed to be a function of time and the applied strain.

(3) The fatigue response was dominated by the creep deformation.

(4) The stiffness of the neat matrix increased when exposed to elevated temperature (427°C).

0° Lamina Fatigue Response

(1) The initial nonlinear response of the 0° lamina above a strain level of .55% was due to plastic deformation of the matrix.

(2) Matrix creep was a significant deformation mechanism.

(3) The fatigue response of the 0° lamina above a maximum strain level of .73% was dominated by fiber

fractures. This was accompanied by the plastic and creep deformation of the matrix.

(4) The fatigue response of the 0° lamina below a maximum strain level of .73% was described by a two stages. In Stage I, the response was dominated matrix creep, which was accompanied by matrix plastic deformation when the maximum strain level was above .55%. In this stage, a state of self-equilibrating creep developed in the matrix, which was an incubation period for the initiation of matrix cracks. Finally, in Stage II, the matrix cracks began to propagate, which also induced some damage to the fiber-matrix interface. The fiber-matrix interface damage was also influenced by oxidation. As a result of these damage mechanisms, a loss in stiffness was observed.

(5) The fatigue life of the 0° lamina under strain control was partitioned into three regions. Region I was defined by the specimens that exhibited the fiber dominated failure mode. Region II was defined by the specimens that exhibited the matrix dominated failure mode. Finally, based on the data obtained in this study, and that from the literature, the matrix fatigue limit (Region III) was defined when fatigue occurred below a maximum strain level of .3%.

90° Lamina Fatigue Response

(1) The fiber-matrix interface damage was a significant factor in the fatigue response of 90° lamina.

(2) The initiation of the fiber-matrix interface damage was observed to occur on the first loading cycle above a strain level of .1%.

(3) The initial nonlinear stress-strain response of the 90° lamina was a combination of the fiber-matrix interface damage coupled with a statistical distribution of these interface failures.

(4) Plastic deformation of the matrix was observed for those specimens loaded above a strain level of .25%.

(5) After the initial fiber-matrix interface damage, for those specimens subjected to fatigue above a strain level of .35%, the dominant damage mechanism was matrix cracking. The propagation and coalescence of these cracks led to fracture of the specimen.

(6) After the initial fiber-matrix interface damage, for those specimens tested in fatigue above a maximum strain of .23%, but less than .35%, the progression of fatigue damage was: the development of small non-propagating matrix cracks originating at the fiber-matrix interface, and then a progression of the fiber-matrix interface damage and matrix creep.

(7) When fatigue occurred below a maximum strain level of .23%, the fatigue damage was limited to fiber-matrix interface damage.

(8) The fatigue curve of the 90° lamina under the strain control mode was partitioned into three regions. Region I was defined by those specimens that exhibited failure due to the propagation of matrix cracks. Region II was defined by those specimens that showed a 75% reduction in stress. This region was further partitioned into two subregions. In Subregion IIa, the specimens exhibited a combination of small non-propagating matrix cracks, progressive fiber-matrix interface damage, and matrix creep. In Subregion IIb, the only damage was the fiber-matrix interface damage, but some matrix creep did occur. Finally, based on the data obtained in this study, and the micromechanical analysis shown in the next chapter, Region III was defined as the fiber-matrix interface fatigue limit.

V. Analysis - Model Development

Details of the analytical models used for predicting the fatigue behavior of the unidirectional SCS-6/Ti-15-3 MMC are explained in this chapter. The basic principles of the concentric cylinder model (CCM) and a unit cell model are presented first. This is then followed a description of the scheme used to model the elastic-viscoplastic response of the matrix. In the next chapter, these models are applied to better understand the behavior of the MMC when subjected to fatigue.

Concentric Cylinder Model

The concentric cylinder model (CCM) was used to predict the stresses in the lamina and constituents as a function of fatigue cycles for the 0° MMC. This section provides the details of the CCM and its applications in this study. The material model is presented along with the strain displacement equations, constitutive equations, and boundary conditions [100] required to solve for the stresses of the lamina and constituents.

A schematic of the CCM is shown in Figure 5.1. The CCM is composed of a cylindrical fiber with radius r_f, which is surrounded by a cylindrical matrix of radius r_m. The following assumptions apply to this model:

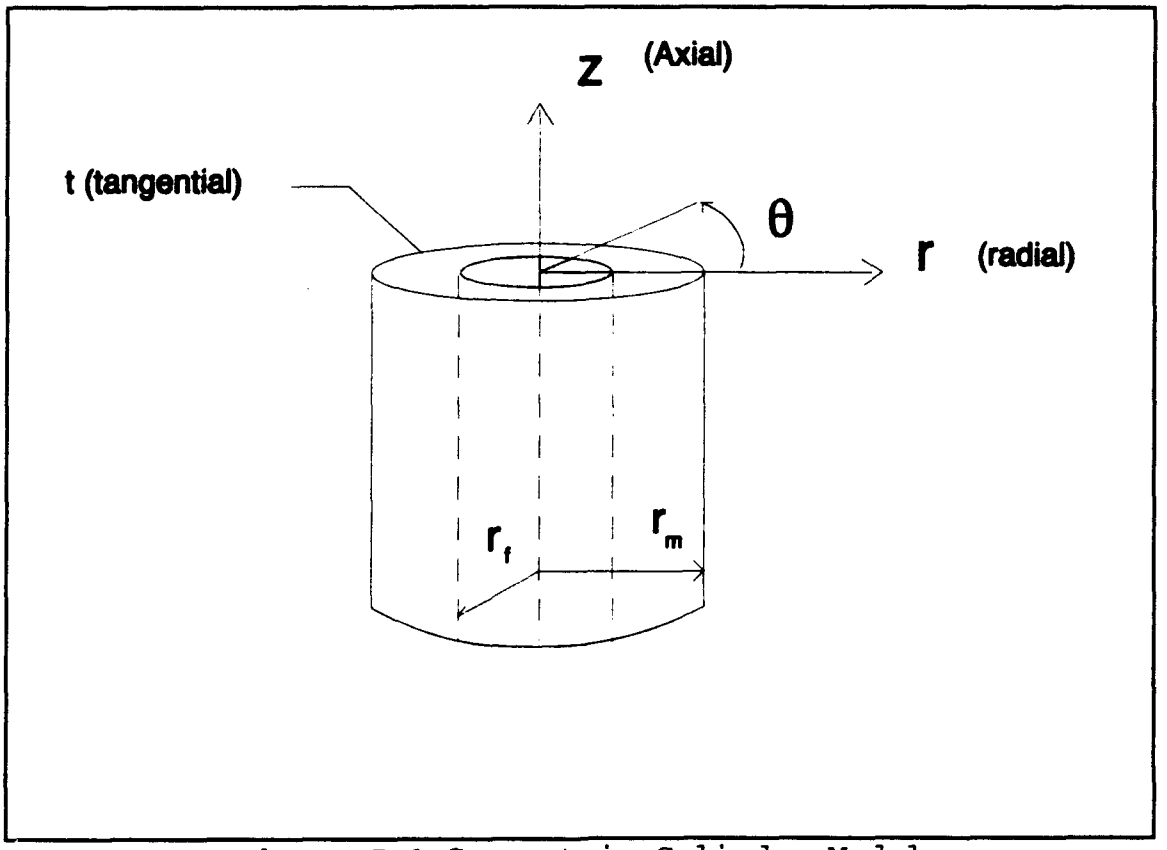

Figure 5.1 Concentric Cylinder Model

(1) A state of axisymmetric, generalized plane strain exists

(2) The matrix and fiber are isotropic materials

(3) The matrix and fiber properties are temperature independent

(4) The fiber is linear elastic

(5) The matrix is elastic-viscoplastic.

The general elastic displacement solution which satisfies the equilibrium condition is given by

$$u_r = Ar + \frac{B}{r} \tag{5.1}$$

where A and B are constants that need to be determined through the application of the boundary conditions. Equation 5.1 can be used to represent the matrix and fiber radial displacements as:

$$u_m = A_m r + \frac{B_m}{r} \qquad for\ r_f \le r \le r_m \tag{5.2}$$

$$u_f = C_f r_f \qquad for\ r \le r_f \tag{5.3}$$

where the subscripts m and f refer to matrix and fiber, respectively. For the axisymmetric, generalized plane strain condition, the strain-displacement relations are:

$$\begin{aligned} \epsilon_{zz} &= \epsilon'_o \\ \epsilon_{rr} &= \frac{\partial u_r}{\partial r} \\ \epsilon_{\theta\theta} &= \frac{u_r}{r} \end{aligned} \tag{5.4}$$

where ϵ_o' is the applied mechanical strain. The following incremental stress-strain relationships apply in the cylindrical coordinate system:

$$\Delta\sigma_{rr} = \frac{E_i}{(1+\nu_i)(1-2\nu_i)}[(1-\nu_i)\Delta e_{rr} + \nu_i \Delta e_{\theta\theta} + \nu \Delta e_{zz}] - \frac{E_i}{1-2\nu_i}\alpha_i \Delta T \tag{5.5}$$

$$\Delta\sigma_{\theta\theta} = \frac{E_i}{(1+\nu_i)(1-2\nu_i)}[\nu_i \Delta e_{rr} + (1-\nu_i)\Delta e_{\theta\theta} + \nu_i \Delta e_{zz}] - \frac{E_i}{1-2\nu_i}\alpha_i \Delta T \tag{5.6}$$

$$\Delta\sigma_{zz}=\frac{E_i}{(1+\nu_i)(1-2\nu_i)}[\nu_i\Delta e_{rr}+\nu_i\Delta e_{\theta\theta}+(1-\nu_i)\Delta e_{zz}]-\frac{E_i}{1-2\nu_i}\alpha_i\Delta T \qquad (5.7)$$

where E_i, ν_i, and α_i refer to the instantaneous modulus, Poisson's Ratio, and the coefficient of thermal expansion (CTE), respectively, of the fiber or matrix.

Three boundary conditions are required to solve for A_m, B_m, and C_f for the case of an applied strain ϵ_o'. Additionally, when the cylinders are free to deform in the longitudinal direction due to thermal expansion, a fourth boundary condition is required to solve for the longitudinal thermal strain (ϵ_{th}). The first boundary condition requires displacement compatibility at the fiber-matrix interface:

$$u_f(r_f) = u_m(r_f) \qquad (5.8)$$

The second condition requires that the radial stress of the matrix is zero at $r = r_m$:

$$\sigma_r(r_m) = 0 \qquad (5.9)$$

The third condition requires force equilibrium at the fiber-matrix interface:

$$\sigma_{r_m}(r_f) = \sigma_{r_f}(r_f) \qquad (5.10)$$

When the cylinders are free to deform in the longitudinal direction due to thermal expansion, the fourth boundary condition requires that the fiber and matrix force resultant sum to zero in the longitudinal direction:

$$2\pi\int_0^{r_f}\sigma_{z_f} r\,dr + 2\pi\int_{r_f}^{r_m}\sigma_{z_m} r\,dr = 0 \qquad (5.11)$$

The thermal stresses in the constituents were found first by by solving the system of equations

$$\begin{bmatrix} P \end{bmatrix}\begin{Bmatrix} C_f \\ A_m \\ B_m \\ \epsilon_{th} \end{Bmatrix} = \begin{Bmatrix} b \\ \\ \end{Bmatrix} \qquad (5.12)$$

for the unknowns, where [P] and {b} are given in Appendix C. The stresses of the lamina and constituents were then obtained for an applied strain ϵ_o'. This system of equations is similar to that shown in Equation 5.12 and is also given in Appendix C.

For each increment of strain or temperature, the system of equations was developed and the unknowns were found by using an LU decomposition routine. After obtaining these unknowns, the incremental fiber and matrix stresses were then determined using Equations 5.2 through 5.7. The total stresses were then found from:

$$\begin{aligned} \sigma_{zz_i} &= \sigma_{zz_{i-1}} + \Delta\sigma_{zz_i} \\ \sigma_{rr_i} &= \sigma_{rr_{i-1}} + \Delta\sigma_{rr_i} \\ \sigma_{\theta\theta_i} &= \sigma_{\theta\theta_{i-1}} + \Delta\sigma_{\theta\theta_i} \end{aligned} \qquad (5.13)$$

where i indicates the current increment. Finally, the longitudinal stress of the lamina was calculated from the rule-of-mixture theory [55]

$$\sigma_{l_i}=\sigma_{f_i}v_f+\sigma_{m_i}(1-v_f) \qquad (5.14)$$

where v_f refers to the fiber volume fraction of the MMC.

Strip Model

This section describes the application of a unit cell model to predict the transverse response of a unidirectional SCS-6/Ti-15-3 MMC. Derivations of the equations required to compute the lamina properties are reviewed. Also, the one dimensional equations to calculate the thermal and mechanical stresses are presented[6]. A method is proposed to account for the fiber-matrix interface damage, which was observed in the experiments and discussed in Chapter IV

Basic Concept

The model applied to predict the fatigue response of the 90° lamina is based on assuming the fibers are arranged in a rectangular array (Figure 5.2). In this case, a single fiber and matrix region can be used as a representative volume element (RVE). This RVE (unit cell) has been used in a few investigations [19, 20, 82, 93] to predict the transverse material properties and the stress-strain response of a unidirectional MMC. One particular

[6] The derivation of lamina properties and stresses can be found in References 48 and 79 and are reviewed here for completeness.

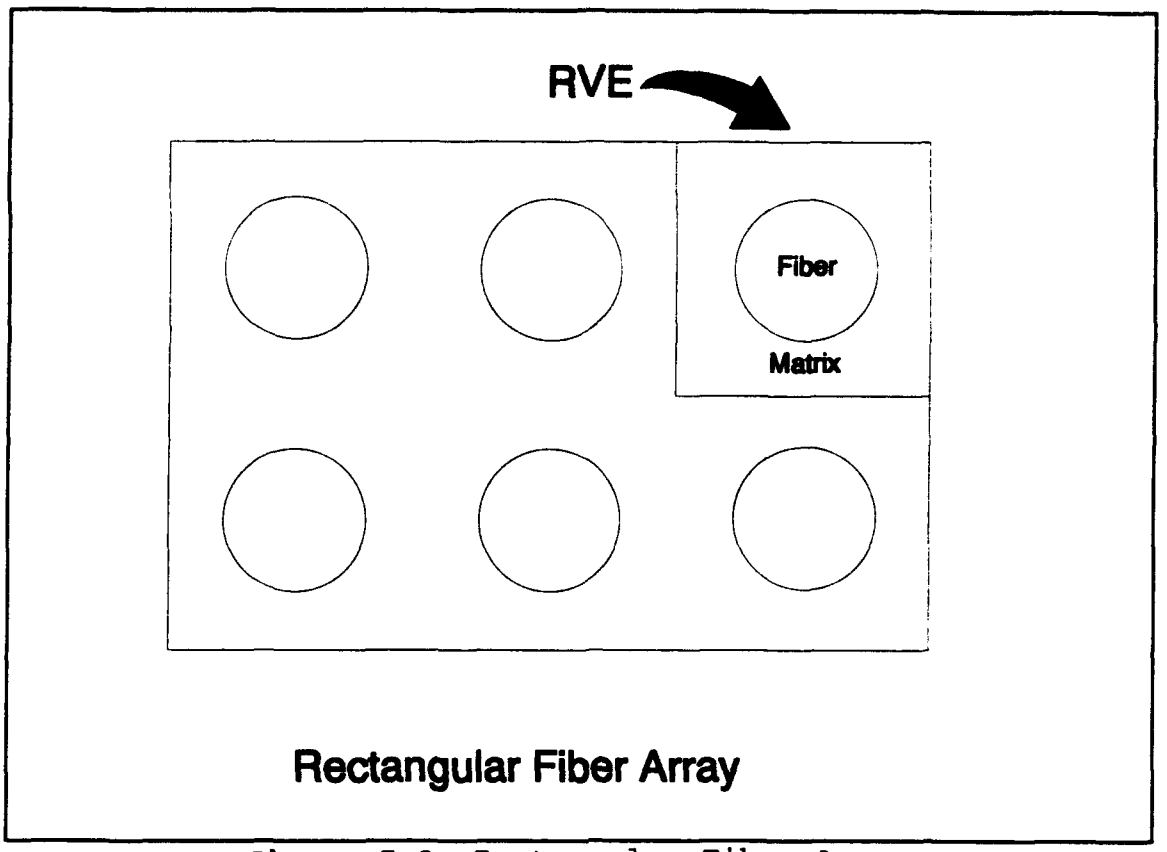

Figure 5.2 Rectangular Fiber Array

application of the unit cell has been proposed by Hopkins and Chamis [48], which is discussed next.

Hopkins and Chamis modeled the response of a MMC with the multi-cell Model (MCM), which is shown schematically in Figure 5.3. This configuration of the unit cell does not lend itself to analyzing the incremental breakdown of the interface as observed in this study. For the analysis of ceramic matrix composites, Murthy and Chamis [79] extended this concept by dividing the MCM into several strips (Figure 5.4a), which will now be referred to as the strip model

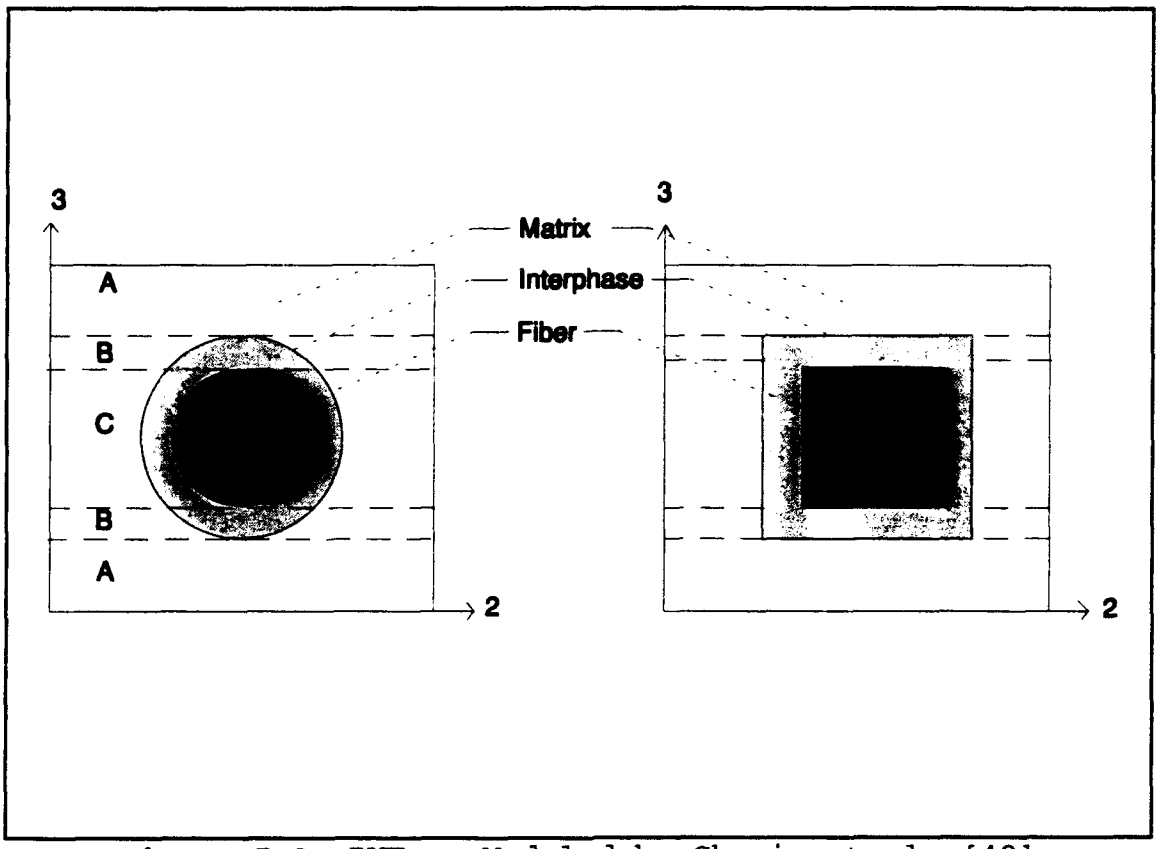

Figure 5.3 RVE as Modeled by Chamis et al. [48]

(SM). Due to symmetry, it is sufficient to model the RVE as shown in Figure 5.4b, which improves the computational efficiency. This model was adopted in this study for predicting the response of the 90° MMC subjected to fatigue. The next few sections describe: the development of the transverse properties of the strips and lamina, the calculation of the transverse stresses in the strips and lamina, and the method proposed for modeling the fiber-matrix interface damage.

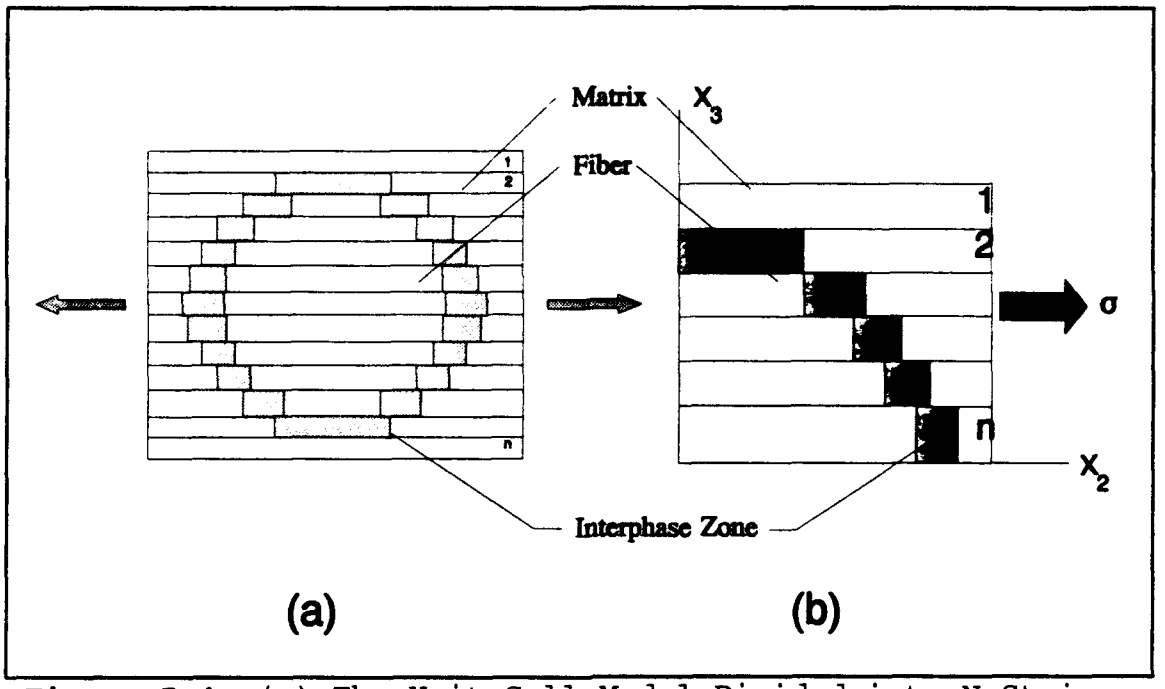

Figure 5.4 (a) The Unit Cell Model Divided into N Strips, (b) The Final Model Used by Applying Symmetry

Transverse Properties of the Strip and Lamina

Strip Properties

The development of the lamina properties begins by developing the properties of a single strip. This is then extended to the lamina level. The following assumptions apply in the SM:

(1) Both the matrix and fiber are isotropic

(2) The matrix and fiber properties are temperature independent

(3) The fiber is linear elastic

(4) The matrix is elastic-viscoplastic

(5) Displacement along the both free edges of the unit

cell must be equal (i.e. each strip must displace equally in the transverse direction)

(6) In each strip, the fiber, matrix, and interphase zone act in series.

A representative strip element is shown in Figure 5.5. The strip consists of fiber, interphase, and matrix materials[7]. These three materials are assumed to act in series. Thus, strain compatibility for the k^{th} strip is requires that

$$\epsilon_k=\epsilon_f V_f+\epsilon_i V_i+\epsilon_m V_m \qquad (5.15)$$

where ϵ_k is the applied strain, and the subscripts k, f, i, and m correspond to the strip, fiber, interphase, and matrix, respectively. Equilibrium requires that the stress in the k^{th} strip is equal to the stress in each of its constituents:

$$\sigma_k=\sigma_f=\sigma_i=\sigma_m \qquad (5.16)$$

The strain in each constituent with respect to its own material properties is expressed as:

[7] The general development of the equations includes the interphase zone. However, during the analysis, the volume fraction of this zone was set equal to zero.

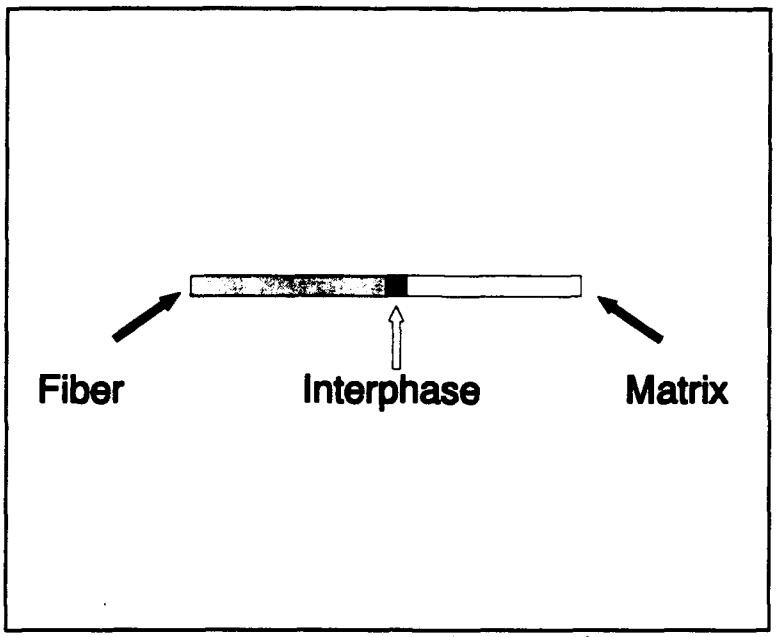

Figure 5.5 Representative Strip Element

$$\epsilon_f = \frac{\sigma_f}{E_m} + \alpha_f \Delta T$$
$$\epsilon_i = \frac{\sigma_i}{E_i} + \alpha_i \Delta T \qquad (5.17)$$
$$\epsilon_m = \frac{\sigma_m}{E_m} + \alpha_m \Delta T$$

Likewise, the strain in any strip in relationship to its own properties can be expressed by

$$\epsilon_k = \frac{\sigma_k}{E_k} + \alpha_k \Delta T \qquad (5.18)$$

The transverse modulus (E_{22}) and transverse CTE (α_{22}) of any strip can be found by substituting Equations 5.17 and 5.18 into Equation 5.15 and applying the equilibrium condition (Equation 5.16):

$$\frac{\sigma}{E_k}+\alpha_k\Delta T=\sigma\left[\frac{V_f}{E_f}+\frac{V_i}{E_i}+\frac{V_m}{E_m}\right]+\left[\alpha_f V_f+\alpha_i V_i+\alpha_m V_m\right]\Delta T \qquad (5.19)$$

Comparing like terms on the left and right side of Equation 5.19, E_{22} of the k^{th} strip is

$$E_{22_k}=\frac{E_m E_f E_i}{E_m E_i V_f+E_m E_f V_i+E_f E_i V_m} \qquad (5.20)$$

while α_{22} of the k^{th} strip is

$$\alpha_k=\alpha_f V_f+\alpha_i V_i+\alpha_m V_m \qquad (5.21)$$

Equations 5.20 and 5.21 are the only properties of the strip required for the one dimensional analysis.

Lamina Properties

Once the properties of the individual strips have been determined, the lamina properties can be calculated by assuming the strips act in parallel. This condition requires displacement compatibility along the right face of the unit cell:

$$\epsilon_l=\epsilon_k \quad k=1,\ldots,n \qquad (5.22)$$

where the subscript 1 refers to the lamina. Additionally, the stress in the lamina is determined from

$$\sigma_l=\sum_{k=1}^{n}\sigma_k V_k \qquad (5.23)$$

where v_k is the volume fraction of the k^{th} strip.

The lamina properties can now be determined from the properties of the individual strips. Substituting Equations 5.17 and 5.18 into Equation 5.23 yields

$$E_1\epsilon_1-\alpha_1E_1\Delta T=(E_1\epsilon_1-\alpha_1E_1\Delta T)\,v_1+\ldots+(E_n\epsilon_n-\alpha_nE_n\Delta T)\,v_n \qquad \textbf{(5.24)}$$

Applying strain compatibility along the right face (Equation 5.22) and combining like terms, the transverse modulus and CTE of the lamina can be determined. The transverse modulus of the lamina is

$$E_{22_1}=E_{22_1}v_1+E_{22_2}v_2+\ldots+E_{22_n}v_n \qquad \textbf{(5.25)}$$

or

$$E_{22_1}=\sum_{k=1}^{n}E_{22_k}v_k \qquad \textbf{(5.26)}$$

while the transverse CTE of the lamina is

$$\alpha_{22_1}=\frac{\alpha_1E_1v_1+\ldots+\alpha_nE_nv_n}{E_{22_1}} \qquad \textbf{(5.27)}$$

or

$$\alpha_{22_1}=\frac{\sum_{k=1}^{n}\alpha_{22_k}E_{22_k}v_k}{E_{22_1}} \qquad \textbf{(5.28)}$$

A comparison of the these properties predicted by the SM with other models [12] is shown in Table 5.1. The method-of-cells, AGLPLY, and METCAN models were described in Chapter II, and the DFM is a three dimensional finite

Table 5.1 Predicted Transverse Properties

	E_{22} (GPa)	α_{22} (mm/mm/°C)
AGLPLY	130	8.46
Method of Cells	139	8.28
METCAN	134	7.76
DFM	148	8.28
SM	**132**	**7.51**

element solution [12]. The SM shows reasonable agreement with these other approaches, especially with METCAN which is also formulated on a one dimensional approach.

Transverse Strip and Lamina Stresses

Thermal Stresses

Once the properties of the strips and the lamina have been determined, the thermal stress in each strip can be computed. Applying strain compatibility for the strips acting in parallel (Equation 5.22), and representing the lamina strain in terms of its own properties yields

$$\frac{\sigma_{22_l}}{E_{22_l}} + \alpha_{22_l}\Delta T = \frac{\sigma_{22_k}}{E_{22_k}} + \alpha_{22_k}\Delta T \qquad \textbf{(5.29)}$$

Rearranging terms and setting the applied lamina stress to zero (i.e. thermal stress only), the thermal stress in a strip can be found from

$$\sigma_{22_k} = E_{22_k}\left[(\alpha_{22_l} - \alpha_{22_k})\Delta T\right] \qquad \textbf{(5.30)}$$

Figure 5.6 shows a comparison of the distribution of thermal stress predicted by the strip model to other existing models [12]. Again, the results of the present analysis are comparable to these models. One of the more

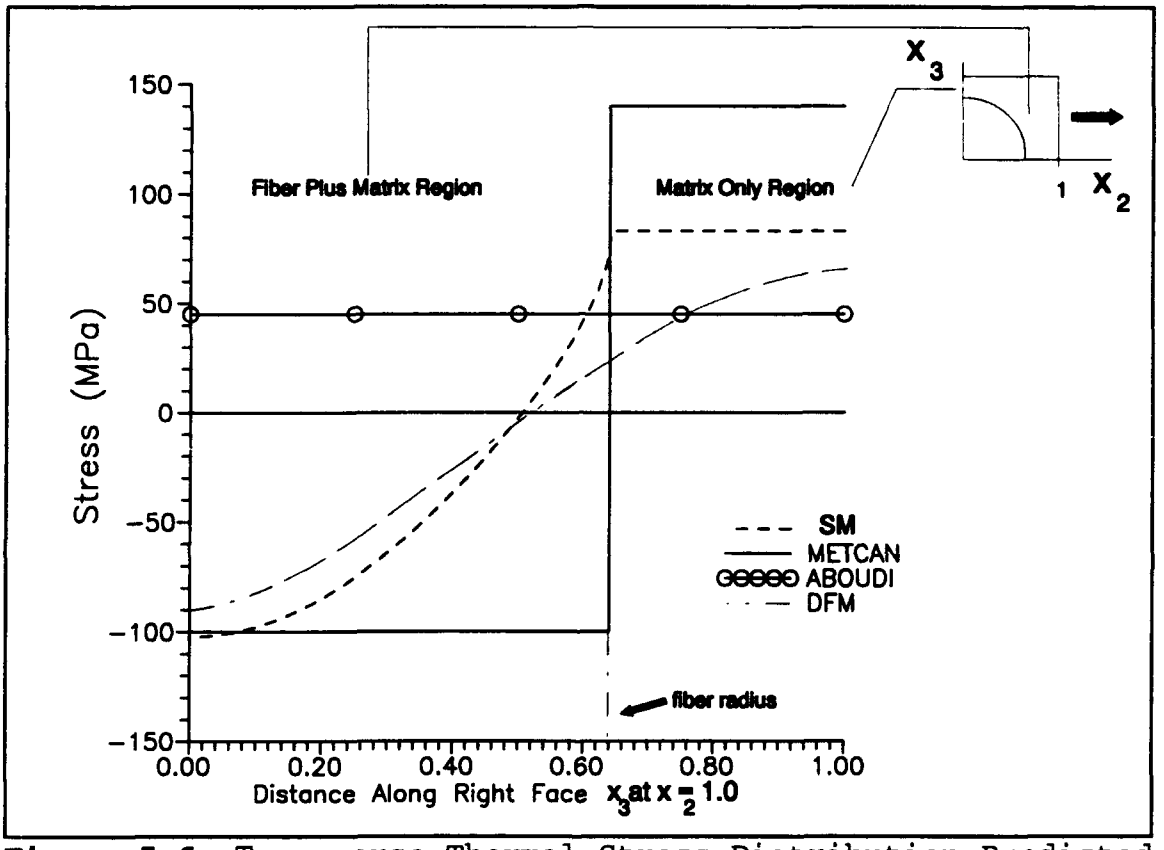

Figure 5.6 Transverse Thermal Stress Distribution Predicted by the SM and Other Micromechanical Models

notable aspects of this approach is illustrated here. The variation of stress across the lamina predicted by the SM has a similar representation as in the case of the finite element approach (DFM). On the other hand, METCAN, which is

based on the same one dimensional formulation, shows no such variation.

Mechanical Loads

After the initial thermal stresses were computed, the incremental stress in each strip was determined by the instantaneous stress-strain relationship

$$\Delta\sigma_{22_k} = E_{22_k}\Delta\epsilon \tag{5.31}$$

Equation 5.31 was than added to the total stress for each strip to obtain

$$\sigma_{22_{k_i}} = \sigma_{22_{k_{i-1}}} + \Delta\sigma_{22_{k_i}} \tag{5.32}$$

where i refers to the current increment. Finally, the lamina stress was determined using these stresses and applying Equation 5.23.

Modeling the Fiber-Matrix Interface Damage

In Chapter IV, it was shown that the fiber-matrix interface damage had a dominant affect on the response of the 90° lamina. Most of this damage initiated during the loading portion of the first fatigue cycle, but some damage did occur in fatigue. To accurately predict the fatigue response of the 90° lamina, this damage must be included in the analysis. The method proposed here assumes that the fiber-matrix interface damage can be modeled as a progressive damage mechanism (Figure 4.49). The details of this approach are discussed next.

Criteria for Failing the Fiber-Matrix Interface

Consider any strip whose normal to the actual fiber-matrix interface is at an angle θ (Figure 5.7). The normal stress at the fiber-matrix interface in this strip can be broken down into two components (Figure 5.8): the thermal stress component (σ_{th}), and the component due to an applied load (σ_n). The SM only computes a one dimensional thermal stress (σ_{22}), which is not always compressive (Figure 5.6). Since the residual stress of the n^{th} strip (i.e. $\theta = 0$) best represents the compressive stress on the interface (Figure 1.2), the residual stress of each strip was set equal to the residual stress of the n^{th} strip. This was only used to compute the failure criteria and was not used to determine the stress in a strip. The normal component of stress on at the interface for an applied stress (σ) [87] is given by

$$\sigma_n = \sigma \cos^2(\theta) \qquad (5.33)$$

where n designates the normal to the plane.

When the sum of these two components of stress exceeded the assigned bond strength, the fiber-matrix interface failed. As a consequence, a gap opens between the fiber and matrix. This gap can be interpreted as a spring with zero stiffness. Equation 5.20 requires that the modulus of the strip corresponding to the failed region be zero. Thus, a failed strip is incapable of carrying any further tensile load.

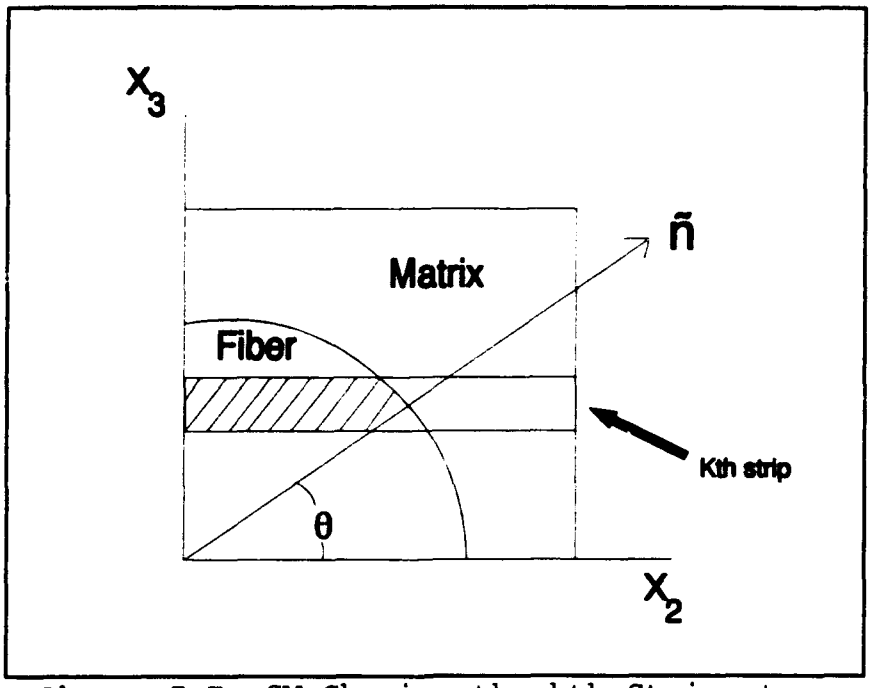

Figure 5.7 SM Showing the kth Strip at an Angle θ

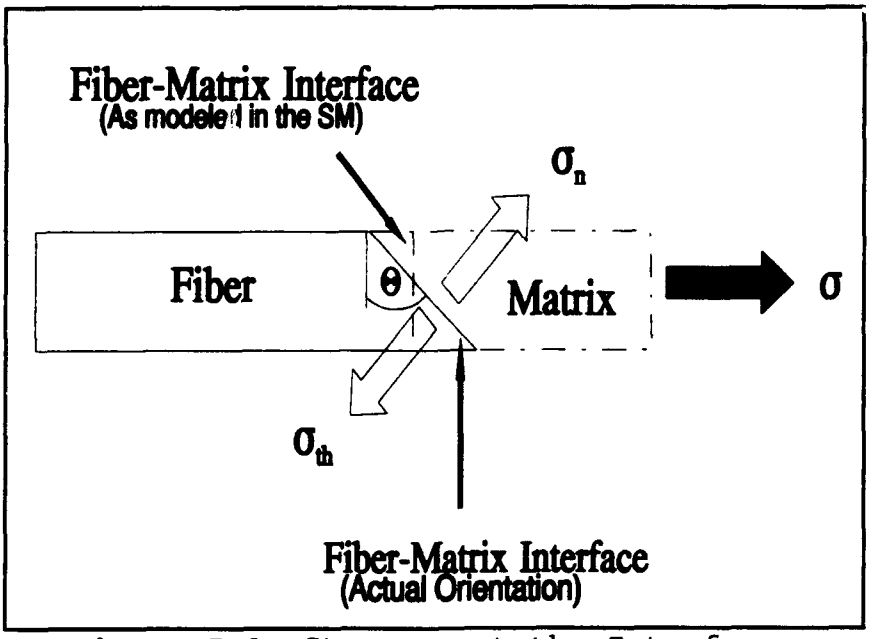

Figure 5.8 Stresses at the Interface

For a bond strength that was initially greater than zero, a non-zero stress was present in the strip before failure. It is proposed for the present analysis that the stress in the strip becomes zero after the interface has failed, and the load does not get redistribution. This technique produces a succession of drops in the lamina stress, but it will be shown later that the magnitude of these drops approach zero as the number of strips increases.

The procedures described above modeled the loading portion of a fatigue cycle, but the unloading portion of the cycle also requires special attention. For a strip that had failed during loading, it was incapable of carrying any further tensile load. However, it was capable of carrying a compressive load when the displacement of the gap between the fiber and the matrix returned to zero. This point was determined during the loading portion of the fatigue cycle. When σ_n of the strip was equal to the σ_{th}, the displacement of the matrix was measured. The gap between the fiber and matrix was considered to have closed when this displacement was reached during the unloading portion of the cycle. As a result, the modulus of the strip returned to its pre-failure value, and a compressive load was allowed to be transferred across the interface.

Once the fiber-matrix interface of strip had failed, the bond strength was set equal to zero on the subsequent

loading cycles. Thus, the interface separated again when σ_n of the strip was equal to the σ_{th}. This implies that, when the gap displacement is zero, there will always be a mechanical bond due to the compressive residual stresses at the fiber-matrix interface.

Determining the Fiber-Matrix Interface Bond Strength

A value of the fiber-matrix interface bond strength must be determined in order to predict the fatigue response of the 90° lamina. As a first step, two extreme conditions were examined: a strongly bonded interface, and a weakly bonded interface. The strongly bonded condition implies an infinite bond strength (i.e. no fiber-matrix interface damage), while the weakly bonded condition implies a zero bond strength.

Figure 5.9 shows the predicted results[8] for these two conditions compared to the experimental counterpart. For the perfectly bonded interface, the SM predicted a much stiffer stress-strain response than was observed in the experiment. The nonlinear behavior was due to plastic deformation of the matrix. The technique used for predicting this are discussed later. On the other hand, the SM predicted a stress-strain response that was too weak for the case of a zero bond strength. These results indicate

[8] 50 strips were used in the SM. The manner in which this number was chosen will be explained shortly.

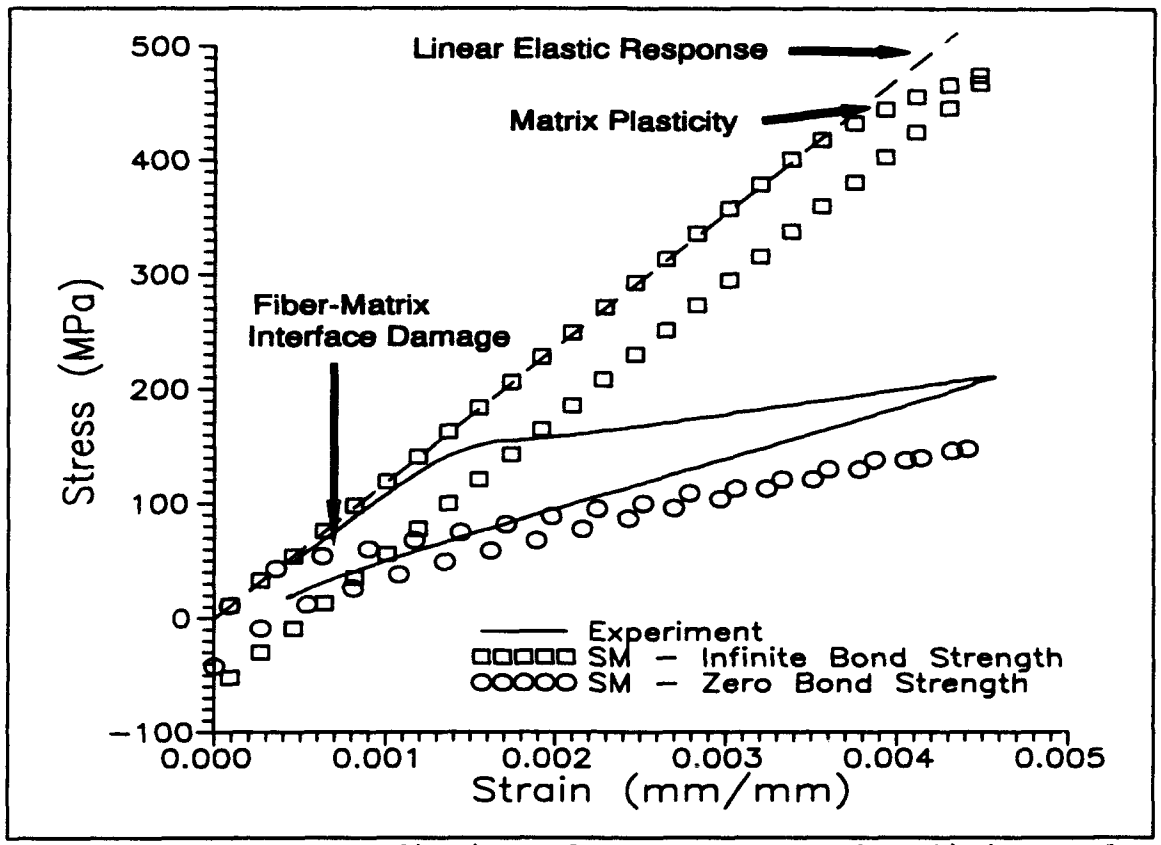

Figure 5.9 SM Predictions for the Cases of Infinite and Zero Bond Strengths Compared to the Experiment

that some finite bond strength is associated with the fiber-matrix interface.

The next step was to determine a bond strength so that the stress-strain response of the 90° lamina could be accurately predicted. It is proposed that this strength can be calibrated from one stress-strain curve, whether it be for a monotonic loading condition or the loading portion of the first stress-strain curve of specimen subjected to fatigue. The latter case was used for this analysis. Once

this is accomplished, the predicted stress-strain response should fall within acceptable limits to its experimental counterpart for any test with a lower strain level.

To determine the bond strength, an iteration was performed by assigning a single bond strength to all of the strips. When the total normal component of stress in the strip ($\sigma_n + \sigma_{th}$) was equal to bond strength, the fiber-matrix interface failed. Two typical, but significant, cases are shown in Figure 5.10 and compared to the experimental counterpart. These are for the cases of a bond strength equal to 100 MPa and 175 MPa. For the case where a bond strength of 100 MPa was used, the SM underestimated the experimental curve, but the knee in this curve is just slightly lower than that observed in the experiment. This was considered an approximate lower bound of the bond strength. In the other case (bond strength equal to 175 MPA), the predicted result was improved, except for the area around the knee in the loading curve. This suggests that 175 MPa is an upper bound of the bond strength.

The dip in this curve (bond strength equal to 175 MPa) is the result of a rapid failure of the strips with higher stiffnesses. These are those strips with the highest volume fraction, which are those strips located closest to the x_2 axis (Figure 5.4b). There are at least three methods to smooth out this initial dip. The first is to increase the

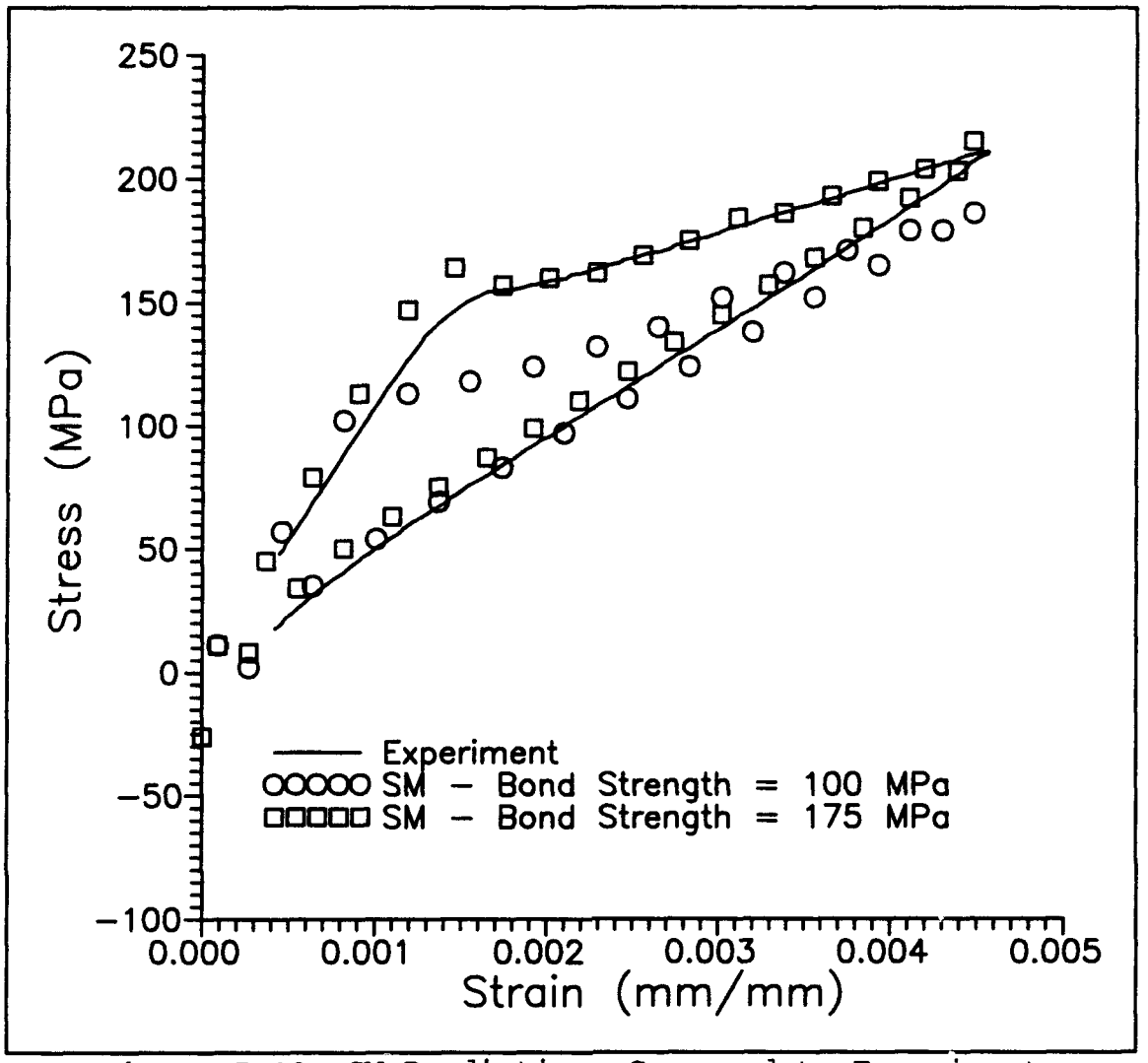

Figure 5.10 SM Predictions Compared to Experiment Using Finite Bond Strengths

number of strips in the area were the stiffnesses of the strips are high (i.e. refine the mesh). Another method would be to include a scheme to gradually reduce the stress in a broken strip to zero, as opposed to an instantaneous drop as is presently done. Finally, the bond strengths of

the strips in this area could be reduced. For this study, the last approach was selected.

Figure 5.11 shows the bond strength in all of the strips for the cases (100 MPa and 175 MPa) discussed above. The bond strength distribution that best fit the experiment

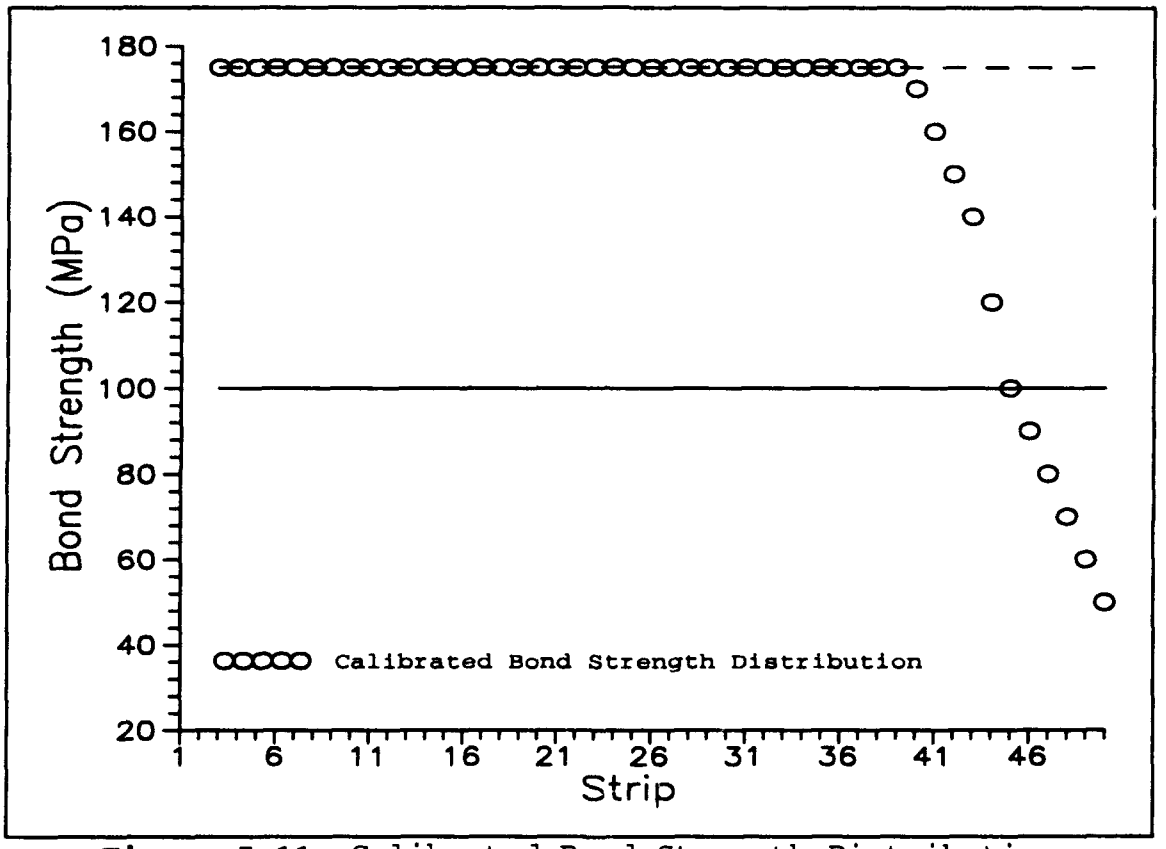

Figure 5.11 Calibrated Bond Strength Distribution

is also shown. This distribution was determined by examining the predicted stress-strain response shown in Figure 5.10. It was observed that the initial knee in the loading curve could be better predicted by failing some of

the strips at a lower level of stress. To be consistent with the assumption of a progressive damage mechanism, the bond strength of the strips starting along the x_2 axis were lowered (Figure 5.4b).

Figure 5.12 compares the predicted stress-strain response using the adjusted or final bond strength distribution to the experimental stress-strain curve. As expected, the predicted loading curve was in good agreementwith its experimental counterpart. The unloading curve was also predicted properly, as well as the fiber-matrix interface gap closure. This shows that the interfacial damage between the fiber and the matrix was well characterized. Hence, a required bond strength distribution was obtained to predict the effect of fiber-matrix interface damage on the response of the 90° lamina. This same distribution is used in the next chapter to predict the response of the 90° lamina subjected to fatigue.

Progressive Fiber-Matrix Interface Damage

In the previous chapter, it was mentioned that the fiber-matrix interface damage progressed during fatigue. The methods described above characterized the initiation of the interface damage. It was also desired to characterize the progression of the fiber-matrix interface damage. This was accomplished by imposing an additional criteria on the bond strength of the strips. For each strip, its bond

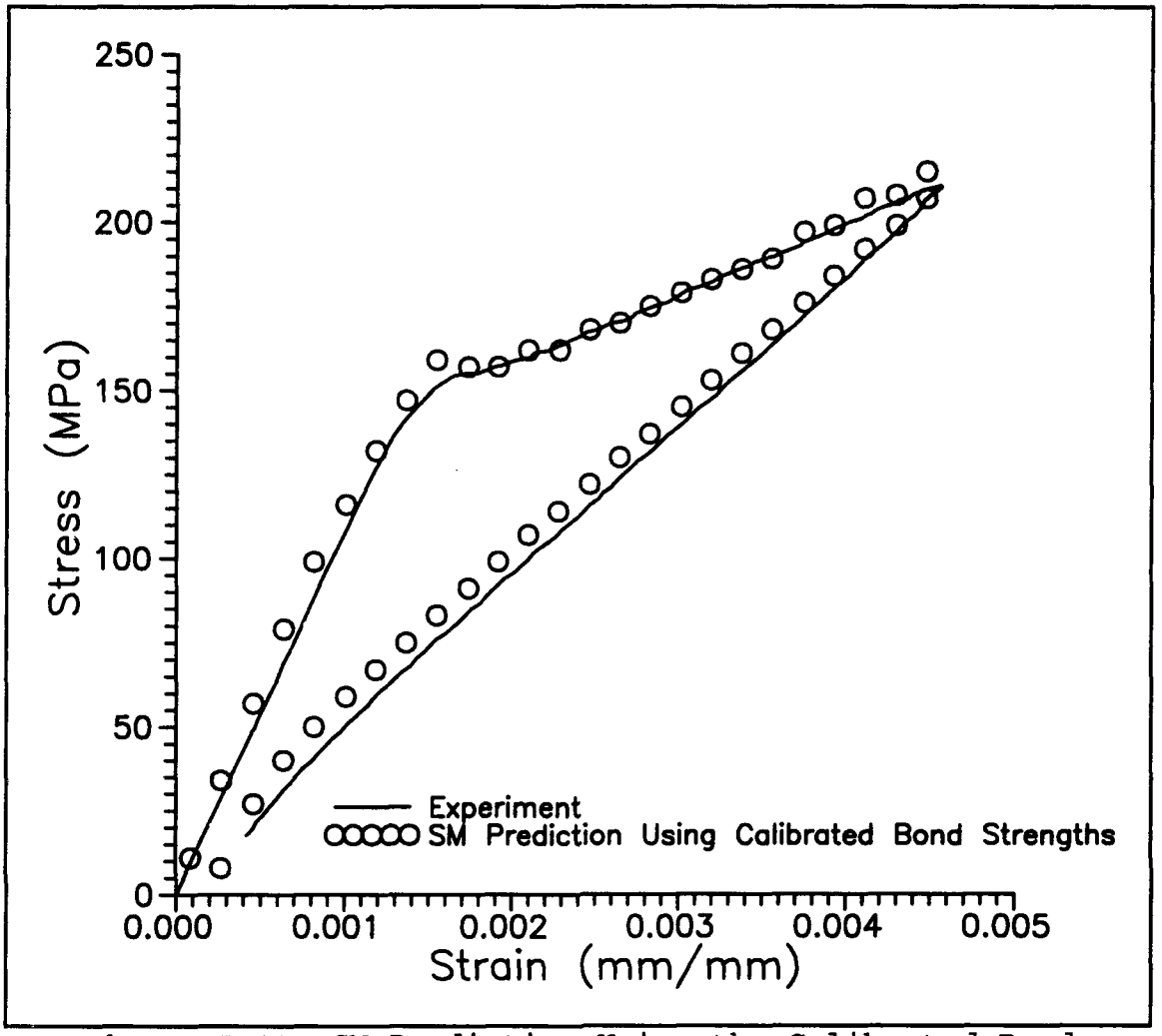

Figure 5.12 SM Prediction Using the Calibrated Bond Strength Distribution

strength was assumed to degrade as a function of cycles:

$$\sigma_{k_{bondstr}}(n) = \sigma_{k_{bondstr}}(0)\, f(n) \qquad \textbf{(5.34)}$$

where k refers to the strip. The function f(n) was defined by

$$f(n) = \begin{cases} 1 & for\ n=0 \\ 0 & for\ n \geq n' \end{cases} \qquad \textbf{(5.35)}$$

where n' specifies the cycle at which the bond strength in the strip becomes totally weak. For this analysis, f(n) was chosen as a linearly decreasing function:

$$f(n) = \frac{-n}{n'} + 1 \qquad \textbf{(5.36)}$$

where n is the total number of fatigue cycles.

To determine a value of n', it is proposed that the history of the stress from one fatigue test be correctly predicted using Equation 5.36. Then, using this same f(n), the effect of the progression of fiber-matrix interface damage at other strain levels could be better understood. The one test chosen to determine f(n) was for the 90° specimen subjected to fatigue at maximum strain level of .1%. This test was selected since the only damage observed was that at the fiber-matrix interface (Figure 4.56). These results obtained by applying Equation 5.36 are discussed in the next the chapter.

Selection of the Number of Strips

As previously mentioned, after the stress in the strip had exceeded the bond strength, the stress in that strip became zero. No redistribution of this stress was performed, which resulted in a series of drops in the

stress-strain curve. It is shown next that these stress drops approach zero as the number of strips increases.

Figures 5.13 through 5.15 show three stress-stress curves predicted by the SM using 10, 20, and 100 strips, respectively. A single bond strength of 175 MPa was used for these predictions. The prediction when using 50 strips and a bond strength of 175 MPa was shown earlier (Figure 5.10). It can be observed that as the number of strips increases, the dips in the stress-strain response approach zero, and the overall prediction improves. The best predictions occur when using 50 and 100 strips, but it did not significantly improve between these two cases. Therefore, 50 strips was considered appropriate for this study.

Matrix Viscoplastic Deformation

Experimental results revealed that the matrix exhibited both plastic and creep deformation type mechanisms. To predict this behavior, a few unified elastic-viscoplastic constitutive models were investigated [1] [14] [94]. However, these unified models were unable to handle the creep behavior of the matrix at the lower stress levels [94], or the data required to calibrate them was unavailable. Other techniques [27] to model the time dependent behavior of the matrix were also investigated, but they proved to be impractical to apply. As a result, the

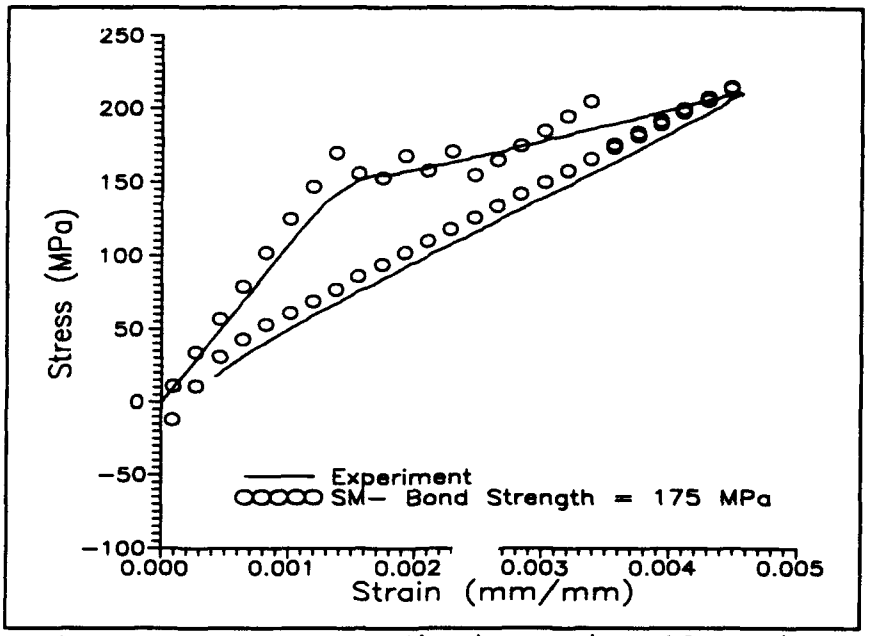

Figure 5.13 SM Prediction using 10 Strips

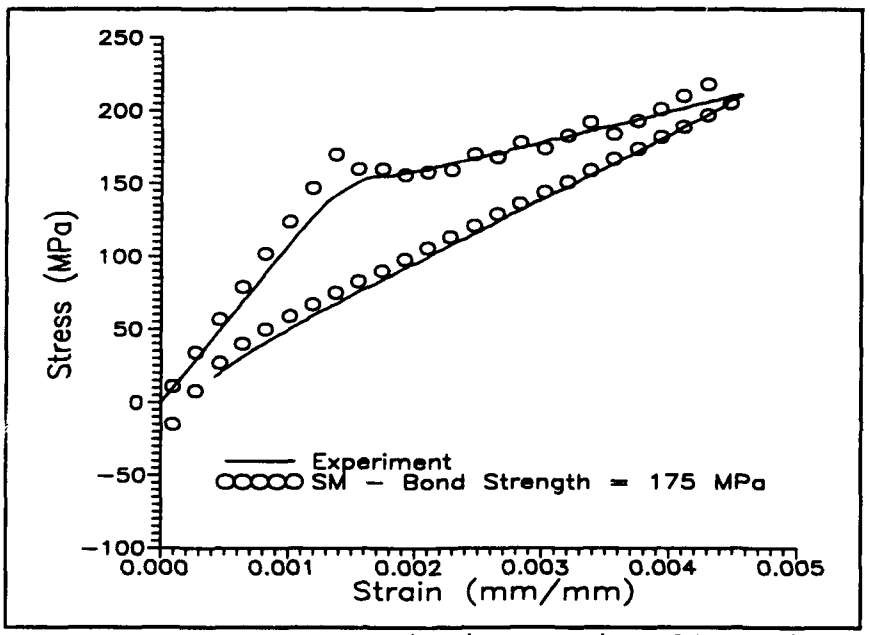

Figure 5.14 SM Predictions using 20 Strips

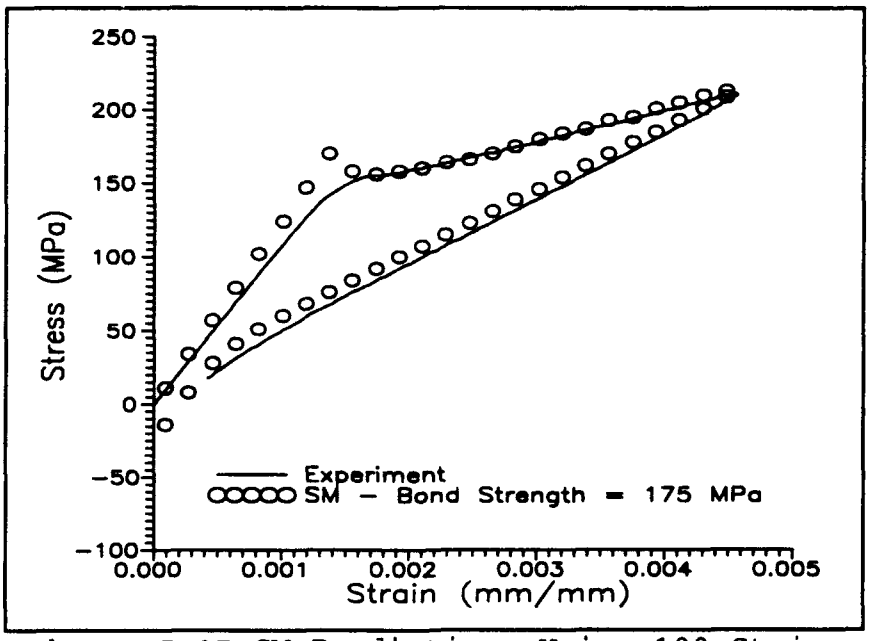

Figure 5.15 SM Predictions Using 100 Strips

two deformation mechanisms were decoupled and solved for separately. The plastic deformation was modeled by assuming the matrix behavior as bilinear elastic-plastic and applying the appropriate criteria to determine the onset of plastic flow. Creep deformation of the matrix was modeled by applying a simple relaxation scheme. This scheme was developed based on the data obtained from the relaxation tests conducted on the neat matrix (Figure 4.7).

Matrix Plastic Deformation

Concentric Cylinder Model

In the CCM, plastic deformation of the matrix was approximated by using an incremental solution approach. The onset of plastic flow was determined by using Von Mises isotropic linear strain hardening rule [74]:

$$\bar{\sigma} = \sqrt{\frac{1}{2}\left((\sigma_r - \sigma_\theta)^2 + (\sigma_\theta - \sigma_z)^2 + (\sigma_z - \sigma_r)^2\right)} = k(\kappa) \qquad (5.37)$$

where k is a material constant, and $\bar{\sigma}$ is the effective stress. For this analysis, k was taken as the uniaxial yield stress (σ_{ys}) of the neat matrix.

Equation 5.37 was computed for each increment of strain in the loading curve. Plastic deformation of the matrix was considered to have occurred when the effective stress exceeded the yield stress. At this point, the tangential modulus (E_T) and the value of Poisson's Ratio in plasticity (.5) of the matrix were used for further incremental calculations of stress in the loading curve[9], (i.e. bilinear elastic-plastic). For this study, the values of σ_{ys} and E_T were 515 MPa and 7.00 GPa, respectively [35].

The method used in this study to solve for the incremental stresses requires that the entire matrix cylinder was either linearly elastic or plastic. Thus, a representative location in the CCM must be selected to evaluate the effective stress (Equation 5.37). The maximum effective stress occurs at the fiber-matrix interface, which suggests that this will be the initiation site of plastic flow. Optical microscopy revealed that, on the average, the entire grain was observed to have slipped (Figure 4.27).

[9] Actually, an iteration at this point would provide for a more accurate calculation of stress. However, for sufficiently small strain increments, this error is small. This study employed the latter approach.

Thus, experiments have indicated that yielding (i.e. slip bands) had extended beyond the fiber-matrix interface.

A comparison was made between calculating the onset of plastic flow at the fiber-matrix interface and at a location halfway between the interface and the matrix free edge. These predictions were compared to the experimental counterpart for a specimen subjected to fatigue at a maximum strain of .77% (Figure 5.16). Evaluating the effective stress at the midpoint of the matrix cylinder provided a better comparison with the experiment, so this location will be used for further analysis in this study.

The present CCM model was compared to another program FIDEP [23]. It is not the purpose here to discuss the efficacy of each solution. Instead, it was intended to verify the solution obtained from the present CCM analysis. FIDEP designates a CCM model based on a FInite Difference Elastic Plastic solution. In addition to radially dependent radial and hoop stresses, FIDEP computes a varying axial stress across the matrix cylinder. The formulation of FIDEP does not require the matrix to yield at all of the radial locations, as opposed to the current application of the CCM where the entire matrix cylinder yields. Figures 5.17 through 5.20 show the comparisons of the solutions from the present CCM and FIDEP for a 0° SCS-6/Ti-15-3 specimen loaded to a maximum strain of .77% at 427°C. The constituent

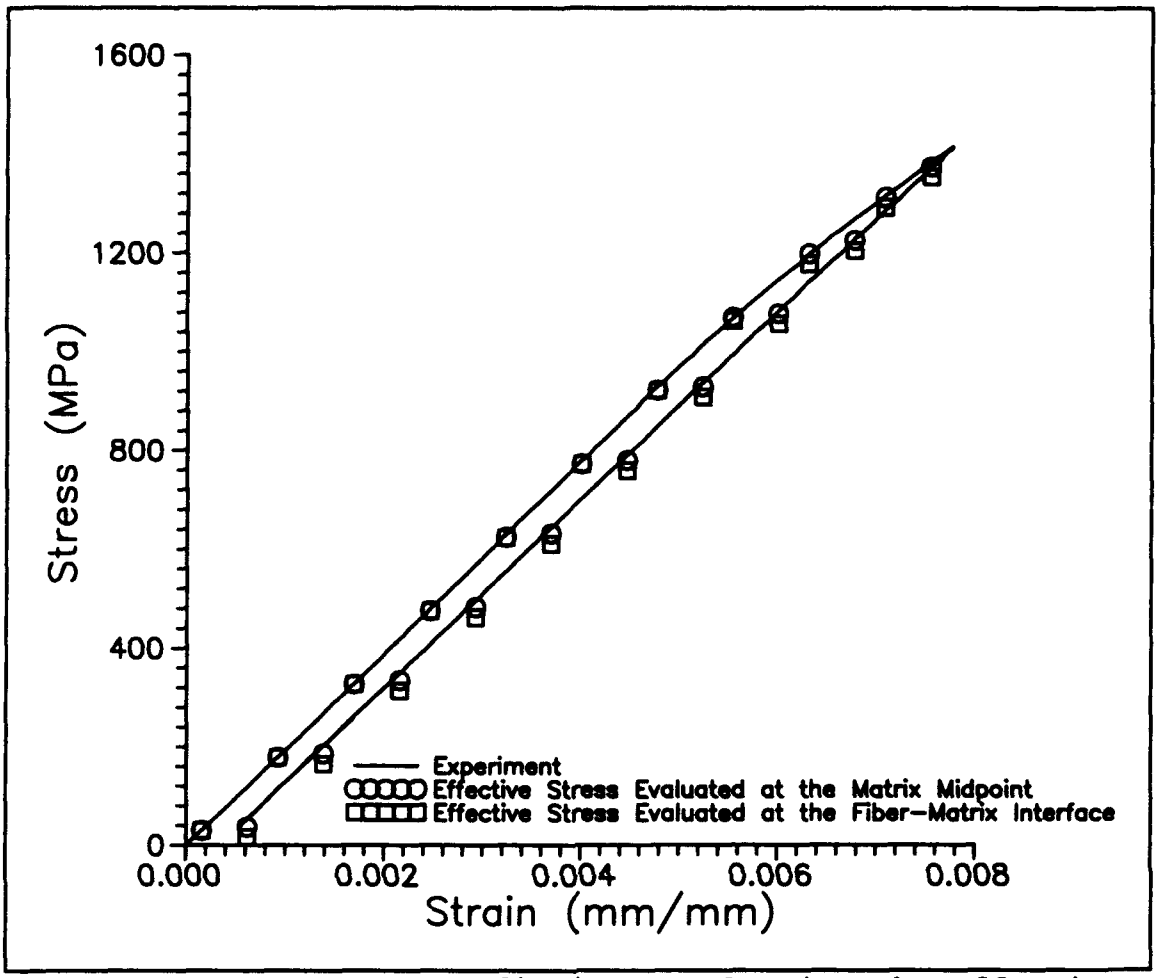

Figure 5.16 CCM σ-ϵ Predictions Evaluating the Effective Stress at Two Different Locations in the Matrix Cylinder

stresses (Figures 5.18-5.20) are plotted at the maximum strain (.77%). Both solutions agree very well with each other. Hence, with the parameters used in this study, the CCM should provide an accurate representation of the fatigue response of the MMC.

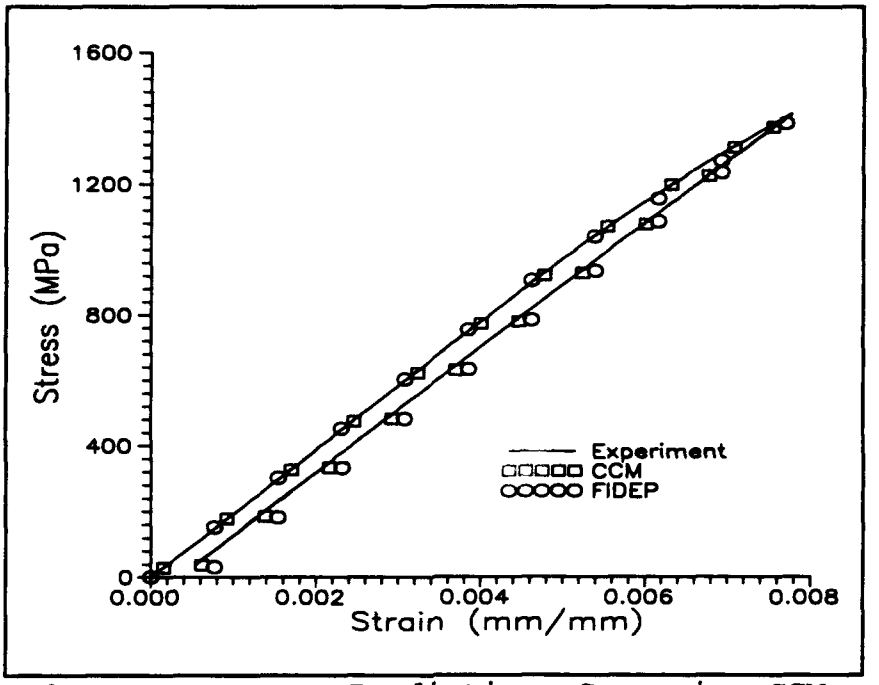

Figure 5.17 σ-ϵ Predictions Comparing CCM, FIDEP, and Experiment

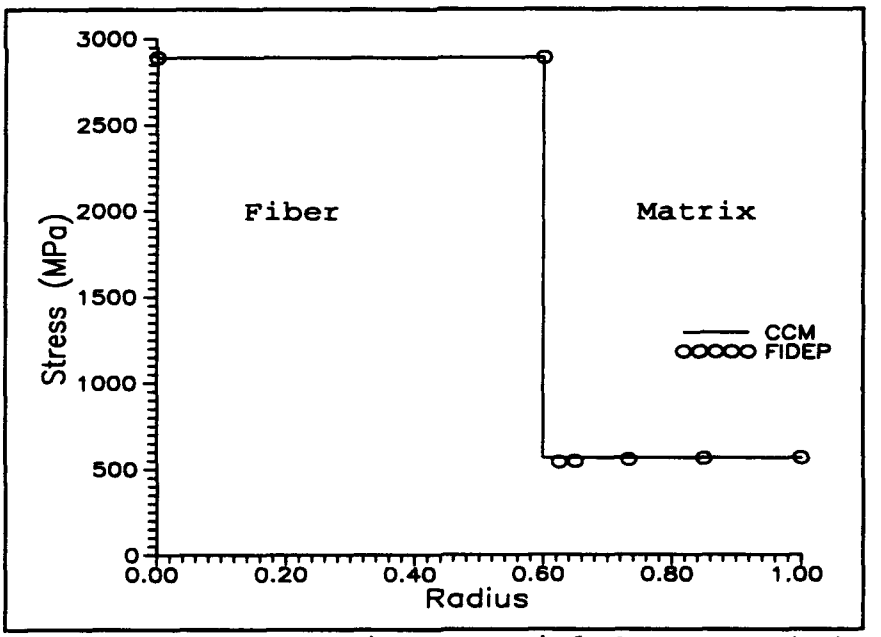

Figure 5.18 Constituent Axial Stresses (σ_z) Predicted by CCM and FIDEP

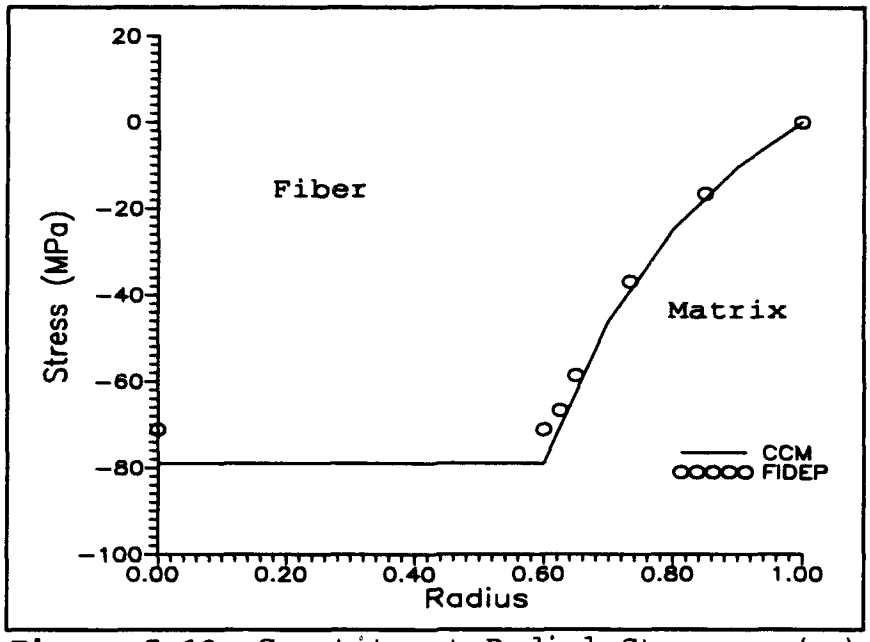

Figure 5.19 Constituent Radial Stresses (σ_r) Predicted by CCM and FIDEP

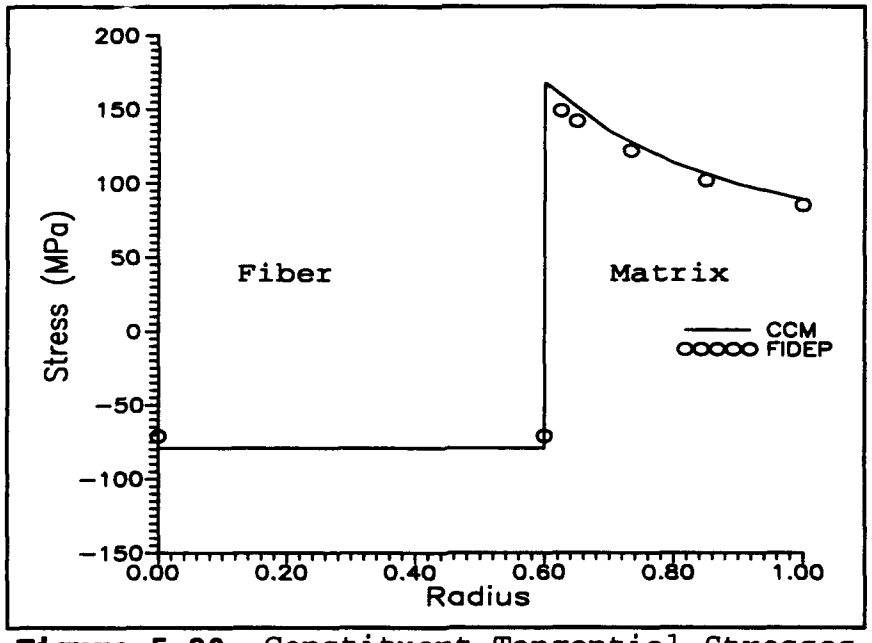

Figure 5.20 Constituent Tangential Stresses (σ_θ) Predicted by CCM and FIDEP

Strip Model

Similar to the analysis used in the CCM, an incremental solution was used in the SM. The procedures for calculating the stresses in the strips and lamina were reviewed previously. To predict the onset of plastic flow, the stress in each strip was compared to the matrix uniaxial yield stress:

$$\sigma_k > \sigma_{ys_k} \qquad (5.38)$$

where the subscript k designates the kth strip. When the condition in Equation 5.38 was satisfied, the modulus of the matrix was set equal to E_t, and a new value for the transverse modulus of the strip was computed (Equation 5.20). This technique implies that the entire matrix portion of the strip has plastically deformed.

Matrix Creep Deformation (Relaxation Scheme)

The above procedures described how the matrix plasticity was accounted for in each of the micromechanical models used in this study. It was previously mentioned that creep deformation of the matrix also needed to be taken into account. In this study, a relaxation scheme was developed to take into account the time dependent response of the matrix. The general approach taken to develop this scheme was to first determine a single function to express the change in stress with respect to time, and then apply this function at each strain increment in a fatigue cycle to

determine the incremental matrix stress due to relaxation. The details of the development and application of this function are described next.

General Relaxation Function

First a general function to express the change in stress in the neat matrix with respect to time ($\dot{\sigma}$) was determined. This was found simply by fitting the data from the relaxation tests at each strain level (Figure 4.7) with second order polynomials:

$$\sigma(t) = a + bt + ct^2 \qquad \textbf{(5.39)}$$

where t is the total time, and a, b, and c are constants. Next, the derivative of Equation 5.39 was taken with respect to time for each of the polynomial fits:

$$\dot{\sigma}(t) = b + 2ct \qquad \textbf{(5.40)}$$

The coefficients (b and c) found from the second order polynomial fits are shown in Table 5.2. General expressions

Table 5.2 Coefficients from Polynomial Fits

Strain (%)	-b	c
.6%	4.3	.01
.5%	2.5	.0032
.3%	1.4	.0019

for each of these coefficients were found next, which were determined by plotting the coefficients as a function of the

applied strain (Figures 5.21 and 5.22, respectively). These data were then fitted with power law relationships, which were found to be:

$$b(\epsilon) = -8460\,\epsilon^{1.5}$$
$$c(\epsilon) = 330\epsilon^{2} \qquad \textbf{(5.41)}$$

Substituting these expressions into Equation 5.40 yields

$$\dot{\sigma}(t,\epsilon) = -8460\epsilon^{1.5} + 330\epsilon^{2}t \qquad \textbf{(5.42)}$$

In this manner, a single expression to express the rate of change in stress in the neat matrix with respect to time was empirically determined.

A comparison of the experimental results obtained in this study to those obtained by applying Equation 5.42 is shown in Figure 5.23. The good fit was not surprising since the function was determined based on these data. It was shown simply to verify the empirical relationship given in Equation 5.42. A scheme to apply this function for predicting the fatigue response of the matrix is formulated next.

Application to Fatigue Behavior

A method was developed to predict the fatigue response of the matrix based on Equation 5.42. This relaxation scheme was motivated by an approach suggested by Rabotnov [74]. Rabotnov proposed a method to predict the creep response for a metal under changing load conditions, which is shown schematically in Figure 5.24. A simple strain

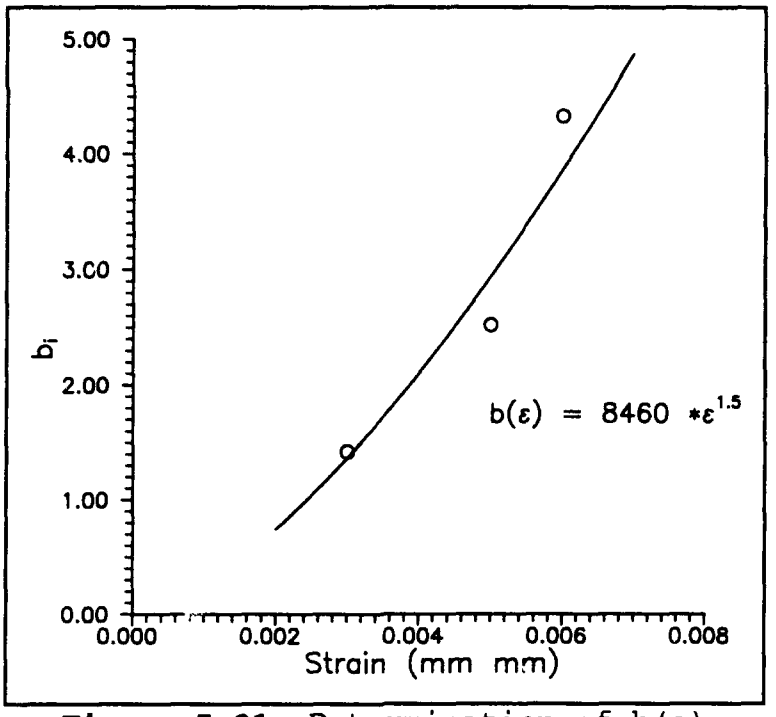

Figure 5.21 Determination of b(ϵ)

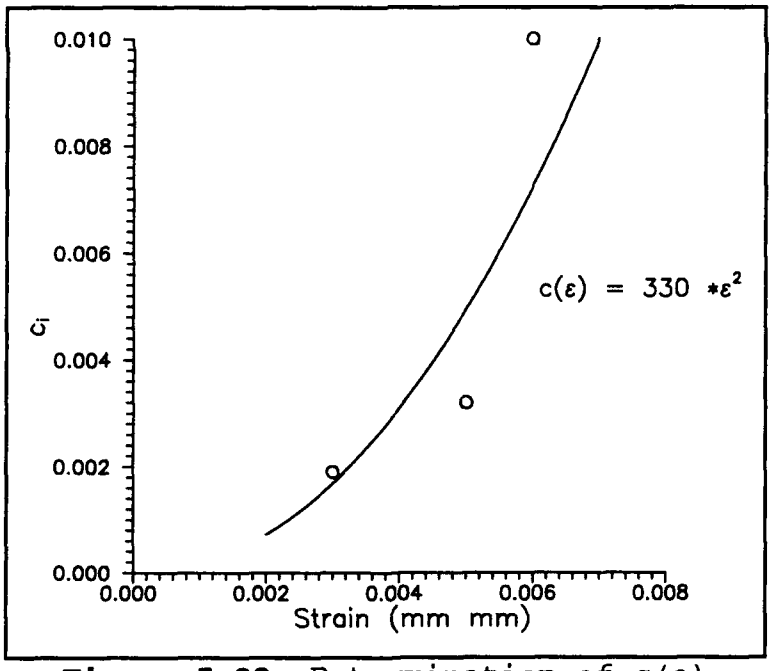

Figure 5.22 Determination of c(ϵ)

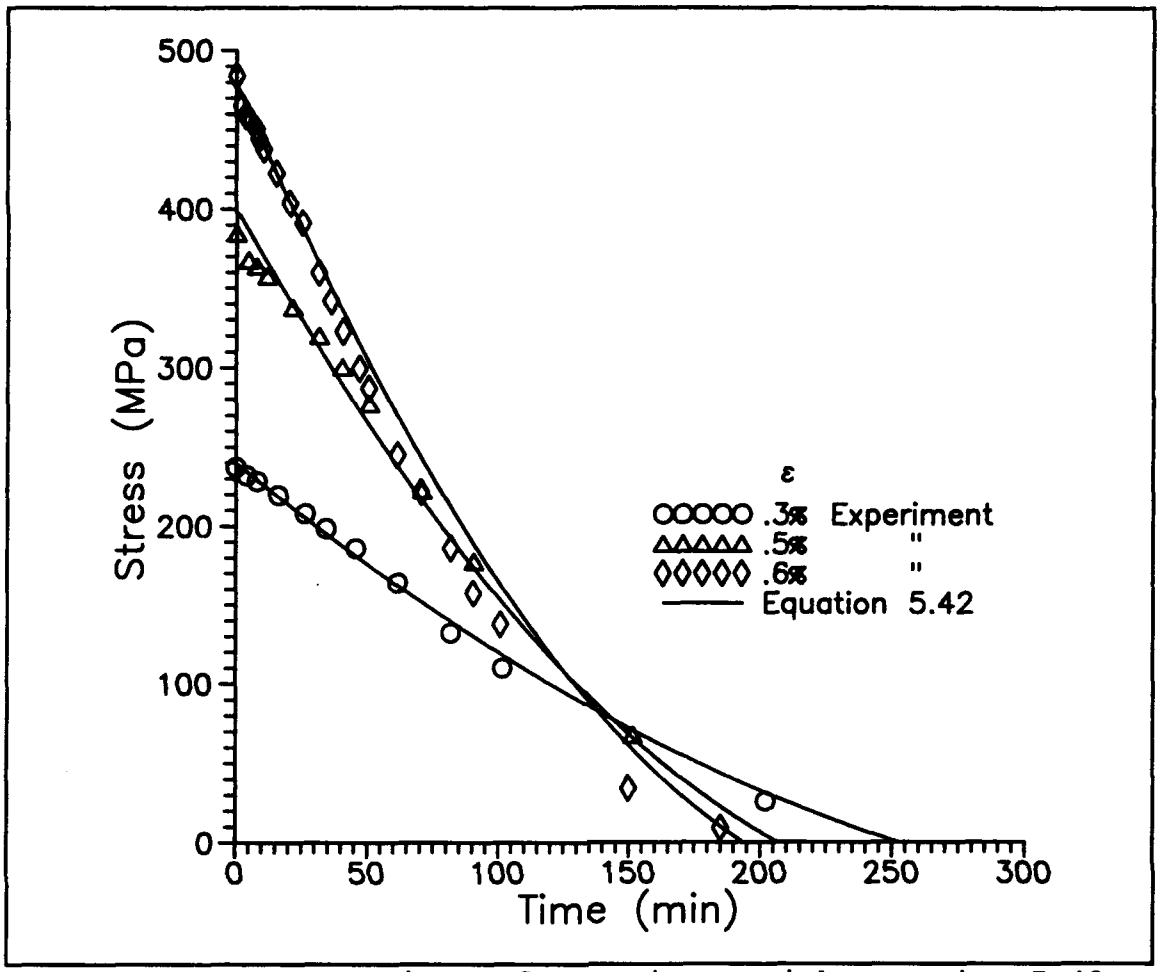

Figure 5.23 Comparison of Experiment with Equation 5.42, Neat Matrix Relaxation Tests at 427°C

hardening rule would predict that the strain rate would increase from O to A as the load is increased from σ_1 to σ_2. Mendelson [74] has reported that this approach works fairly well. However, Rabotnov suggested that for a rapid increase in the load, the strain rate changes from O to D, so some higher strain rate is achieved than a strain

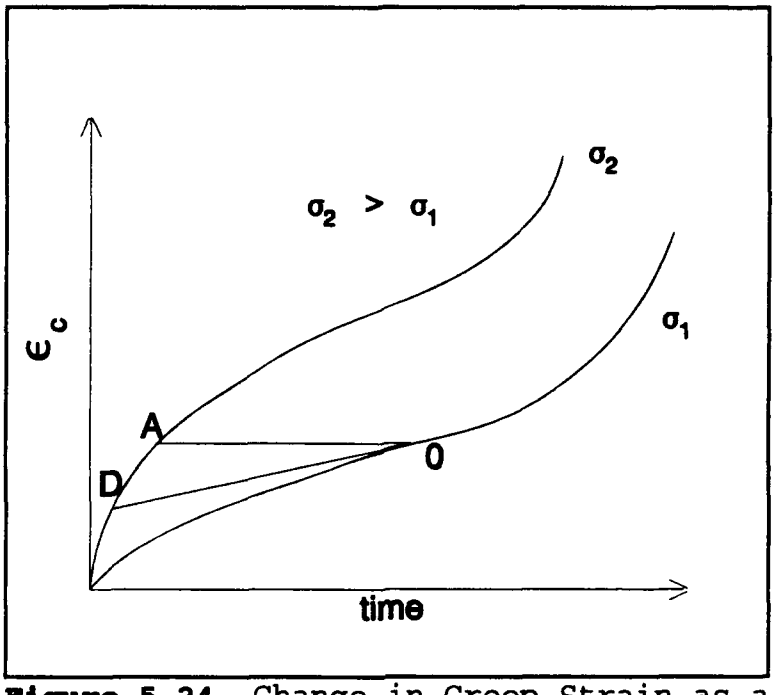

Figure 5.24 Change in Creep Strain as a Function of Changing Stress

hardening rule would predict. A similar concept was used in this investigation and is explained next.

Figure 5.25 shows the typical ramp function used in this study to subject a specimen to fatigue. For simplicity, each portion of the fatigue cycle (loading and unloading) was approximated by two step functions. For an initial step strain ($\Delta\epsilon = \epsilon_1$), the stress relaxation of the matrix predicted by Equation 5.42 would follow the curve corresponding to $\epsilon = \epsilon_1$ shown in Figure 5.26. For the next increment of strain, the incremental elastic stress would increase the total stress from A to B. This point (B) is above the relaxation curve for a total applied strain of

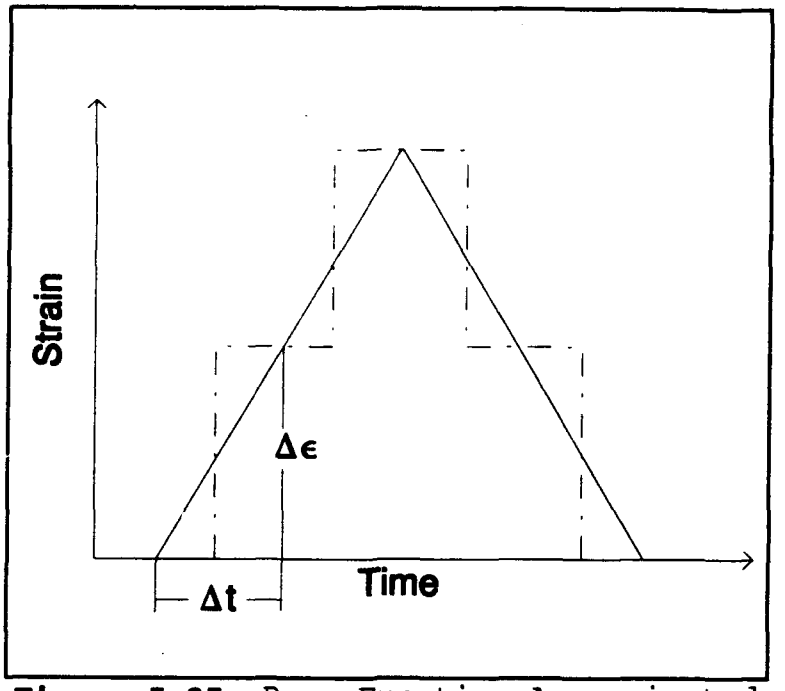

Figure 5.25 Ramp Function Approximated by Step Functions

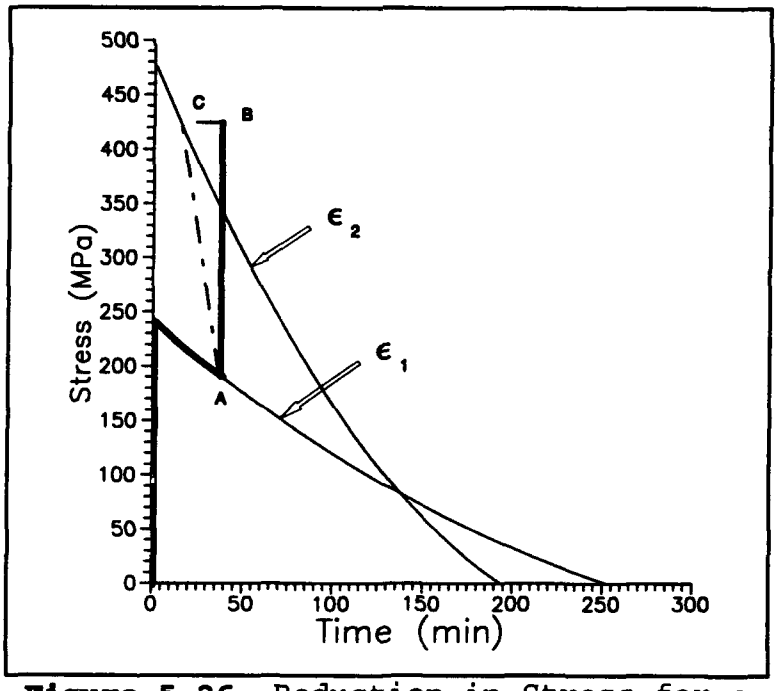

Figure 5.26 Reduction in Stress for a Changing Applied Strain

ϵ_2 (ϵ_1 + $\Delta\epsilon$). Instead of determining $\dot{\sigma}$ at B, it was determined at a point C on the relaxation curve by solving

$$\sigma(t) = E\epsilon + b(\epsilon)\, t + c(\epsilon)\, t^2 \qquad (5.43)$$

for t, where σ(t) is the current value of total stress, ϵ is the total applied strain, and b(ϵ) and c(ϵ) were defined earlier. $\dot{\sigma}$ can then be determined using this value of time in Equation 5.42.

An example of how the relaxation scheme was applied to predict the fatigue response of the neat matrix is given here. The same general approach applies to both of the micromechanical models used in this study. First, the incremental stress of the matrix was added to the existing total stress:

$$\sigma_i = \sigma_{i-1} + E\,\Delta\epsilon \qquad (5.44)$$

where E is the instantaneous modulus of the matrix, $\Delta\epsilon$ is the incremental strain, and i is the current step. Second, the relaxation scheme was applied to predict the incremental change in stress due to matrix relaxation:

$$\Delta\sigma_{R_i} = \dot{\sigma}_i\, \Delta t \qquad (5.45)$$

The creep response of the matrix was assumed to be the same in either tension or compression. Thus, when the matrix was in tension, the relaxation stress was negative, and when the matrix was in compression, the relaxation stress was positive. Third, this incremental change in stress was then

added to the total stress

$$\sigma_i = \sigma_i \pm \Delta\sigma_{R_i} \qquad (5.46)$$

Figure 5.27 shows the results of applying the relaxation scheme using the material properties of the neat matrix. These results are for a specimen subjected to fatigue at a maximum strain of .5% under the constant amplitude strain control mode. The effect of increasing the number of strain increments on the history of the stress is also demonstrated. These results show that the solution converges after applying 10 increments of strain on each portion, (loading and unloading) of the fatigue cycle. As expected, a smoother curve is predicted by applying more steps. When using the SM, more than 10 increments were required to accurately predict the fiber-matrix interface debonding. Based on these two observations, fifty increments of strain were used in each portion of the fatigue cycle in both the SM and the CCM.

Computational Algorithms

Now that all the tools for the analysis have been described, an algorithm for applying the models is discussed. A flowchart describing the computational algorithm for each micromechanical model can be found in Appendix D. Only a few salient points are given here. A few investigations [34, 63] have assumed that no plastic deformation of the matrix occurs during cool down from the

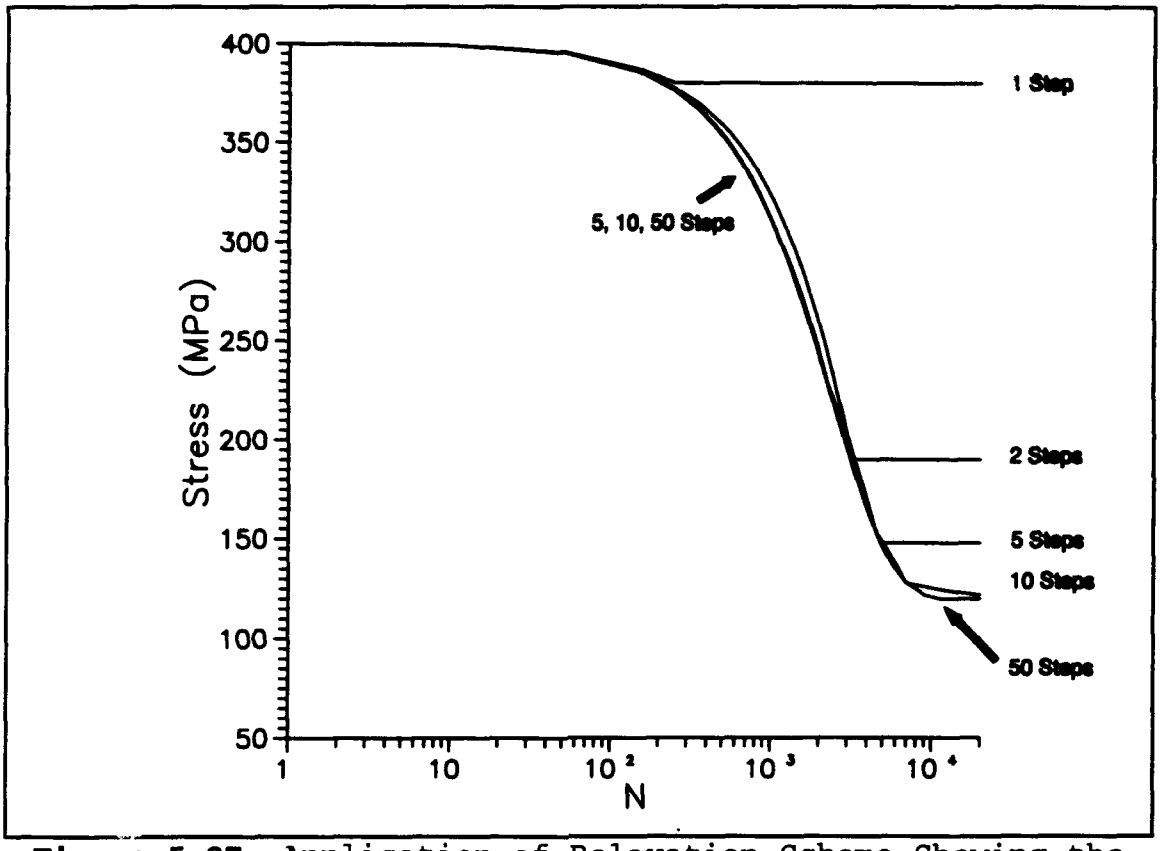

Figure 5.27 Application of Relaxation Scheme Showing the Convergence with Increasing Number of Steps

processing temperature. Further, the material was considered to be stress free (i.e. no residual thermal stresses) at the end of the 24 hour, 700°C, aging process [63]. The temperature was then instantaneously dropped to from 700°C to 427°C. This provided the initial state of stress in the lamina. At this point, the calculation of the stress in the lamina due to fatigue was begun. For each strain increment, the incremental stress was calculated. The procedures for computing these incremental stresses have

been previously described for each model. These incremental stresses were then added to the total existing stress. The relaxation scheme was then applied to the total matrix stress in the CCM or the total stress in the strip for the SM. Upon unloading, the minimum strain was increased if the lamina stress was less than zero. This was similar to the procedure used in the experiments.

Model Development Summary

The details of two micromechanical models were explained in this chapter. The first model discussed was the concentric cylinder model (CCM), which will be used in the next chapter to predict the fatigue response of the 0° lamina. The second model presented was the strip model (SM). It will be used in the next chapter to predict the fatigue response of the 90° lamina. This model included some unique methods to model the initiation and progression of fiber matrix interface damage.

A scheme to predict the elastic-viscoplastic response of the matrix was also discussed. This scheme was based on the data available from a few relaxation tests conducted on the neat matrix. In the next chapter, this scheme is used in both the CCM and the SM to predict the fatigue response of the MMC.

VI. Analysis - Results and Discussion

In the previous chapter, the details of two micromechanical models were discussed, which were the concentric cylinder model (CCM) and the strip model (SM). These models are applied in this chapter to predict the fatigue response of the 0° and 90° laminas, respectively. Also, a verification of the relaxation scheme is shown. These models provided: a support for the conclusions drawn from experimental observations, a valuable insight into the fatigue behavior of the constituents, and in insight into the observed damage mechanisms.

Neat Matrix Analysis

In Chapter IV, it was shown that the fatigue behavior of the neat matrix was not affected by matrix cracking or ply delamination. Thus, the data obtained from these fatigue tests provided an excellent verification of the relaxation scheme.

Stress-Strain Response

Figure 6.1 compares a few predicted stress-strain curves with the experimental data for a neat matrix specimen loaded in fatigue at a maximum strain of .7%. In this case, the peak stress on the first fatigue cycle was above the matrix proportional limit. This can be observed by noting

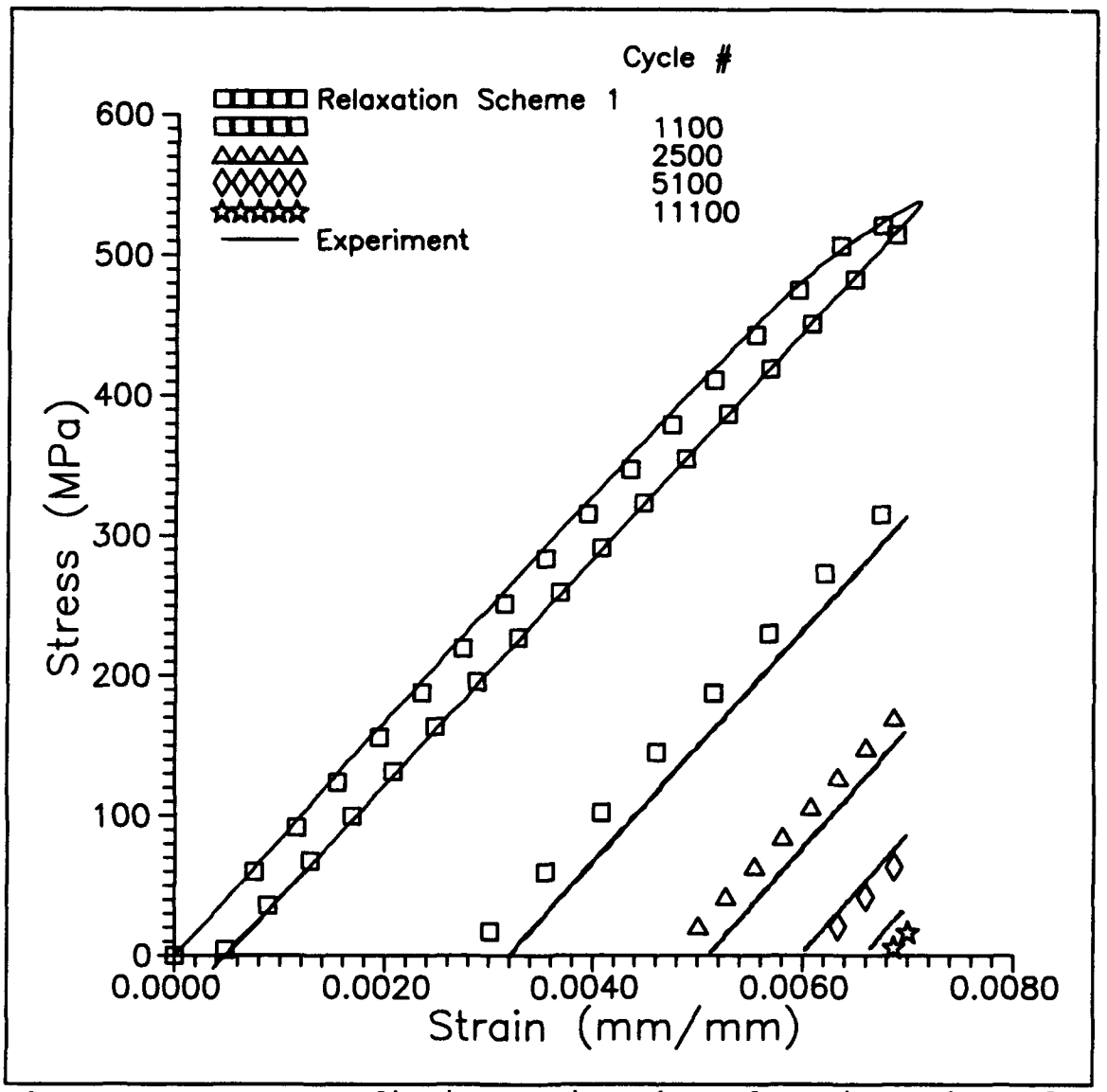

Figure 6.1 σ-ϵ Predictions Using the Relaxation Scheme for the Ti-15-3 Neat Matrix, ϵ_{max} = .7%

the nonlinear stress-strain response. This response was a result of plastic deformation of the matrix, which was verified by noting that the linear loading and unloading modulii were equivalent in the experiment. The same

nonlinear response was predicted when considering only the plastic deformation. Some stress relaxation did occur on the first cycle but was less than 1 MPa. Hence, matrix plasticity was the dominant deformation mechanism. The subsequent stress-strain curves were also predicted well by the relaxation scheme. These results show that the matrix instantaneous plasticity and the matrix creep deformation mechanisms can be decoupled to predict the fatigue response of the neat matrix.

Stress Histories

Figure 6.2 shows the predicted histories of the maximum stress versus the corresponding experimental data for several neat matrix specimens subjected to fatigue. All of the curves are in good agreement with the experiment. This verifies that the fatigue behavior of the neat matrix was dominated by creep deformation. These results also show that the fatigue behavior of the neat matrix can be characterized on the availability of data from only a few relaxation tests and a static test.

Constant Strain vs. Decreasing Strain Amplitude - An Analytical Comparison

The state of stress of the fiber-reinforced matrix is quite different than that of the neat matrix. For example, it will be shown later that the matrix stress actually

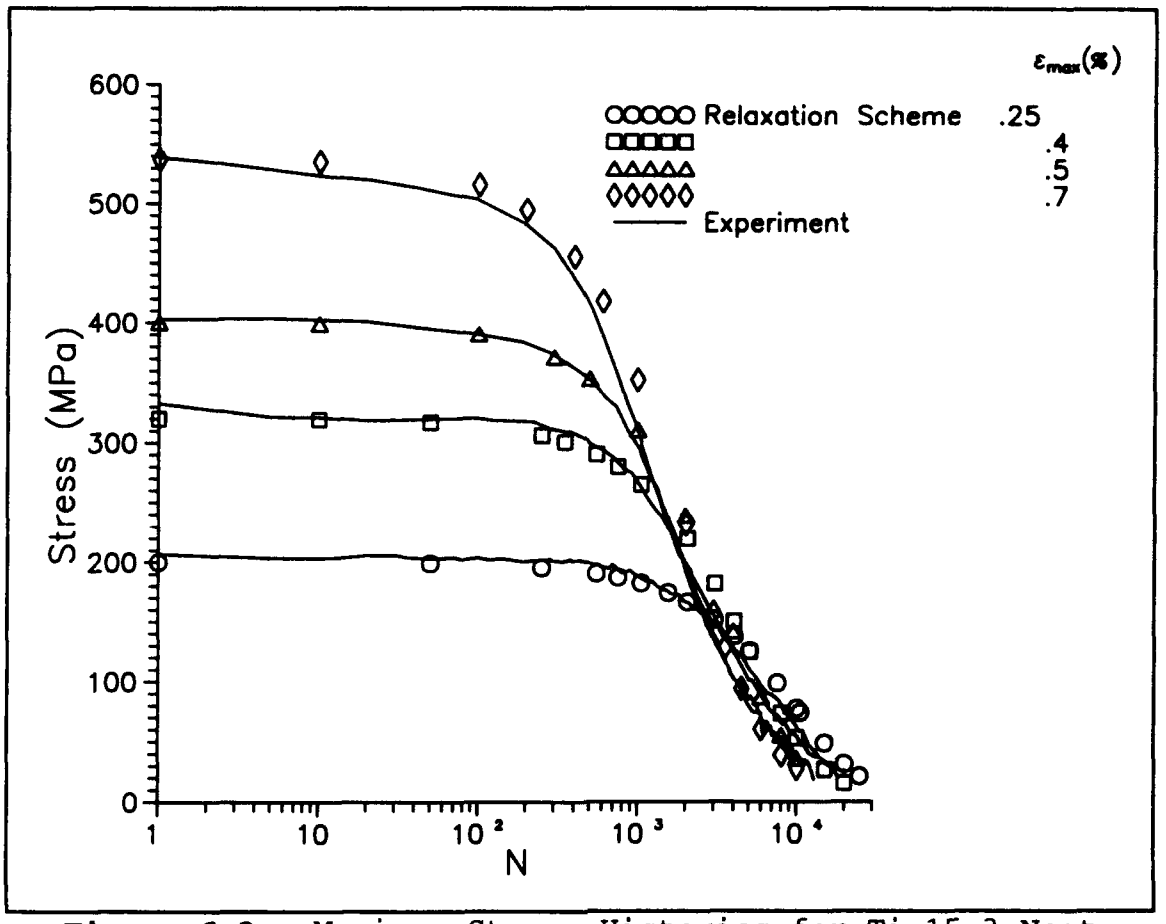

Figure 6.2 Maximum Stress Histories for Ti-15-3 Neat Matrix, Experiment vs. Predictions

achieves a state of tension-compression stress during the fatigue life of the 0° lamina. To understand how the matrix behaves in this condition, the above analysis was repeated, but the strain range was held constant. The results of this analysis are discussed next.

Figures 6.3 shows the typical fatigue response of the neat matrix predicted by the relaxation scheme for the constant amplitude strain control mode and the hybrid

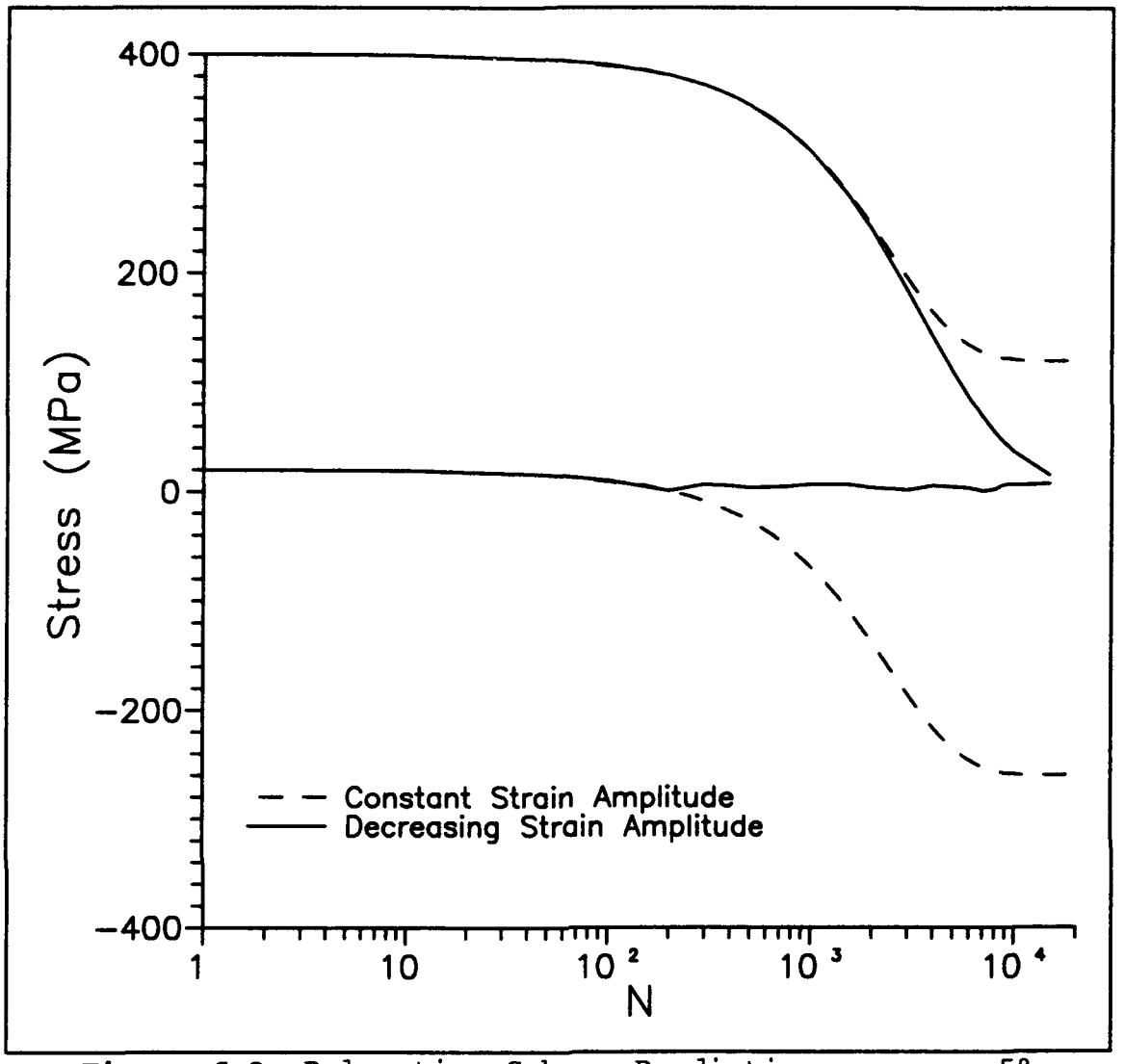

Figure 6.3 Relaxation Scheme Predictions, ϵ_{max} = .5%

(decreasing amplitude), strain control mode employed in this study. As described in Chapter III, the ratio of the minimum strain to the maximum strain was .05. Initially, the fatigue behavior of the two control modes showed excellent agreement. After the minimum stress of the matrix had relaxed to zero, the response of the matrix started to

diverge. For the hybrid strain control mode, the zero stress constraint forced the minimum stress to remain at zero for the remainder of the fatigue life. No balancing of the matrix creep in tension and compression occurs in this case. As a result, the maximum stress continued to relax to a near zero value. Conversely, for the constant strain amplitude case, the minimum stress was allowed to become compressive. Some of the creep occurring during the tensile loading portion of the fatigue cycle was counteracted by negative creep occurring when the stress was compressive. The stress response for the neat matrix then steadied out when the matrix creep in tension was exactly matched by that occurring in compression. Thus, the mean stress remained constant. This phenomena was called "self-equilibrating creep" in this study.

0° Lamina Analysis

This section discusses the predicted results obtained from the CCM. Predicted results are shown for the cases described in Chapter IV as: the fiber dominated failure mode, and the matrix dominated failure mode. An analytical comparison was also made between the hybrid strain control mode used in this study with the constant amplitude strain control mode.

Region I - Fiber Dominated Failure Modes

Stress-Strain Response

In Chapter IV, it was shown that fiber fractures were the dominant failure mode when the maximum strain was greater than .73%. Figure 6.4 compares a few representative stress-strain curves predicted by the CCM to the experimental counterparts for a specimen subjected to fatigue at a maximum strain of .75%. Excellent agreement was observed.

The stress-strain response of the lamina and constituents for the first cycle are shown in Figure 6.5. This shows that the nonlinear response in the first cycle was the result of plastic deformation of the matrix above a strain level of .55%. After the first loading cycle, the effective stress in the matrix did not exceed the yield stress. Thus, the remainder of the predicted stress-strain curves (Figure 6.4) were dominated by matrix creep. The excellent agreement in the results verify that the plastic and the matrix creep deformation could be decoupled to analyze the fatigue response of fiber-reinforced matrix.

Stress History

Figure 6.6 compares the predicted histories of the maximum stress and minimum stress to their experimental counterparts for the previous case. The Stage I deformation mechanisms described in Chapter IV are shown. For the

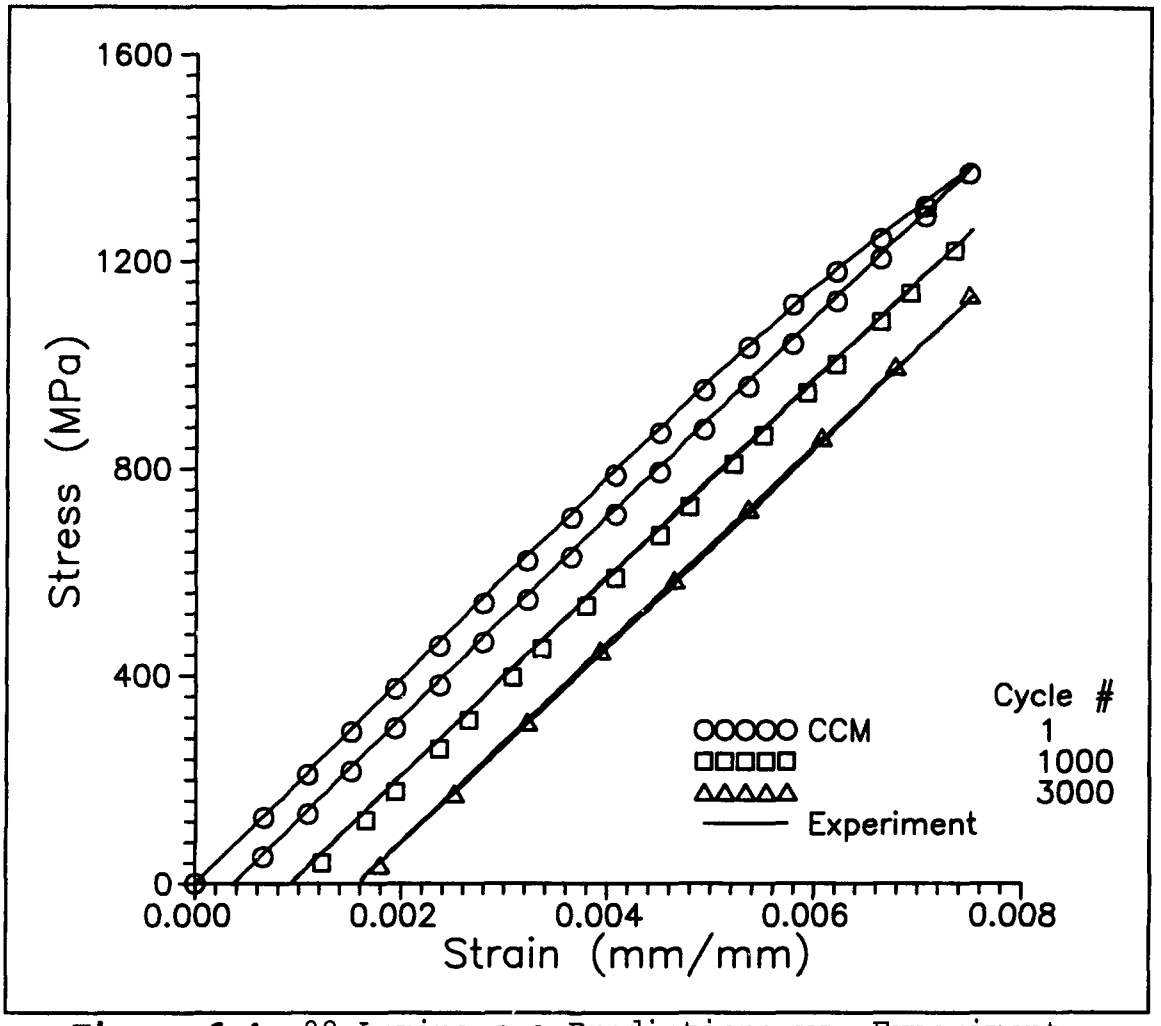

Figure 6.4 0° Lamina σ-ϵ Predictions vs. Experiment, ϵ_{max}= .75%

entire fatigue life, the predicted stress response showed excellent agreement with the experimental data. Since only creep and plasticity of the matrix were modeled, these results show that the failure was non-progressive (i.e. no growth in damage). Instead, it was instantaneous. This type of response is indicative of a failure mode dominated by fiber fractures.

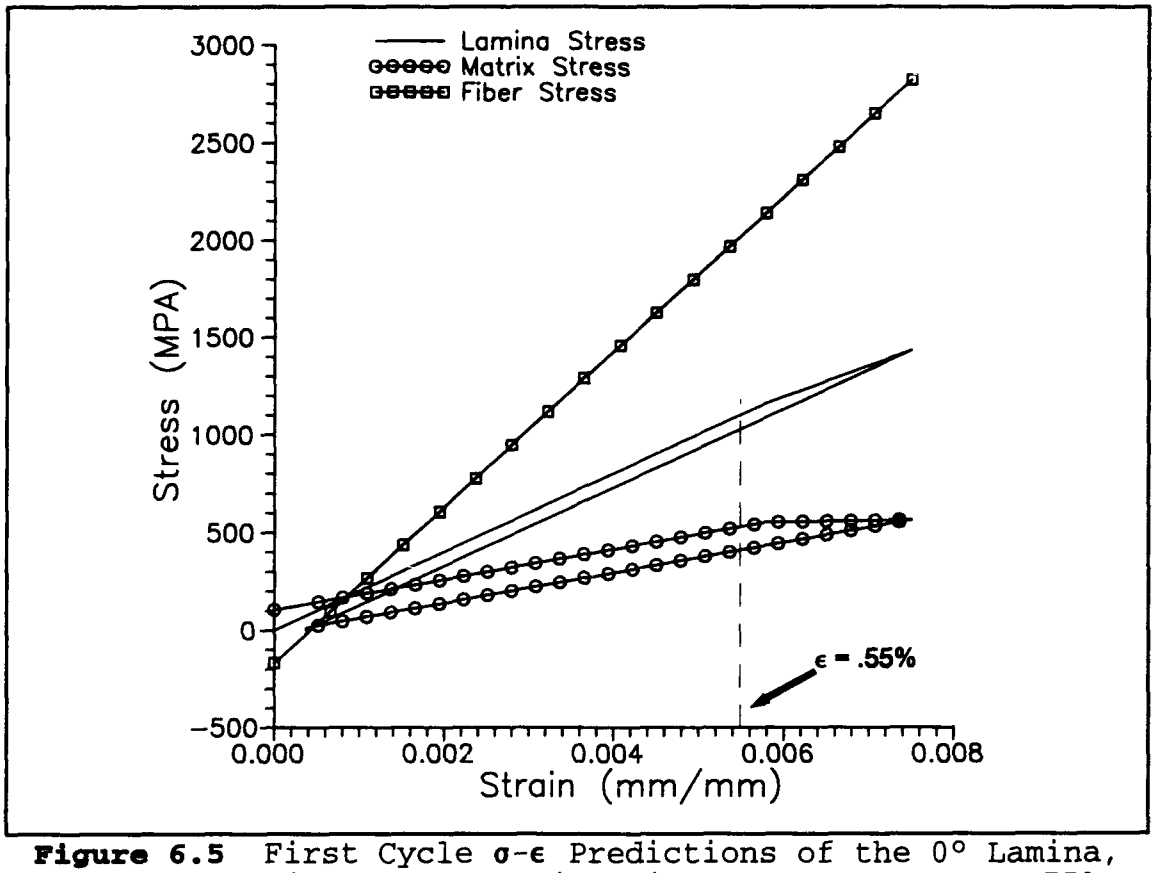

Figure 6.5 First Cycle σ-ϵ Predictions of the 0° Lamina, Fiber, and Matrix Axial Stresses, ϵ_{max} = .75%

Thus, the CCM has verified the experimental observations. It showed that: the first cycle was a result of plastic deformation of the matrix, and the subsequent fatigue response was dominated by matrix creep. These results indicate that the responses of the constituents were predicted with reasonable accuracy and can be studied to further describe the fatigue response of the lamina.

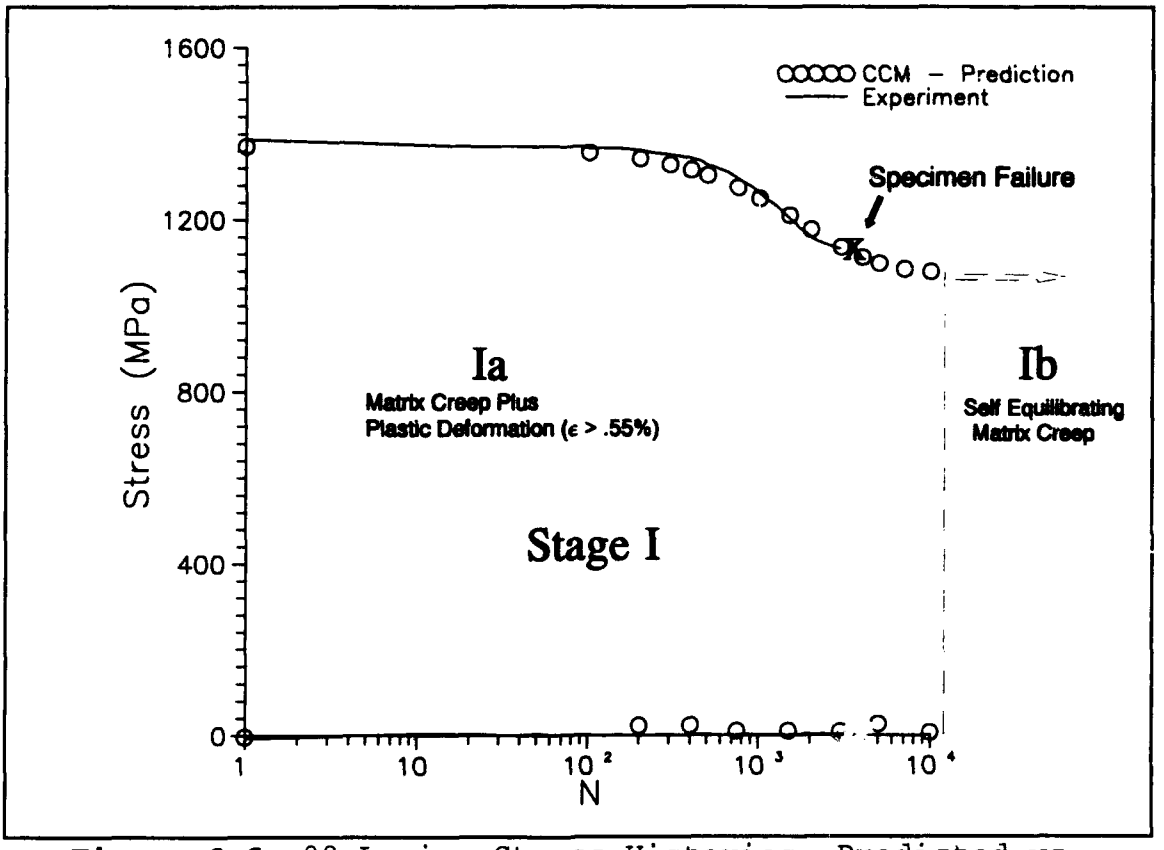

Figure 6.6 0° Lamina Stress Histories, Predicted vs. Experiment, ϵ_{max} = .75%

Constituent's Response

For the above case, Figure 6.7 shows the predicted histories of the: minimum axial stress in the fiber, maximum axial stress in the fiber, minimum axial stress in the matrix, and the maximum axial stresses in the matrix. The two stage stress response, discussed in Chapter IV, are also labeled in the figure. Examining these predictions helped to better understand the lamina response.

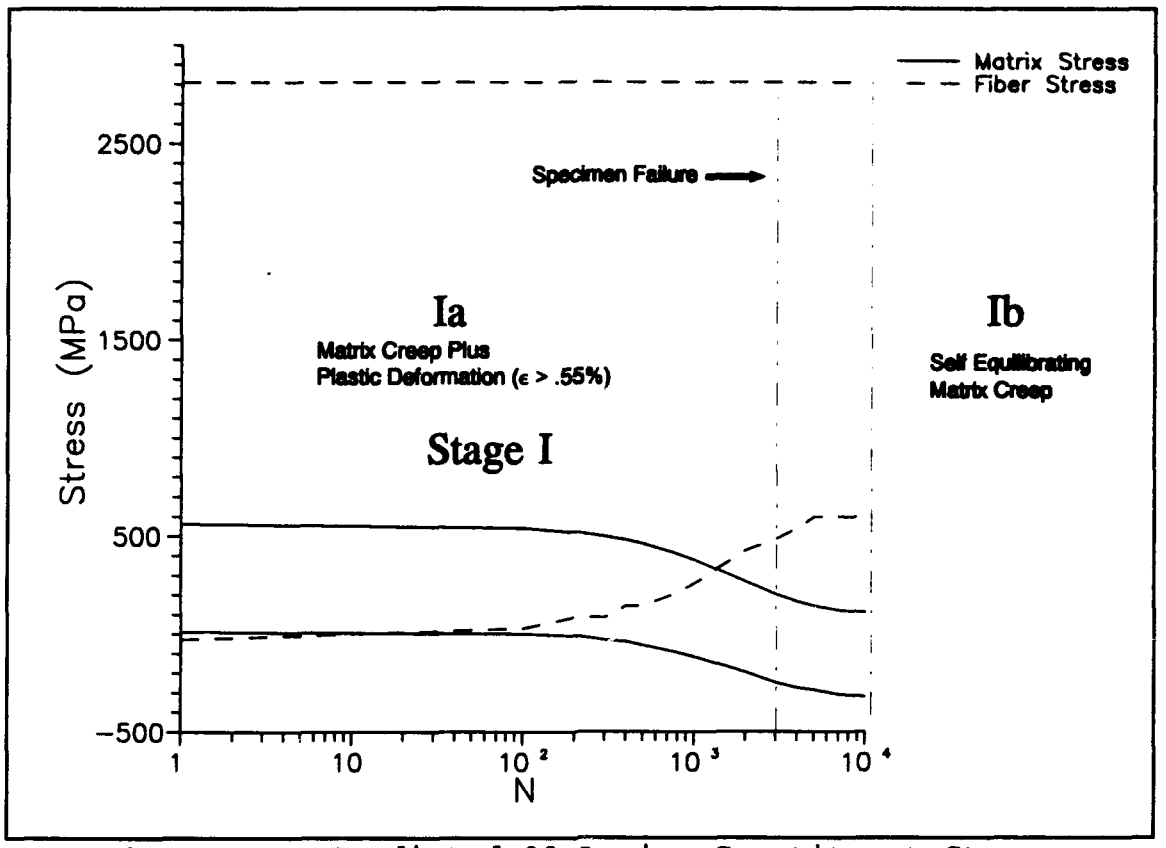

Figure 6.7 Predicted 0° Lamina Constituent Stress Histories, ϵ_{max}=.75%

Since there is no load transfer to the fiber in the strain control mode, the maximum fiber stress remains constant when the matrix stress relaxes. This verifies that the reduction in the lamina stress was the result of matrix creep. The analysis also shows that the minimum stress of the matrix was compressive in substage Ia, even though a zero stress constraint was enforced on the lamina. In order to maintain this constraint, the minimum stress in the fiber had to increase, which was due to the increase in the

minimum strain. Thus, although the fiber was in a tension-tension state, the matrix actually achieved a state of tension-compression stress.

The results predicted by the CCM confirm that the progression of deformation and damage for the fiber dominated failure mode is:

(1) Plastic deformation of the matrix

(2) Creep deformation of the matrix

(3) The fibers begin to fracture and the specimen fails

As shown above, there was no increase in the fiber stress, but in the experiments the fibers still fractured. This suggests that the phenomenon of the fiber fracture would need to be modeled by applying statistical analysis techniques and obtaining a better understanding of the degradation in the fiber strength due to fatigue.

Region II - Matrix Dominated Failure Mode

Stress-Strain Response

In Chapter IV, it was shown that matrix cracking was the dominant failure mode when fatigue occurred below a maximum strain of .73%. Figure 6.8 compares a few representative stress-strain curves predicted by the CCM to their experimental counterparts for a specimen subjected to fatigue at a maximum strain of .6%. As mentioned above, the non-linear response in the first cycle was due to plastic

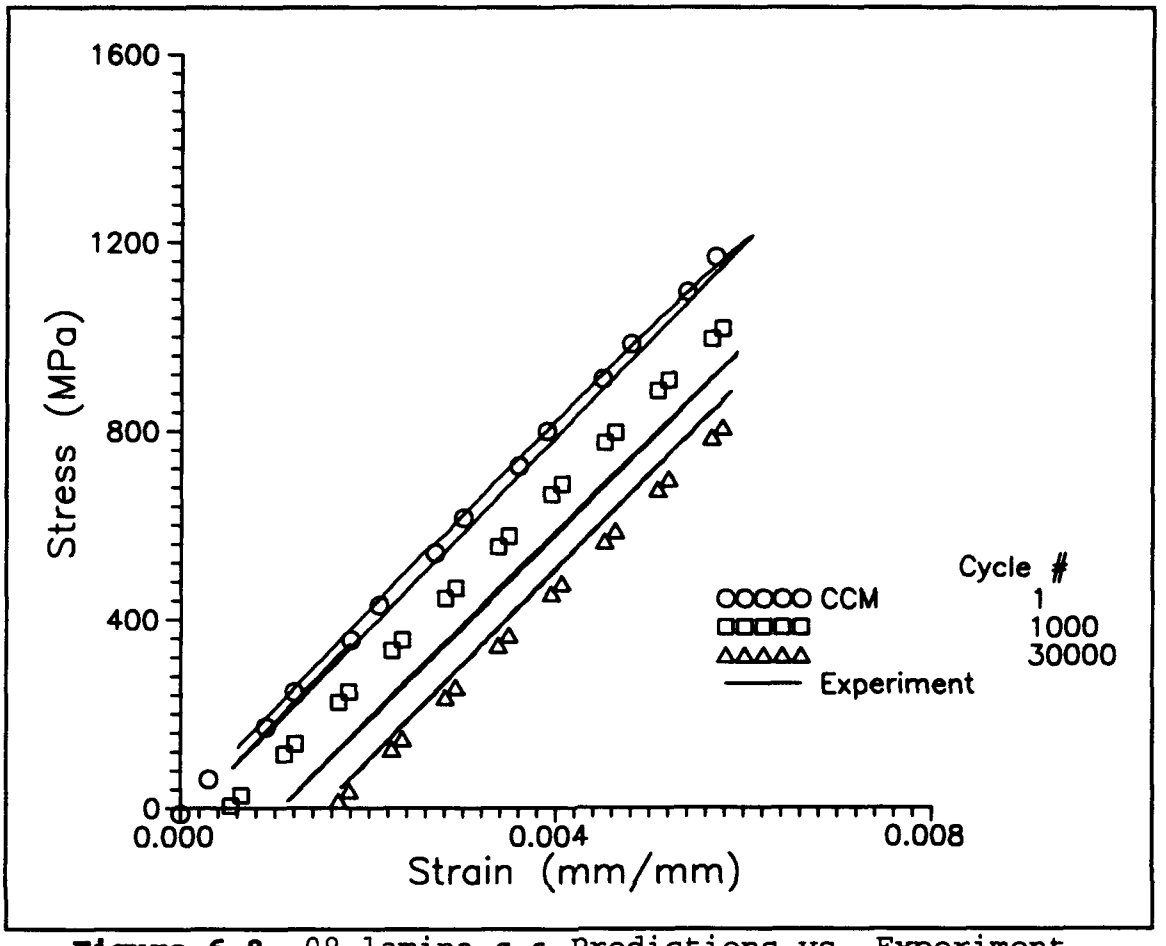

Figure 6.8 0° lamina σ-ϵ Predictions vs. Experiment, ϵ_{max} = .6%

deformation of the matrix (Figure 6.5). Reasonable agreement was obtained between the predictions and the experiment for the first 30,000 fatigue cycles. However, the predicted response was unchanged after 30,000 cycles. This was the result of not modeling matrix cracking in the CCM, and, as mentioned in Chapter IV, matrix cracks resulted in a reduction in the stiffness and stress of the lamina after 32,000 fatigue cycles.

Stress History

Figure 6.9 compares the predicted minimum stress and maximum stress of the lamina to the results obtained from the experiment for the previous loading condition. It was in shown Chapter IV that for specimens whose failure mode was dominated by the matrix cracking, a two stage stress response was observed. These stages are shown in Figure 6.9. In substage Ia, the predicted results showed excellent agreement with its experimental counterpart. Consistent with experiment, the CCM predicted a constant mean stress in substage Ib. After this, the predicted stress response remained constant for the remainder of the fatigue life, while experimental data showed a steady decrease in stress starting at approximately 32,000 fatigue cycles. This was shown to be the result of matrix cracks (Figure 4.24), which was not modeled in the present analysis. These results show the need for an evolutionary law that would characterize the 0° lamina response due to the initiation and progression of matrix cracks.

Constituent's Response

Figure 6.10 shows the predicted fatigue response of the constituents for this same loading condition. As in the case of the fiber dominated failure mode, the first stage was a result of matrix creep. This was accompanied by the plastic deformation of the matrix, during the first loading

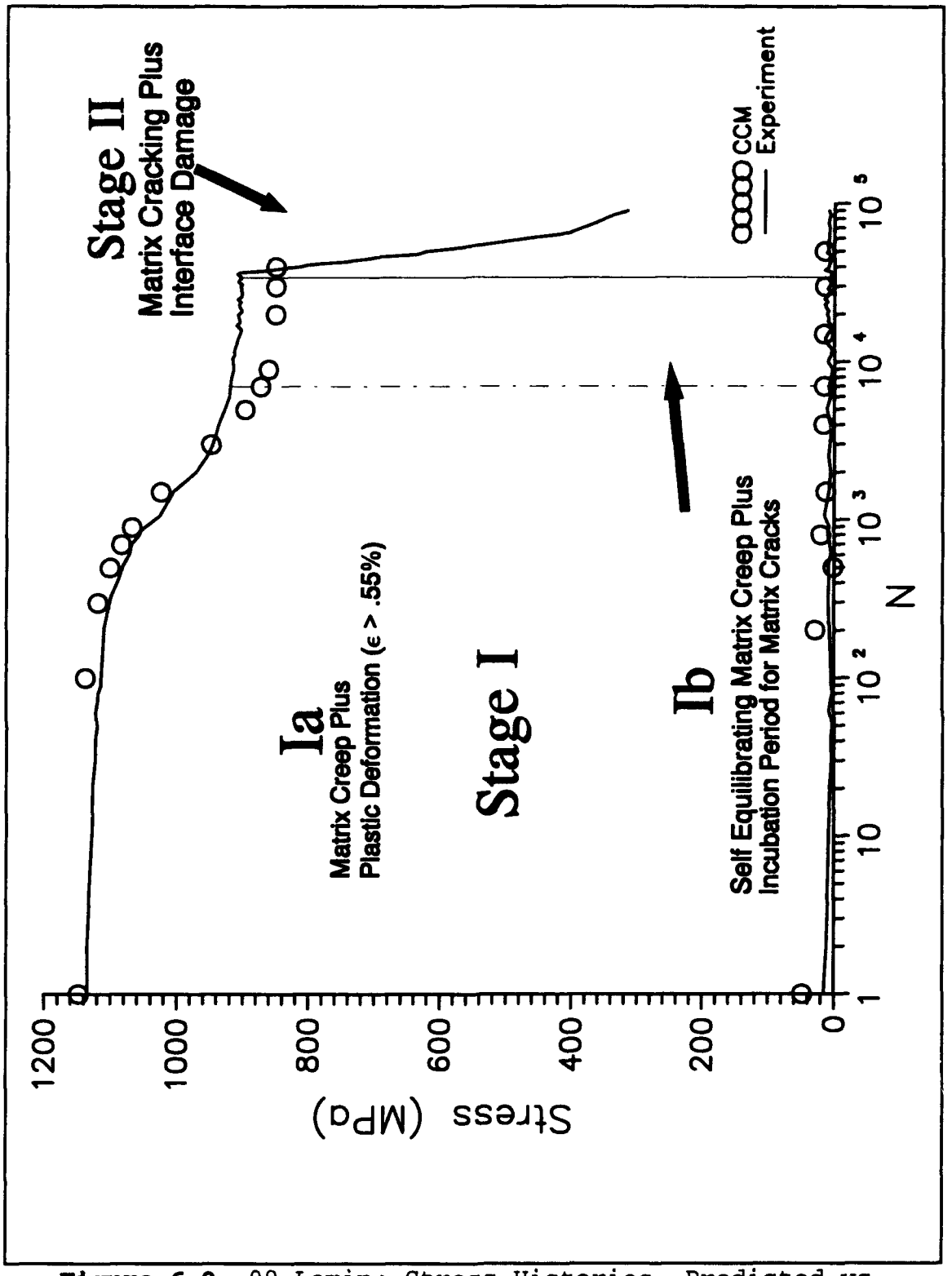

Figure 6.9 0° Lamina Stress Histories, Predicted vs. Experiment, ϵ_{max} = .6%

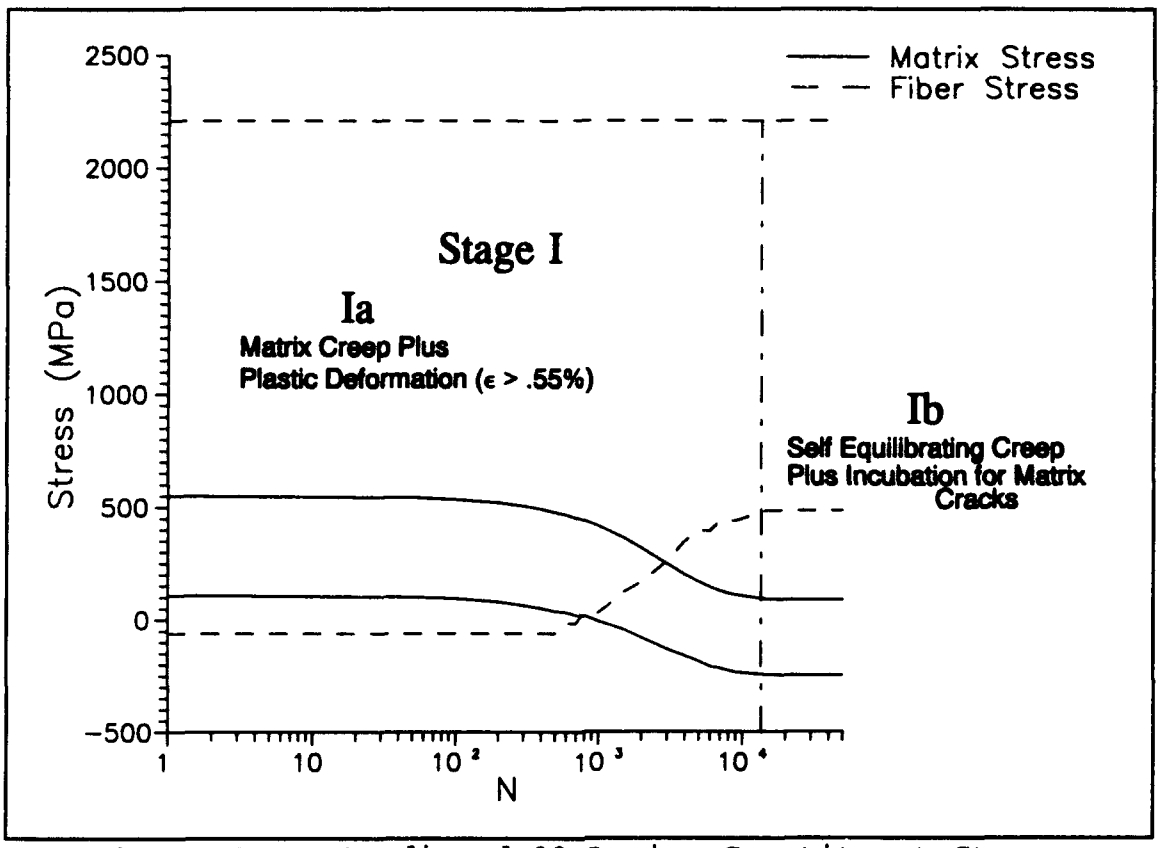

Figure 6.10 Predicted 0° Lamina Constituent Stress Histories, ϵ_{max} = .6%

cycle, when the maximum strain level was above of .55%. As can be observed in Figure 6.10, the lamina stress achieved a constant mean stress (substage Ib). The analysis now shows that this occurs because the mean stress in the matrix was constant, which was a result of the matrix creep in tension being balanced by the matrix creep in compression (self-equilibrating matrix creep). Since no further reduction in the stress due to matrix creep occurs, the matrix cracks begin to develop in this substage.

The CCM has shown that the two stage behavior described in Chapter IV contains the following progression of damage:

(1) The matrix plastically deforms when the matrix strain level in fatigue is above .55%.

(2) the matrix creeps, leading to a reduction in lamina stress

(3) a state of self-equilibrating matrix creep occurs and matrix cracks begin to develop

(4) These matrix cracks begin to propagate through the specimen which results in a loss in stiffness.

Constant Strain vs. Decreasing Strain Amplitude- An Analytical Comparison

There was no experimental data available in the literature or obtained in this study for the 0° lamina under the constant amplitude strain control mode. The CCM was used to explore the differences between this control mode and the hybrid strain control mode used in this study. Figure 6.11 compares the predicted histories of the maximum stress and minimum stress of the lamina for the two control modes. As expected, the only difference in the two responses occurs at the minimum strain level. This behavior was explained by examining the constituent stresses, which are discussed next.

Figure 6.12 shows the predicted histories of the constituent stresses for the above case. There was no

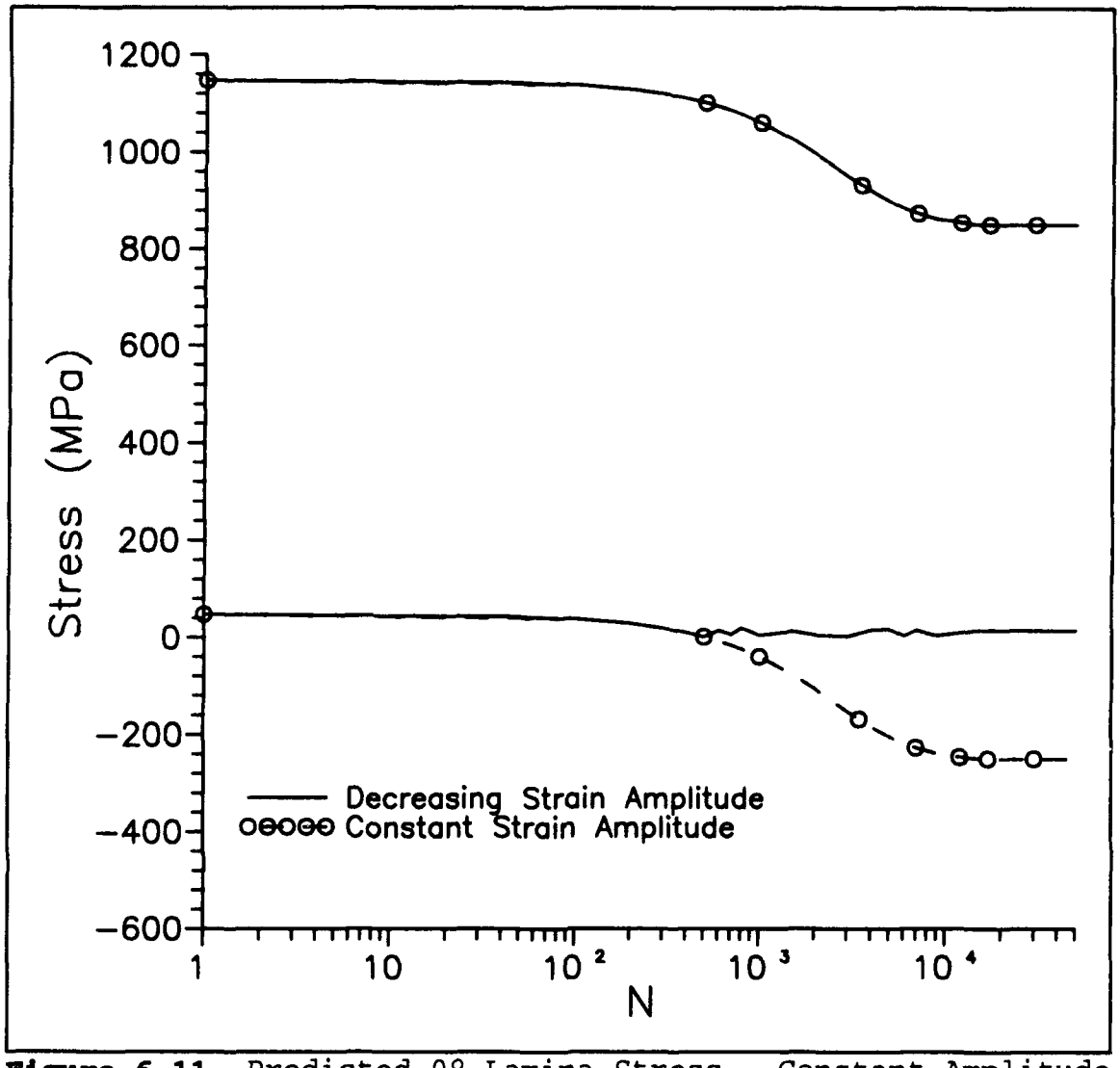

Figure 6.11 Predicted 0° Lamina Stress - Constant Amplitude vs. Hybrid Strain Control, ϵ_{max} = .6%

difference in the predicted maximum stress of the fiber between these two techniques. Hence, for either technique, there should be no difference in the fatigue life nor should there be any difference in the progression of damage when the failure is dominated by fiber fractures. As expected,

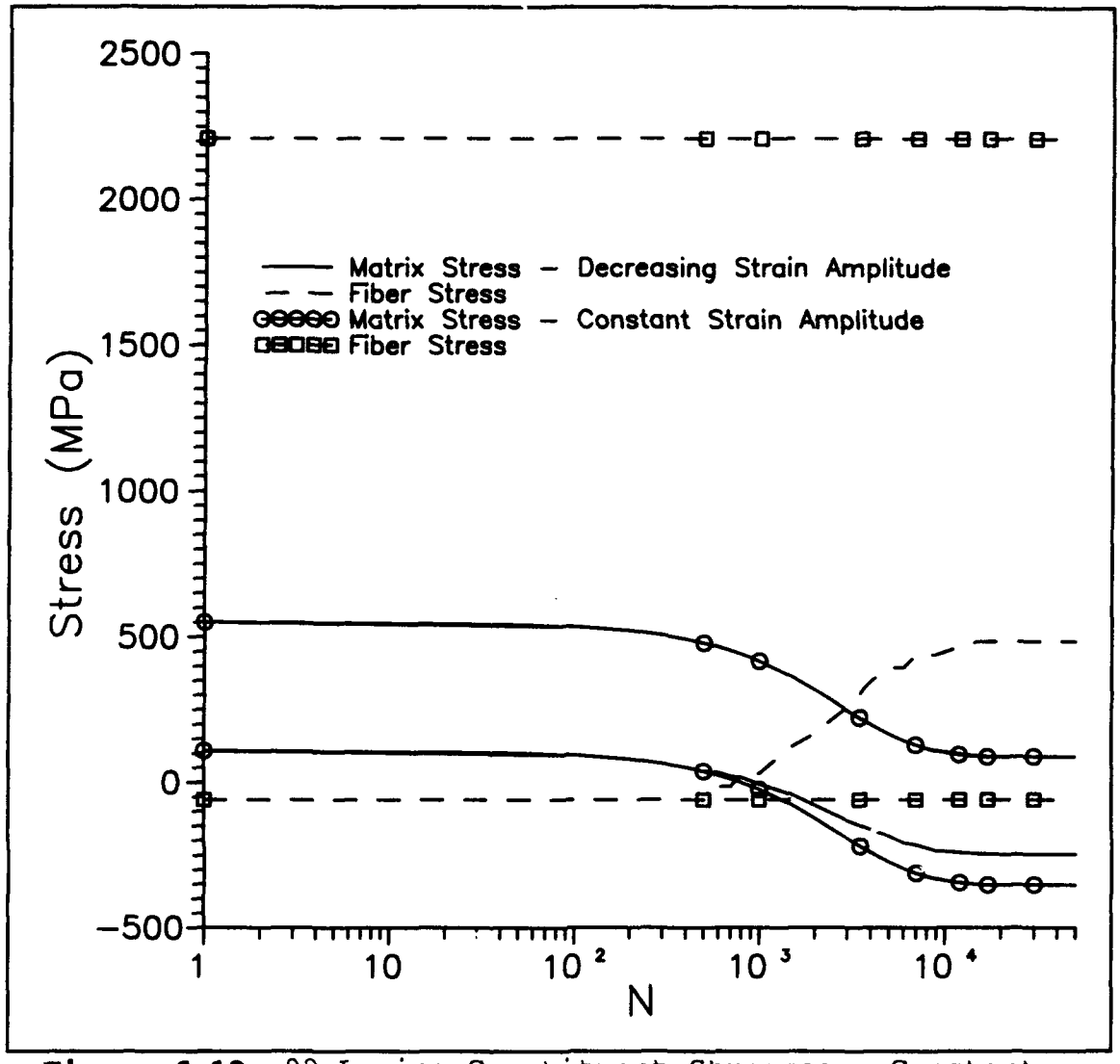

Figure 6.12 0° Lamina Constituent Stresses - Constant Amplitude vs. Hybrid Strain Control, ϵ_{max}= .6%

there was generally a large difference in the minimum fiber stress between the two control techniques. There is no evidence to show that the fiber is sensitive to stress range, so the control technique should not affect the fiber damage.

As with the fiber, there was a difference in the stress range in the matrix. There was no difference in the predicted maximum stress of the matrix. The difference was in the minimum stress, and, as a result, there was a difference in the stress range. Several investigations [34, 35, 69] have shown that the matrix is sensitive to stress range. However, the difference in the predicted stress range, using the present analysis, is small compared to what is required to affect the fatigue life. Again, no difference in the damage mechanisms nor the fatigue life should be observed subjecting a specimen to fatigue using either of these techniques.

This analysis showed that there will be a difference in the lamina stress response between the constant amplitude and hybrid strain control mode. However, the predicted results suggests that no difference in fatigue lives nor the damage mechanisms should be observed. A thicker and more expensive specimen would be required to run the constant amplitude strain controlled tests to prevent buckling. These preliminary results suggests that this may not be required.

90 Lamina Analysis

The strip model (SM) was used to predict the fatigue response of the 90° lamina. This section discusses the

ability of the SM to predict the lamina damage, and the insight it can provide to the locations of matrix plasticity and matrix cracking. Results are shown for the fatigue responses described in Chapter IV as: progressive fiber-matrix interface damage, matrix cracking plus the progressive fiber-matrix interface damage, and matrix cracking. Also, a discussion is presented to show the differences between the hybrid strain control mode and the constant amplitude strain control mode.

First Fatigue Cycle Predictions Using the Strip Model Stress-Strain Response

Figures 6.13 through 6.15 compare the predicted (first cycle) stress-strain responses to the experimental data for the cases of maximum strain levels of .1%, .2%, and .3%, respectively. It was previously stated that the bond strength distribution for the SM was determined from the loading curve of a specimen subjected to fatigue at a maximum strain of .45% (Figures 5.11 and 5.12). This same distribution was also used for these predictions.

It was observed that the SM predicted the stress-strain response at these strain levels within reasonable experimental error. In each case, the predicted loading response and peak stresses showed good agreement with the experimental counterpart. The predicted behavior of the unloading responses also showed reasonable agreement with

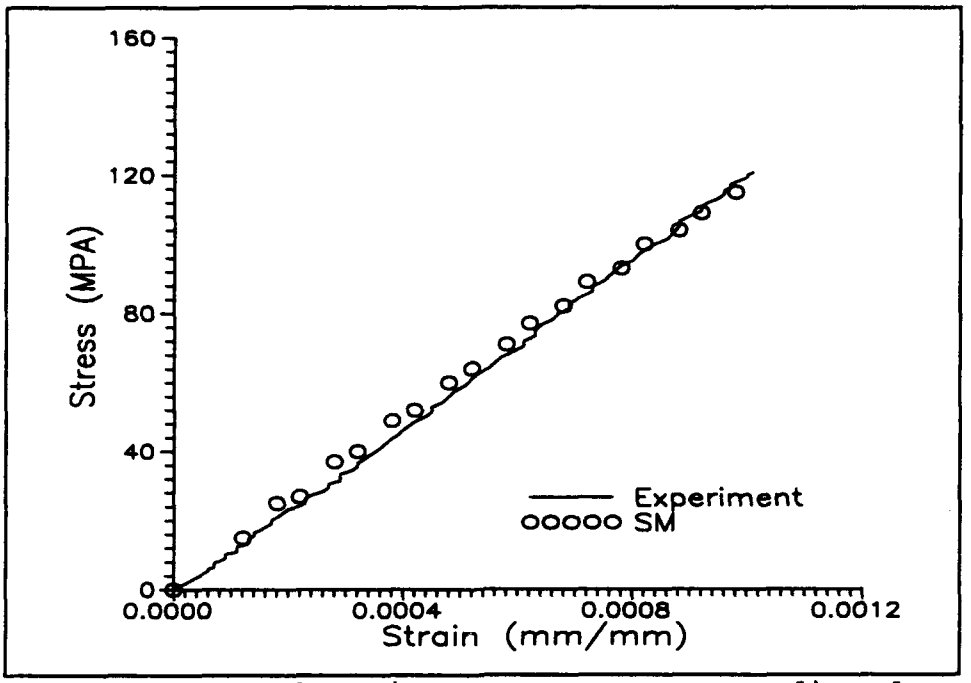

Figure 6.13 90° Lamina σ-ϵ Response, Predicted vs. Experiment, ϵ_{max} = .1%

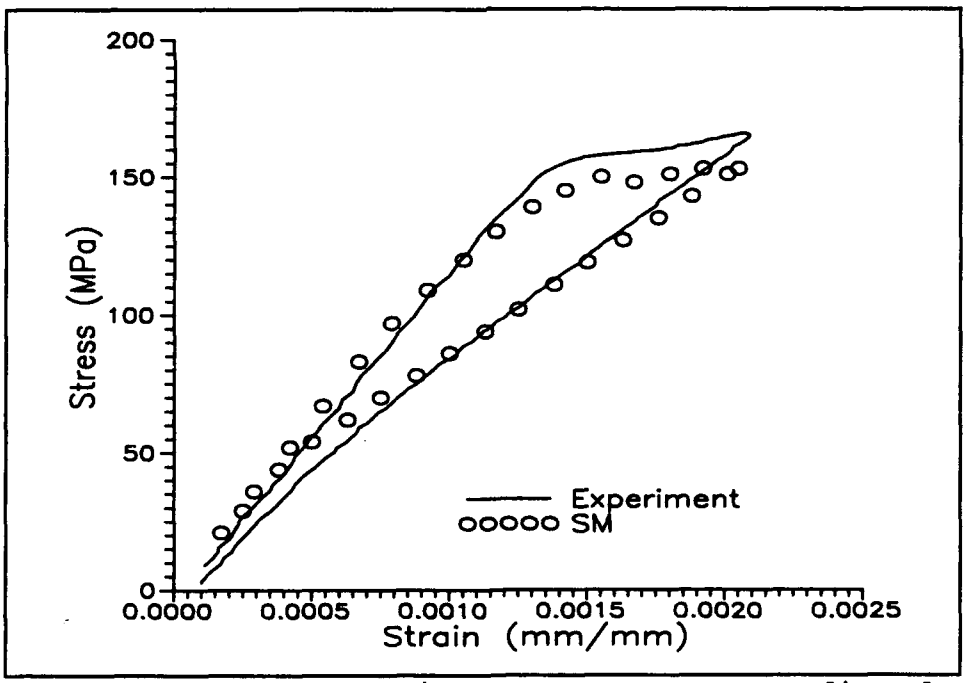

Figure 6.14 90° Lamina σ-ϵ Response, Predicted vs. Experiment, ϵ_{max} = .2%

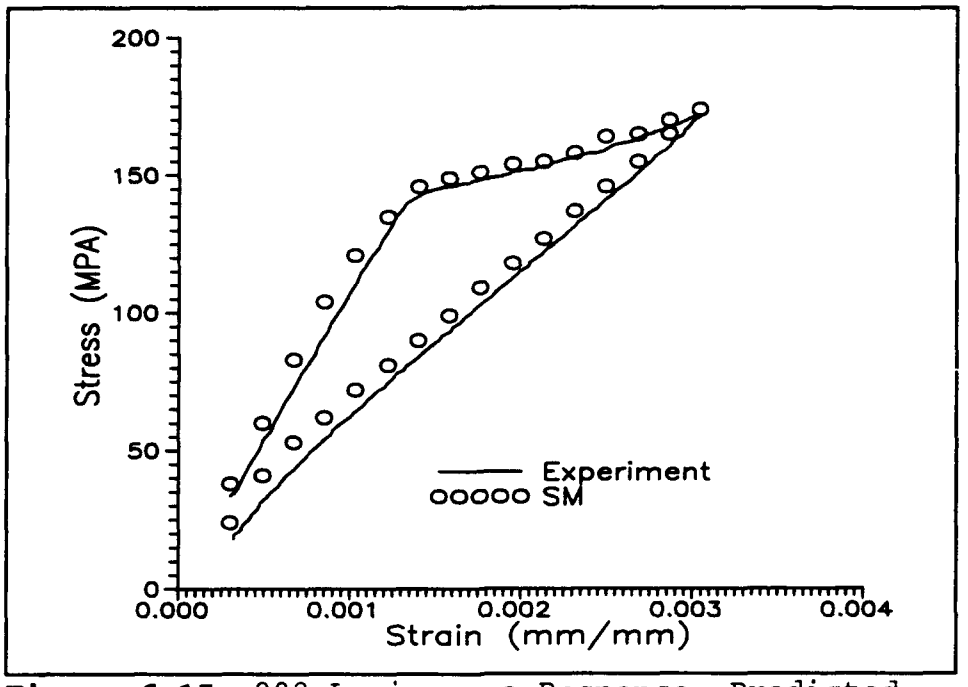

Figure 6.15 90° Lamina σ-ϵ Response, Predicted vs. Experiment, ϵ_{max}= .3%

the experiments. This illustrates that the SM was able to predict the correct stress-strain response, for all the strain levels tested in this study, by modeling the damage of the fiber-matrix interface as a progressive mechanism and calibrating the bond strengths of the strips with one loading curve.

Lamina Stress Distribution

In addition to characterizing the initiation of fiber-matrix interface damage, the SM can also provide an insight into the other observed deformation and damage mechanisms. Figure 6.16 shows predicted stress distributions across the unit cell for the first loading cycle. This is for the

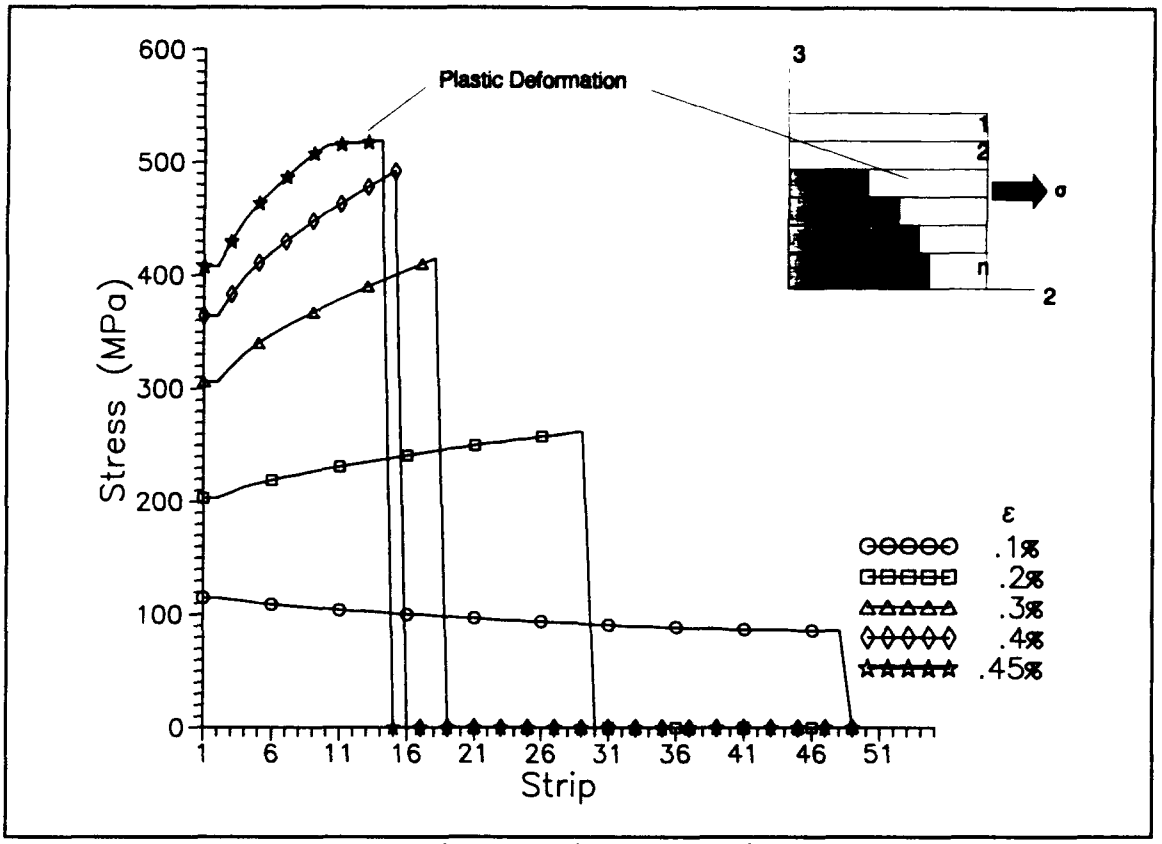

Figure 6.16 Predicted First Loading Cycle Stress Distribution, ϵ_{max} = .45%

case of a specimen loaded to a maximum strain level of .45%. The stress distribution at five intermediate strain levels in the loading cycle are shown. These strain levels correspond to those used to test the 90° lamina in fatigue.

The SM predicted matrix plasticity to occur at an angle of approximately 51° with respect to the loading axis and at a strain level of .45%. This approximate location is shown schematically on the SM model (see insert). In Chapter IV, it was shown that matrix plastic deformation (i.e. slip

bands) was observed at this location, but it initiated at a strain level of .25% (Figure 4.54). Albeit, the SM predicted the plasticity at a higher strain than observed in the experiment, but, nevertheless, the correct location was predicted.

The plastic deformation observed in the experiment was a localized phenomena due to a local stress concentration at the fiber-matrix interface, which the SM does not account for. As explained in Chapter V, the entire matrix portion of the strip is either elastic or plastic. Prediction of this localized plasticity may require an analysis (i.e. finite elements) which can predict the multi-dimensional state of stress and take into account the stress concentration at the fiber-matrix interface.

Even though the plastic deformation was predicted at a higher strain level than actually occurred, the stress-strain response was well predicted by the SM (Figures 6.13 through 6.15). Thus, when fatigue occurs below a strain level of .45%, plastic deformation of the matrix was a secondary mechanism to the fiber-matrix interface damage. This has also been observed in other investigations of the SCS-6/Ti-15-3 90° lamina [68].

The SM only considers the fiber-matrix interface damage. It can characterize the initiation of damage on the first loading cycle and, as it will be shown next, can

provide some insight into the propagation of the fiber-matrix interface damage. The discussion presented above shows that the SM can also provide data on stress ranges (i.e. minimum and maximum stresses in each strip). In future work, these data may be used with an evolutionary law to predict the development and propagation of matrix cracks.

Fatigue Response

Region IIb - Progressive Fiber-Matrix Interface Damage

In Chapter IV, a linearly elastic response was observed during the first cycle of the specimen tested in fatigue at a maximum strain level of .1%. The SM accurately predicted this response (Figure 6.13). For this test condition, optical microscopy showed that no matrix cracking initiated but that there was fiber-matrix interface damage (Figure 4.57). Thus, this test was chosen to calibrate the bond strength degradation function (Equation 5.42).

Figure 6.17 shows the predicted histories of the maximum stress and minimum stress compared to their experimental counterparts for the specimen subjected to fatigue at a maximum strain of .1%. The predicted curves were determined by using the SM and applying Equation 5.34 using different values of n'. When n'= 5,000, this implies that the entire fiber-matrix interface had failed by 5,000 fatigue cycles. An infinite value of n' implies that no degradation in the fiber-matrix interface bond strength

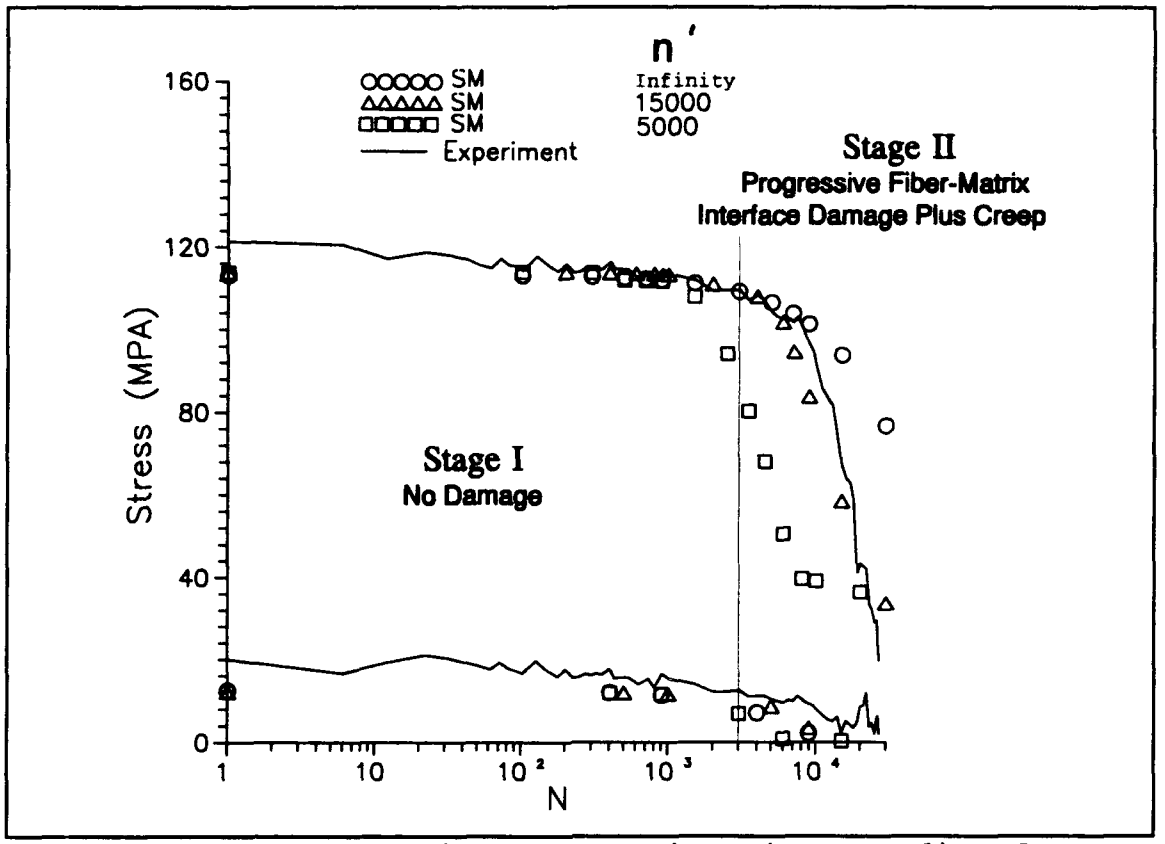

Figure 6.17 90° Lamina Stress Histories, Predicted vs. Experiment, ϵ_{max}=.1%

occurs. In the latter case, the only reduction in stress would be due to creep deformation of the matrix. As expected, in the case of no degradation in the bond strength, the prediction shows that matrix creep itself was not enough to account for the total reduction in stress observed in the experiment. The prediction improves by assuming the bond strength becomes totally weak by 15,000 cycles.

The results obtained by applying the degradation function provides more of a qualitative than quantitative assessment. However, it clearly demonstrates that the progression of fiber-matrix interface damage can affect the fatigue response of the 90° lamina.

Region IIa - Progressive Fiber-Matrix Interface Damage and Matrix Cracking

Stress-Strain Response

Figure 6.18 shows the predicted history of the stress-strain response compared to the experimental counterpart for a specimen subjected to fatigue at a maximum strain .3%. In this case, the bond strength was not degraded. This figure is shown simply to demonstrate the ability of the SM to predict the stress-strain response after the first fatigue cycle. As explained in Chapter V, a strip has a zero bond strength after it has failed. This lowers the loading modulus on the subsequent fatigue cycles, as is clearly shown in Figure 6.18. It is shown next that the history of the maximum stress can be better predicted by degrading the bond strength.

Stress History

Figure 6.19 compares the predicted histories of the maximum stress and minimum stress to their experimental counterparts for a specimen tested in fatigue at a maximum strain of .3%. Two values of n' were used in this case

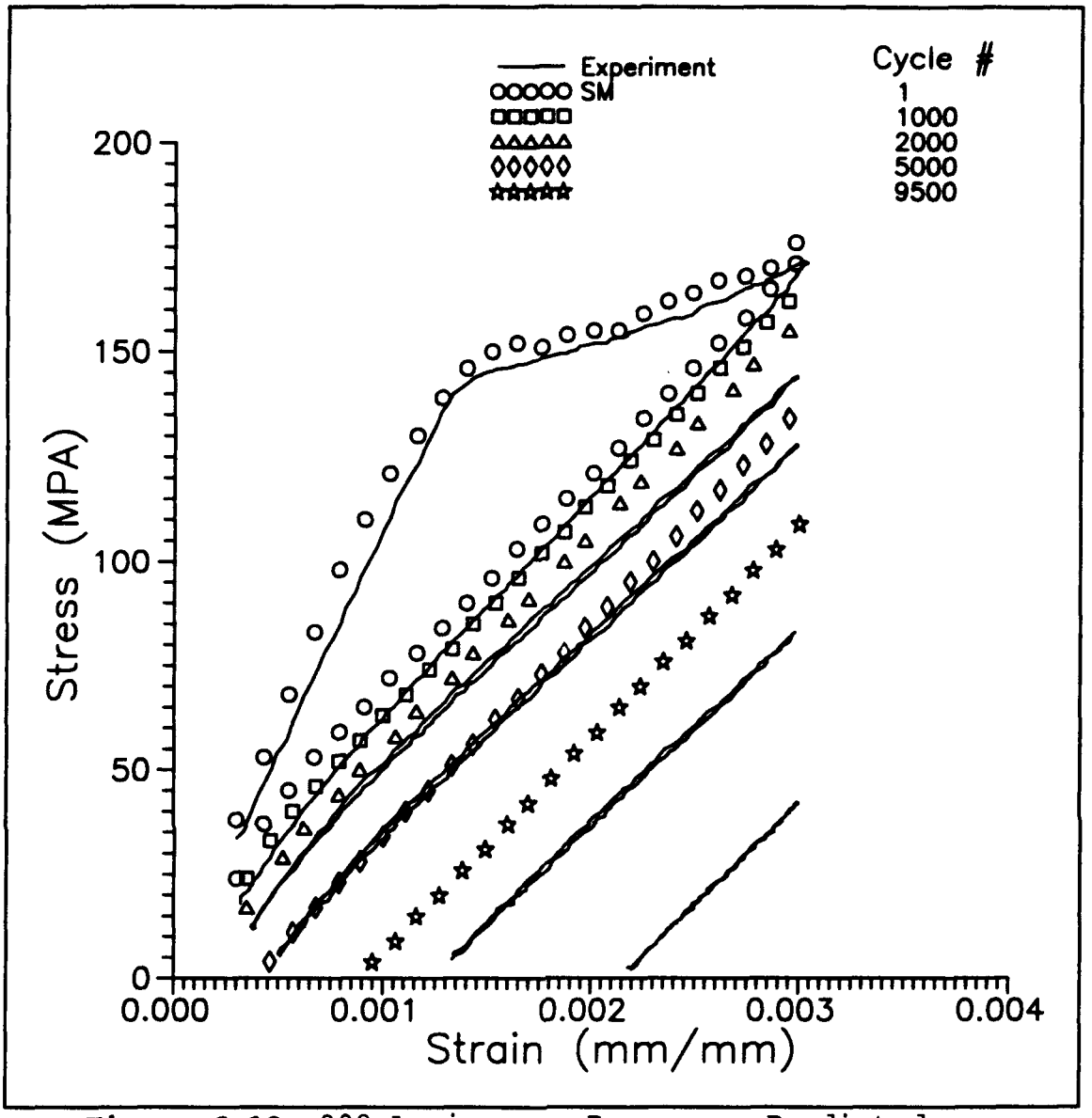

Figure 6.18 90° Lamina σ-ϵ Response, Predicted vs. Experiment, ϵ_{max}=.3%

(infinity and 15,000). The latter value was found from the case of a specimen subjected to fatigue with a maximum strain level of .1%. The predictions shows that the creep deformation (n'= infinity) can account for a large amount,

but not all, of the reduction in stress. Assigning a value of $n' = 15,000$ improves the prediction, but it still does not account for the total reduction in stress. Naturally, the propagation of the fiber-matrix interface damage is dependent on the state of stress at the interface, and it is also heavily dependent on the environmental affects, which was shown earlier (Figure 4.25). In was shown in Chapter IV that, when fatigue occurred in this region, small matrix cracks were observed at the fiber-matrix interface. These cracks also contribute to the reduction in stress. To improve the predicted fatigue response requires: an evolutionary law for the initiation and propagation of the matrix cracks, and further investigation into the degradation of the bond strength to determine its dependence on strain level and the environment.

Region I - Matrix Cracking

Figure 6.20 compares the histories of the minimum stress and maximum stress predicted by the SM to their experimental counterparts for the specimen tested in fatigue at a maximum strain of level .45%. As in the previous cases, two values of n' were used (infinity and 15,000). There was no difference in the two predictions, which was due to the short fatigue life. The specimen failed before any serious degradation in the bond strength could occur. Also, the analysis shows that there is only a small affect

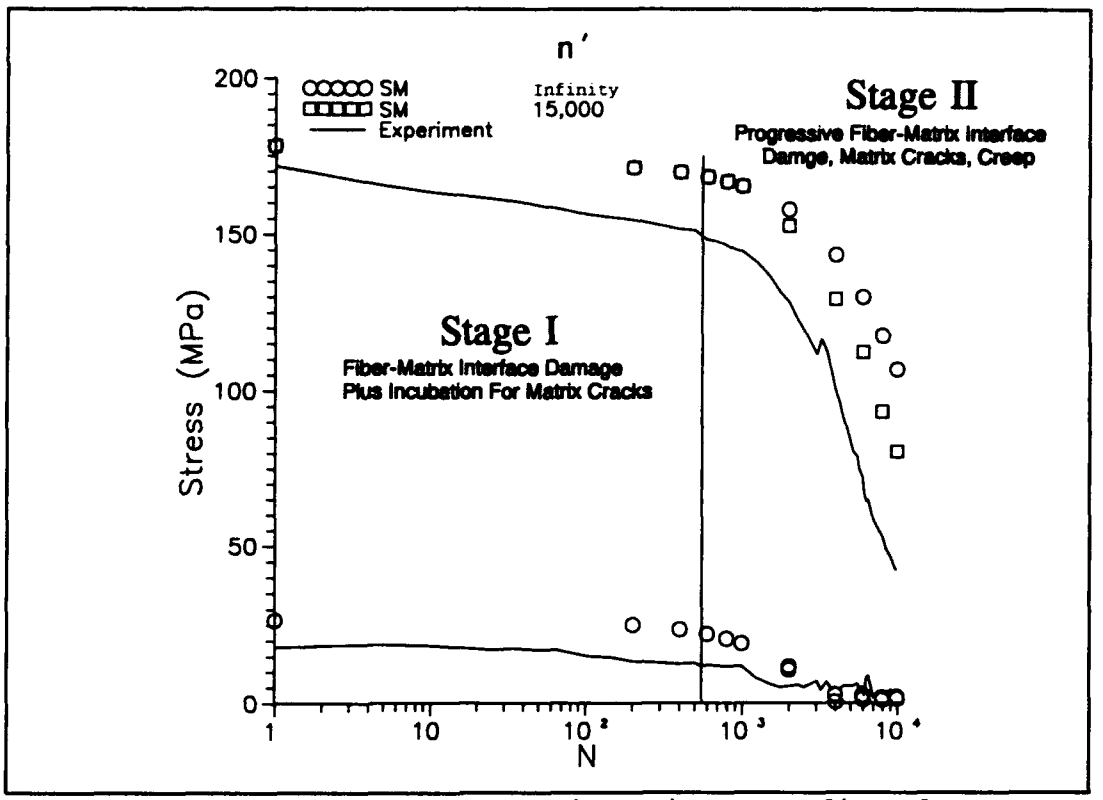

Figure 6.19 90° Stress Histories, Predicted vs. Experiment, ϵ_{max}= .3%

on the specimen response due to creep deformation. It was shown in Chapter IV that matrix cracking was the dominant damage mechanism when a specimen was tested in fatigue with a maximum strain greater than .35%. The SM has demonstrated the dominance of matrix cracking on the specimen response in this region. This shows again the need for an evolutionary law describing the initiation and propagation of matrix cracks to predict the response of the 90° lamina tested in fatigue.

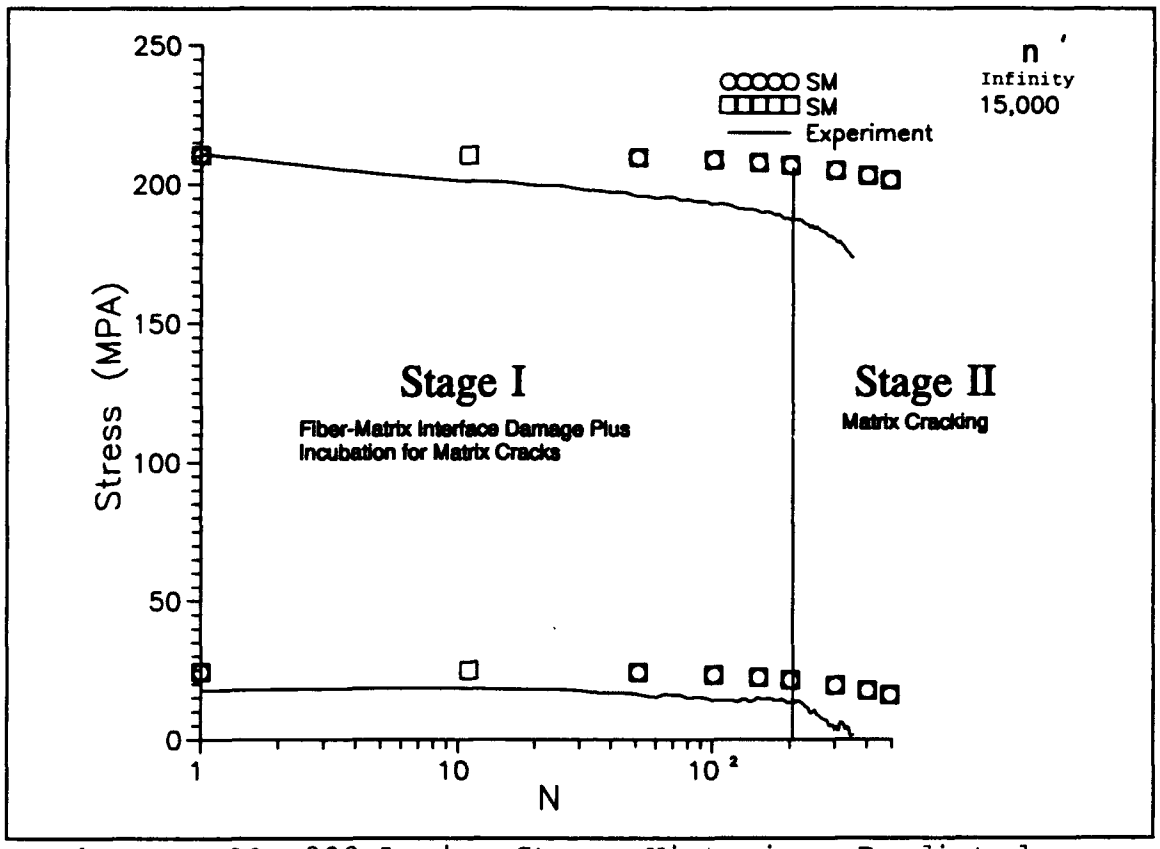

Figure 6.20 90° Lamina Stress Histories, Predicted vs. Experiment, ϵ_{max}=.45%

Constant Strain vs. Decreasing Strain Amplitude

It was shown in Chapter IV that there was good agreement in the fatigue lives between the constant amplitude strain control mode and the hybrid (decreasing amplitude) strain control mode (Figure 4.58). Figure 6.21 compares the stress responses for: the experiments using each control technique, and the SM predictions using each control technique. Both techniques show excellent agreement in the history of the maximum stress. As expected, there

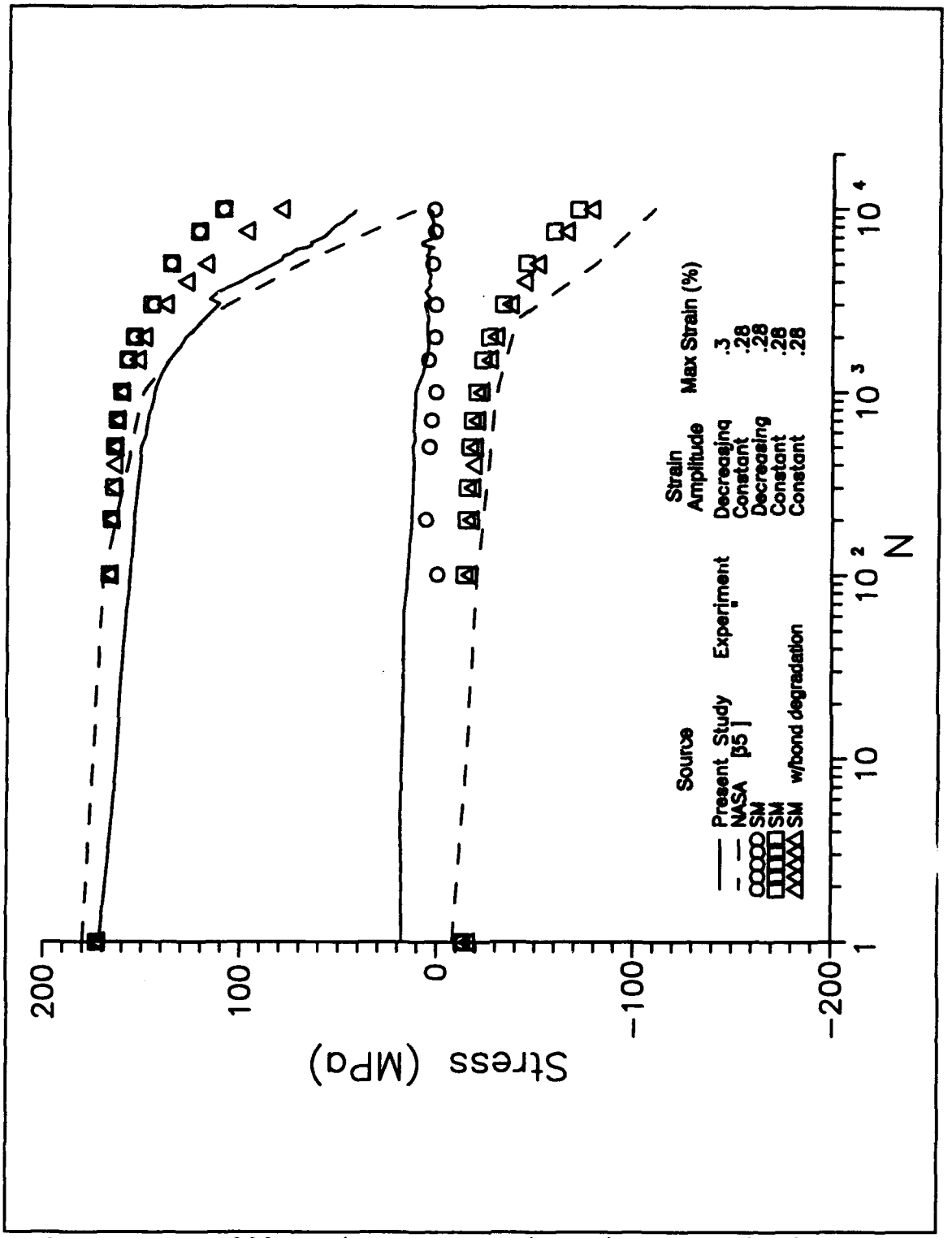

Figure 6.21 90° Lamina Stress Histories, Predictions for Hybrid and Constant Amplitude Strain Control vs. Experiment

was a difference in the history of the minimum stress. The SM was applied to better understand these differences.

As mentioned above, Figure 6.21 also shows the typical SM predictions for the constant amplitude strain control mode and the hybrid strain control mode. These predictions were for the case of a maximum strain level of .28%. It was previously shown that, for the hybrid strain control mode, the prediction can be improved by degrading the bond strength over the fatigue life. In this case, the effect of degrading the bond strength on the lamina stress was shown only for the constant amplitude technique. As expected, the prediction was improved.

The analysis suggests that the only difference between the two control modes will be due to creep deformation of the matrix. In the constant amplitude technique, some of the creep in tension will be recovered by the reverse creep in compression. This will not occur in the hybrid technique since the specimen was constrained from going into compression. However, it has been shown in this study that the matrix creep at the low strain levels is small. This suggests that the amount of reverse creep accumulated in the constant strain amplitude technique is negligible. As a result, the fatigue response (except for the minimum stress), damage mechanisms, and the fatigue life of a

specimen under the two strain control techniques were similar.

Analysis Summary

This chapter discussed the application of two micromechanical models to predict the fatigue response of the unidirectional SCS-6/Ti-15-3 MMC at elevated temperature under the strain controlled loading condition. The CCM was applied to predict the fatigue response of the 0° lamina, while the SM was used to predict the response of the 90° lamina. The findings from the analyses are summarized below:

Neat Matrix

(1) The fatigue response of the neat matrix under strain control was predicted from the results of a few relaxation tests and one static test at the application temperature (427°).

(2) The plastic and creep deformation mechanisms were successfully decoupled to predict the fatigue response of the neat matrix.

(3) For the hybrid strain control mode, the fatigue response of the neat matrix was dominated by creep deformation.

0° Lamina

(1) The nonlinear stress-strain response of the 0° lamina, on the first loading cycle, was the result of the matrix plastically deforming above a strain level of .55%.

(2) For the fiber dominated failure mode (maximum strain greater then .73%) the progression of damage in the 0° lamina was: matrix plastic deformation, matrix creep deformation, and finally, rapid fracture of the fibers leading to specimen failure.

(3) For the matrix dominated failure mode (maximum strain less than .73%) the progression of damage was: plastic deformation of the matrix when the maximum strain level was above .55%, matrix creep deformation, a period of self-equilibrating matrix creep and the matrix cracks to develop, and finally, propagation of the matrix cracks result in a loss of stiffness.

90° Lamina

(1) The initiation of fiber-matrix interface damage was modeled as a progressive damage mechanism.

(2) A simple degradation of the bond strength, as a function of fatigue cycles, was applied to model the propagation of the fiber-matrix interface damage.

(3) The analysis suggested that the fiber-matrix interface of the SCS-6/Ti-15-3 MMC has a non-zero bond strength.

(4) The damage in the 90° lamina subjected to fatigue with a maximum strain level below .23% was dominated by the initiation and progression of fiber-matrix interface damage. This damage was accompanied by creep deformation of the matrix.

(5) After the initiation of fiber-matrix interface damage in the first loading cycle, the progression of fatigue damage in the 90° lamina tested in fatigue with a maximum strain level above .23%, but less then .35%, was: the development of small matrix cracks, and then a progression of the fiber-matrix interface damage and an accumulation of matrix creep deformation.

(6) After the initiation of fiber-matrix interface damage in the first loading cycle, the damage in the 90° lamina tested in fatigue with maximum strain level greater than .35% was dominated by the initiation and propagation of matrix cracks.

VII. Conclusions and Recommendations

The fatigue behavior of a unidirectional Metal Matrix Composite (MMC) was characterized at elevated temperature (427°C) using a hybrid strain controlled loading mode. Through a systematic series of experiments, the 0° and 90° MMC (SCS-6/Ti-15-3) laminas subjected to fatigue were investigated. Also, an extensive microscopic analysis was performed to identify the initiation and progression of damage mechanisms due to fatigue. These two parts of the study led to the development of fatigue life curves, which related the number of fatigue cycles to failure to the dominant damage mechanism. Finally, the results obtained from the fatigue tests and the microscopic analysis were verified by analytical techniques.

For the 0° lamina (fibers parallel to the loading direction), the fatigue response was dictated by one of two failure modes. For the specimens subjected to fatigue above a maximum strain of .73%, the fatigue response was initially dominated by plastic and creep deformation of the matrix. However, fiber fractures resulted in specimen failure. When a specimen was subjected to fatigue below a maximum strain of .73%, the dominant failure mode was matrix cracking. It was shown that the stress response could be partitioned into two stages. In Stage I, matrix creep was the dominant

deformation mechanism, which was accompanied by plastic deformation of the matrix above a strain level of .55%. Eventually, a period of self-equilibrating creep occurred in the matrix. This was an incubation period for the development of matrix cracks. In Stage II, these cracks began to propagate, which resulted in a loss of stiffness and a concurrent reduction in the lamina stress.

The results obtained from the fatigue tests and the microscopic analysis were used to generate a fatigue life curve. This fatigue curve was partitioned into three regions. Each region was associated with a specific failure mode. In Region I, the failure was dominated by fiber fractures, which was shown to occur when the maximum strain was greater than .73%. Fatigue life of the MMC in Region II was shown to be dominated by matrix cracks. This region was defined for those specimens subjected to fatigue at a maximum strain less than .73% but greater than .3%. Finally, when the maximum strain was less than .3%, the matrix fatigue limit was reached. The fatigue life of a specimen subjected to fatigue at these strain levels would be greater than 10^7 cycles.

For the 90° lamina (fibers perpendicular to the loading direction), the fatigue response was dominated by the fiber-matrix interface damage. On the first loading cycle, this damage mechanism was observed to initiate at a strain level

above .1%. The subsequent fatigue response was also dependent on the maximum strain level. For example, for the specimens loaded in fatigue above a strain level of .35%, the dominant damage mechanism was the propagation of matrix cracks. For those specimens subjected to fatigue at a strain level below .35%, but greater than .23%, small matrix cracks were found emanating from the fiber-matrix interface. These cracks did not propagate through the specimen to cause failure. Instead, a progression of the fiber-matrix interface damage occurred, along with a significant accumulation of matrix creep deformation. For those specimens subjected to fatigue below a strain level of .23%, only a small amount of fiber-matrix interface damage occurred on the first loading cycle. In fact, the stress-strain response was linearly elastic below a strain level of .1%. There was no evidence of matrix cracks when the strain level was below .23%. In these cases, the damage was limited to a progression of fiber-matrix interface damage.

As in the case of the 0° lamina, the results obtained from the fatigue tests and the microscopic analysis were used to generate a three region fatigue life curve. In Region I, the fatigue life was shown to be dominated by matrix cracks, which occurred for those specimens loaded above a maximum strain greater than .35%. Region II was further partitioned into two subregions. The first

subregion (IIa) was defined when the maximum strain was in the range of .23% to .35%. In this subregion, the fatigue damage was a combination of small matrix cracks and a progression of the fiber-matrix interface damage. Subregion IIb was defined by those specimens subjected to fatigue below a strain level of .23%. The damage in this region was limited to a breakdown of the fiber-matrix interface. Finally, Region III was defined as the fiber-matrix interface fatigue limit. The upper limit of this region was defined at a maximum strain level of .05%, which was approximated by combining the results observed in the experiments with those predicted in the analysis. There should be no fiber-matrix interface damage in this region.

To complement the experiments and microscopic analysis, analytical techniques were applied to provide further insight into the fatigue behavior of the MMC. Two micromechanical models were used in the analysis to predict the fatigue response of the 0° and 90° lamina, which were the concentric cylinder model (CCM) and the strip model (SM), respectively. There were two methods incorporated into the SM for predicting the fiber-matrix interface damage. The first method characterized the initiation of damage, which occurs on the first loading cycle. It was shown that the parameters used for this method could be calibrated from only one loading curve of the 90° lamina.

The second method characterized the progression of the fiber-matrix interface damage, which occurs when the specimen is loaded in fatigue.

A scheme was proposed to predict the fatigue response of the neat matrix. This scheme was based on the availability of data from a few relaxation tests of the neat matrix and one static test of the neat matrix. The relaxation scheme was successfully applied, in the CCM and the SM, to predict the fatigue response of the MMC at elevated temperature.

The recommendations for future research include investigations in both the experimental and the analytical areas and are summarized below:

(A) Experiments

(1) Conduct fatigue tests using the hybrid strain controlled loading mode on the 0° lamina at strain levels less than or equal to .3%. This will help to better identify the lamina fatigue limit.

(2) Conduct fatigue tests using the hybrid strain controlled loading mode on the 90° lamina at strain levels less than or equal to .05%. This will help to better identify the fiber-matrix interface fatigue limit.

(3) Conduct fatigue tests using the same strain range but different mean strains. This will quantify the dependence of the fatigue life on the strain range.

(4) Conduct fully reversed, strain controlled fatigue tests on the unidirectional lamina (0° and 90°). This will better simulate the actual loading conditions.

(B) Analysis

(1) Extend the SM to account for the development and propagation of matrix cracks. One possible method is to formulate an evolutionary law which relates the number of fatigue cycles at a given stress level to the crack propagation rate.

(2) Include the effects of matrix cracking and fiber-matrix interface damage in the CCM. These methods could be similar to the method proposed for the SM.

(3) Study the effects of fiber fracture on the fatigue response of the 0° lamina.

(4) There has been no systematic study to relate the fatigue life of a laminate to its basic lamina. A natural extension of this work would be to perform a systematic series of fatigue tests, using the strain control mode, on the [0/90] laminate. This should be coupled with a micromechanical analysis and a thorough microscopic evaluation.

References

1. Aboudi, J., "Elastoplasticity Theory for Composite Materials," Solid Mechanics Archives, Vol. 11, 1986, pp 141-183.

2. Aboudi, J.,"Closed Form Constitutive Equations for Metal Matrix Composites," International Journal of Engineering Science, Vol. 25, 1987, pp. 1229-1240.

3. Adams, D.F., "Micromechanical Modeling of Yielding and Crack Propagation in Unidirectional Metal Matrix Composites,"Testing Technology of Metal Matrix Composites, ASTM STP 964. P.R. DiGiovanni and N.R. Adsit, Eds., American Society for Testing and Materials, Philadelphia, 1988, pp. 93-103.

4. Ankem S., Seagle S.R., "Heat Treatment of Metastable Beta Titanium Alloys."Beta Titanium Alloys in the 80's, Boyer, R.R., Rosenberg H.W., Eds., A Publication of the Metallurgical Society of AIME, 1984, pp 107-126.

5. Argon, A.S., Physics of Strength and Plasticity. The Massachusetts Institute of Technology, 1969.

6. Bahie-El-Din, T.A., "Plasticity Analysis of Metal Matrix Composite Laminates,". Ph.D. Dissertation, Duke University, 1979.

7. Bahie-El-Din Y.A., "Plasticity Analysis of Fibrous Composite Laminates Under Thermomechanical Loads," Thermal and Mechanical Behavior of Metal Matrix and Ceramic Composites, ASTM STP 1080. J.M. Kennedy, H.H. Moeller, and W.S. Johnson, Eds., American Society for Testing and materials, Philadelphia, 1990, pp 20-39.

8. Bania, P.J., Lenning G.A., Hall, J.A., "Development and Properties of Ti-15V-3Cr-3Sn-3Al (Ti-15-3)." Beta Titanium Alloys in the 80's, Boyer, R.R., Rosenberg H.W., Eds., A Publication of the Metallurgical Society of AIME, 1984, pp 209-229.

9. Bartolotta P.A. and Brindley P.K. "High Temperature Fatigue Behavior of a SiC/Ti-24Al-11Nb Composite," NASA TM-103157, April 1990.

10. Bartolotta, P.A., "Low Cycle Life Prediction of A Intermetallic Matrix Composite at Elevated Temperatures," NASA Lewis research Center, Cleveland, Ohio.

11. Bhatt, R.T., Phillips, R.E., "Laminate Behavior for SiC Fiber-Reinforced reaction-Bonded Silicon Nitride Matrix Composites," NASA TM-101350, October 1988.

12. Bigelow, C.A., Johnson, W.S., Naik, R.A., "A Comparison of Various Micromechanics Models for Metal Matrix Composites", NASA Langley Research Center, Hampton, Virginia. Presented at the Third Joint ASCE/ASME Mechanics Conference, University of California, San Diego, La Jolla, California, July 1989.

13. Blackburn, M.L., Williams, J.C., "Phase Transformations in Ti-Mo and Ti-V Alloys." Transactions of the Metallurgical Society of AIME, Volume 242, December 1968, pp 2461-2469.

14. Bodner, S.R., "Review of a Unified Elastic-Viscoplastic Theory," Unified Constitutive Equations for Plastic Deformation and Creep of Engineering Alloys. A.K. Miller, Ed., Elsevier Applied Science Publishers, 1987.

15. Bowen, A.W., "Omega Phase Formation in Metastable β-Titanium Alloys."Beta Titanium Alloys in the 80's, Boyer, R.R., Rosenberg H.W., Eds., A Publication of the Metallurgical Society of AIME, 1984, pp 85-103.

16. Broek, D, Elementary Engineering Fracture Mechanics. Netherlands: Martinus Nijhoff Publishers, 1986.

17. Brown, H.C. and Chamis, C.C., "Computational Characterization of High-Temperature Composites Via METCAN". NASA Conference Publication 10051, HITEMP Review October, 1990. pp. 46-1-6.

18. Brindley, R.A. MacKay, Bartolotta, "Thermal Cycling Isothermal Fatigue of SiC/Ti-24-11Nb", NASA Conference Publication 10051, HITEMP Review October, 1990. pp 38-1-38.

19. Caruso, J.J., Chamis, C.C., "Assessment of Simplified Composite Micromechanics Using Three-Dimensional Finite Element Analysis," Journal of Composites Technology & Research, Vol. 8, No 3, Fall 1986, pp. 77-83.

20. Caruso, J.J., Chamis, C.C., "Superelement Methods Applications to Micromechanics of High Temperature Metal Matrix Composites.

21. Chamis, C.C. and Hopkins D.A., "Thermoviscoplastic Nonlinear Constitutive Relationships for Structural Analysis of High-Temperature Metal Matrix Composites," Testing Technology of Metal Matrix Composites, ASTM 964, P.R. Digiovanni and N.R. Adsit, Eds., American society for Testing and Materials, Philadelphia, 1988, pp. 177-196.

22. Chamis, C.C., Murthy, L.N., and Hopkins, D.A. "Computational Simulation of High-Temperature Metal Matrix Composites Cyclic Temperature," Thermal and Mechanical Behavior of Metal Matrix and Ceramic Matrix Composites, ASTM 1080, J.M. Kennedy, H.H. Moeller, and W.S. Johnson, Eds., American Society of Testing and Materials, Philadelphia, 1990, pp. 56-69.

23. Coker, D., Ashbaugh, N.E., Elastic-Plastic Finite Difference Analysis of Unidirectional Composites Subjected to Thermomechanical Cyclic Loading, WL-TR-93-000, December 1992.

24. Continuum Damage Mechanics, edited by Krajcinovic D. and Lemaitre J, CISM, Udine, 1987.

25. Costa, J.E., Banerjee, D., Williams, J.C. "Hydrogen Effects in β-Titanium Titanium Alloys."Beta Titanium Alloys in the 80's, Boyer, R.R., Rosenberg H.W., Eds., A Publication of the Metallurgical Society of AIME, 1984, pp 107-126.

26. Ermer, Capt Paul G. Investigation of the Failure Modes in a Metal Matrix Composite Under Thermal Cycling. MS Thesis, AFIT/GAE/ENY/89D-07. School of Engineering, Air Force Institute of Technology (AU), Wright-Patterson AFB OH, December 1989.

27. Findley, W.N., Lai J.S., Onaran K.. Creep and Relaxation of Nonlinear Viscoelastic Materials with an Introduction to Linear Viscoelasticy. North-Holland Publishing Company, 1976.

28. Folias, E.S., "On the Prediction at a Fiber/Matrix Interface in a Composite Subjected to a Transverse Tensile Load.". Journal of Composite Material, Vol. 25 1991.

29. Foye, R.L., " An Evaluation of Various Engineering Estimates of the Transverse Properties of Unidirectional Composites," Proceedings of the Tenth National SAMPE Symposium - Advanced Fibrous Reinforced Composites, November 1966.

30. Gabb, T.P, Gayda, J. and Learch, B.A.. "The Effect of Environment on the Fatigue Life of SiC/Ti-15-3 Composite,"The Sixth Thermomechanical Fatigue Workshop, NASA Lewis Research Center, Cleveland, Ohio, June 5-6, 1991.

31. Gabb, T.P, Gayda, J. and MacKay, R.A.. "Isothermal and Nonisothermal Fatigue Behavior of a Metal Matrix Composite,"Journal of Composite Materials, Vol. 24 - June 1990.

32. Gabb, T.P, Gayda, J. and MacKay, R.A.. "Nonisothermal Fatigue Degradation of a SiC/Ti," Journal of Composite Materials, Vol. 24 - June 1990.

33. Gabb T.P., Gayda J., Learch B.A., Halford G.R.. "The Effect of Matrix Mechanical Properties on $[0]_8$ Unidirectional SiC/Ti Composite Fatigue Resistance." Scripta Metallurgica, Vol. 25 pp 2879-2884, 1991

34. Gayda, J, Gabb, T.P. and Freed, A.D. "The Isothermal Fatigue Behavior of Unidirectional SiC/Ti Composite and the Ti Alloy Matrix," NASA TM-101984, April 1989.

35. Gayda, J, Gabb, T.P. " Isothermal Fatigue Behavior of a $[90]_8$ Sic/Ti-15-3 Lamina at 426°C," NASA TM-103686, January 1991.

36. Gayda, J. and Gabb, T.P. "Effect of Heating Mode and Specimen Geometry on Fatigue Properties of a Metal Matrix Composite", NASA Conference Publication 10051, HITEMP Review October, 1990. pp 31-1-8.

37. Harmon, D.M., Saff, C.R., Graves, D.L., "Strength Predictions for Metal Matrix Composites," Metal Matrix Composites: Testing, Analysis, and Failure Models, ASTM STP 1032. Johnson, W.S., Ed, American Society for Testing and Materials, Philadelphia, 1989, pp 222-236.

38. Halford, G.R., "Low Cycle Thermal fatigue." NASA TM-87225, February 1986.

39. Hartman, G and Nichlos T. "An Enhanced Laser Interferometer for Precise Displacement Measurement", Experimental Techniques, February, 1987.

40. Hashin, Z. "The Elastic Moduli of Heterogeneous Materials", Journal of Applied Mechanical, March, 1962. pp 143-150.

41. Hashin Z., Rosen B.W., "The Elastic Moduli of Fiber-Reinforced Materials."Journal of Applied Mechanical, June, 1964. pp 223-219.

42. Hashin, Z. "Viscoelastic Behavior of Heterogeneous Media", Journal of Applied Mechanical, September, 1965. pp 630-636.

43. Herakovich, C.T., Aboudi, J., Lee, S.W., "Nonlinear Composite Materials Micromechanics Model", Report on GE P.O.#200-14-14P94319, General Electric Company, September 1987.

44. Hicks, A.G., RosenBerg, H.W., "Ti-15-3 Foil Properties and Applications." Beta Titanium Alloys in the 80's, Boyer, R.R., Rosenberg H.W., Eds., A Publication of the Metallurgical Society of AIME, 1984, pp 231-237.

45. Highsmith, A.L., Reifsnider, K.L., "Stiffness-Reduction Mechanisms in Composite Laminates," Damage in Composite Materials, ASTM STP 775, K.L. Reifsnider, Ed., American Society for Testing and Materials, 1982, pp 103-117.

46. Highsmith, A.L., Reifsnider, K.L., "Internal Load Distribution Effects During Fatigue Loading of Composite Laminates." Composite Materials: Fatigue and Fracture, ASTM STP 907, H.T. Hahn, Ed., American Society for Testing and Materials, Philadelphia, 1986, pp. 233-251.

47. Highsmith, A. L., Shin, D., and Naik, R.A. "Local Stresses in Metal Matrix Composites Subjected to Thermal and Mechanical Loading," Thermal and Mechanical Behavior of Metal Matrix Composites and Ceramic Matrix Composites, ASTM STP 1080, J.M. Kennedy, H.H. Moeller, and W.S. Johnson, Eds., American Society for Testing and Materials, Philadelphia, 1990, pp. 3-19.

48. Hopkins, D.A. and Chamis, C.C. "A Unique Set of Micromechanics Equations for High Temperature Metal Matrix Composites," NASA TM-87154.

49. Hwang, W. and Han, K.S., "Fatigue of Composite Materials - Damage Model and Life Prediction," Fatigue and Fracture, Second Volume, ASTM STP 1012, Paul A. Lagace, Ed., American Society for Testing and Materials, Philadelphia, 1989, pp. 87-102.

50. Jackson A.G., Handbook of Crystallography. Springer-Verlag, 1991

51. Jansson, S., Leckie, F.A., "Thermal, Mechanical, and Creep Behavior of Metal Matrix Composites," NASA Conference Publication 10051, HITEMP Review October, 1990. pp 31-1-8.

52. Jeng S.M., Yang, C.J., Alassoeur P., Yang J.M.," Deformation and Fracture Mechanisms of Fiber Reinforced Titanium Alloy Matrix Composites. Department of Materials Science and Engineering, UCLA, CA.

53. Johnson, W.S., "Fatigue Testing and Damage Development in Continuous Fiber Reinforced Metal Matrix Composites," NASA TM-100628, June 1988.

54. Johnson, W.S., Lubowinski, S.J. and Highsmith, A.L.. "Mechanical Characterization of Unnotched SCS_6/Ti-15-3 Metal Matrix Composites at Room Temperature," Thermal and Mechanical Behavior of Metal Matrix and Ceramic Matrix Composites, ASTM STP 1080, J.M. Kennedy, H.H. Moeller, and W.S. Johnson, Eds., American Society of Testing and Materials, Philadelphia, 1990, pp. 193-218.

55. Jones, R.M.. Mechanics of Composite Materials. Hemisphere Publishing Corporation, 1975.

56. Kachanov L.M., Introduction to Continuum Damage Mechanics, Martinus Nijhoff Publishers, 1986.

57. Kobaib, M, "Creep Behavior of SCS-6/β-21S Composite" National Institute of Composites Steering Committee Meeting, St. Louis Mo, June 25-26, 1993.

58. Learch, B.A., "Fatigue Behavior of SiC/Ti-15-3 Laminates,"NASA Conference Publication 10051, HITEMP Review October, 1990. pp 35-1-8

59. Learch, B.A., "Matrix Plasticity in SiC/Ti-15-3 Composite," NASA TM 103760, July 1991.

60. Learch, B.A. and Hull, D.R., "As-Received Microstructure of SiC/Ti-15-3 Composite," NASA TM-100938, August 1988.

61. Learch B.A., Melis M.E., "Experimental and Analytical Analysis of Stress-Strain Behavior in a $[90/0]_{2s}$, SiC/Ti-15-3 Laminate," NASA TM-104470, August 1991.

62. Learch B.A., Gabb T.P and MacKay, R.A. "Heat Treatment Study of the SiC/Ti-15-3 Composite System," NASA TP-2970, January 1990.

63. Learch B.A., Saltsman J.F.. "Tensile Deformation Damage in SiC Reinforced Ti-15V-3Cr-3Al-3Sn." NASA TM-103620, April 1991.

64. Lee, H. and Murthy, L.N., "METCAN Updates for High-Temperature Composite Behavior: Simulation/Verification". NASA Conference Publication 10051, HITEMP Review October, 1990. pp 43-1-9.

65. Lee Y.S., Gungor, M.N., Liaw P.K., "Modeling of Transverse Mechanical Behavior of Continuous Fiber Reinforced Metal Matrix Composites." Journal of Composite Materials, Vol. 25, May 1991.

66. Majumdar, B.S, and Newaz G.M., "Thermo-Mechanical Fatigue Response and Damage in an Angle-Ply Metal Matrix Composite," Battelle Memorial Institute, Columbus, OH. Submitted to The Journal of Engineering Materials and Technology - ASME, October, 1989.

67. Majumdar, B.S, and Newaz G.M., "Thermo-Mechanical Fatigue of a Quasi-Isotropic Metal Matrix Composite," Battelle Memorial Institute, Columbus, OH. Presented at the Third Symposium on Composite Materials: Fatigue and Fracture, Orlando, Fla. November, 1989.

68. Majumdar, B.S, and Newaz G.M., "Inelastic Deformation of Metal Matrix Composites:Plasticity and Damage Mechanisms", Philosophical Magazine , 1992, Vol. 66, No. 2, 187-212.

69. Majumdar, B.S, and Newaz G.M., "Mechanisms of Fatigue Damage and Failure of a SCS6/Ti-15-3 Composite", ASM/TMS Proceedings of Mechanisms of Composite Fractures, Oct 1993.

70. Mahulikar, D.S., Park, T.H., Marcus H.L.. "Environmental Influences on the Fracture and Fatigue Properties of Titanium Metal-Matrix Continuous Fiber Composites," Fracture Mechanics: Fourteenth Symposium - Volume II: Testing and Applications, ASTM STP 791, J.C. Lewis and Sines, Eds., American Society for Testing and Material, 1983 pp. II-579-II-597.

71. Mall, S., Ermer, P.G., "Thermal Fatigue Behavior of a Unidirectional SCS6/Ti-15-3 Metal Matrix Composite."Journal of Composite Materials, Vol. 25, December 1991, pp 1668-1686.

72. Masters, J.E., Reifsnider, K.L., "An Investigation of Cumulative Damage Development in Quasi-Isotropic Graphite/Epoxy Laminates," Damage in Composite Materials, ASTM STP 775, K.L. Reifsnider, Ed., American Society for Testing and Materials, 1982, pp. 40-62.

73. Mechanical Metallurgy, Edited by Meyers, M.A. and Chawla, K.K., New Jersey: Prentice-Hall, Inc., 1984.

74. Mendelson, A., Plasticity:Theory and Application. Robert E. Krieger Publishing Company, 1983.

75. Micricon Control PID Adjustments, Research Inc., Minneapolis Mn, 1981

76. Micricon User's Manual. Research Inc., Minneapolis, MN, 1986.

77. Mirdamadi, M., Johnson W.S., Bahie-El-Din Y.A., Castelli, M.G.. "Analysis of Thermomechanical Fatigue of Unidirectional Titanium Metal Matrix Composites," NASA TM 104105, July 1991.

78. Mitchell, M.R.. Fatigue and Microstructure, ASM Materials Science Seminar, ASM, St Louis, MO, 1978, pp 385-437.

79. Murthy P.L.N., Chamis, C.C., "Micromechanics for Ceramic Matrix Composites", NASA Lewis Research Center, Cleveland, Ohio, Unpublished.

80. Newaz G.M., Majumdar B.S., "Thermal Cycling Response of Quasi-Isotropic Metal Matrix Composite," Battelle Memorial Institute, Columbus, OH. Submitted to The Journal of Engineering Materials and Technology - ASME.

81. Nimmer, R.P., "Fiber-Matrix Interface Effects in the Presence of Thermally Induced Residual Stresses", General Electric Company, Corporate Research and Development, Schenectady, New York.

82. Nimmer R.P., Bandert R.J., Russell E.S., Smith G.A., "Micromechanical Modeling of Fiber/Matrix Interface Effects in SiC/Ti Metal Matrix Composites." General Electric Company, Corporate Research and Development, Schenectady, New York. Case # 89-0576

83. O'Brien, T.K., Reifsnider, K.L., "Fatigue Damage Evolution through Stiffness Measurements in Boron-Epoxy Laminates," Journal of Composite Materials, Vol. 15, January 1981, p 55.

84. Plumtree, A.,"Fatigue Damage Evolution and Life Prediction," Proceedings From Fatigue 90.

85. Pollock, W.D. and Johnson W.S. "Characterization of Unnotched SCS-6/Ti-15-3 Metal Matrix Composites at 650°C," NASA TM-102699, September 1990.

86. Polmear, I.J., Light Alloys. Metallurgy of the Light Metals. Edward Arnold Publishers Ltd, 1981.

87. Popov, E.P., Mechanics of Materials, second edition. Prentice-Hall, Inc., 1976

88. Pernot, Capt John J., Crack Growth Rate Modeling of A Titanium-Aluminide Alloy Under Thermal-Mechanical Cycling. Dissertation, AFIT/DS/AA/91/3. School of Engineering, Air Force Institute of Technology (AU), Wright-Patterson AFB OH, December 1991.

89. Portner, Capt Barry D. Investigation of the Fatigue Damage Mechanisms in a Metal Matrix Composite Under Elevated. MS Thesis, AFIT/GAE/ENY/90D-07. School of Engineering, Air Force Institute of Technology (AU), Wright-Patterson AFB OH, December 1990.

90. Reinsch, W.A., Rosenberg, H.W., "Three Recent Developments in Titanium Alloys." Metals Progess, March 1980.

91. Reifsnider, K.L., Schulte, K, Duke, J.C., "Long Term Fatigue Behavior of Composite Materials." Long Term Behavior of Composites, ASTM STP 813, T.K. O'Brien, Ed., American Society for Testing and Materials, Philadelphia, 1983, pp. 136-159.

92. Reifsnider K.L. and Stinchcomb W.W., "A Critical Element Model of the Residual Strength and Life of Fatigue Loaded Composite Coupons,", Composite Material:Fatigue and Fracture, ASTM STP 907, H.T. Hahn, Ed., American Society for Testing and Materials, Philadelphia, 1986, pp. 298-313.

93. Robertson, Capt Dave D. MicroMechanical Modeling of the Fiber/Matrix Interface Region in a Metal Matrix Composite. MS Thesis, AFIT/GAE/ENY/90D-022. School of Engineering, Air Force Institute of Technology (AU), Wright-Patterson AFB OH, December 1990.

94. Rogacki, J., Tuttle M., "An Investigation of the Thermoviscoplastic Behavior of a Metal Matrix Composites at Elevated Temperatures," NASA CR 189706, October 1992.

95. RosenBerg, H.W., "Ti-15-3 Property Data. "Beta Titanium Alloys in the 80's, Boyer, R.R., Rosenberg H.W., Eds., A Publication of the Metallurgical Society of AIME, 1984, pp 107-126.

96. Rotem, A., Hashin, Z., "Fatigue Failure of Angle Ply Laminates.", AIAA Journal, Vol. 14, NO.7, July 1976, pp 868-872.

97. Rotem A., Nelson H.G., "Fatigue Behavior of Graphite-Epoxy Laminates at Elevated Temperature," Fatigue of Fibrous Composite Material, ASTM STP 723, American Society for Testing and Materials, 1981, pp 152-173.

98. Rudy, E., "Compendium of Phase Diagram Data, AFML-TR-65-2, Part V. Air Force Materials Laboratory, Metals and Ceramics Division, Wright-Patterson AFB, Ohio

99. Russ S.M., Nicholas T., Bates M., Mall S., "Thermomechanical Fatigue of SCS-6/Ti-24Al-11NB Metal Matrix Composite." Symposium on "Failure Mechanisms in High Temperature Composites", 1991 ASME Winter Annual Meeting, Atlanta, GA, Dec. 1-6, 1991.

100. Sadda A.S.. Elasticity Theory and Applications, Robert E. Krieger Publishing Company, 1987.

101. Schubbe, Capt Joel J. Investigation of the Damage Mechanisms in a Cross Ply Metal Matrix Composite Under Thermo-Mechanical Loading. MS Thesis, AFIT/GAE/ENY/90D-07. School of Engineering, Air Force Institute of Technology (AU), Wright-Patterson AFB OH, December 1990.

102. Sullivan, B.J., Buesking, K.W., "Effects of Carbon Interface Morphology on the Residual Stresses in Silicon Carbide/Titanium Composites", 21st Carbon Conference, Buffalo, NY, June 13-18, 1993.

103. Sun C.T., Chen J.L., "A Simple Flow Rule for Characterizing Nonlinear Behavior of Fiber Composites." Journal of Composite Materials, Vol. 24 October 1989.

104. Sun C.T., Chen J.L., "A Micromechanical Model for Plastic Behavior of Fibrous Composites." Composites and Science Technology, February 1990.

105. Sun C.T., Chen J.L., Sha G.T., Koop W.E., "Mechanical Characterization of SCS-6/Ti-6-4 Metal Matrix Composites." Journal of Composite Materials, Vol. 24 October 1990.

106. Talreja, R. Fatigue of Composite Materials, Technomic Publishing Company, 1987.

107. Whitney, J.M., "A residual Strength Degradation Model for Competing Failure Modes," Long Term Behavior of Composites, ASTM STP 813, T.K. O'Brien, Ed., American Society for Testing and Materials, Philadelphia, 1983, pp. 225-245.

108. Worthem, D.W., "Flat Tensile Specimen Design for Advanced Composites" NASA Contract Report 185261, November 1990.

Appendix A

Additional Experimental Results - 0° Lamina

This appendix contains additional raw data that was not presented in other locations of the document. This includes plots of the:

(1) Histories of the maximum strain and minimum strain for all of the specimens tested in fatigue

(2) Histories of the stress-strain response

(3) Histories of the minimum stress, maximum stress, and modulus showing the stages of damage and deformation as described in Chapter IV.

In all of the plots the lines are drawn to show the data trend and are not predictions.

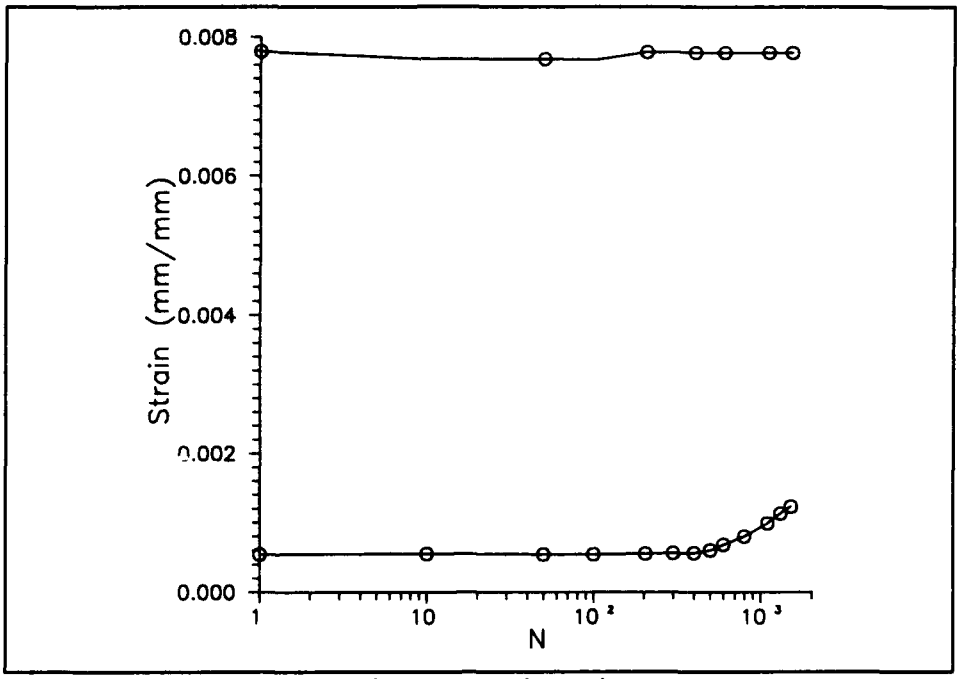

Figure A.1 0° Lamina Strain history, ϵ_{max}= .77%

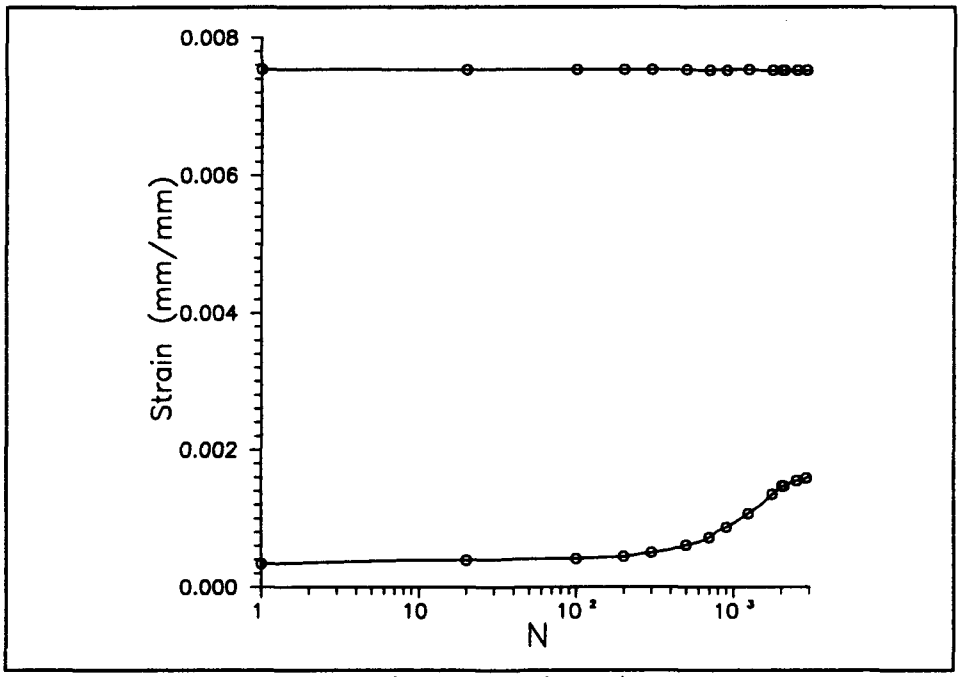

Figure A.2 0° Lamina Strain History, ϵ_{max}=.75%

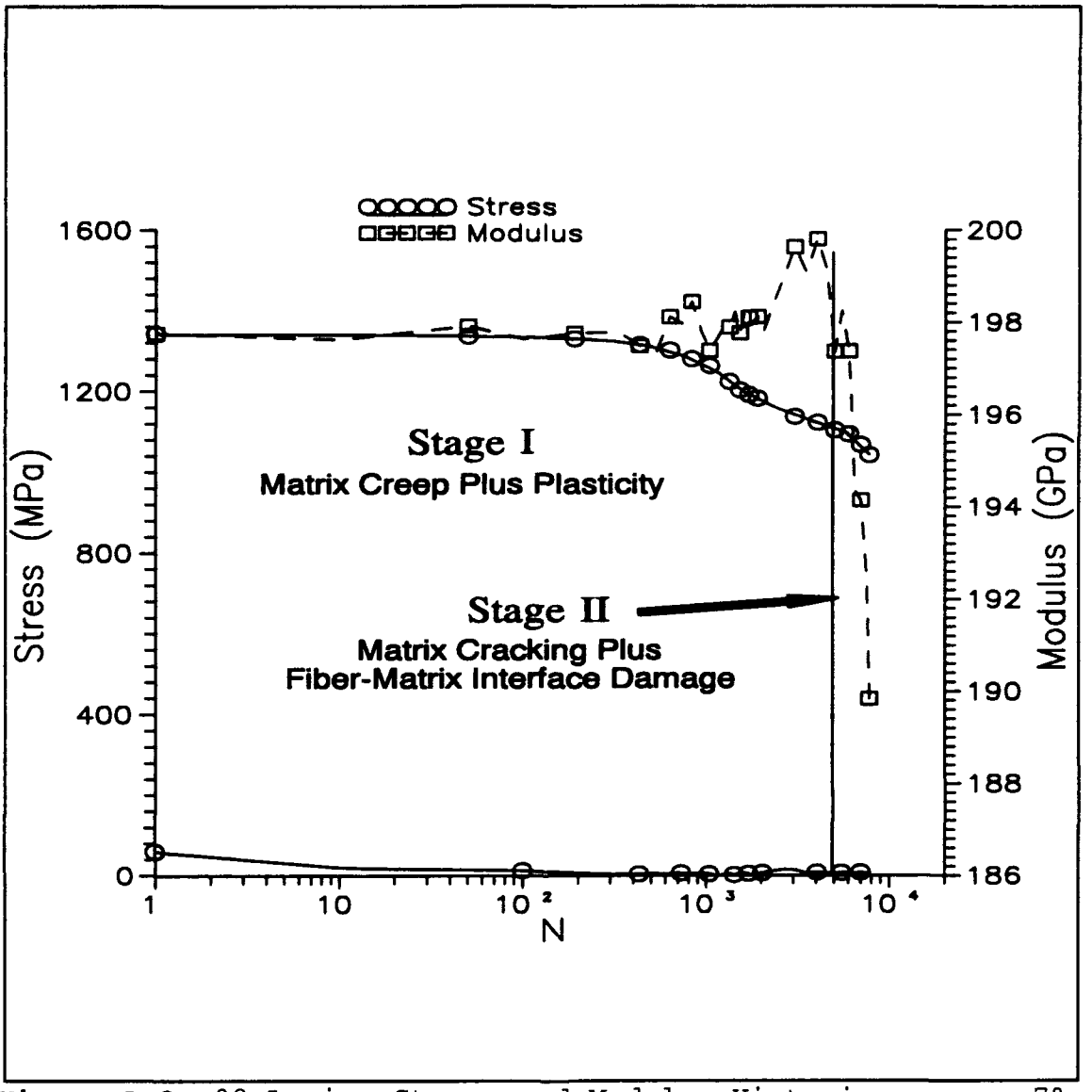

Figure A.3 0° Lamina Stress and Modulus Histories, ϵ_{max}= .7%

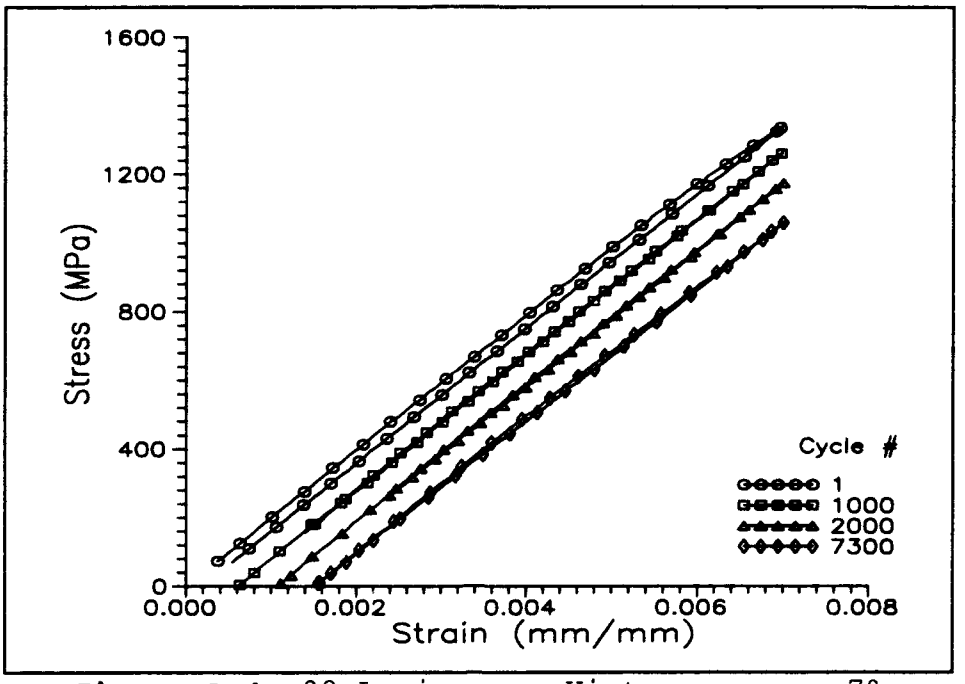

Figure A.4 0° Lamina σ-ϵ History, ϵ_{max}= .7%

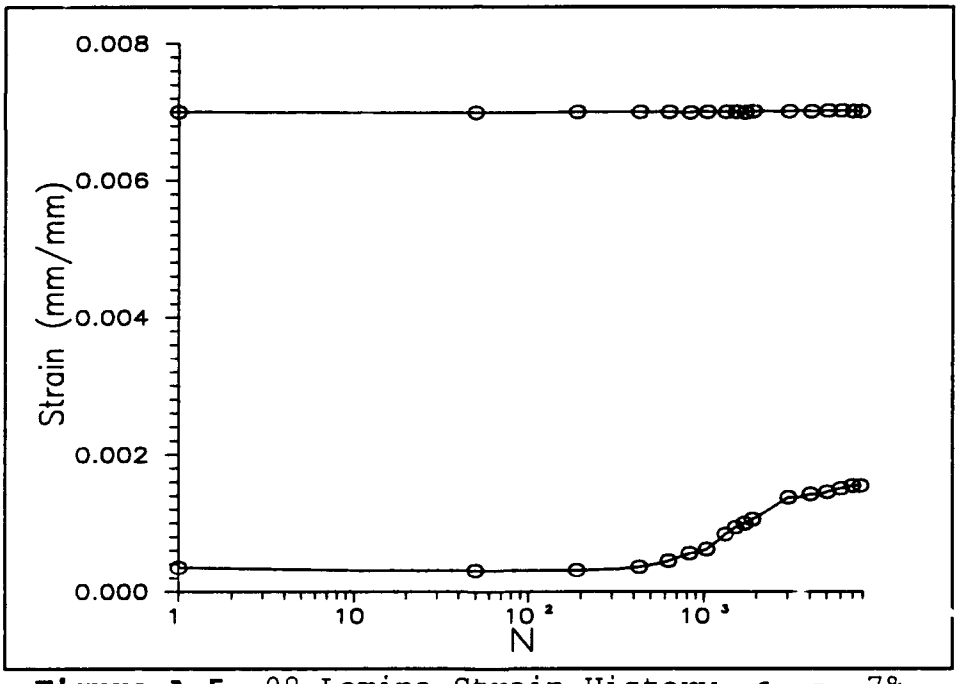

Figure A.5 0° Lamina Strain History, ϵ_{max}= .7%

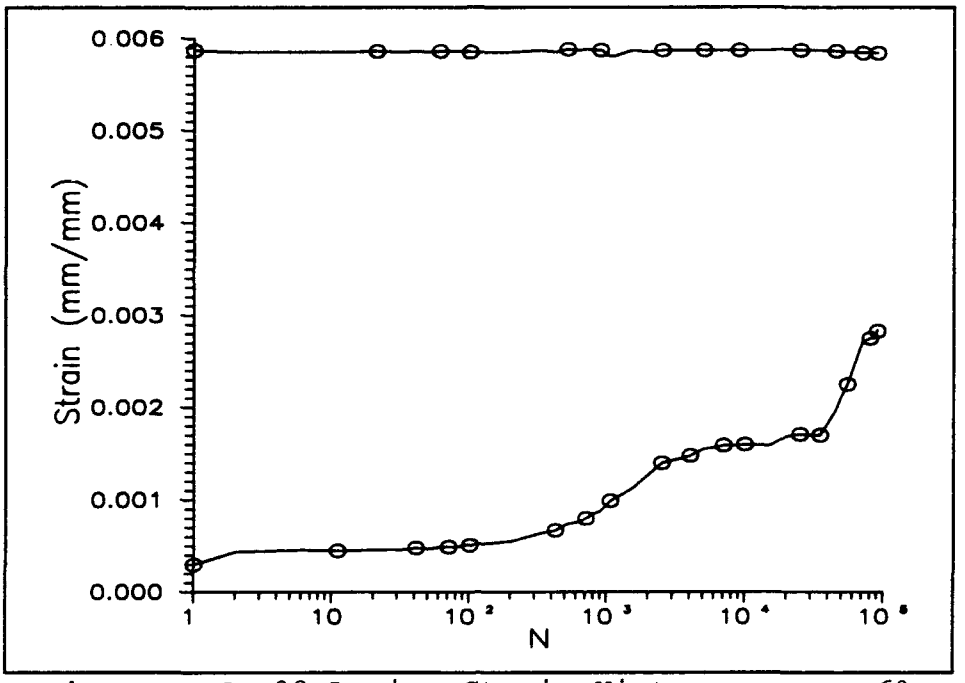

Figure A.6 0° Lamina Strain History, ϵ_{max}= .6%

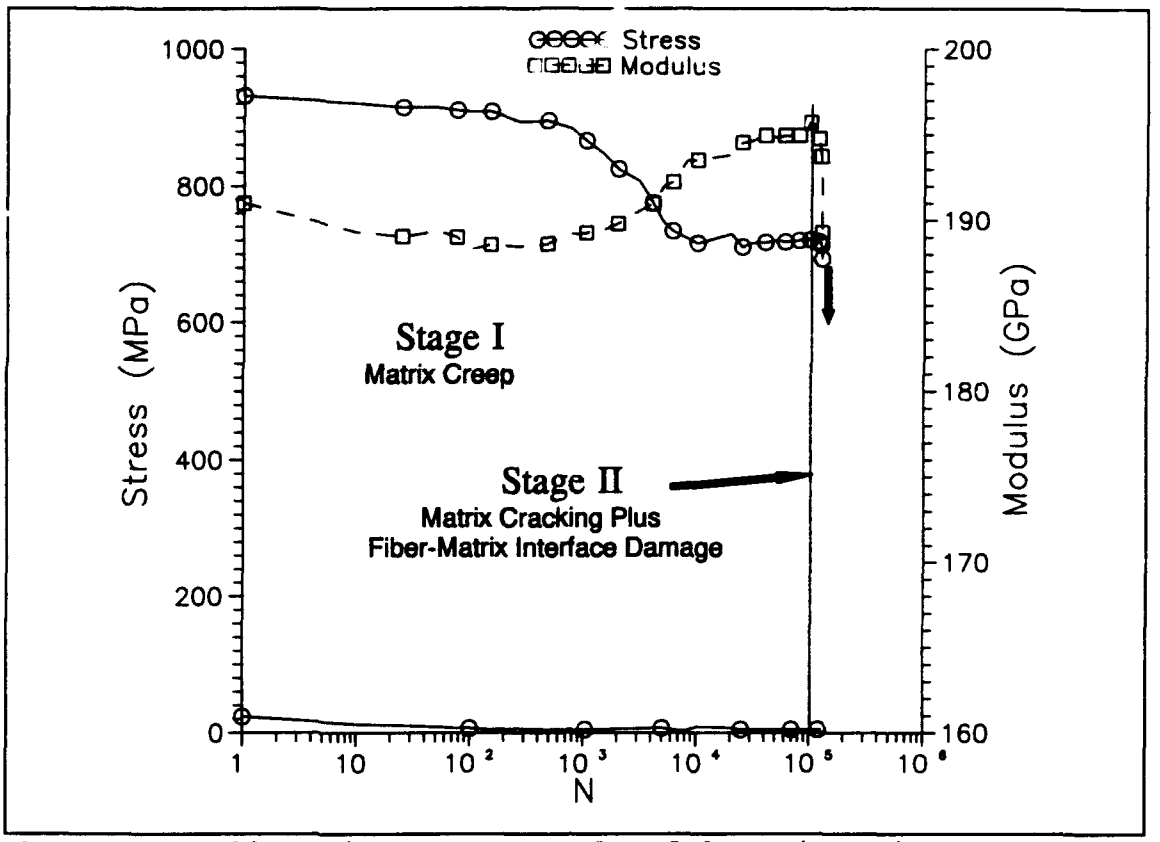

Figure A.7 0° Lamina Stress and Modulus Histories, ϵ_{max}=.5%

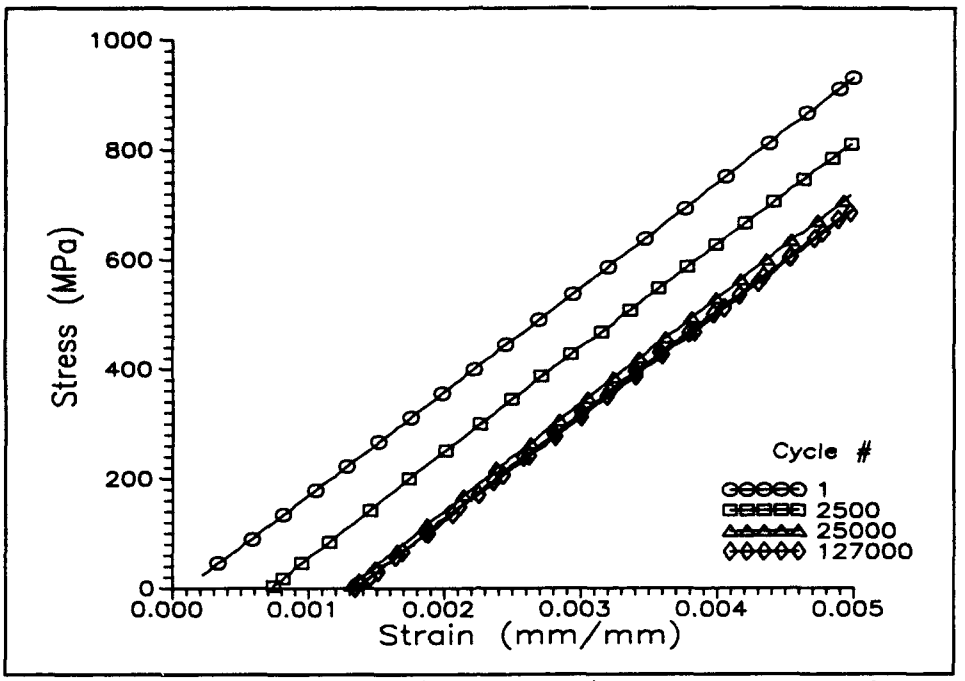

Figure A.8 0° Lamina σ-ϵ History, ϵ_{max}= .5%

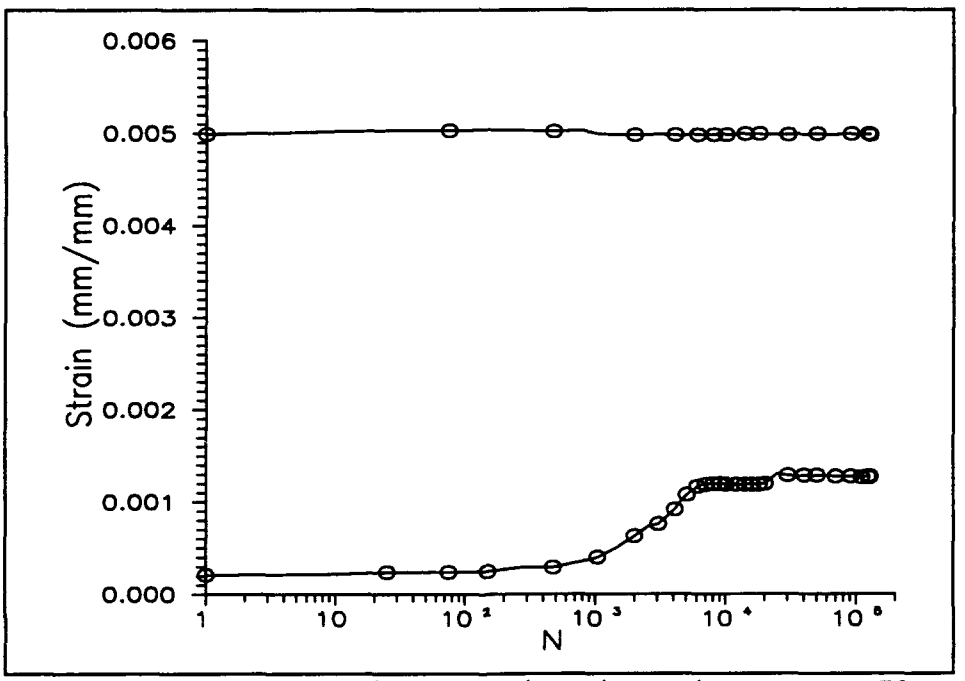

Figure A.9 0° Lamina Strain Histories, ϵ_{max}=.5%

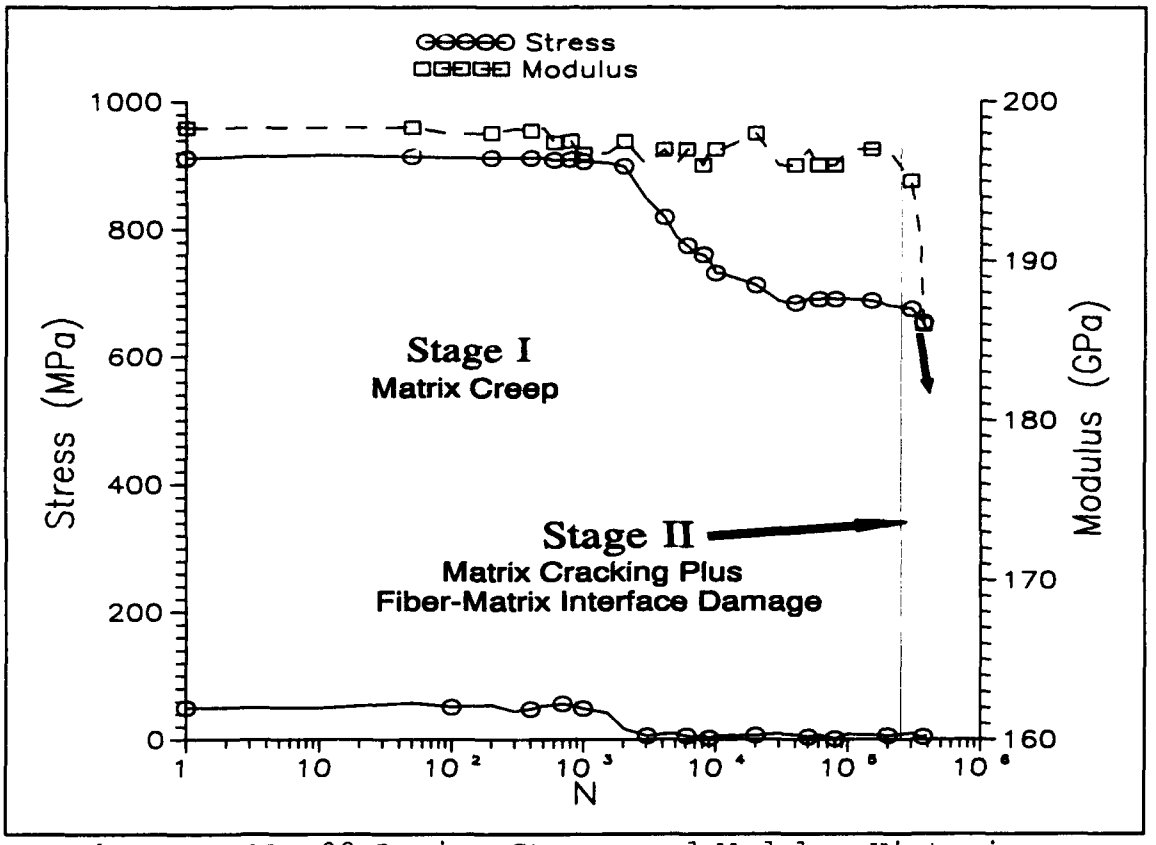

Figure A.10 0° Lamina Stress and Modulus Histories, ϵ_{max}= .45%

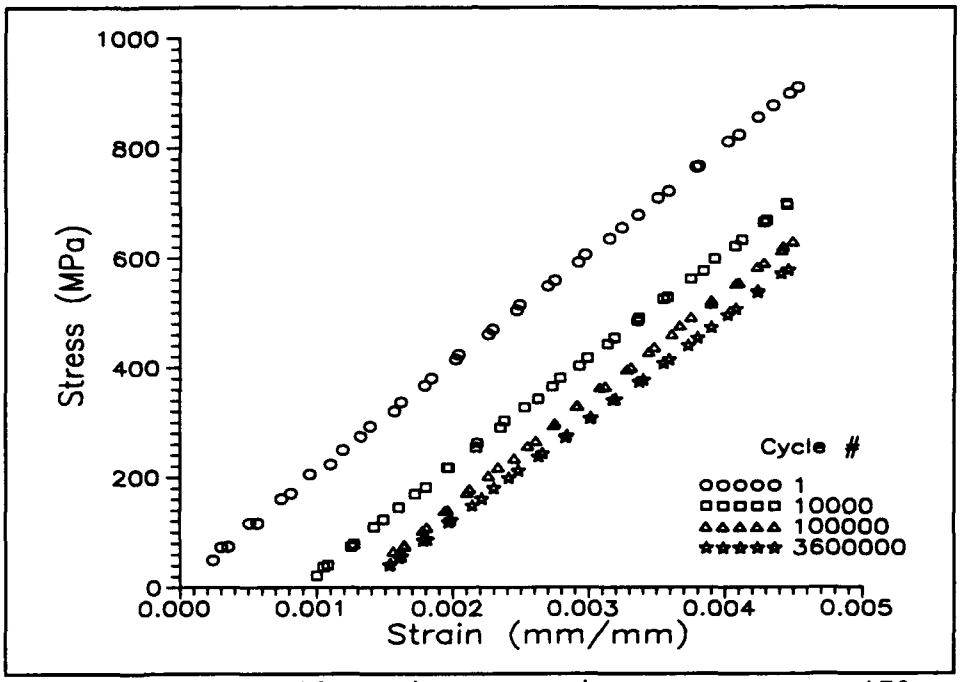

Figure A.11 0° Lamina σ-ϵ History, ϵ_{max} = .45%

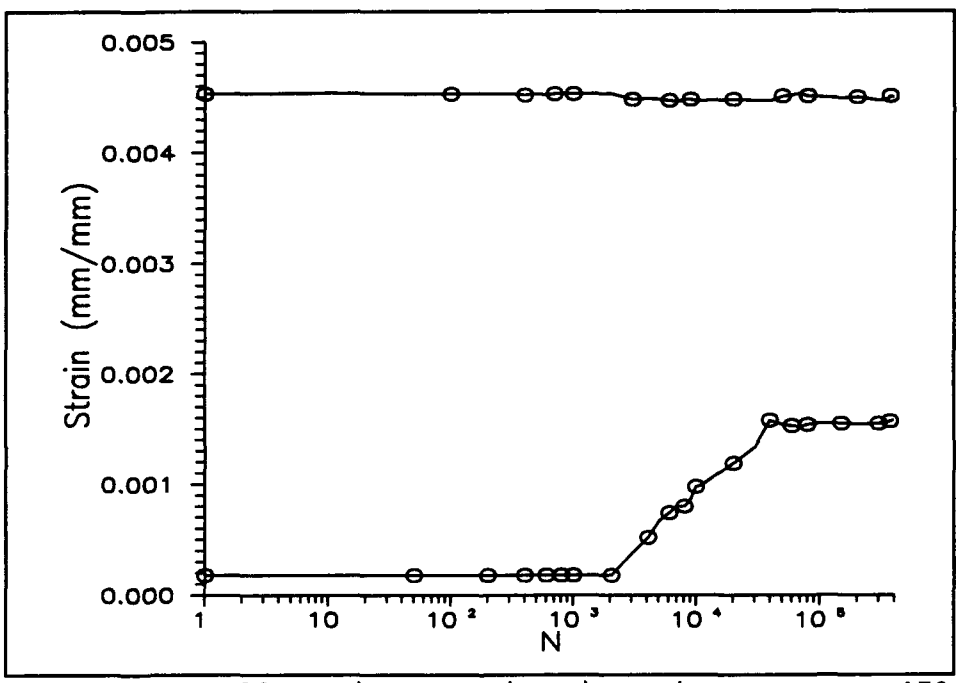

Figure A.12 0° Lamina Strain Histories, ϵ_{max} = .45%

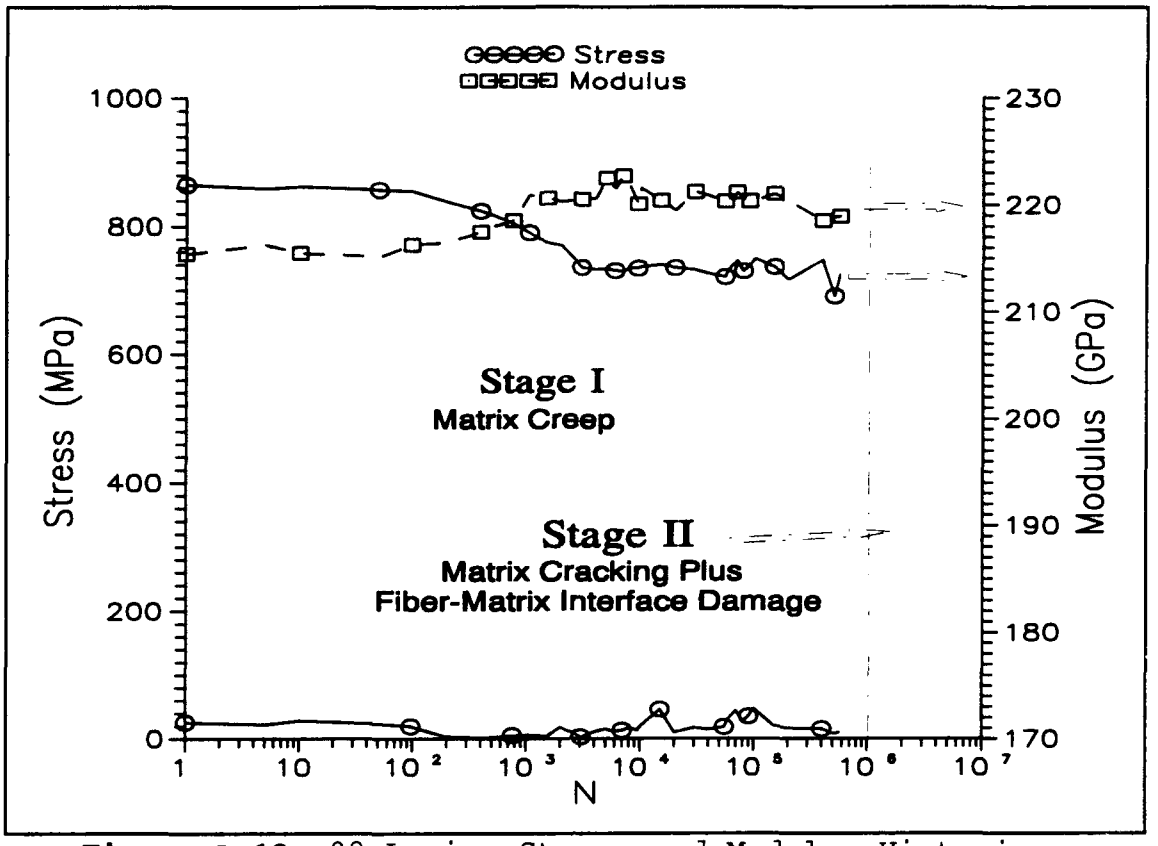

Figure A.13 0° Lamina Stress and Modulus Histories, ϵ_{max} = .4%

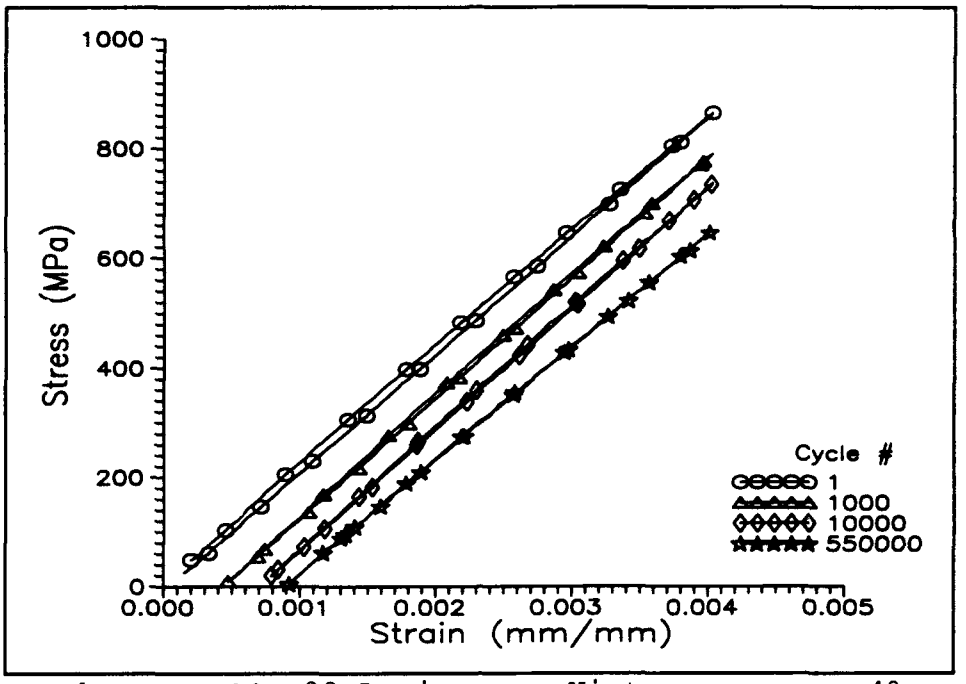

Figure A.14 0° Lamina σ-ϵ History, ϵ_{max} = .4%

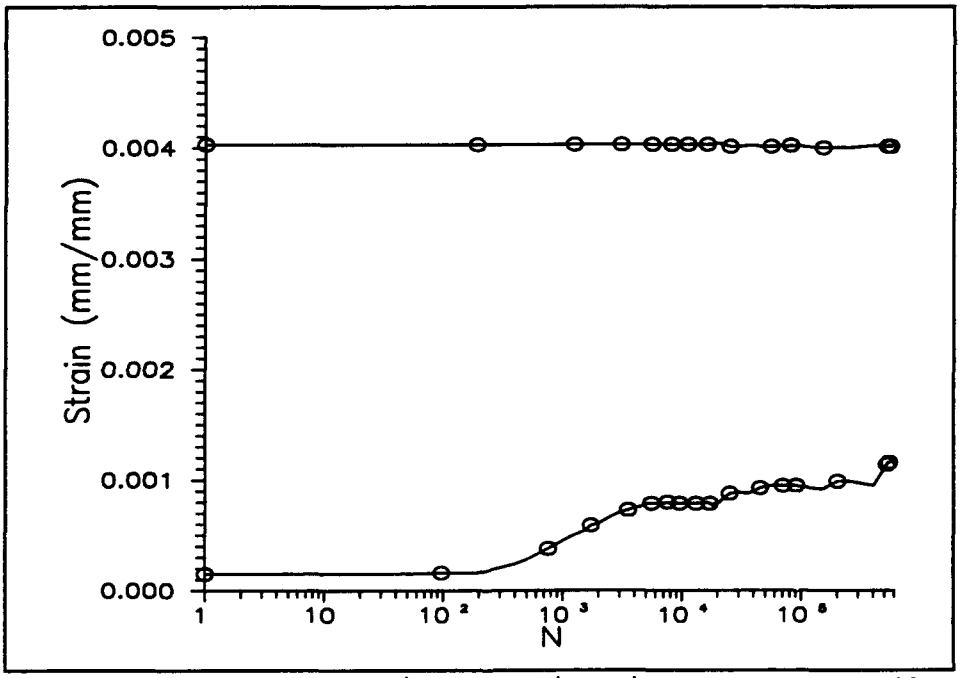

Figure A.15 0° Lamina Strain History, ϵ_{max}= .4%

Appendix B

Additional Experimental Results - 90° Lamina

This appendix contains additional raw data that was not presented in other locations of the document. This includes plots of the:

(1) Histories of the maximum strain and minimum strain for all of the specimens tested in fatigue

(2) Stress-strain response histories

(3) Histories of the minimum stress, maximum stress, and modulus showing the stages of damage and deformation as described in Chapter IV.

In all of the plots, the lines are drawn to show the data trend and are not predictions. An example is also included to show how the modulus was measured for the 90° specimens tested in fatigue.

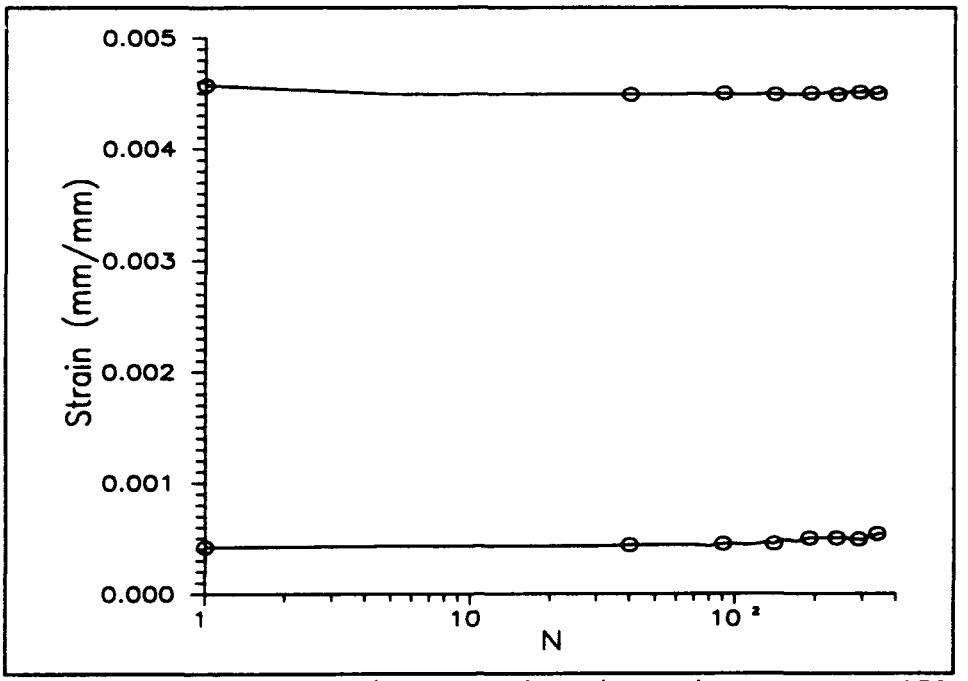

Figure B.1 90° Lamina Strain Histories, ϵ_{max}=. 45%

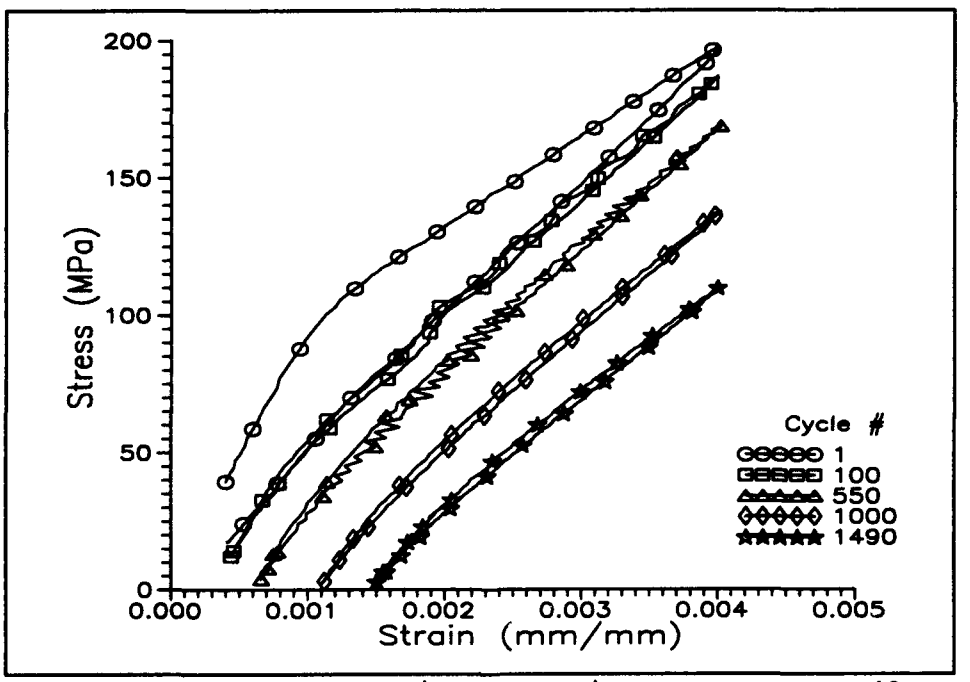

Figure B.2 90° Lamina σ-ϵ History, ϵ_{max} = .4%

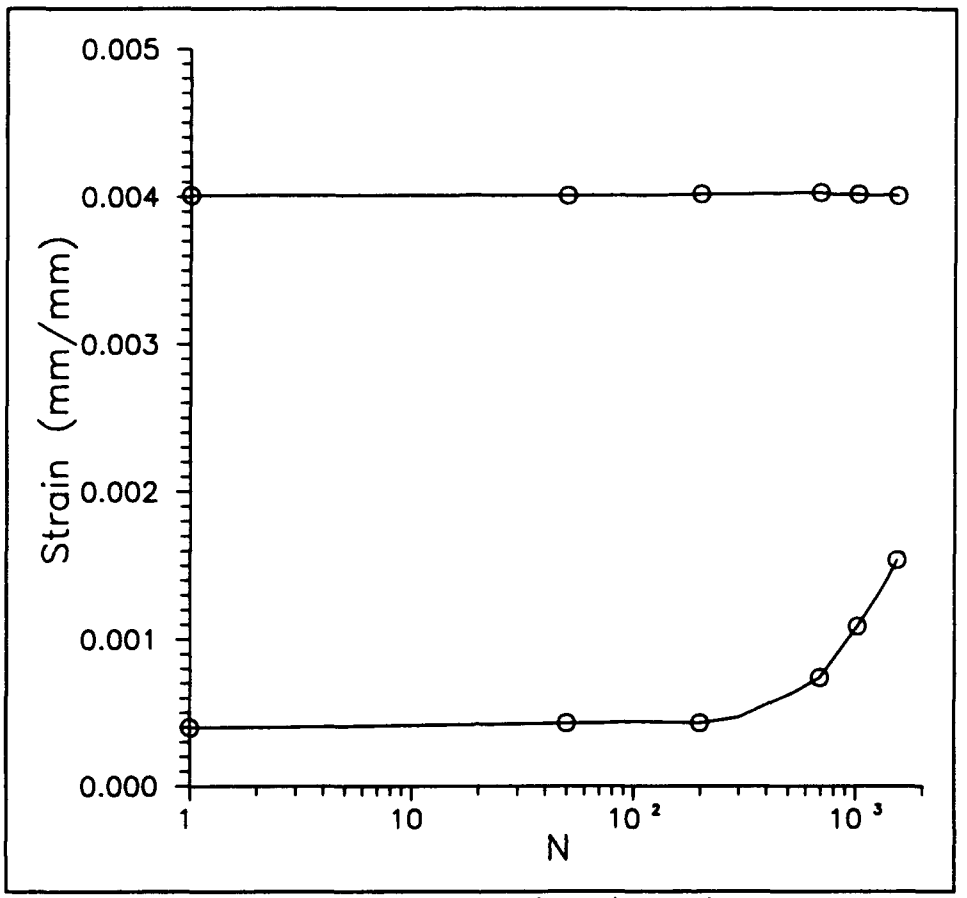

Figure B.3 90° Lamina Strain Histories, ϵ_{max}= .4%

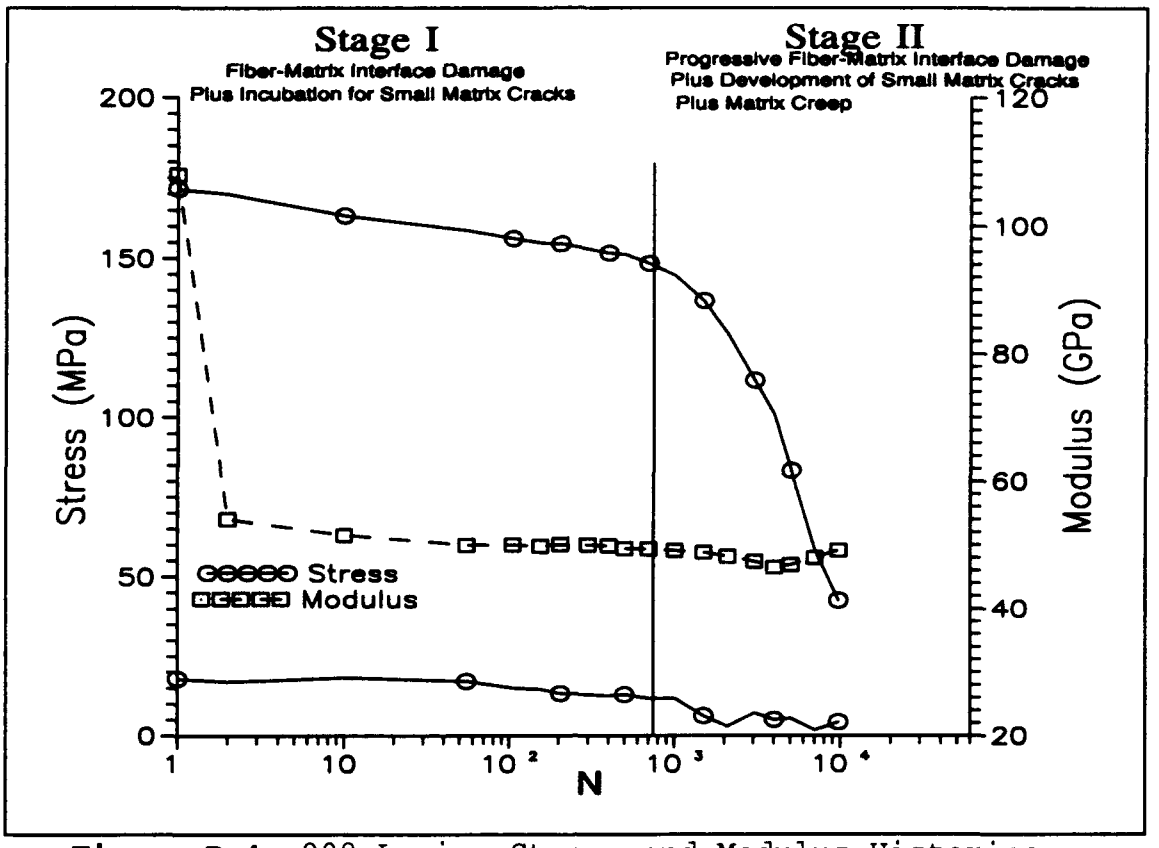

Figure B.4 90° Lamina Stress and Modulus Histories, ϵ_{max} = .3%

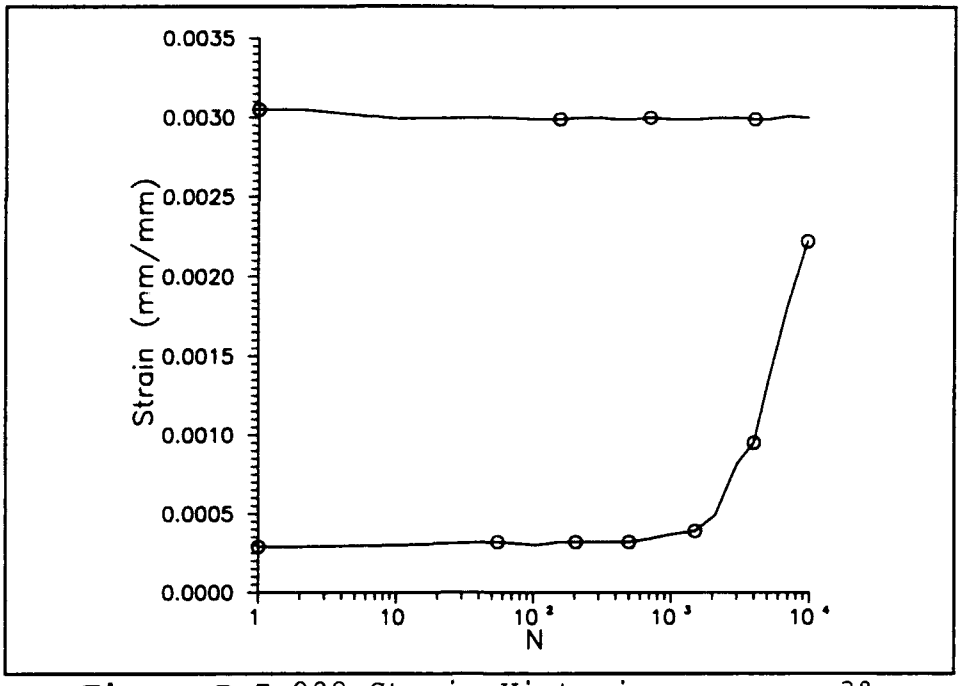

Figure B.5 90° Strain Histories, ϵ_{max} = .3%

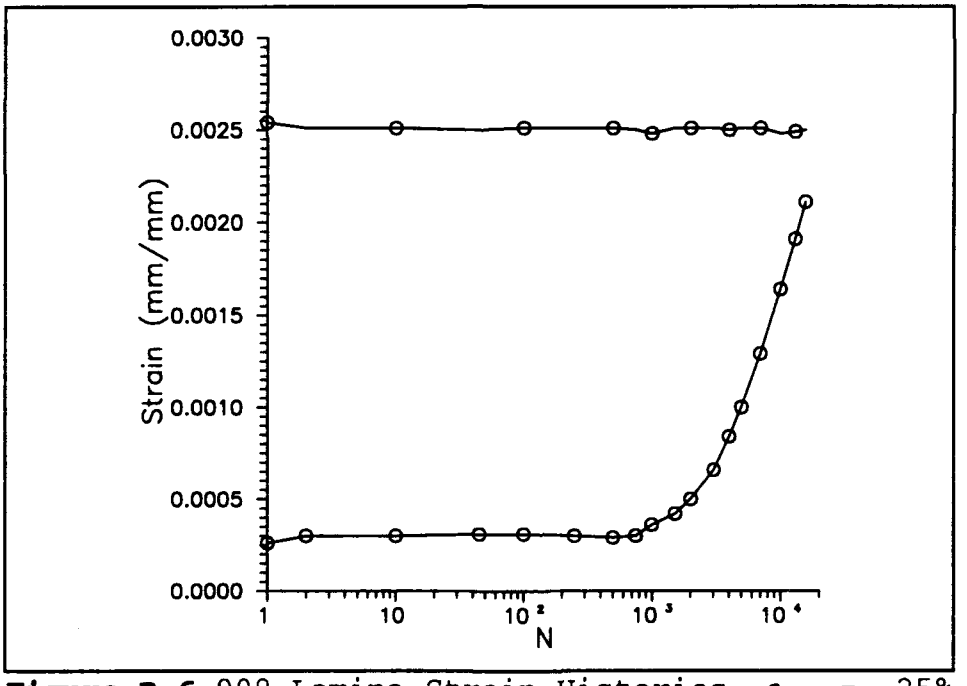

Figure B.6 90° Lamina Strain Histories, ϵ_{max} = .25%

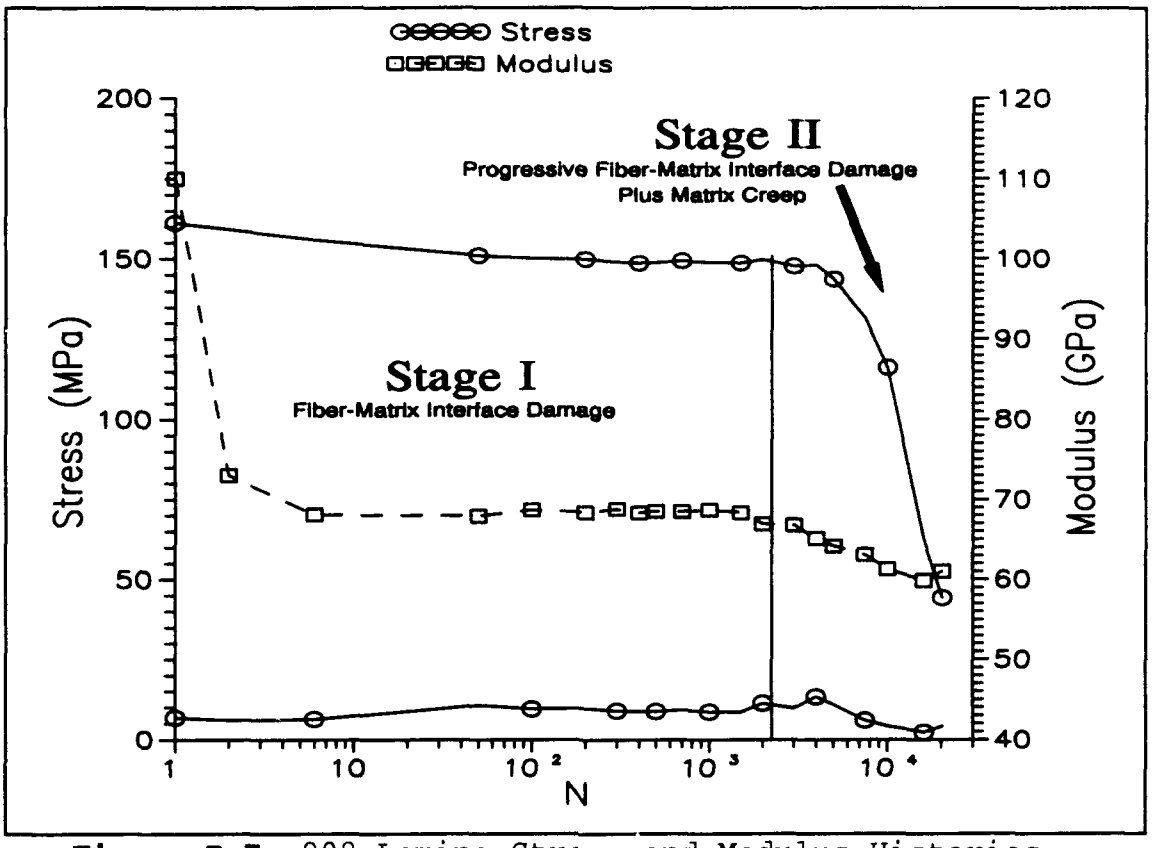

Figure B.7 90° Lamina Stress and Modulus Histories, ϵ_{max}= .2%

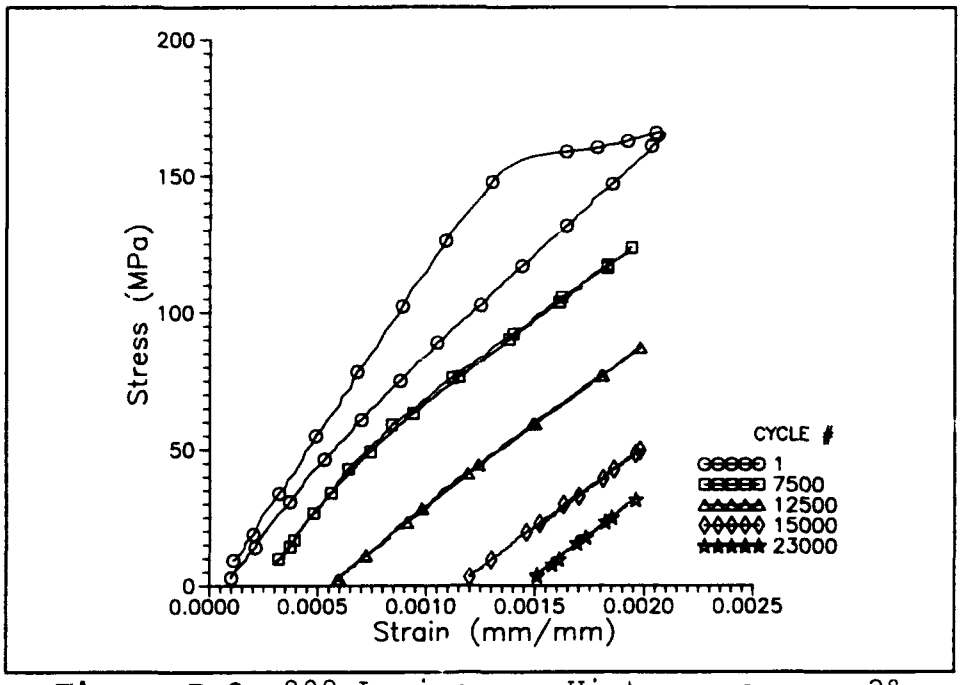

Figure B.8 90° Lamina σ-ϵ History, ϵ_{max} = .2%

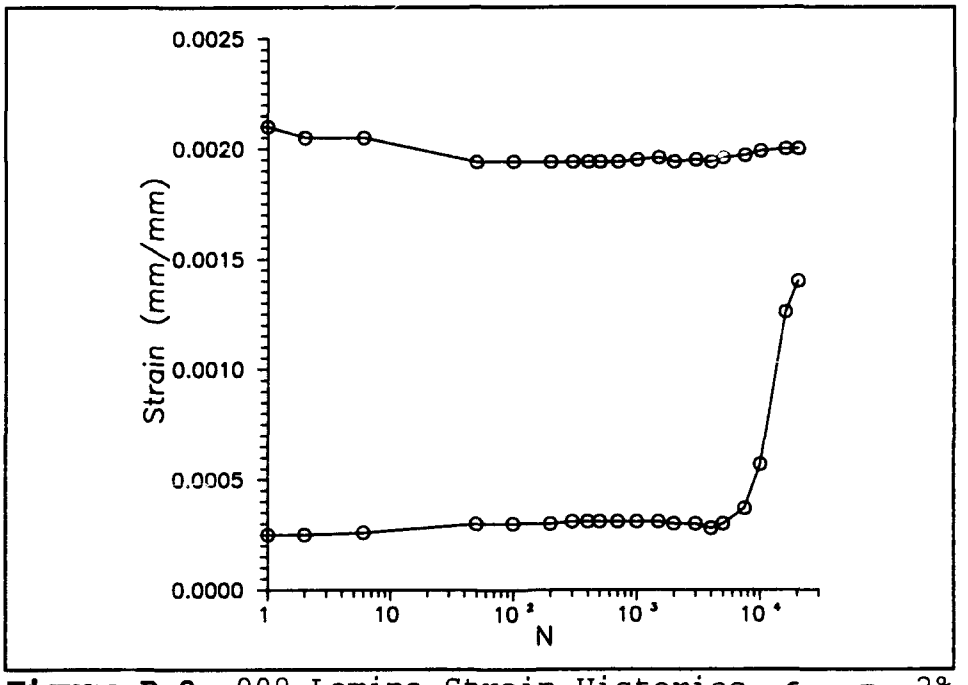

Figure B.9 90° Lamina Strain Histories, ϵ_{max} = .2%

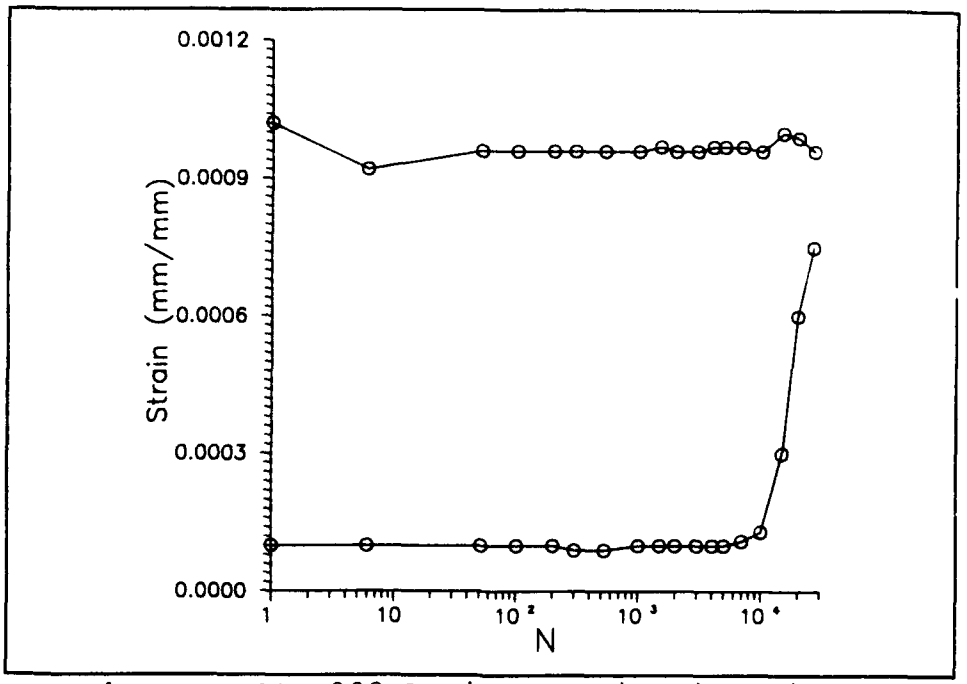

Figure B.10 90° Lamina Strain Histories, ϵ_{max} = .1%

Young Modulus Measurement - 90° Lamina

The stress-strain curves of the 90° specimens tested in fatigue at a maximum strain level greater than .1% were slightly nonlinear (Figure B.11). There are typically two choices to calculate the modulus for specimens that exhibit this behavior. The first is the secant modulus, which is defined as

$$E_s = \frac{\sigma_{max} - \sigma_{min}}{\epsilon_{max} - \epsilon_{min}} \qquad \textbf{(B.1)}$$

and the second is the least squares method. For this study, the latter approach was used. All of the stress and strain data over the fatigue cycle were used in the fit, except for

the first fatigue cycle. For the first fatigue cycle, only the initial linear loading portion of the curve was used. However, there was one graph were the first fatigue cycle unloading modulus curve was used (Figure 4.48). Figure B.11 shows the least square fits (solid lines) to the measured stress-strain data for a specimen subjected to fatigue at a maximum strain level of .3%. It can be observed that the least squares fit consistently gave a good representation of the specimen stiffness.

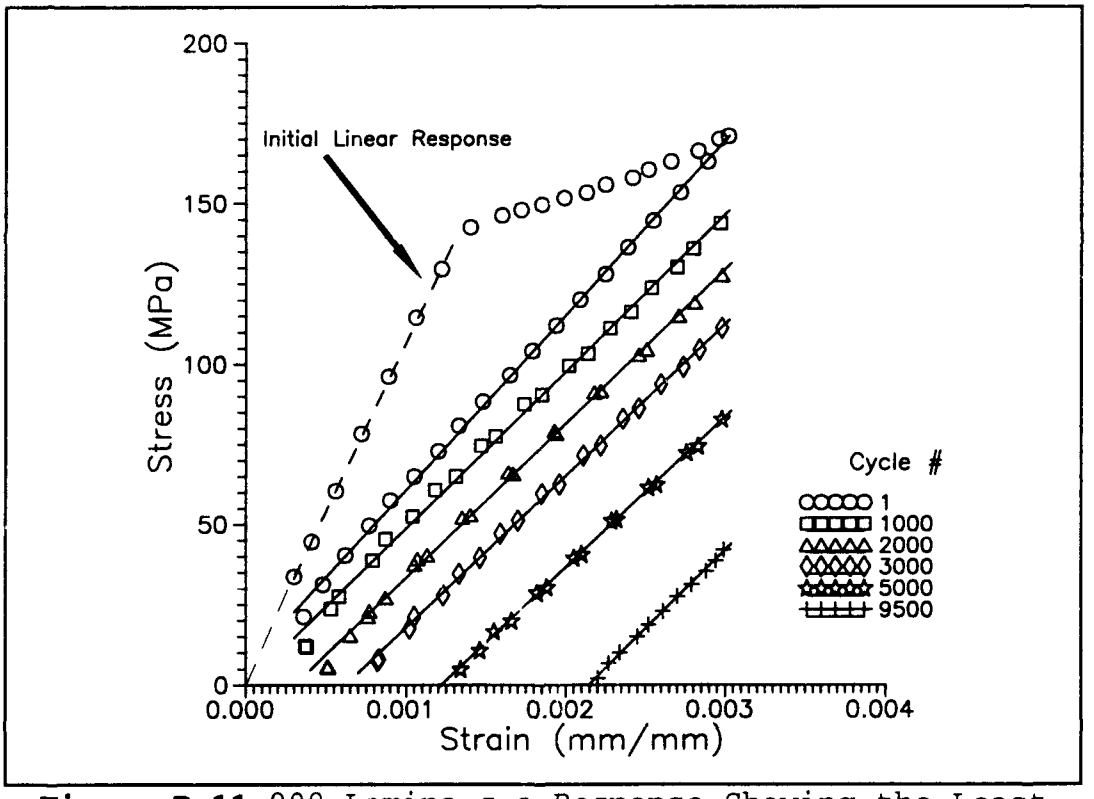

Figure B.11 90° Lamina σ-ϵ Response Showing the Least Squares Fits

Appendix C

Matrices and Vectors Used in The CCM

In Chapter V, Analysis, it was shown that two systems of equations, of the form [P]{x} = {b}, were solved to obtain the displacements in the CCM. Futher, the constitutive equations and the boundary conditions to develop these systems were reviewed. The methodology to develop these systems of equations was adapted from Reference 34 and are shown below.

First, when the cyclinder was allowed to deform freely in the longitudinal direction (i.e thermal expansion) the following 4x4 system of equations was solved:

$$[P] = \begin{bmatrix} r_f & -r_f & -\frac{1}{r_f} & 0 \\ 0 & k_{1m}+k_{2m} & \frac{(k_{2m}-k_{1m})}{r_m^2} & k_{2m} \\ -k_{1f}-k_{2f} & k_{1m}+k_{2m} & \frac{(k_{1m}-k_{1m})}{r_f^2} & k_{2m}-k_{2f} \\ 2r_f^2 k_{2f} & 2(r_m^2-r_f^2)k_{2m} & 0 & r_m^2 k_{1m}-r_f^2(k_{1m}-k_{1f}) \end{bmatrix} \quad \textbf{(C.1)}$$

$$\{b\} = \begin{Bmatrix} 0 \\ k_{tm}\alpha_m \\ (\alpha_m k_{tm}-\alpha_f k_{tf}) \\ k_{tf}\alpha_f r_f^2 + k_{tm}\alpha_m (r_m^2-r_f^2) \end{Bmatrix} \Delta T \quad \textbf{(C.2)}$$

where

$$K_{1i} = \frac{E(1-\nu)}{(1+\nu)(1-2\nu)}$$

$$k_{2i} = \frac{\nu E}{(1+\nu)(1-2\nu)} \qquad \textbf{(C.3)}$$

$$k_{ti} = \frac{E}{(1-2\nu)}$$

and i refers to m and f or the matrix and fiber properties, respectively, and

$$\{x\} = \begin{Bmatrix} C_{1f} \\ C_{1m} \\ C_{2m} \\ \epsilon_{th} \end{Bmatrix} \qquad \textbf{(C.4)}$$

where ϵ_{th} refers to the longitudinal thermal strain.

When a mechanical strain was applied the following 3x3 system of equations was solved:

$$[P] = \begin{bmatrix} r_f & -r_f & -\frac{1}{r_f} \\ 0 & k_{1m}+k_{2m} & \frac{(k_{2m}-k_{1m})}{r_m^2} \\ -k_{1f}-k_{2f} & k_{1m}+k_{2m} & \frac{(k_{1m}-k_{1m})}{r_f^2} \end{bmatrix} \qquad \textbf{(C.5)}$$

$$\{b\} = \begin{Bmatrix} 0 \\ -k_{2m} \\ k_{2f}-k_{2m} \end{Bmatrix} \Delta\epsilon \qquad \textbf{(C.6)}$$

$$\{x\} = \begin{Bmatrix} C_{1f} \\ C_{1m} \\ C_{2m} \end{Bmatrix} \qquad \text{(C.7)}$$

Appendix D

Flowcharts of the CCM and SM

This appendix contains flowcharts for the concentric cylinder model (CCM) and the strip model (SM). The details of these models were explained in Chapter IV.

CCM FLOWCHART

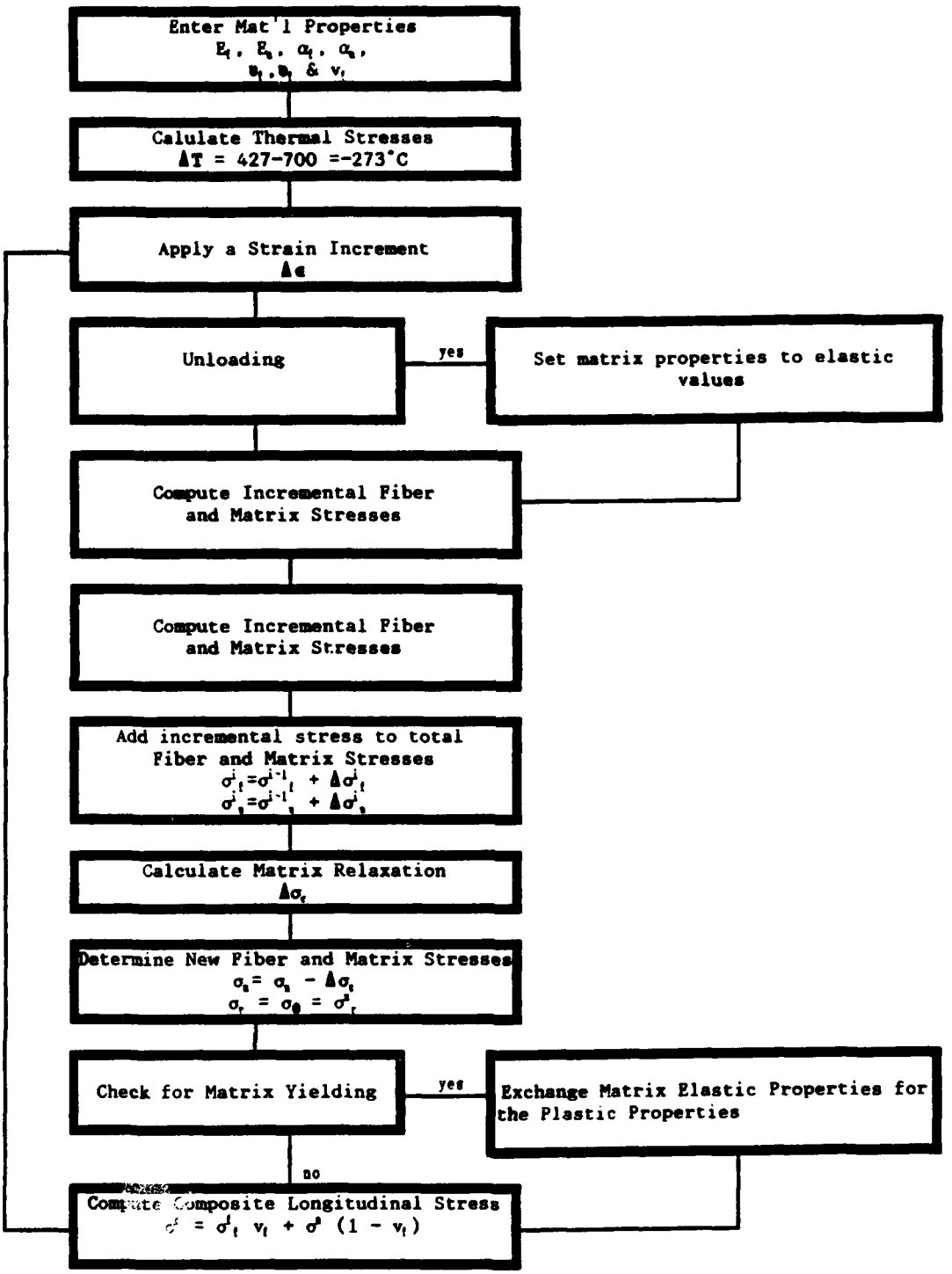

SM FLOWCHART

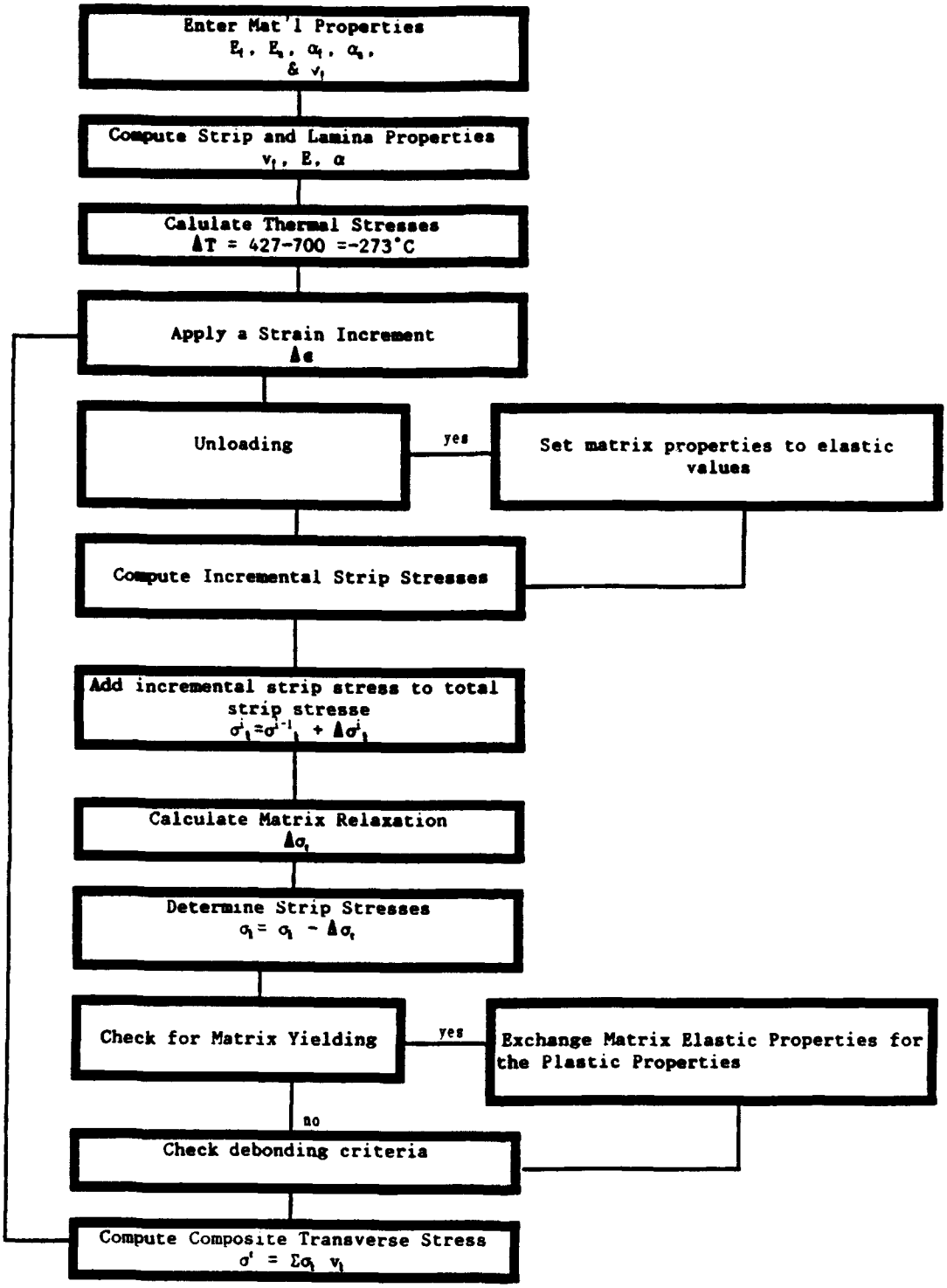

Vita

Captain Brian P. Sanders was born July 12, 1959 in Westfield, New Jersey. He graduated from Westfield High School in 1977 and entered the USAF in 1980. His first tour of duty was at Holloman AFB, New Mexico. There he was a weapons team crew chief in the 479th AGS. In 1985, he graduated from the University of Southern California with a Bachelor of Science in Aerospace Engineering, then graduated from Officer Training School in October of the same year. His first tour of duty as a commissioned officer was at WPAFB, Ohio. There he was a logistics engineer in the Short Range Attack Missile II Program Office. He graduated from the University of Dayton in 1987 with a Master of Science in Aerospace Engineering. He entered the Graduate School of Engineering of the Air Force Institute of Technology in June of 1989.

Permanent Address: 2841 N. Ocean Blvd
Fort Lauderdale, Fla 33308

REPORT DOCUMENTATION PAGE

Form Approved
OMB No 0704-0188

1. AGENCY USE ONLY (Leave blank)	2. REPORT DATE	3. REPORT TYPE AND DATES COVERED
	December 1993	Dissertation

4. TITLE AND SUBTITLE
Characterization of Fatigue Damage In A Metal Matrix Composite (SCS-6/Ti-15-3) At Elevated Temperature

5. FUNDING NUMBERS

6. AUTHOR(S)
Captain Brian P. Sanders, USAF

7. PERFORMING ORGANIZATION NAME(S) AND ADDRESS(ES)
Air Force Institute of Technology
Wright-Patterson AFB, OH 45433-7765

8. PERFORMING ORGANIZATION REPORT NUMBER
AFIT/DS/AA/93-4

9. SPONSORING/MONITORING AGENCY NAME(S) AND ADDRESS(ES)
Dr. Walter Jones
AFOSR/NA
Bolling AFB, DC 20322-6448

10. SPONSORING/MONITORING AGENCY REPORT NUMBER

11. SUPPLEMENTARY NOTES

12a. DISTRIBUTION/AVAILABILITY STATEMENT
Approved for public release; distribution unlimited

12b. DISTRIBUTION CODE

13. ABSTRACT *(Maximum 200 words)*

The fatigue characteristics of a unidirectional titanium based metal matrix composite (MMC) were investigated at elevated temperature (427°C). A hybrid strain controlled loading mode was used to subject the 0° and 90° laminas to fatigue. Along with the fatigue tests, microscopy and analytical modeling were also conducted. This combination of activities led to defining the initiation and progression of damage and deformation in the MMC. When loading was parallel to the fiber direction, the fatigue behavior was initially dominated by creep deformation of the matrix. Then, depending on the maximum strain, specimen failure was the result either fiber fractures or matrix cracking. In contrast, when loading was perpendicular to the fiber direction, the fatigue response was first dominated by the initiation of fiber-matrix interface damage. Then, if the maximum strain was above .35%, the dominant damage mechanism was matrix cracking. Below this strain level, the damage was a mixture of matrix microcracks and the progression of fiber-matrix interface damage. The analysis for this fiber orientation included unique methods to model the interface damage. This hybrid approach involving experiments, microscopy, and analytical modeling provided better understanding of the fatigue behavior of the MMC.

14. SUBJECT TERMS	15. NUMBER OF PAGES
Metal Matrix Composites, Fatigue, Damage, Strain control	321
	16. PRICE CODE

17. SECURITY CLASSIFICATION OF REPORT	18. SECURITY CLASSIFICATION OF THIS PAGE	19. SECURITY CLASSIFICATION OF ABSTRACT	20. LIMITATION OF ABSTRACT
Unclassified	Unclassified	Unclassified	UL